AN ABSTRACT OF THE THESIS OF

TZER-HSIANG HUANG (name) for the DOCTOR OF PHILOSOPHY (degree)

in CHEMISTRY (major) presented on June 9, 1972 (date)

Title: Infrared and Raman Spectra of Solid Phosphine

Redacted for privacy

Asbtract approved: Dr. J. C. Decius

The IR spectra of the liquid and the α phases of PH_3, and the IR and the Raman spectra of the δ, β, and γ phases of PD_3 and PH_3 have been recorded. It was found that the δ form of PH_3 did not undergo any phase change between 30.29°K and 4°K. The transition between the α and the β phases of PH_3 is believed to be a disorder-to-disorder one, whereas the δ-β and γ-β transitions of both PH_3 and PD_3 involve a change between the ordered and disordered crystal structures. The configurational entropy of the β phase of PH_3 is removed at the λ-point which is chatacterized by the freezing-in of the β phase observed unequivocally in the Raman δ-β phase transition experiment. The difficulty of the β to γ transition of PH_3 suggests that a crystal repacking is involved. Assuming that the crystal is repacked in the hexagonal form, the most probable space groups of the γ phase are D_{3h}^2, D_{3h}^4, and D_{6h}^2, site group being definitely C_s. The site symmetry of the δ phase can not be C_s.

The transition temperatures of solid PD_3 are similar to those of solid PH_3. The $\gamma \rightarrow \beta$ and δ-β transition points of PD_3 are 56±1°K

and 33±1°K respectively. Vibrational spectroscopy gives no appreciable evidence for the λ-transition. The δ and β phases, particularly the latter, of PD_3 are rather unstable with respect to the γ phase.

A vibrational coordinate analysis has been performed on PH_2D and PHD_2 isolated in solid PH_3 and PD_3, using the most general force field within the harmonic approximation. The calculated frequencies agree with observation quite well.

It was found that the δ phase film of PH_3 contained small domains which were in the γ phase.

Infrared and Raman Spectra of Solid Phosphine

by

Tzer-hsiang Huang

A THESIS

submitted to

Oregon State University

in partial fulfillment of
the requirements for the
degree of

Doctor of Philosophy

June 1973

APPROVED:

Redacted for privacy

Professor of Chemistry
in charge of major

Redacted for privacy

Chairman of Department of Chemistry

Redacted for privacy

Dean of Graduate School

Date thesis is presented June 9, 1972

Typed by Tzer-hsiang Huang and Mrs. Carol Miller

ACKNOWLEDGMENTS

First, I would like to heartily extend my gratitude to Dr. J. C. Decius for his inspiration and guidance in the last five years. My sincerest thanks are also due to Dr. J. W. Nibler who helped my experimentation, computer calculations, etc. I would also like to thank Dr. R. E. Carlson and Mr. R. D. Cooke for helpful discussions. My gratitude is also extended to Miss Karen Grant for correcting the English in the first draft of this thesis. The friendship with Mr. Duane Starr has been delightful. My wife deserves particular credit for enabling me to concentrate wholeheartedly on course work and research.

I want to thank the National Science Foundation for providing partial financial support for my thesis project. As a student from Taiwan, I want to thank also the Department of Chemistry, Oregon State University, Oregon State, the U. S. A. for allowing me to study here.

TABLE OF CONTENTS

I.	INTRODUCTION	1
II.	GASEOUS SAMPLE PREPARATION	4
	Preparation of PH_3	4
	Preparation of PD_3	6
	Preparation of Matrix Isolated Species	8
	General Comments on the Gaseous Samples	11
III.	LOW TEMPERATURE INFRARED AND RAMAN EXPERIMENTS	12
	Sample Preparation	12
	Sample Made from Liquid	12
	Sample Deposited from Gas	15
	Temperature Measurement	17
	Windows	21
	Integrated Absorption Intensity Measurement	22
	Specular Reflection Spectrum	23
	Low Temperature Raman Sampling Optics	24
IV.	INSTRUMENTATION	29
	Beckman IR 7	29
	Cary 82	31
	Cryo-Tip	33
	Displex TM Cryogenic Refrigerator	38
V.	SPECTRA OF PHASE TRANSITIONS	44
	PH_3	44
	PD_3	61
VI.	THE INFRARED AND RAMAN SPECTRA OF SOLIDS PD_3 and PH_3	66
	The Survey Scans	66
	PH_3	66
	PD_3	91
	The High Resolution Scans	94
	PH_3	94
	PD_3	118
VII.	COMBINATIONS AND OVERTONES	127
IIX.	THE INTERMOLECULAR VIBRATIONS	134
	The Beta, Supercooled Beta, and Delta Phase	134
	The Gamma Phase	137
IX.	THE INFRARED AND RAMAN SPECTRA OF THE ISOLATED SPECIES	145
	Frequency Calculation of PH_2D and PHD_2 Isolated in Solid PH_3 and PD_3	145
	Spectra of PH_2D and PHD_2 Isolated in Solid PH_3 and PD_3	151
	Spectra of PH_3 Isolated in Solid PD_3 and Vice Versa	159

TABLE OF CONTENTS (Continued)

X.	PHASE TRANSITIONS AND STRUCTURAL INTERPRETATION	166
	Phase transitions	166
	The gas-liquid, liquid-alpha, and alpha-beta transitions	167
	The beta-gamma transition	169
	The beta-delta transition	172
	The gamma phase structure deduction	176
	Interpretation of the ν_2 spectrum of the delta phase	183
	Inversion is unlikely	183
	Hindered rotation	187
	Many molecules per unit cell	191
	APPENDIX	192
	BIBLIOGRAPHY	213

LIST OF FIGURES

Figure		Page
1.	Heat capacity (C_p) in calories per degree per mole of PH_3	1
2.	Specular reflection optics	23
3.	Low temperature Raman sampling optics	25
4.	Intermolecular-spectrum variation of solid HCl relative to the angle between the incident beam and the substrate surface	26
5.	The helium-hydrogen expansion Cryo-Tip	34
6.	The Displex TM Cryogenic Refrigerator	39
7.	The PV diagram for the Displex TM Cryogenic Refrigerator	40
8.	The elementary cooling circuit for the Displex Refrigerator	40
9.	A schematic diagram of the expander (first stage only) of the Displex TM Cryogenic Refrigerator	42
10.	The β-to-γ transition of PH_3 observed in the IR ν_2 region	45
11.	The δ-to-γ transition of PH_3 observed in the IR ν_2 region	46
12.	The sequence of the β-to-δ, δ-to-β, and γ-to-β transitions of PH_3 observed in the IR ν_2 region	47
13.	The γ-to-β transition of PH_3 observed in the Raman ν_2 region	48
14.	The γ-to-β and β-to-δ transitions of PH_3 observed in the Raman lattice region	49
15.	The δ-to-β transition of PH_3 observed in the Raman stretching region	50
16.	The spectrum variation in the ν_2 region of PH_3 due to rapid temperature drop below its lambda point.	51

Figure		Page
17.	The γ-to-β , β-to-δ, δ-to-β, and β-to-γ transitions of PD_3 observed in the IR ν_2 region	52
18.	The γ-to-β transition of PD_3 observed in the Raman ν_2 region	53
19.	The β-to-γ-to-β transition of PD_3 observed in the Raman lattice region	54
20.	The survey scans of the liquid and α phases of PH_3 observed in the infrared	72
21.	The survey scans of the β and δ phases of PH_3 observed in the infrared	73
22.	The survey scans of the δ phase of PH_3 observed in the infrared	74
23.	The survey scans of the β phase of PH_3 observed in the Raman	75
24.	The survey scans of the supercooled β phase of PH_3 observed in the Raman	76
25.	The survey scans of PH_3 (mostly in the γ phase) observed in the Raman	77
26.	The survey scans of PD_3 (in different phases) observed in the infrared	78
27.	The survey scans of PD_3 (in the β and δ phases) observed in the infrared.	79
28.	The survey scans of PD_3 (in the β and γ phases) observed in the Raman	80
29.	The IR-spectrum-variation of the ν_2 of solid PH_3 relative to deposition condition	95
30.	The ν_2 IR and Raman spectra of δ-PH_3	96
31.	The ν_2 IR and Raman spectra of δ-PD_3	97
32.	The ν_2 IR spectrum of δ-PH_3 obtained by conventional transmission and specular reflection	98
33.	The ν_2 IR and Raman spectra of γ-PH_3	99

Figure		Page
34.	The ν_2 IR and Raman spectra solid PD_3	100
35.	The ν_4 IR and Raman spectra of solid PH_3	101
36.	The ν_4 IR and Raman spectra of solid PD_3	102
37.	The ν_1 and ν_3 spectra of PH_3 in IR and Raman	103
38.	The ν_1 and ν_3 spectra of PD_3 in IR and Raman	104
39.	The combination-overtone spectra of PD_3 in IR	131
40.	The combination-overtone spectra of PD_3 in IR	132
41.	The lattice spectrum of PH_3	135
42.	The lattice spectrum of PD_3	136
43.	The IR and Raman spectra of isolated PHD_2 and PH_2D	155
44.	The IR spectrum of isolated PH_3	160
45.	The IR spectrum of isolated PD_3	161
46.	The potential function of an inversion doubling system	185
47.	The relative vibration-rotation line intensity in the IR ν_2 region of a hypothetical PH_3 gas at 20°K	188
48.	The relative vibration-rotation line intensity in the IR ν_2 region of a hypothetical PH_3 gas at 4°K	189

LIST OF TABLES

1. Vibrational frequencies of PH_3 and PD_3 in the γ phase 67

2. Vibrational frequencies of PH_3 and PD_3 in the δ phase 69

3. Vibrational frequencies of PD_3 in the β phase and PH_3 in the liquid, α, and β phases 71

4. Vibrational frequencies of the isolated PH_2D, PHD_2, PH_3, and PD_3 152

5. Infrared frequencies of PH_3 isolated in the inert-gas-matrices 154

INFRARED AND RAMAN SPECTRA OF SOLID PHOSPHINE

I. INTRODUCTION

Solid phosphine has been studied previously by Hardin and Harvey(hereafter HH)(1), Von A. Heinemann(2), Marie D. Francia(3), and Stephenson and Giauque(hereafter SG)(4). The thermodynamic investigation by SG reveals that solid phosphine exists in the following phases(the phase designations are those of HH):

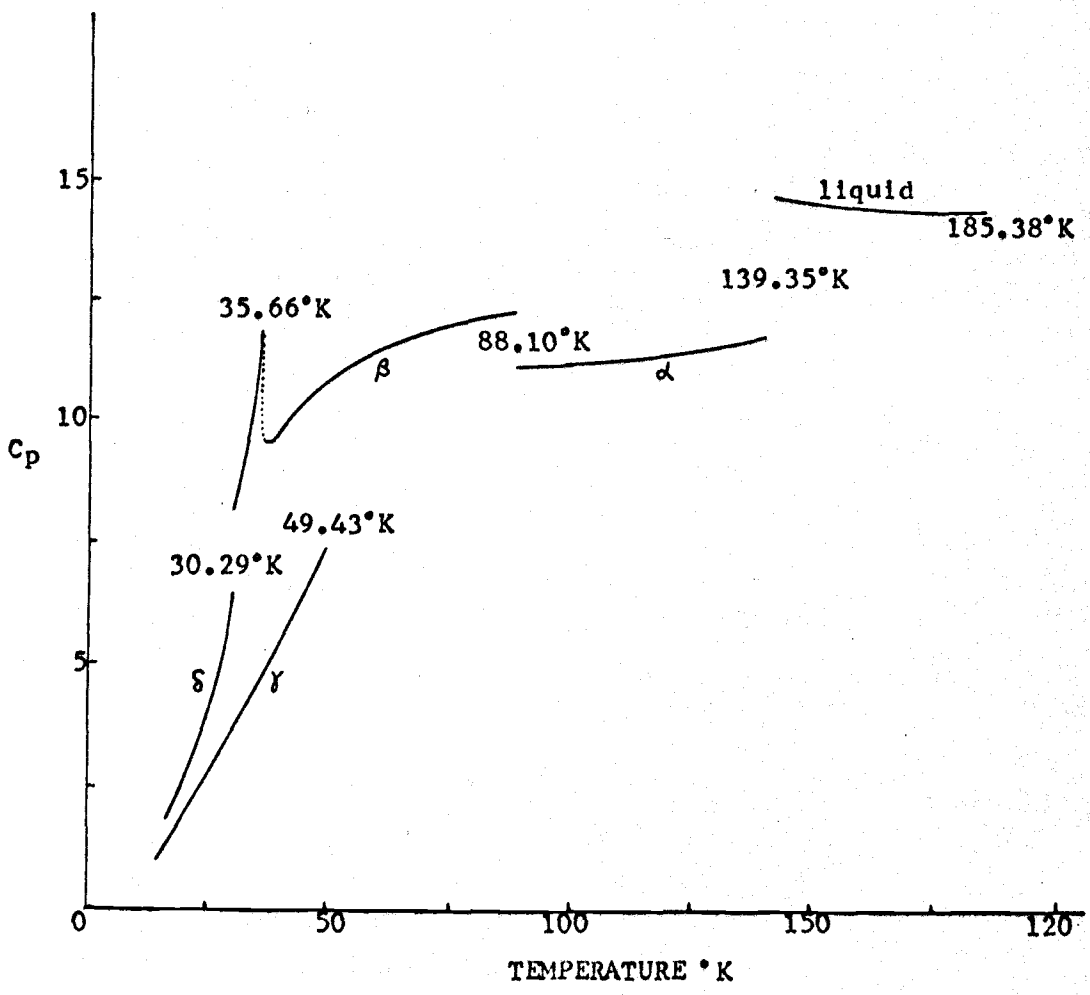

Figure 1. Heat capacity(C_p) in calories per degree per mole of PH_3 (ref. 4)

According to the diagram, the beta phase exists between 88.1 °K and 30.28°K, while the delta phase exists between 30.29°K and 0°K. However, HH found a difference in the spectrum taken at nominal temperature of 25°K and 4°K, which seems to imply the existence of a new phase with a transition temperature somewhere below 25°K. Evidence to be presented later in this thesis will show that the two spectra reported by HH in fact undergo a transition near 29°K, not below 25°K, and are therefore the calorimetrically known phases, beta and delta. Most probably HH encountered a temperature error. Moreover, HH did not observe any spectral change accompany- the alpha-beta transition, but SG asserted that the characteristic heat capacity curve between 25°K and 35°K was associated with molecular rotation. One of the main reasons for undertaking this project was to study the various phases of phosphine and to clarify the phase transitions.

SG concluded that the phosphine molecules rotate in the beta phase. However, HH found no indication of molecular rotation. Instead, they argued from the band half-widths that the form existing above 10°K has some degree of disorder(but vide supra). This is in contradiction with SG's demonstration that the entropy of both the delta and gamma phases can be extrapolated to zero as the temperature approaches zero. Therefore, in accord with the third law of thermodynamics, these two phases must be perfect crystals.

We were also interested in determining whether or not the phosphine molecules rotate in inert gas matrices.

Further, HH showed that the nondegenerate bending mode of phosphine exhibits about 10 fine bands below 10°K, while the degenerate bending and stretching bands are primarily broad. If the 10-peak structure of ν_2 is reversible, the interpretation will be challenging.

Solid PD_3 was also investigated to see if this 10-peak structure was unique for solid PH_3 or not. Another reason for the PD_3 investigation was to find out if solid PD_3 has phase transitions similar to those of PH_3. Finally, the frequencies of solid PD_3 were used to calculate the most general force field of the system. Solid AsH_3 was also studied briefly to see if it has multiplet structure in the ν_2 region, but none was found.

II. GASEOUS SAMPLE PREPARATION

Preparation of PH_3

The phosphine samples were prepared by simply dropping water onto calcium phosphide in a high vacuum system constructed entirely of glass. The equation for the reaction is

$$6H_2O + Ca_3P_2 \longrightarrow 3Ca(OH)_2 + 2PH_3.$$

Although this reaction does give rise to some by-products such as H_2, P_2H_4, and yellow phosphorus, it is preferred to the following reaction which generated purer PH_3.

$$PCl_3 + LiAlH_4 \longrightarrow PH_3 + \text{etc.}$$

because of the simplicity and the lower prices of the reactants. Moreover, the impurities can be easily separated by vacuum distillation.

The preparation system is described as follows: A one-column mercury manometer and a dropping funnel containing the proper amount of water and tightly sealed with a ground glass stopper were connected to two of the three standard tapers of the reaction flask. The third standard taper was connected, in sequence, to C_2H_5OH-liquid N_2 slush baths 1 and 2, a gas sample bulb to collect produced PH_3, a two-column manometer, a vacuum gauge, and liquid N_2 trap to prevent corrosive gases from entering the pumps. The slush bath 1 was next to the reaction flask. High vacuum stopcocks were install-

ed at proper places to guarantee operational convenience.

The calcium phosphide, about 20 grams, of Alfa Inorganics, Inc. was placed in the three-mouth reaction flask. The calcium phosphide is usually in the form of small balls. To help water get to the core of the balls, a magnetic stirrer was also placed in the flask. After the whole system had been subjected to a vacuum of better than $1X10^{-5}$ mm Hg overnight, distilled water(about 50 grams) contained in the dropping funnel was admitted slowly to the flask. Air dissolved in the distilled water was removed by bubbling pre-purified nitrogen through the water for several minutes and then quickly putting the greased ground-glass-stopper on the dropping funnel. During the whole course of reaction, the stopper was kept closed. The one-column manometer measured the pressure inside the reaction flask. On one occasion, the reaction flask was kept open to the liquid nitrogen trap, which acted as a pump. The pressure in the reaction system was low, and the yield thus obtained was very poor. From then on, the flask pressure was kept as high as possible. The reaction was usually complete in about half an hour. Most of the reaction by-products, P_2H_4 and P_4, and the unreacted water were trapped in slush bath 1.Only a very small amount passed over to bath 2. All of the PH_3 product was condensed at the cold finger of the storage bulb by a liquid nitrogen bath. Hydrogen produced in the reaction could not be trapped by any of the baths, so it was usually pumped away. At the end of the preparation, a great deal of the yellowish residue was observed on the inside of the

glass system between bath 1 and the reaction flask and also in the flask itself. About 100 ml X 760 mm Hg of phosphine was produced usually in this way.

The phosphine sample so produced was further subjected to vacuum distillation through an ethanol-liquid nitrogen slush bath several times before storing. In all the infrared and Raman runs, the sample was always purified immediately before use, either by vacuum distillation or by first trapping all the material in the sample bulb which was already at the deposition position in a liquid nitrogen bath, next pumping away any uncondensable gases, and finally exchanging the liquid nitrogen bath with a ethanol-liquid nitrogen bath. At this bath temperature, the vapor pressure of P_2H_4 is negligible compared with that of PH_3. The PH_3 vapor, which has a finite pressure at this temperature, was allowed to deposit on the precooled substrate.

Preparation of PD_3

The procedure is essentially the same as that used for the preparation of phosphine except that 99.8 mole percent heavy water of Bio-Rad Laboratory was used in place of water, and steps were taken to reduce any possible sources of hydrogen. The dropping funnel was replaced with a small, glass, matrix-isolation-tube whose volume usually ranges from about 5 ml to about 20 ml, depending on how concentrated the matrix-isolated species will be. The MI tube used was first pumped down to better than $1X10^{-5}$ mm Hg

for days and then exposed to heavy water molecules overnight in order to exchange all hydrogen atoms on the interior of the tube and in the Apiezon N stopcock grease with the deuterium atoms in heavy water. The same precautions were also taken for the whole vacuum system in preparing phosphine-d_3. Moreover, the first batch of the sample produced was usually discarded.

In working with isotopic species, it is always desirable to separate the storage glassware used for one isotopic species from that used for another isotopic species. The two-column manometer was specially designed to allow use of one column for the D species and the other column for the H species.

Although every conceivable precaution was taken to reduce the hydrogen content in the PD_3 sample, the 20°K spectrum still showed some PHD_2 and tiny amount of PH_2D. The existence of these two intermediate species complicates the assignment of the spectra of their stretching vibrations. An effort was then made to try to replace the residual H atoms in the PD_3 sample with D atoms.

R. E. Weston(5) mentioned the feasibility of the following reaction.

$$PH_2D(g) + H_2O(1) \rightleftharpoons PH_3(g) + HDO$$

We have tried to carry out the reaction

$$PD_2H(g) + D_2O(1) \rightleftharpoons PD_3(g) + HDO$$

using D^+ as the catalyst, which was obtained from the following reaction :

$P_2O_5 + 3D_2O \rightleftharpoons 2D_3PO_4$.

To carry out the exchange, the matrix-isolation bulb containing heavy water(99.8 mole percent), a reaction flask containing P_2O_5 and a stirring bar, and the gas sample bulb containing mostly PD_3, some PHD_2, and very little PH_2D, were connected, in parallel, to the pumping system. The exchange system was first pumped down to better than $1X10^{-3}$ mm Hg for at least 24 hours. Then the reaction flask was heated with a heat gun until no pressure rise was shown by the thermocouple vacuum gauge. Sublimation of P_2O_5 onto the upper part of the flask was observed during the heating. The next step involved collection of all the D_2O, PD_3, PH_2D, and PHD_2 in the P_2O_5 flask in which a magnetic stirrer was slowly turning. After 45 hours, the exchange was stopped, and the sample was collected for a gas phase infrared analysis. It was found that no significant degree of exchange had occurred.

Preparation of Matrix Isolated Species

Matrix isolation studies were done on PH_3 in PD_3, Ar, Kr, and Xe; PD_3 in PH_3; and PH_2D and PHD_2 in PH_3 and PD_3.

For the PH_3-in-Ar sample, a suitable amount of PH_3 was first collected in a matrix isolation tube whose volume had been determined beforehand, and then transferred to a gas storage bulb. Ar can not be quantitatively condensed by a liquid nitrogen trap. Therefore, the matrix gas from a high pressure tank was allowed to thrust into the PH_3-gas-storage bulb at room temperature. The tank

overpressure prevents PH_3 from coming out.

Xe is more expensive than Ar, but it is also easier to condense at liquid nitrogen temperature. It is desirable to collect the matrix material into a known amount of the guest sample as quantitatively as possible. The PH_3-in-Kr and PH_3-in-Xe samples were obtained in this way.

Enough time was always allowed for the guest and host gases to mix thoroughly before the run. This became a problem in the PH_3-in-PD_3 and PD_3-in-PH_3 experiments. Usually isotopic exchange occurred during this period of blending. The stretching spectra of the PH_2D and/or PHD_2 interfere with those of the isolated species. To avoid this isotopic exchange, the guest and host gases were allowed to approach the deposition port of the low-temperature cell separately, via a Y-shaped, glass tube. One can also shoot these jets at the window simultaneously and separately, while using flowmeters to monitor the concentration of the guest species.

The samples of PHD_2 and PH_2D in PD_3 did not have to be made separately. The PD_3 samples that we made usually contained some PHD_2 and a little PH_2D. For the PH_2D- and PHD_2-in-PH_3 experiment, the following method was used to calculate the initial numbers of hydrogen and deuterium atoms. Since the high temperature classical limit is assumed in this calculation, the results are correct to the order of magnitude.

Let H be the probability of having a hydrogen atom at any one of the three X_i positions in the following picture and let D be similarly defined.

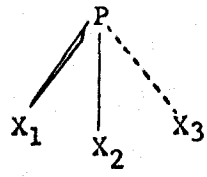

Then, $1 = \sum_{i=0}^{N} \binom{N}{i} H^{N-i} D^{i}$, where $\binom{N}{i}$ is the binomial expansion coefficient and N the total number of possible aspects. In our case, N is the total number of possible positions of a deuterium or an hydrogen atom . Suppose there are x hydrogens and y deuteriums in the reactants, then

$$1 = \binom{3}{0}\left(\frac{x}{x+y}\right)^3 + \binom{3}{1}\left(\frac{x}{x+y}\right)^2\left(\frac{y}{x+y}\right) + \binom{3}{2}\left(\frac{x}{x+y}\right)\left(\frac{y}{x+y}\right)^2 + \binom{3}{3}\left(\frac{y}{x+y}\right)^3$$

The coefficients are called thermodynamic probabilities which are defined as the number of ways to achieve a given distribution of the hydrogen and deuterium atoms in a given distribution of the hydrogen and deuterium atoms in a given molecule. For example, there are three possible ways to obtain the distribution of two hydrogen and one deuterium atoms. These ways are

X_1	X_2	X_3
H	H	D
H	D	H
D	H	H

As an example, the numbers of hydrogen and deuterium atoms required to begin a reaction aiming at a ratio of 200 PH_3 to 1 PH_2D are calculated as follow:

$$\frac{\#\text{ of } PH_3}{\#\text{ of } PH_2D} = \frac{x^3/(x+y)^3}{3x^2y/(x+y)^3} = \frac{x}{3y} = \frac{200}{1} \Rightarrow \frac{x}{y} = \frac{600}{1}$$

Therefore, 600 hydrogen atoms are needed for every deuterium atom in the reactants. With this starting ratio, the probability of having species PHD_2 is very, very small.

$$\frac{\#\text{ of } PH_3}{\#\text{ of } PHD_2} = \frac{x^3/(x+y)^3}{3xy^2/(x+y)^3} = \frac{x^2}{3y^2} = \frac{(600)^2}{1} = 120000$$

General Comments on the Samples

We have observed, in agreement with previous workers, that phosphine burns explosively on contact with air. However, when phosphine was mixed with 1.06 mole % of oxygen, no similar phenomenon occurred. Some chemistry textbooks claim that it is the impurity, P_2H_4, which makes PH_3 inflammable, but our spectra of thick phosphine films show no evidence of P_2H_4. It seems fair to conclude that phosphine does explode, but only when in contact with an excess of air.

Phosphine has not caused us much of a problem in storing. After several months of storage in the gas phase, both PH_3 and PD_3 did not decompose to the point of detection by the manometer except little yellowish(in the case of PH_3) and milky(in the case of PD_3) deposits were observed at the bottom of the gas bulbs. The sample must be purified before storing. If the used sample is stored with the mother sample under liquid nitrogen without further purification, in one month or so, all the sample is decomposed. Impurities seemed to catalyze the decomposition. We have found that gaseous PH_3 reacts with the iridium filament of a hot cathode tube of a vacuum gauge, when the tube was working.

III. LOW TEMPERATURE INFRARED AND RAMAN EXPERIMENTS

Sample Preparation

Sample Made from Liquid

A low temperature sample can be obtained by deposition techniques or by cooling the gas sample to liquid first and then solidifying the liquid. In general, the latter is preferred, although the former is less involved and more often practiced. A deposited film is always polycrystalline, while solidified films tend to contain large domains of single crystals having translational symmetry on which all the vibrational selection rules are based. A single crystal can be obtained from liquid if the temperature is changed very slowly, particularly at the transition points.

Another advantage of the solidified film is that the sample temperature can be raised until it turns into liquid without worrying about pumping off the sample. The reason is that the sample is constricted in a separated sample chamber(or liquid cell) inside the low temperature cell, and the high overpressure in the sample line will stop the liquid from evaporation.

The design of this liquid cell(6) involves squeezing two CsI windows against a thin brass ring, and using indium as a low temperature gasket. Several screws were used to hold the windows in position and to adjust the thickness of the gap between the windows.

The gas inlet of this liquid cell was installed opposite the protruded and threaded part which was then connected to the cooling

tip of the low temperature cell. With this design, a temperature gradient across the sample chamber may be created so that the chamber can be used to grow single crystals in the future.

Copper, due to its excellent thermal conductivity at low temperatures, is generally used for low temperature work. However, our liquid cell was made of brass, because copper of the required dimensions was not readily available. Again, due to the lack of availability of high vacuum tubings with proper dimension and low thermal conductivity, such as those made of Nylon and Teflon, a Tygon tubing was used to connect the liquid cell to the sample port of the low temperature cell. In order to reduce the conduction heating, the Tygon tubing was made as long as possible, and coiled several times, and also tempered at the cold tip before reaching the sample port of the cold cell. The loops of the Tygon tubing were completely detached from the liquid cell and were held in position by thin Nylon strings coming down from the cold tip of the low temperature cell. The lowest temperature registered by the gold-2.1 atomic % cobalt-vs-copper thermocouple, which was soldered with Woods metal next to the gas inlet of the sample compartment, was about 26°K, while that shown by the gold-0.07 atomic % iron-vs-copper thermocouple, which was also soldered with Woods metal along with the Chromel-vs-Constantan thermocouple at the cold tip of the low temperature cell was about 25°K. Thus, when a larger temperature is desired for single-crystal growing, the gas inlet must be heated.

The thickness of the film in the liquid cell required for a proper absorption intensity was first estimated from the amount of phosphine used in the deposition experiments(in the order of 100 μ mole) and the diameter of the sample compartment of the liquid cell. To measure the thickness, three methods were tried. First, direct measurement with a micrometer caliper takes a particular skill. Although the caliper reads down to 1/1000"(proper film thickness is several microns), human error usually amounts to the order of 1/1000". Second, the nonparallelness of the two windows make it very hard to measure the gap with the interference fringes. Finally, using the absorbance of liquid benzene at 1393 cm^{-1} as the reference of the gap thickness of the liquid cell was found to be most practical. The absorbance of benzene at 1393 cm^{-1} was first calibrated with an adjustable micro-liquid cell. A plot of absorbance vs thickness was made. To measure the gap of the liquid cell for low temperature purposes, benzene was injected into the cell and the absorbance at 1393 cm^{-1} was measured with exactly the same scanning conditions used in the calibration. The thickness was then read from the plot.

In the runs with the liquid cell, the gas sample was usually liquefied at the lower part of the sample compartment. The liquid was then pulled up to fill the entire space by the vacuum. The surface tension kept the liquid in position. Please refer to reference 6 for the details of growing a single crystal.

Sample Deposited from Gas

Most of the low-temperature samples were obtained by spraying the room-temperature, gaseous sample onto a precooled substrate. Most of the PH_3 and PD_3 films were deposited in short spurts at about 77°K, while the films of PH_3 in inert gases were sprayed at about 20°K at such a slow rate that it usually took about four hours to put enough guest molecules(10 to 100 micromoles) on the substrate. Deposition of PH_3 was tried in quick spurts on a substrate precooled to 82°K at which PH_3 has a vapor pressure of about $1X10^{-3}$ mm Hg. This deposition was not successful, because the temperature usually rose a few degrees at the moment the room-temperature gas hit the substrate. This temperature rise brought PH_3 up to a region where its vapor pressure is relatively large. A good film of PH_3 was also obtained by slow spraying(completed in 15 minutes) at about 66°K. This film showed only slight difference in the relative intensity in the fundamental regions. Another PH_3 film deposited at about 74°K in about 40 minutes had the same spectroquality as the one just mentioned. In general, films depostied slowly and continuously are as good as those put on in short spurts when the temperature is high enough. When the temperature is not high enough, one would like to spray on in short spurts. Because, in a slow deposition, the molecules usually do not have time to anneal before they are caught cold, resulting in a glassy film. However, if the substrate temperature is really low, there is no way to avoid getting a vitreous film. For example, PH_3 was sprayed, in

short spurts, onto substrates precooled to 23°K and 38°K. Both resulted in vitreous films(judging from the structurelessness of ν_2). If the deposition had been done slowly, the film would have been vitreous also, as expected. The structureless PH_3 films were usually devitrified by subjecting them to several thermocyclings i.e. the film is warmed slowly through the transition points until it can not be warmed anymore, and then it is cooled down to the lowest temperature. The procedure is repeated several times.

In one of the PD_3 experiments, the PD_3 sample was first solidified in the finger portion of the gas bulb with a ethanol-liquid nitrogen bath. The vapor over the solid was then allowed to condense continuously onto the 74°K substrate. Since PD_3 has a low vapor pressure at the bath temperature(157°K), the condensation occurred in a slow manner. The film obtained this way was annealed, judging from the fact that the structure of ν_2 resembled that of the ν_2 of the delta phase of PH_3. However, the low temperature cell stopped functioning not too long after the film was converted to the stable gamma phase. Therefore, the reversibility of this structure-rich ν_2 of the delta phase of PD_3 has not been proved. In another PD_3 experiment, the sample was deposited on a window at 67°K through a micrometer needle valve in a relatively fast manner. This film showed that ν_2 had only the band contour of the structure-rich ν_2, but this ν_2 structure was reversible. In the following two experiments, the PD_3 films obtained were all vitreous. First, the substrate was at 20°K and the PD_3 sample was trapped in the ethanol-

liquid nitrogen bath, while the PD_3 vapor over the solid was being condensed onto the window. Second, the window was at 12°K and the room temperatue PD_3 gas flowed continuously through a micrometer needle valve to deposit on the window. An unannealed PD_3 film was much easier to devitrify than an unannealed PH_3 film. Only one thermocycle was required. In one of the Raman experiments, the PD_3 sample was deposited onto a 20°K-aluminum substrate in short spurts. The film thus obtained was definitely annealed, since it showed the characteristic band structures of the gamma phase.

It is noteworthy that any attempt to put all the sample on the window in a hurry tends to result in a flaky film. To prevent the film from flaking, a thin film should first be deposited. After subjecting the film to possible phase transitions, another thin layer is deposited. The procedure is repeated until a film of proper intensity is achieved.

Temperature Measurement

During the first half of this project, the thermocouples used were Chromel vs Constantan, Au-2.1 atomic % Co vs Cu, and Au-0.07 atomic % Fe vs Cu. The hydrogen back pressure was also used as an indication of temperature. The first thermocouple has a thermoelectric power of about 60 μv/deg at room temperature. This power reduces down to less than 20 μv/deg at 40°K and about 10 μv/deg at 20°K. On the other hand, the thermoelectric power of the second thermocouple(7) decreases in a slower manner from 43 μv/deg at 300

°K down to about 26 μv/deg at 40°K and about 16 μv/deg at 20°K. At 12°K it still has a 10 μv/deg power. However, the power of the second thermocouple becomes less than 10 μv/deg below 12°K. Although the uncertainty of the potentiometer used was only 0.5 μv, the errors caused by the local inhomogeneities of the thermoelements(which can usually be detected from the roughness of the thermoelectric emf vs temperature curve), can amount to 5 μv for the second thermocouple. Thus, based on the thermoelectric power , the first thermocouple was used at the high temperature and the second thermocouple around 20°K. For temperature below 12°K, the third thermocouple, whose thermoelectric power has a maximal value(15 μv/deg) around 12°K and tapers off on both sides of this maximum until 8.7 μv/deg at 1.763°K and 9.044 μv/deg at 5.999°K(8) was used.

Towards the end of the project, the Chromel(believed to be Chromel-P) vs Au-0.07 atomic % Fe thermocouple(9), which came with the Displex TM Cryogenic Refrigerator, was used to replace the three thermocouples used previously. This thermocouple has a thermoelectric power of more than 10 μv/deg all the way from 85°K down to 3°K. Chromel-P makes a good second thermoelement owing to its positive thermoelectric power to contrast with the negative power of the Au-0.07 atomic % Fe thermoelement.

The vapor pressure of hydrogen was also used to monitor the temperature. In the first half of the experiment, the pressure of hydrogen vapor over liquified hydrogen(or hydrogen back pressure) could only be used as a rough temperature indicator. The Clausius-

Clapeyron equation could not be applied, mainly because the indicated back pressure did not represent the back pressure over the boiling liquid, and also because the scale of back pressure gauge used was not fine enough. Moreover, the incident pressure of the expanding hydrogen gas can also affect the temperature when the back pressure is being held constant. In the last half of the experiment, the hydrogen pressure scale on the Displex TM Cryogenic Refrigerator is much finer and was used to indicate the vapor pressure of hydrogen at the cooling tip directly. However, it was only reliable from about 35°K down to 12°K.

During a low temperature experiment, the temperature of the solid sample can usually be estimated from the cell vacuum gauge. A vacuum of $1X10^{-5}$ mm Hg is necessary to limit convective heat leak to a tolerable level. A sudden increase in the cell pressure warns of a rise in temperature due to thermoleak.

Whenever possible, the measuring junction of the thermocouple was inserted into the CsI window. The junction was held in position by melting the Woods metal powder, already in the hole drilled in the CsI window, with a red hot glass rod of the right dimensions. The junction was then quickly inserted into the hole before the melted metal solidified.

When the junction had to be built into a metal, a hole was drilled and tapped in the metal first, and then the junction was either soft-soldered or Woods-metal soldered on a copper strip which was then screwed onto the metal.

The junctions of the thermocouples were always made by twisting the elements together and then melting them with a very small and intense torch. This method can produce some oxides in the junctions which then affect the thermoelectric emf. This may be the main reason that none of our calibration curves coincide exactly with the literature ones. (Our thermocouples were calibrated against liquid nitrogen and some convenient slush baths of reference 10.) This torch-melting method becomes less workable when the difference in melting points of the two elements gets larger. A better way to make the junction is to spark-weld the elements in inert gasses(9).

In all of our low temperature experiments, the reference junction was led to the outside of the low-temperature cell and immersed in an ice-water bath, after the junction had been carefully tempered at the cold tip. For very precise measurements, the reference junction should be thermally close to the measuring junction. Further, the thermoelements should not be taken through regions where temperature is much different from either junction in order to reduce error caused by the local inhomogeneity of the alloy wires (7). However, our treatment of the reference junction did not introduce any error greater than the temperature precision.

Most of the thermoelements used were in the form of solid solutions. Their concentrations tend to change, and so does their thermoelectric emf and power. These effects were usually caused by rough handling of the thermoelements and, particularly, by rebuilding of the junction. Therefore, calibration of the thermocouples

was done very often.

Too thin a thermoelement should not be used, since it broke easily under rough handling. If it was necessary to use thin thermowires, they were protected by passing them through plastic sleeves.

The best way to measure the temperature of a thin slab is by using a carbon resistance thermometer(11) which can be painted right next to the solid film of interest. Since the thermocouple measuring junction was not in direct contact with the sample film, the temperature registered by the thermocouple was apt to have a couple of degrees of error. The first order phase transition of PH_3 at 30.29°K was used as a reference of our temperature accuracy. The average readings of this transition temperature registered by the Au-2.1 atomic % Co vs Cu thermocouple was 29±1°K. Therefore, our temperature measurement was 1.5 degrees lower than the real value.

Windows

The window used in the midinfrared experiments was CsI. In the far-infrared, silicon was used as the substrate and polyethylene as the outer window. It was found that a polyethylene window of about 0.04" thickness was strong enough to hold a vacuum of $1X10^{-5}$ mm Hg. It usually took a long time to outgas the polyethylene window. The choice of the expensive CsI over the cheap NaCl window would allow use of the far-infrared optical interchange unit in the IR 7.

The windows were polished in order to reduce scattering loss

of the incident energy. The NaCl windows were polished according to standard technique described in any chemical infrared spectroscopy textbook. The CsI window is easily scratched by the flannel which is the softest material readily available. In polishing CsI windows, the cerium oxide powder is wet with as little isopropanol as possible, so that after several quick circular or 8-strokes, the lap is almost dry, and it takes only one or two light strokes on the dry, clean part of the lap to remove the residual isopropanol. It is the latter part of the polishing job which makes the finished surface scratchy.

The silicon window used in the far-infrared experiments was polished with 0.3 μ aluminum oxide powder on pieces of paper. Another way to polish a silicon window is to glue the window on the flat side of a thick metal rod with black wax(Apiezon W) and lap the window on a 0.5 μ chromium oxide polishing paper.

Integrated Absorption Intensity Measurements

The integrated intensities of the two strong bands in the ν_2 region of the γ phase of PD_3 were measured. As many points as necessary were picked from the spectra, whose Y-axis was linear in percent transmission but not linear in absorbance, and then the spectra were replotted, so that the Y-axis was linear in absorbance. The final step was integration of the bands. A Keuffel & Esser planimeter was used to measure the areas under the bands. The area are $\int_{\nu} \log \frac{I_o}{I} d\tilde{\nu}$ which had to be multiplied by 2.303 and divided by $\rho($

concentration) and l(sample thickness) to get the integrated absorption intensity,

$$\tilde{A} = \frac{1}{\rho \ell} \int_{\tilde{\nu}} \ln\left(\frac{I_o}{I}\right) d\tilde{\nu}$$

Note that ρ and ℓ did not actually enter our calculation as we needed only the intensity ratio of the two bands.

Specular Reflection Spectrum

The reflection optics used to take the specular reflection spectrum in the ν_2 region of the delta phase PH_3 is illustrated in Fig. 2.

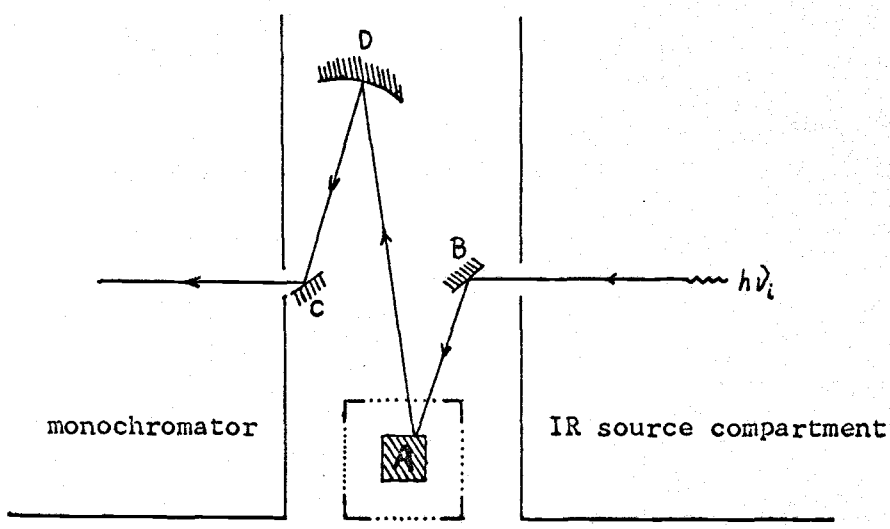

Figure 2. Specular reflection optics

In Fig. 2, A is the aluminum substrate which was polished with jeweler's rouge. The square surrounding A is the lower part of the vacuum shroud mounted with windows (represented by segments of dotted lines). B and C are plain metallic mirrors, and D is a large collimating mirror. To maximize energy, the cell was replaced with

a plain metallic mirror which simulates the sample substrate. An effort was made to make the size of the light image at a certain point beyond the sample compartment as large as it was before inserting this reflection device in the light beam. When this goal was achieved, the maximum energy was obtained. Mirrors B, C, and D were then, fixed on a board. At the same time the position of the simulated substrate was marked on the same board. The optimal energy obtained was about 65% of the original energy at 847 cm^{-1}. This is about right, because one mirror reflects only 90% of the incident energy and four mirror will reflect $(0.9)^4$ of the original energy.

When the simulated substrate was replaced with the cell, the best energy achieved at 847 cm^{-1} was 31%. This further decrease in energy was due to the reflection losses at the CsI outer window and at the sample substrate.

Low Temperature Raman Sampling Optics

The low temperature Raman sampling optics employed in this work was designed by Professor J. W. Nibler for our laboratory and is illustrated in Fig. 3. In this figure, A stands for the cross section of the shiny aluminum substrate (parallelepiped) cut along the scattering plane (defined by the incident and the 90°-scattered beams). B is the vacuum shroud of the low temperature cell (the Displex unit) laid horizontally (i.e. perpendicular to the scattering plane). The dotted segment of a line refers to the glass window. E is the slab sample. C and D came with Cary 82 and their relative positions are fixed. D is a 126 mm focal length lens which focuses the origi-

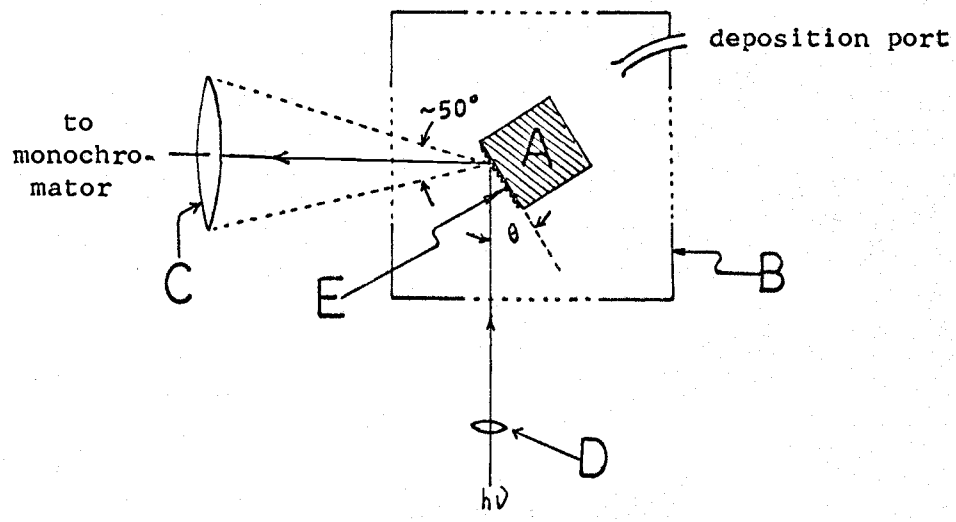

Figure 3. Low temperature Raman sampling optics

nally parallel laser beam at the "sample point". It is very important to note that the laser which incident on the sample is no longer parallel. It is equally important to note that C, which consists of an off-axis ellipse and an aplanat, is a very efficient signal collector. It collects not only 90° Raman scattering, but also all other signals which are scattered into the solid angle shown in figure 3. C was set to work at its f/1 mode with a working distance of some five centimeters measure from the casting face. A could be rotated relative to B for sample deposition.

It is well understood that the near forward scattering (or polariton) has a different frequency from the 90° Raman scattering, and that the polariton frequency decreases as the scattering angle approaches zero. Since the sampling arrangement employed in these low temperature experiments does not select a well defined scattering angle, partly because of the large aperture of the monochromator and partly because of the reflection backing of the film, we needed to

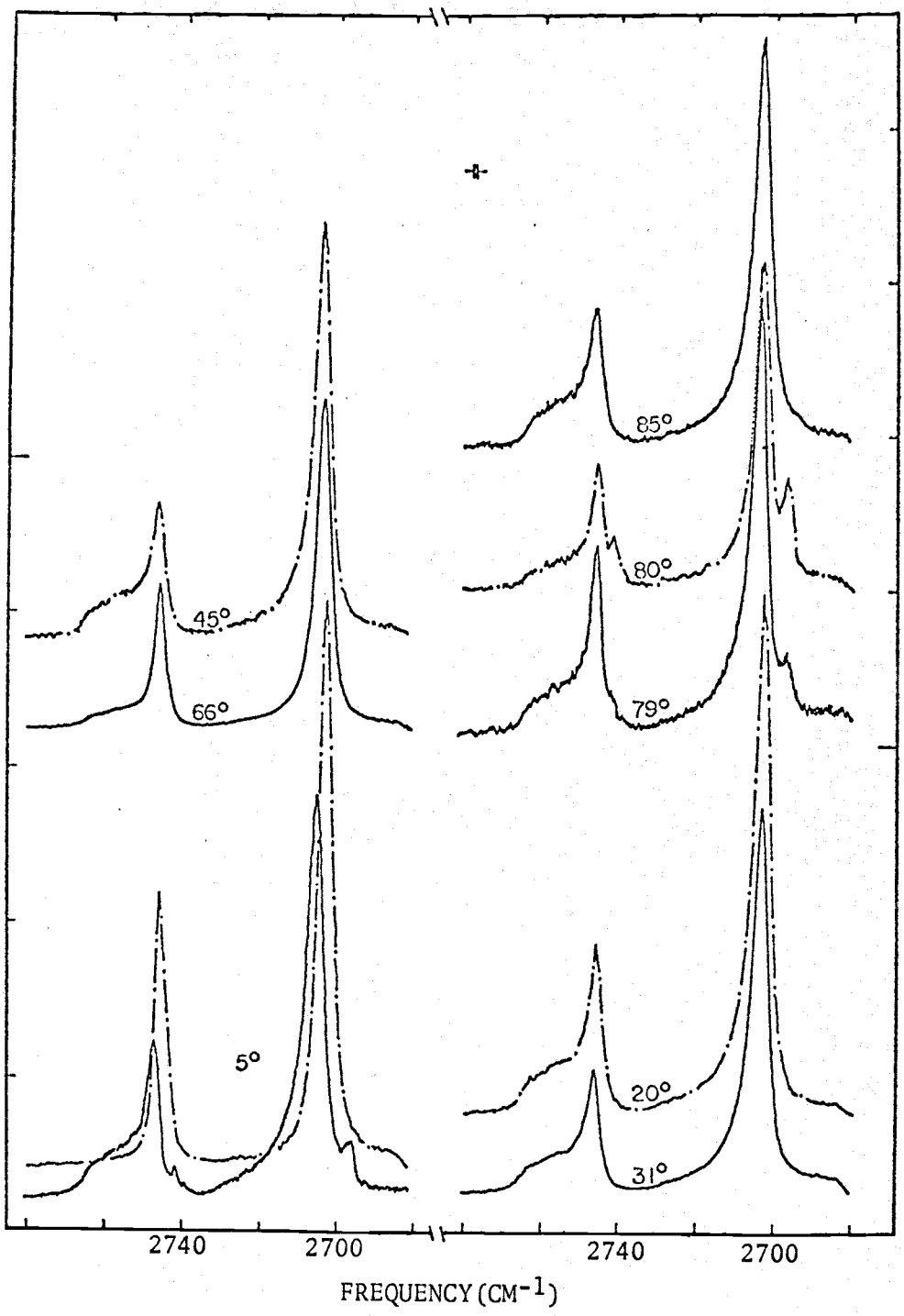

Figure 4. Stretching-spectrum change of solid HCl relative to θ. The dot-dashed trace in the 5° group was taken while laser was focused at lower edge of the substrate.

determine whether the experiments on solid PH_3 were influenced by such directional effects and therefore observed the Raman spectrum of crystalline HCl with the same experimental arrangement. HCl was selected because (a) it is anisotropic and (b) its modes are simultaneously Raman and IR active. These are the conditions under which the directional effects mentioned above might be most significant. Moreover, there exists in the literature a considerable body of data on the Raman spectrum of crystalline HCl presumably under right angle scattering conditions.

In this solid HCl experiment, the frequencies of the internal vibrations were measured as θ varied. The result at 16° K is listed in the following and shown in Fig. 4.

θ°	$\tilde{\nu}$ cm-1	
5	2705	2747
5	2703	2746*
20	2703.5	2746
31		
45	2703.5	2746
66		
79	2705	2746
80	2697 w	2742 w
	2704.5 s	2746 s
85	2704.5	2747

*: laser focused at the lower edge of the substrate

Examining the data and figure 4, it seems fair to say that there was not significant frequency shift due to a change in θ in the intramolecular vibration region. In changing θ, it was observed that the optimum angle for strong signal is around $30^\circ \pm 10^\circ$. This optimum angle can not be judged from the count-per-second as a function of θ. Because the cell was moved whenever the θ was

changed and no attempt was made to get the cell exactly back to the original position as it is not necessary in this experiment. However, this is mandatory for an depolarization ratio experiment, since it was found that intensity varied with the choice of the laser target. For the latter experiment, our usual practice was to hold the analyser fixed but rotate the incident E vector 90° by twisting the half-wave plate 45° .

In the following, we compare our frequencies with the literature values.

this work	Ito,Suzuki,and Yokoyama(13)		Savoie and Anderson(14)	
16°K	4°K	77°K	10°K	77°K
2696 w				
2705 s	2699 vs	2706 vs	2699	2705
	2716 w	2716 m	~2715	~2720
2742 w				
2746 s	2747 s	2745 s	2744	2748
~2755 sh	2753 w	2755 m	~2754	~2758
				408*
		~290 vw,b		
219 m		218 vw,b		221*
136 m	145 w	133 w		138*
113 w				113*
86.6 s	90 m	84 m		87*
58 s	60 m	55 m		59*
				50*

* : obtained from ref. 12

In this comparison, it is noted that there does exist frequency differences. However, they are small. In addition, we mention the aspects which are characteristics of our HCl experiment : (a) the existence of the weak low frequency peaks at 2696 cm^{-1} and 2742 cm^{-1}, (b) the persistent absence of the shoulder at 2715 cm^{-1} with respect to the shoulder at 2755 cm^{-1}, (c) the disappearance of these two shoulders from the $\theta = 5°$-edge experiment.

IV. INSTRUMENTATION

The two main spectrophotometers used were the Beckman IR 7 and the Cary 82. The Beckman IR 11 was used for the far infrared work, which did not reveal many peaks.

The equipment used to achieve low temperatures were the helium -hydrogen expansion Cryo-Tip and the Displex TM Cryogenic Refrigerator, both of Air Products and Chemicals, Inc.

Beckman IR 7

The Beckman IR 7(15) is a double beam fore-prism/grating, recording spectrophotometer, with a Nernst glower as the IR light source. The sodium chloride fore-prism(60 X 75 mm, 60°) sorts order for the reflection grating(75 lines per mm, 64 X 64 mm in area) whose primary blaze frequency is 12 μ(833 cm^{-1}), and the primary range(or first order) is approximately from 600 cm^{-1} to 1125 cm^{-1}. It has a resolution of 0.3 cm^{-1} at 1000 cm^{-1}. Normally, 1 cm^{-1} resolution can be achieved in the region, 700 cm^{-1} to 4000 cm^{-1}, without much noise problem.

All the infrared spectra were taken in the double beam mode. Since the cell was evacuated, the length of the cell in the sample beam was not compensated for by the reference beam. Atmospheric absorptions showed up in the spectra whenever the purging system did not function well.

Frequency calibration of this instrument was carried out once. All the infrared frequencies reported here have been corrected ac-

cording to this calibration, except the ones above 3000 cm^{-1}. whenever the CsI interchange unit was used, the calibration might have been affected. To find out the effect of replacing this interchange unit on the frequency accuracy and also to find out the intrinsic frequency reproducibility of IR 7, the following simple statistics were performed. The frequencies of the peak lowest in energy in nine ν_2-high-resolution-scans of solid PH_3(in the delta form) were recorded. It was found that the nine frequencies drifted between 969.8 $cm^{-1}$and 968.65 cm^{-1} from 2/7/70 to 4/23/71. Thus the replacing of the interchange unit and the intrinsic frequency reproducibility might have caused the calibrated observed frequencies(i.e. the reported frequencies) to deviate ± 0.6 $cm^{-1}$from the real values. It is suspected that this deviation may be random, like the deviation in the frequency calibration. Therefore, the peak highest in energy in the stretching region of the delta phase of PH_3 was used as reference. The four measurements of this peak frequency were found to vary from 2326.6 cm^{-1} to 2324.8 cm^{-1} in the period from 2/7/70 to 4/23/71. Thus, in the stretching region of solid PH_3, the uncertainty of the reported frequencies was ± 0.9 cm^{-1}. When the strongest band in the ν_4 region of the delta phase of PH_3 was used as a reference, the uncertainty was found to ± 0.8 cm^{-1}, with a frequency range of 1094 cm^{-1} to 1095.6 cm^{-1} for four measurements in the period 7/5/70 to 4/23/71. (The frequencies of these three reference peaks were not observed to have appreciable temperature dependence). Therefore, the infrared frequencies were reported with at least ± 1 cm^{-1} confidence.

Cary 82

Cary 82(16) consists of three essential parts: a laser as the light source, sample compartment, and monochromators. This instrument uses the 52 B Ar^+ laser made by Coherent Radiation. This laser has the following lasing lines : 5145Å, 5017Å, 4965Å, 4880Å, 4765Å, 4727Å, 4658Å, and 4579Å. Due to their larger output power, the 5145Å and 4880Å lines are most frequently used ones. Only the former was used in this study. Most of the time, the laser current was adjusted to give a output power in the range, 700 mw to 1000 mw. The 5145Å lasing line has the following plasma lines which are usually sharp : (The numbers in the parentheses are the relative peak heights) 66(7), 77(21), 117(26), 161(3), 267(8), 521(75), 588(4), 909(4), 927(3), 943(4), 1094(3), 1101(6), 1240(7), 1247(3), 1255(3), 1446(10), 1490(4), 1600(12). 1738(8), 1750(3), 1968(3), 2013(3), 2112(7) , 2155(3), 2233(5), 2324(4), 2372(3), 2437(5), 2453(11), 2521(19), 2569(6), 2729(6), 2739(6), 2858(48), 2889(16), 2915(8), 2932(15), 2981(6), 3039(5), 3052(44), 3082(1020), 3106(47), 3146(51), 3164(8), 3190(4), 3234(950), 3273(12), 3311(5), 3339(9), 3349(6), 3410(17), 3417(470), 3554(9), and 3582(14). We take the pain to list these plasma lines, since we will have to determine the spurious Raman shifts in our high resolution spectra in the following chapters.

Before the excitation line interacts with the sample, it is directed through a dispersion-filter system. However, it is difficult to block out the plasma emission completely. The spurious

Raman shifts can also be discriminated from the real Raman shifts by using another excitation line.

In between the dispersion-filter system and the sample, 1 % of the lasing energy is taken to feed the reference phototube. The recorder indicates the ratio of the measured "Raman" energy to this reference energy.

This instrument was calibrated with a 1/3 watt Neon light. Like the calibration of the IR 7, the frequency corrections were very hard to express as some simple mathematical function of frequency. In the case of the loaner Cary 82(two different Raman instruments were used in the course of this research, the loaner Cary 82 and the permanent Cary 82), the three off-axis parabolic collimating mirrors of the monochromators had to be adjusted from time to time to maximize the measured energy. This adjustment did not turn out to be so critical for the permanent unit. All Raman spectra were taken with both the loaner and the permanent one. The frequency calibration was changed whenever this adjustment was made. Although an attempt was made to calibrate the Cary 82 as often as possible, the reported Raman shifts might still be subject to uncertainty. The following simple statistics were performed to estimate the confidence in the reported frequencies. In July, 1971, the 918.5 cm^{-1} of the Neon lines was observed to be in exact agreement with the literature value, and 0.2 cm^{-1} and 1.3 cm^{-1} higher than the literature value in two subsequent calibrations. Thus the collimating-mirror-adjustment (and probably the frequency reproducibility of Cary 82) could vary the 918.5 cm^{-1} peak position within

±0.65 cm^{-1}. The equivalent quantities found for the 1031.2 cm^{-1}, 1458.2 cm^{-1}, 1756.5 cm^{-1}, 2453 cm^{-1}, 2347.9 cm^{-1} Neon lines were ±0.55 cm^{-1}, ±0.8 cm^{-1}, ±0.7 cm^{-1}, ±0.25 cm^{-1}, and ±0.3 cm^{-1}. Thus, the greatest uncertainty in our reported Raman shifts is 1 cm^{-1}. The following observation is reported here to prove that it is rather difficult to be really scientific about the accuracy of frequency. In one run(without adjusting the collimating mirror), the 77 cm^{-1} and 117 cm^{-1} plasma lines appeared in one scan to be .6 cm^{-1} too high and 0.3 cm^{-1} too low respectively, while in another scan they were 1 cm^{-1} too high and in still another scan, 0.5 cm^{-1} too high.

The introduction of the laser into Raman spectrophotometry increases resolution a great deal. One cm^{-1} spectral band width can be achieved easily with the Cary 82 from almost the excitation line to 4000 cm^{-1}, although this was thought to be very difficult before lasers were used. A spectral band width of one cm^{-1} was always used for the high resolution Raman scans unless otherwise indicated.

Cryo-Tip

The Cryo-Tip(17) is an open-cycle, Joule-Thomson(or Joule-Kelvin) expansion refrigerator. The following picture shows the Model AC-2L Cryo-Tip which looks the same as the Model AC-3L which was actually used.

In Fig. 5, the lower and bulkier part of the unit at the left is called the "cell head", which houses a liquid nitrogen reservoir and two heat exchange coils(in the case of AC-3L, one for hydrogen

Figure 5. The helium-hydrogen expansion Cryo-Tip

expansion and the other for helium expansion) packed with adsorbers. The uppermost, rectangular-shaped part of this unit is the window holder and window. Extending down from this part is the helium and hydrogen expansion section (which is longer for the AC-3L, since it houses both the helium and the hydrogen expansions). Surrounding the latter is part of the whole radiation shield which extends all the way down to the nitrogen reservoir and which will be completed if the unit on the left is mounted on the top. The central unit, made in the chemistry department's machine shop, is called the "vac-

uum shroud". Two infrared windows were mounted on the opposite sides of the lower, cubic portion of this shroud. The valve in the upper portion of the shroud is a pumping port. The advantage of having the pumping port installed in the vacuum shroud instead of the cell head is that the substrate window can be rotated without stopping pumping. The small tubing beside the large, cylindrical section is the spray-on port. The radiation shield(right unit) is fastened onto the cell head unit with springs. In operation, it is at the liquid-nitrogen boiling point and reduces radiation heat loss to the sample to less than one percent of their values if the shield were not present.

High-pressure hydrogen gas from the tank is first passed through the room temperature adsorber to be deprived of larger impurity molecules, such as water and carbon dioxide. Smaller molecules such as oxygen and nitrogen in the main stream of hydrogen are removed by molecular sieves packed in a heat exchange coil, which functions at liquid nitrogen temperature . The hydrogen thus purified leaves the expansion controlling panel and enters a similar heat exchange coil embedded in liquid nitrogen at the cell head, to be further purified. This superpure hygrogen had already been precooled by liquid nitrogen in the reservoir to a temperature less than its maximum inversion temperature (202°K). When it is throttled to atmospheric pressure, its temperature drops. The throttle-cooled gas, which travels out of the throttling compartment and the cell, cools the incoming gas. (Therefore, the Cryo-Tip can also be called a countercurrent heat exchanger.) The incoming gas after

throttling becomes still cooler. After many repetitions of these successive coolings, the throttled gas becomes partly liquified. The liquified hydrogen is used to cool the helium which comes in via a separate channel with the same kind of traps. Again helium is liquified after many repetitions of throttling. The Cryo-Tip is not designed to recycle the expanded gas, and hydrogen and helium are vented out of the top of the building. The Cryo-Tip is thus called "open-cycle."

When hydrogen only is going to throttle, the helium circuit must be used; because the latter is closer to the cold tip. If the hydrogen circuit were used, the cooling would not be so efficient.

The explosive range of hydrogen in air is between 4.1% and 74.2 % by volume. Due to its rapid diffusion, the throttled hydrogen quickly attains a concentration below the danger limit after it is vented out of the top of the building. To prevent a dangerous accumulation of hydrogen in the laboratory, all of the joints of the expansion line were checked with soapy water. Whenever a hydrogen tank was connected to the line, a check for leaks was always performed. Although a small amount of hydrogen was always used to flush out the air molecules during a tank connection, a dangerous mixture of hydrogen and air was never attained in the laboratory.

By trial and error, the fastest cooldown was achieved in less than one hour by holding the hydrogen (for single expansion) incident pressure at 500 psi for about 20 minutes as the tip temperature dropped from room temperature to about 273°K, and then increasing the hydrogen incident pressure up to 1000 psi for the rest of the

cooldown process—about 30 minutes. After the temperature was down, about 300 psi incident hydrogen pressure was necessary to keep the window at about 18°K with the AC-3L unit used. At this incident rate, one tank of hydrogen usually lasted only about two hours. (With one of the two AC-2L units that Professor DeKock has, one tank of hydrogen could keep the temperature at the liquid hydrogen boiling point for as long as four hours.) It generally took about two-thirds of a tank to cool down.

The Cryo-Tip is able to function under several operational modes for various temperatures. The modes are nitrogen expansion, hydrogen expansion, and helium-hydrogen expansion. For each mode, temperature can be raised and lowered by increasing and decreasing the back pressure of the liquified gases.

In using the Cryo-Tip, the problem of cell-plugging, which has occurred during some important high resolution scans, has to be faced. It was usually caused by the solidification of molecules of impurities at the expansion nozzle. When it occurred, the cell had to be warmed up and purged over again. Clogging of the throttling nozzle by some mechanical debris carried along by the main stream of the expansion gas sometimes occurred in the AC-2L unit. The most stubborn cases of plugging were those caused by the oxygen and nitrogen impurities. To prevent this, the cold trap in the expansion-controlling panel had to be refreshed every 700 psi. It became necessary to change to the convenient closed-cycle refrigerator.

Displex TM Cryogenic Refrigerator

The Displex TM Cryogenic Refrigerator (18, 19) is a closed-cycle, Joule-Kelvin refrigerator. It is comprised of a standard, air-cooled, oil-lubricated compressor unit with oil separation system, a displacer/expander, whose valves and seals are at room temperature and which operates at slow speeds to cool the load down to 12°K, and the control unit which governs the power of the whole system and has a switch for the cell heater.

Forty-five minutes after the unit is plugged in, the temperature is down to 12°K. There is no consumption (except a very small leak in the system) of working fluid to worry about. The built-in heater allows easy control of temperature. For this reason, the phase transition experiments at low temperature could be done at practical equilibrium states. This unit also made it feasible to observe the phase transitions, which take days to achieve.

Shown in Fig. 6 are the displacer/expander (righ unit) and the vacuum shroud. The former can be located at a distance away from the controlling unit and the compressor for experimental convenience. The lower part of the right unit is called the "valve assembly," which contains a motor for moving the displacer and which regulates the flow of helium in and out the cylinder assembly. The latter is located between the aluminum substrate on the top and the valve assembly.

The cooling process of the Displex Refrigerator is similar to that of a common household refrigerator. The latter uses freon gas

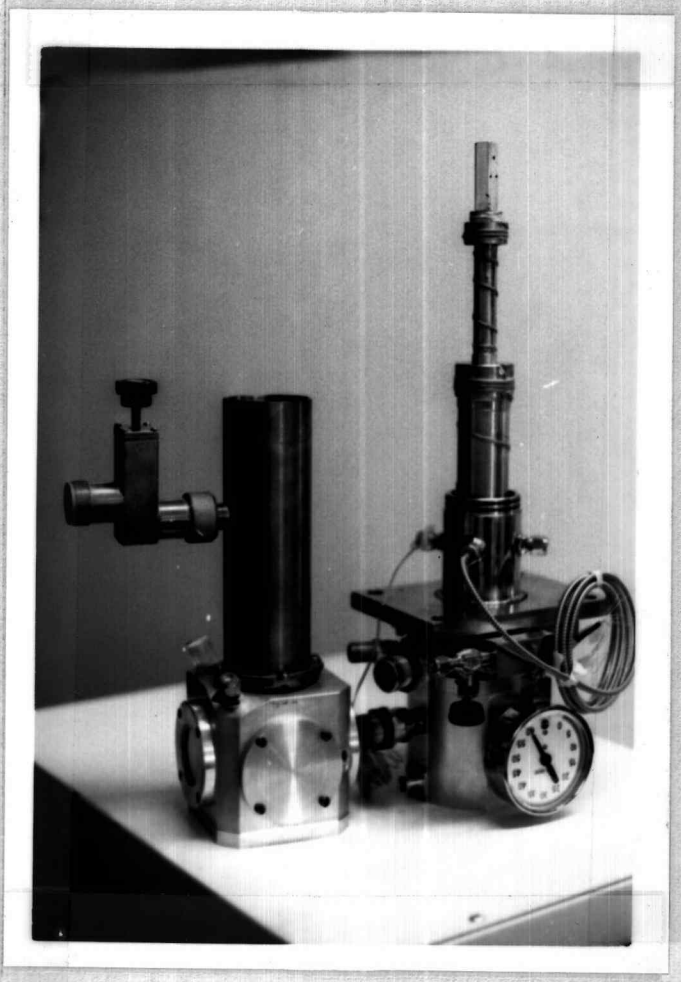

Figure 6. The Displex TM Cryogenic Refrigerator

as the working fluid, while the former used helium which flows in closed cycles in contrast to the Cryo-Tip described previously.

The Sequence of operations can be illustrated by a single cylinder and piston (Fig. 8). The corresponding PV diagram (Fig. 7) represents the reverse Carnot cycle for the refrigeration. The cycle goes as follows.

(1) When A is open and B is closed, helium is isothermally (room temperature) compressed by the compressor and is sent through valve A to push the displacer up and the cy-

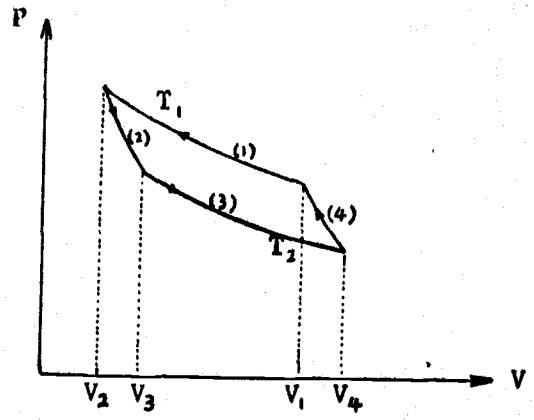

Figure 7. The PV diagram for the Displex TM Cryogenic Refrigerator

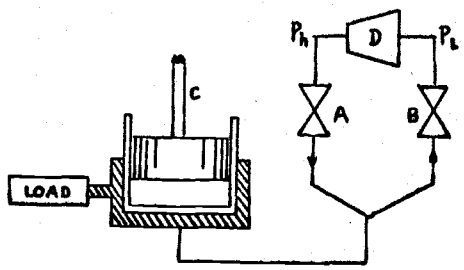

Figure 8. The elementary cooling circuit for the Displex Refrigerator

where

A = inlet valve through which the compressed gas passes

B = exhaust valve leading to the low-pressure side of the compressor

C = piston in a cylinder

D = compressor

linder fills with compressed gas

$$E_1 = 0 \; ; \; Q_1 = W_1 = nRT_1 \ln \frac{V_2}{V_1}$$

(2) When A is closed and B is opened, the gas expands irreversibly and adiabatically into the low-pressure, discharge line and cools.

$$E_2 = -W_2 = C_v(T_1-T_2) \; ; \; Q_2 = 0$$

(3) The resulting temperature gradient across the cylinder wall causes heat to flow from the load into the cylinder. The cooled gas in the cylinder in turn absorbs the heat and further expands isothermally (at the cooled temperature) to some volume V_4.

$$E_3 = 0 \; ; \; Q_3 = W_3 = nRT_2 \ln \frac{V_4}{V_3}$$

(4) The piston then moves down to displace the remaining gas into the exhaust line and to return the work originally done to it to the gas, whose temperature thus rises to its original value.

$$E_4 = -W_4 = C_v(T_2-T_1) \; ; \; Q_4 = 0$$

This oversimplified system, while workable, would not produce the extremely low temperatures required for most low-temperature experiments. Thus a regenerator is put between the valves and the cylinder. A regenerator is a reversing-flow heat exchanger and is packed with a particular matrix which extracts heat from the incoming gas, stores it, and then releases it to the exhaust stream.

Because the regenerator is built right next to the piston (Fig. 9), the gas which passes through the regenerator and fills the space underneath the piston will have about the same temperature as that of the load.

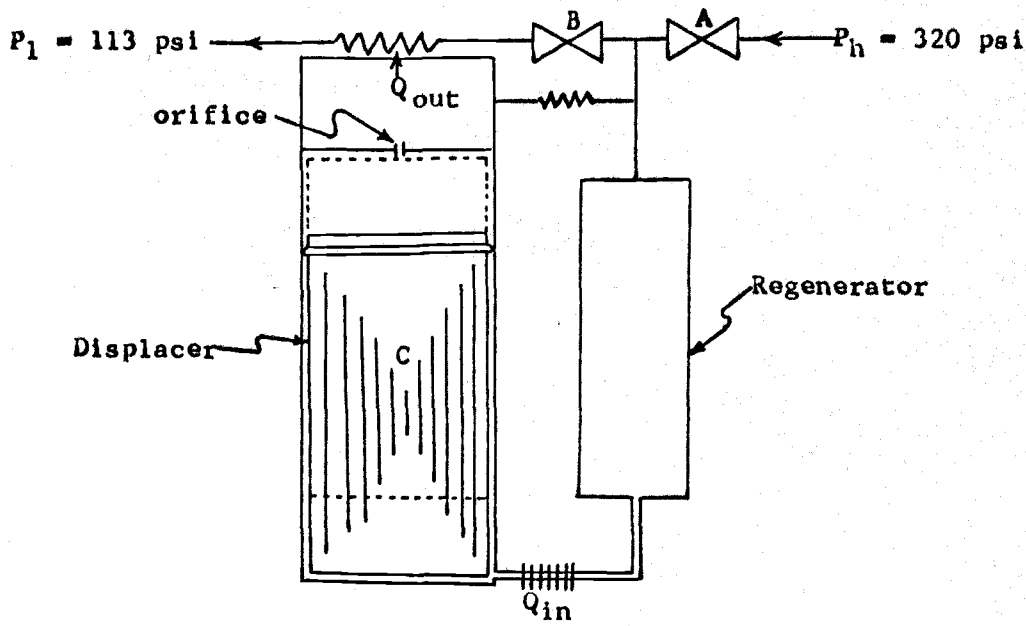

Figure 9. A schematic diagram of the expander(first stage only) of the Displex TM Cryogenic Refrigerator

In the system shown in Fig. 8, the piston must be designed to withstand unbalanced forces. The actual version of the Displex system is shown in Fig. 9. With valve A opened and B closed, C displaces up instantaneously. So the helium right above and underneath the piston is at substantially equal pressure, P_h. The work done to the surroundings (helium right above the piston) by the isothermal compression is dissipated into heat by throttling (Joule-Kelvin effect) in the orifice. This heat is then removed by heat exchange

with the exhaust gas as it leaves the unit. Note that the piston is now more correctly called a "displacer," because it merely moves up and down with no mechanical work introduced into it. Thus the system is said to use a "no-work" cycle.

The single-stage refrigerator shown above can achieve temperatures in the 30° - 77°K range. The Displex unit used in our work is a two-stage refrigerator. The additional stage which works by the same process as the first stage permits useful refrigeration down to 12°K. The three-stage version of this refrigerator has 6° - 12°K cooling capability.

V. SPECTRA OF PHASE TRANSITION

PH_3

Solid PH_3 exists in δ, β, α, and γ phases described earlier in chapter I. The δ and the β phases coexist with the thermodynamically more stable γ phase, owing to the slow formation of the γ phase. This has been elucidated by Stephenson and Giauque before. To the best of our knowledge, no equivalent work has been done on solid PD_3 so far. And the transition temperatures of the solid phases of PD_3 are, thus, still unknown. Phase transition experiments shown in this chapter not only confirm Stephenson and Giauque's work (or rather reassure our confidence about the phases of thin slab PH_3), but also reveal that solid PD_3 exists in a similar modificatoons.

The β-to-γ phase transition of PH_3, monitored in the ν_2 region, is shown in Fig. 10. This transition was very difficult and was made easier by using the Displex Cryogenic Refrigerator. SG reported the optimum rate of conversion at 39° K. We maintained the sample of the β phase at 39 ± 1° K. After some interval of time, spectra were recorded at this conversion temperature (to give Fig. 10) and also at lowest achievable temperature (to give Fig. 11).

In Fig. 10, the $\beta \rightarrow \gamma$ transition is followed by noting the intensity increase of the bands at 974.1 cm^{-1} and 988 cm^{-1}. The following data indicates the absorbance decrease of the broad β peak and the increase in absorbance (compared with the β absorbance) of

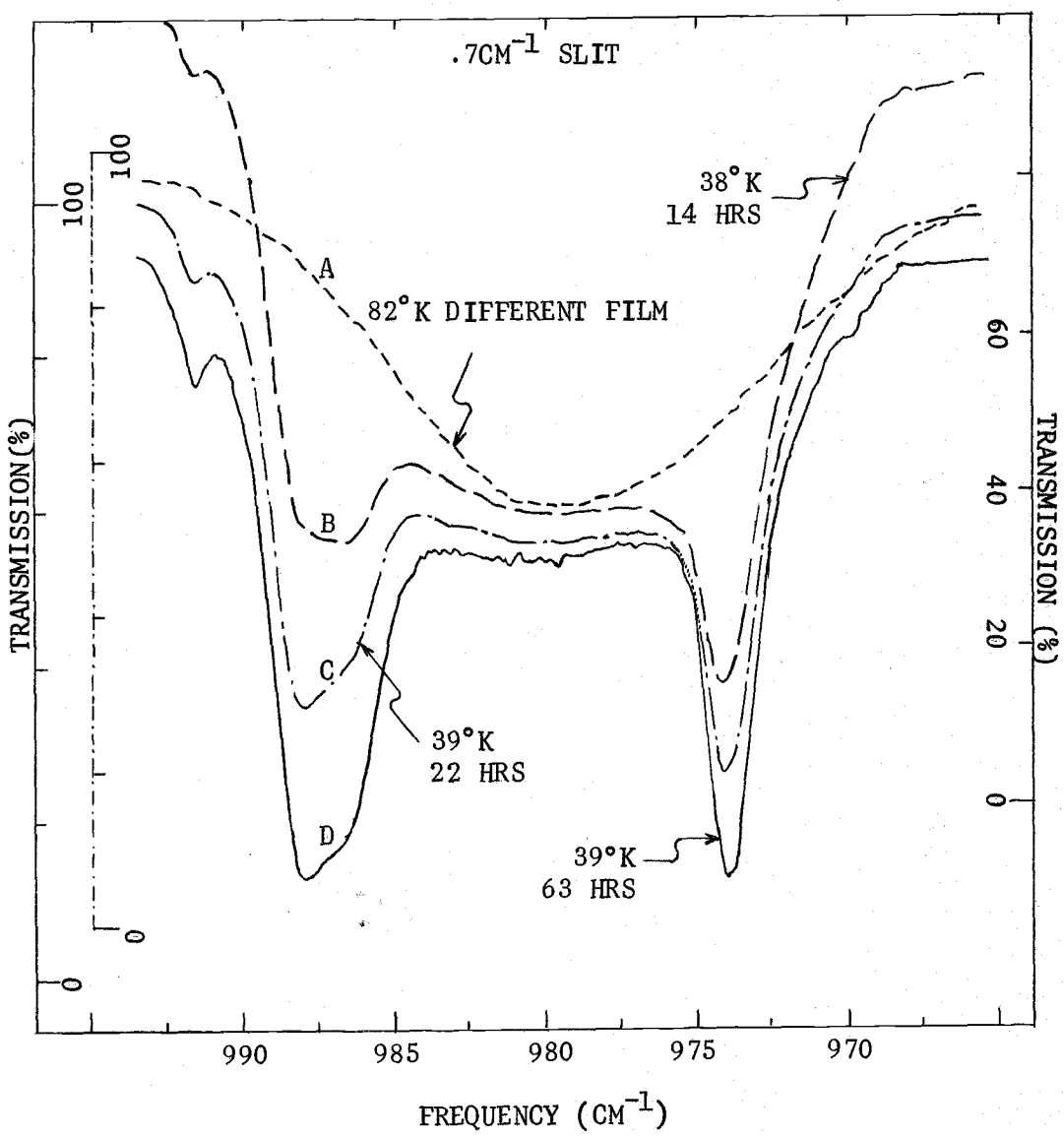

Figure 10. This figure presents the $\beta \rightarrow \gamma$ phase transition of solid PH_3 observed in the ν_2 region of the IR spectrum. Number of hours indicates how long the film had been maintained at $39° \pm 1°$K before the spectrum was recorded. The γ phase content in the film increases with letter order, being zero at A.

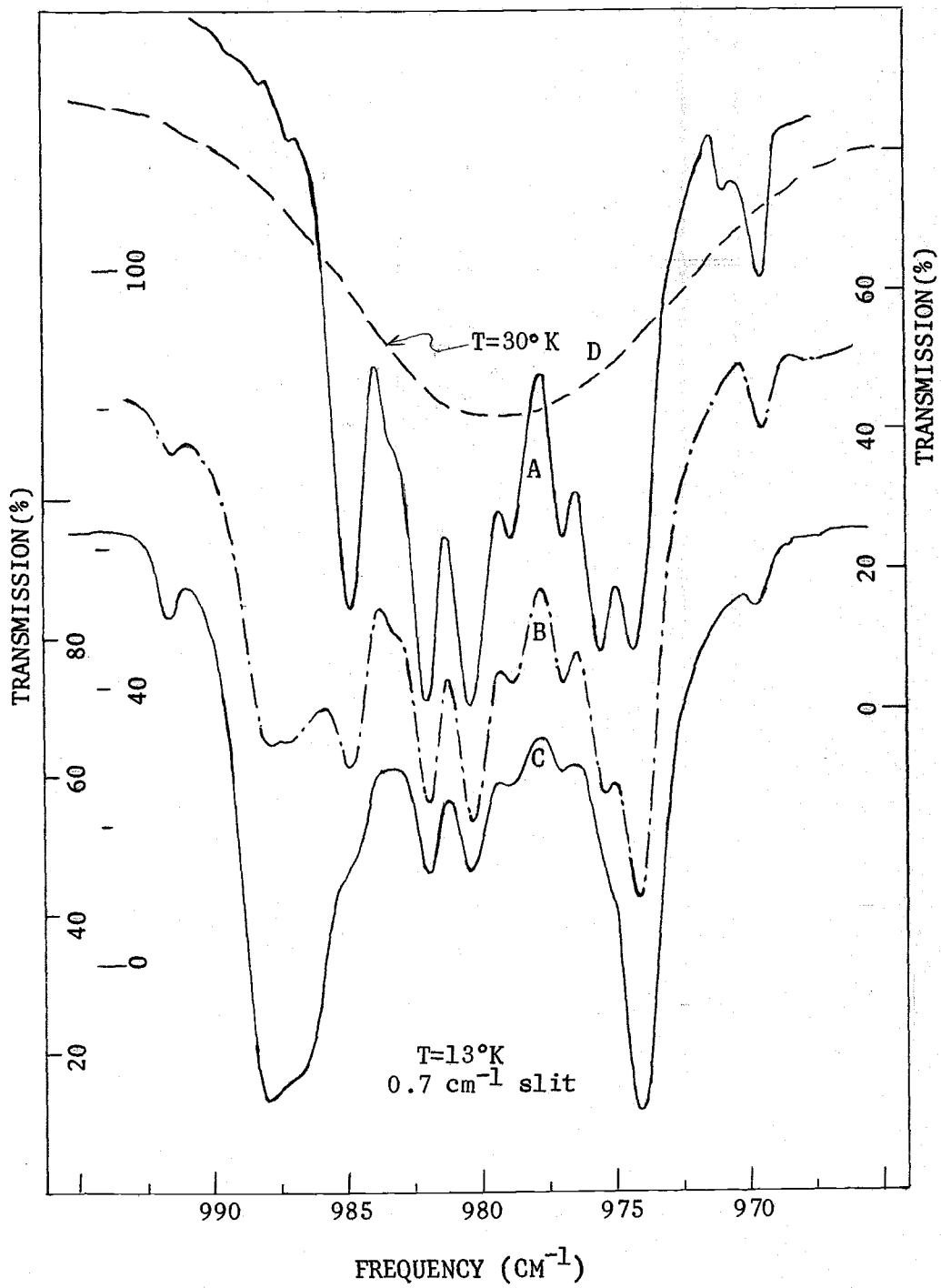

Figure 11. This figure indicates the δ→γ transition. Traces B and C were recorded by cooling films B and D, respectively, of the last figure down to 13°K. Trace A was recorded before the β→γ conversion shown in last figure was started. Also shown in this figure is the β phase (D) in the same region.

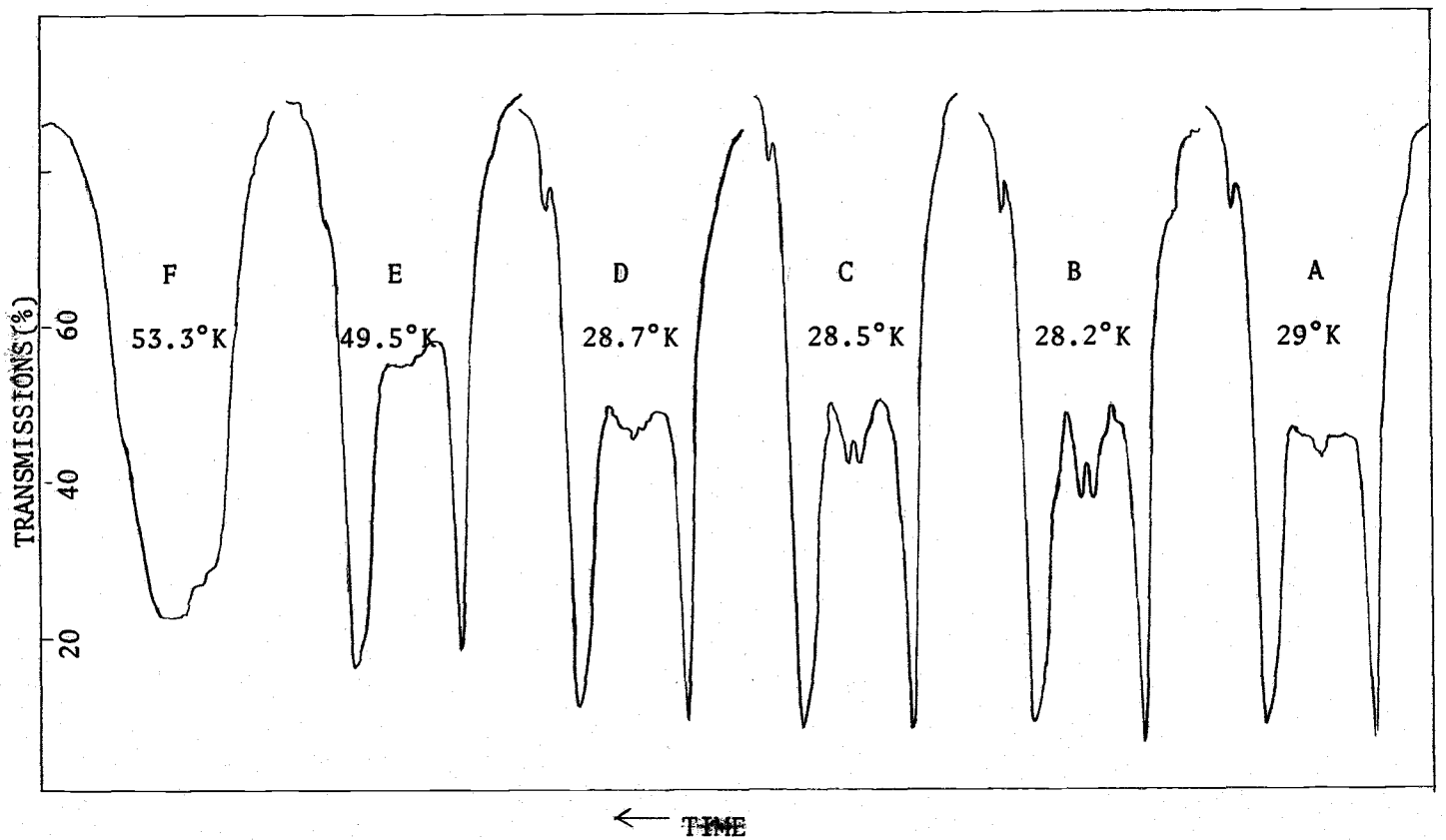

Figure 12. This figure shows, in sequence, the $\beta \rightarrow \delta$(A→B), $\delta \rightarrow \beta$(C→D), and $\gamma \rightarrow \beta$(E→F) phase transitions of solid PH_3 monitored in the ν_2 region in the infrared.

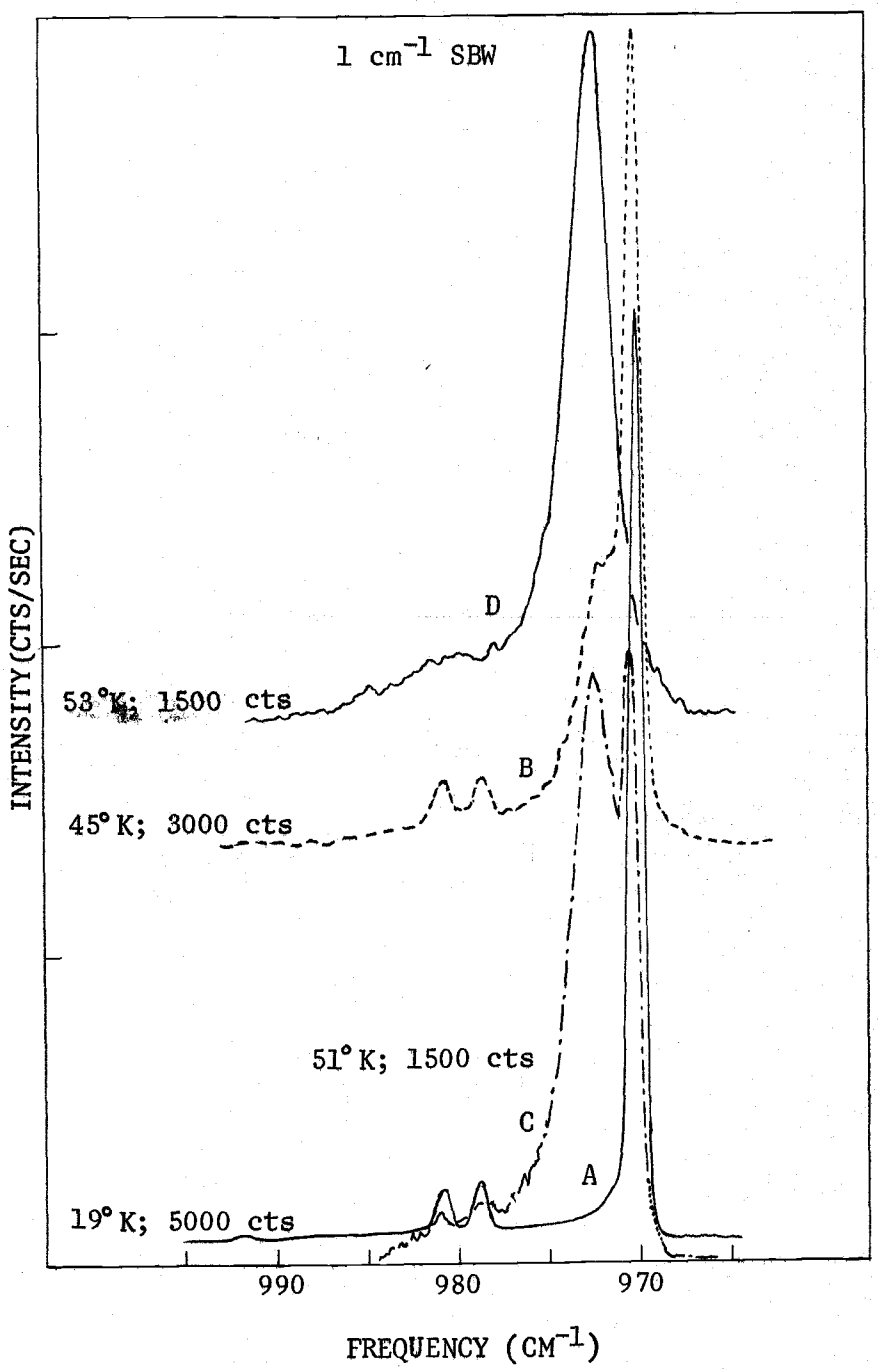

Figure 13. The gamma to beta phase transition of solid PH_3 monitored by the Raman scattering in the symmetric bending mode region. For trace A, the sample was in the gamma phase, trace D in the beta phase.

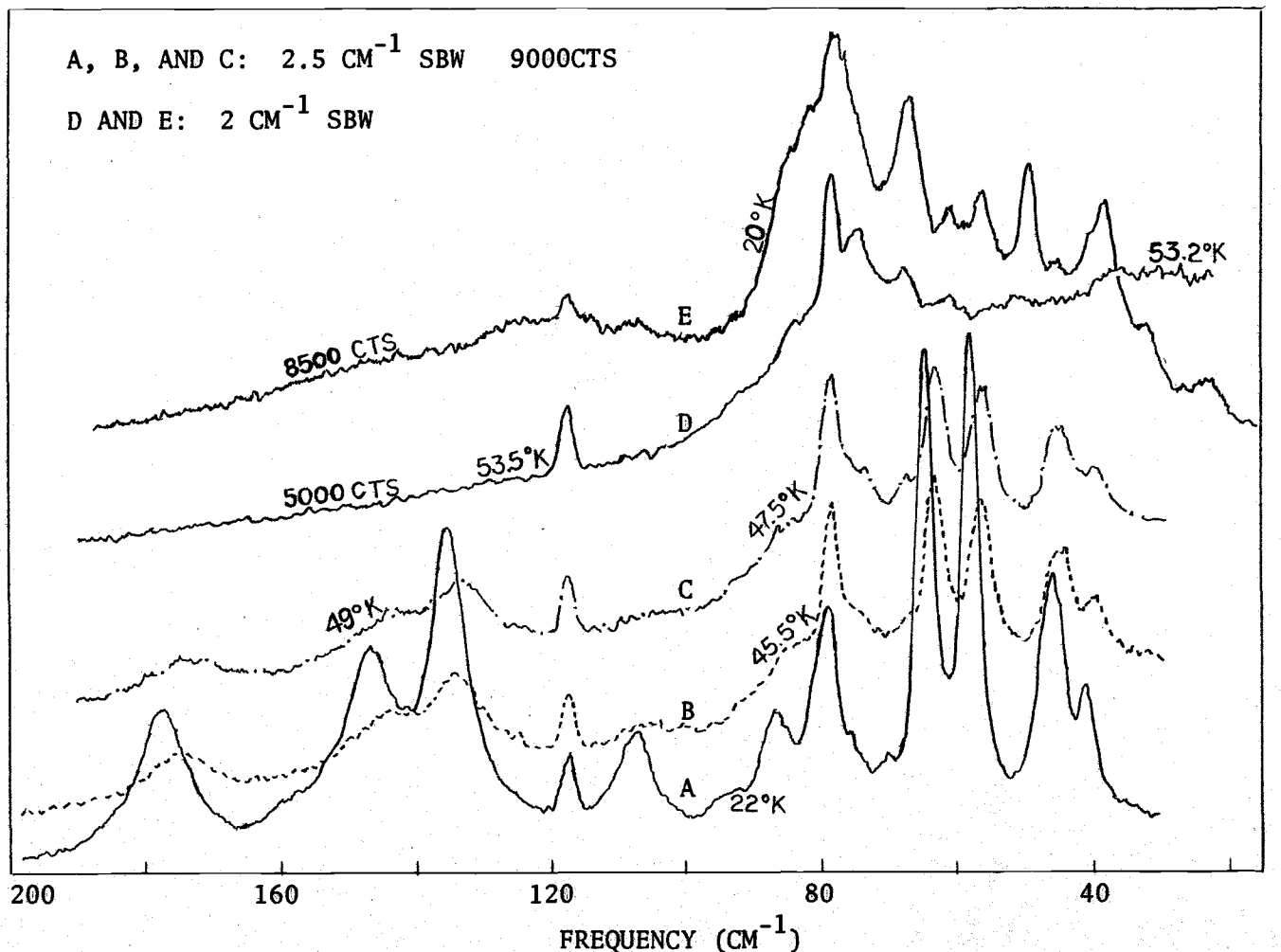

Figure 14. This figure presents the series of Raman PH_3 experiments of $\gamma \rightarrow \beta$(A, B, and C→D) and $\beta \rightarrow \delta$(D→E) phase transitions carried out in the lattice region.

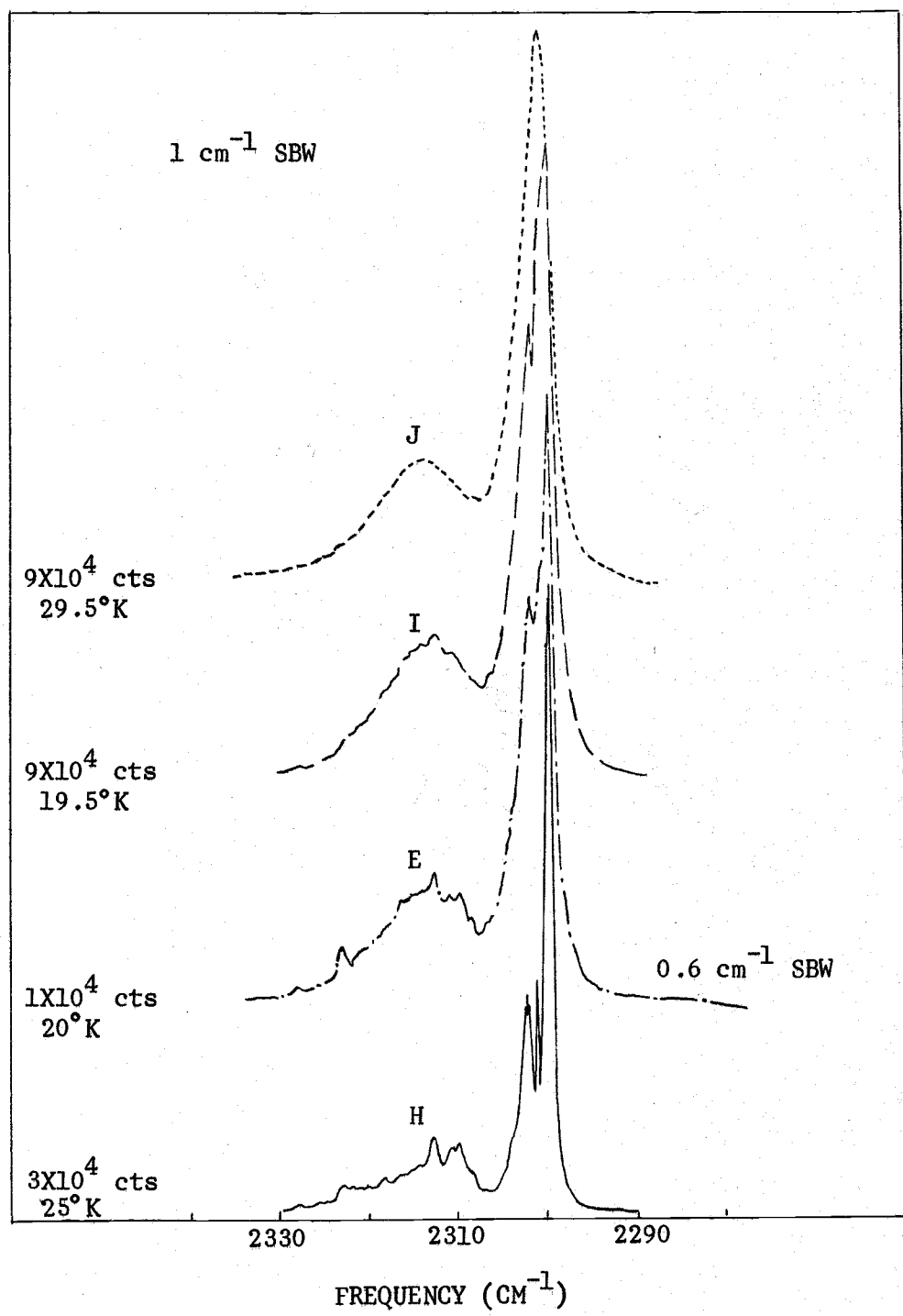

Figure 15. This figure indicates the $\delta(H) \rightarrow \beta$ (J) transition of solid PH_3 monitored in the stretching region in the Raman. Traces E and I contain mixture of the supercooled β and the δ phases.

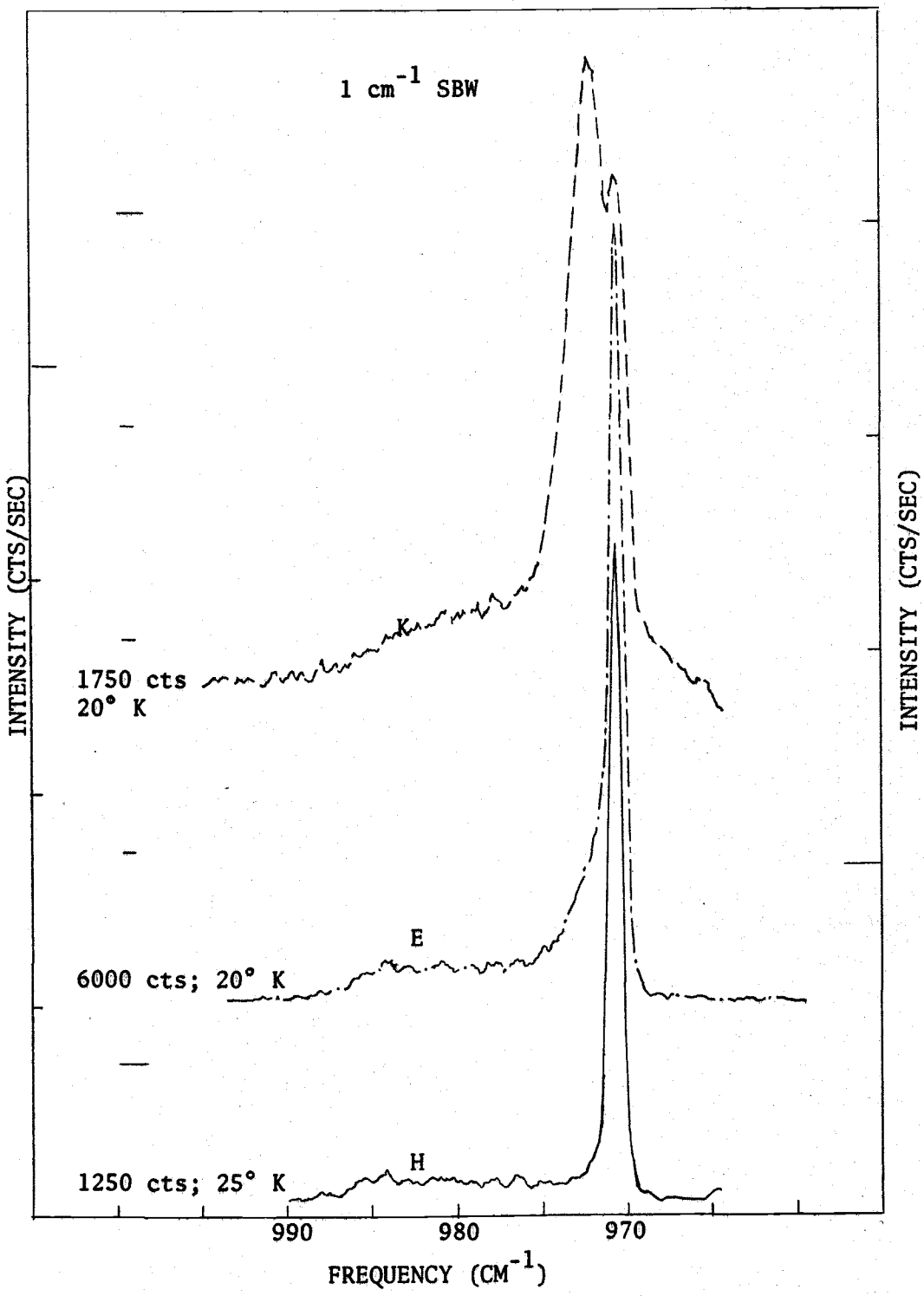

Figure 16. The variation of the spectra in the symmetric bending region obtaining by quickly chilling the solid PH_3 sample through its lambda point. Trace H corresponds to the delta phase, trace E to a mixture of δ plus some supercooled β phases, trace K to mostly the supercooled β phase.

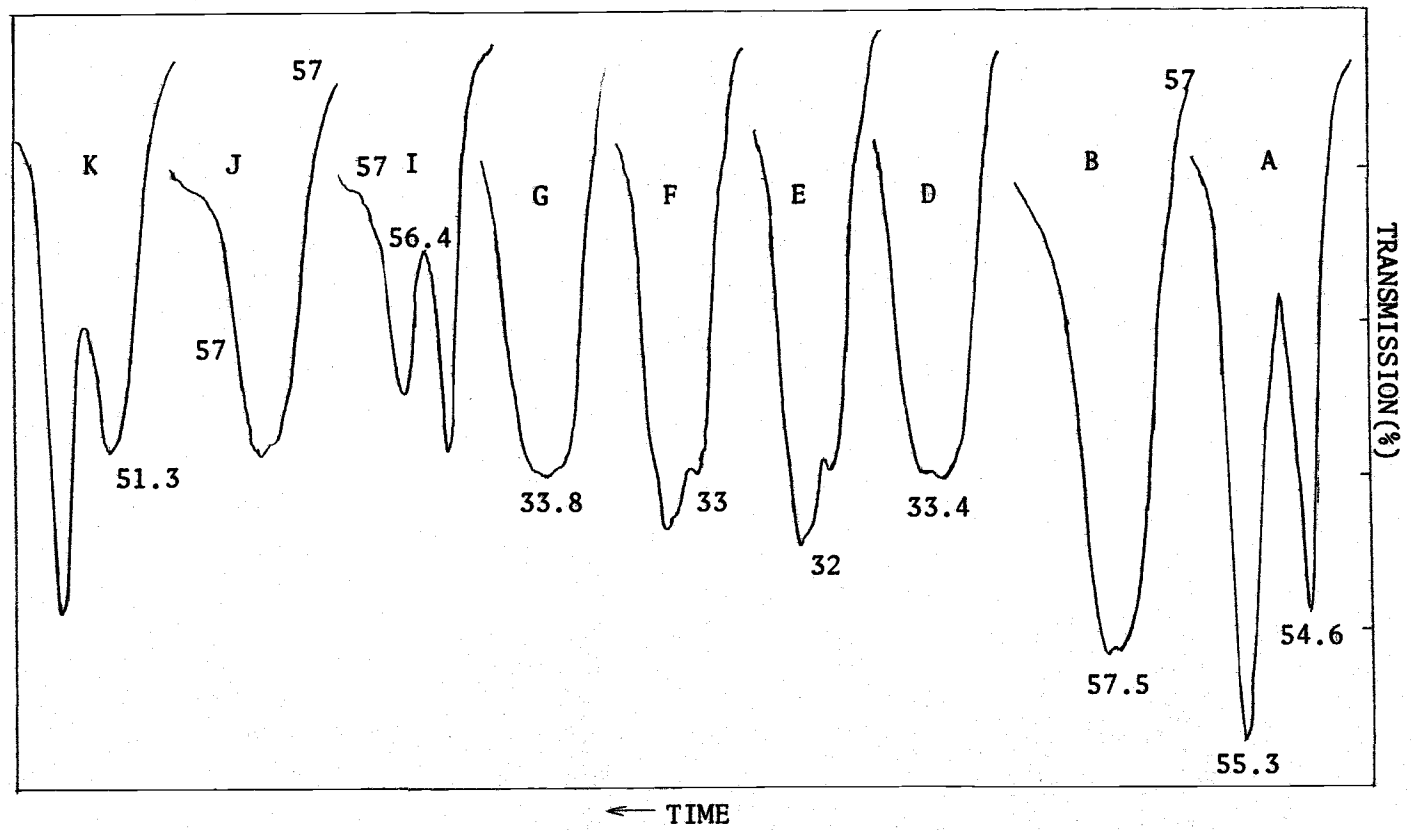

Figure 17. These spectra, taken in letter series, elucidate the β(A→B and I→J), β→δ(D→E), δ→β(F→G), and β→γ(J→K) phase transitions of solid PD_3 observed in the ν_2 region in the infrared. Letters missing in the sequence refer to interruptions for annealing the film. Numbers indicate temperature in degree Kelvin.

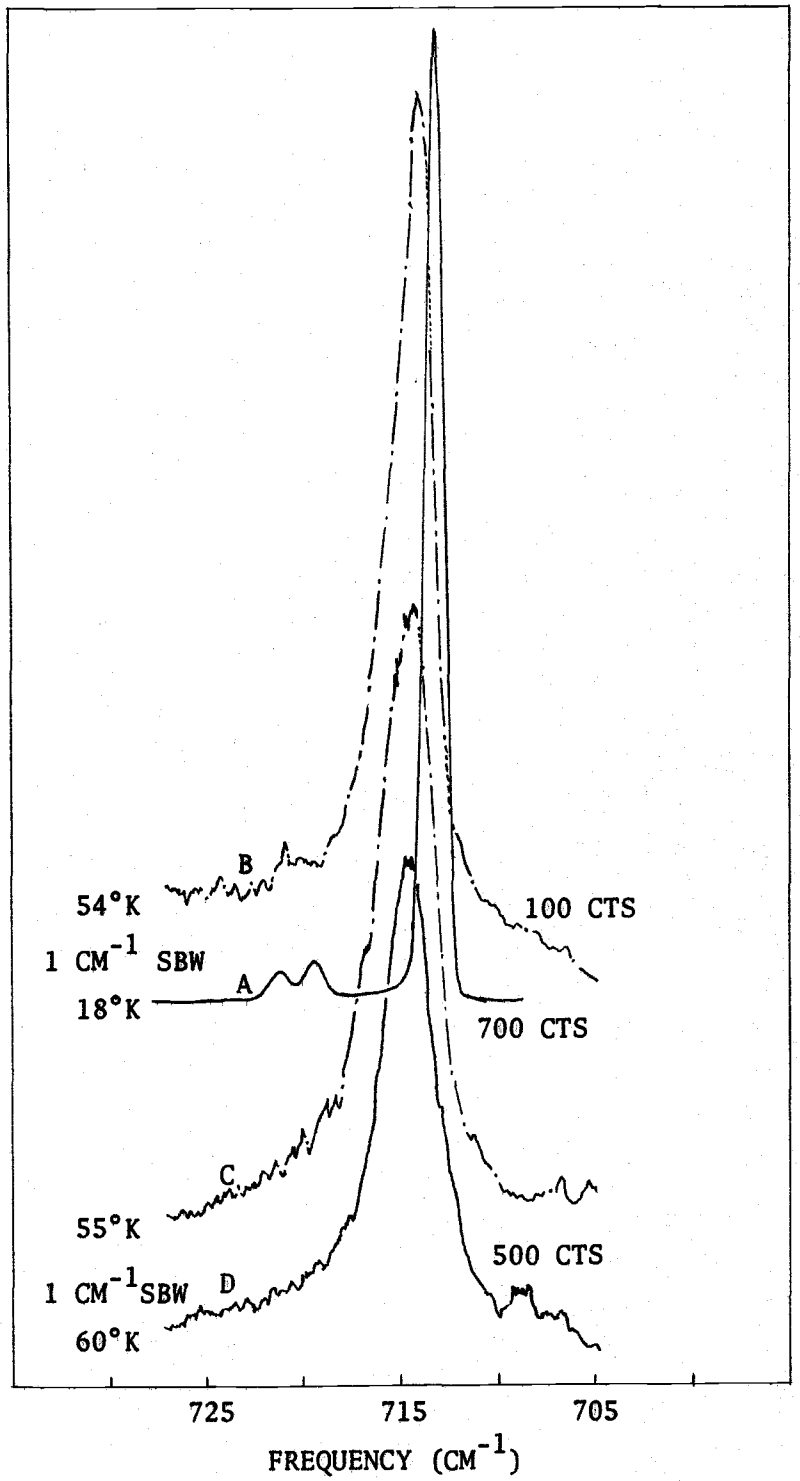

Figure 18. This figure presents, in letter sequence, the γ(A)→ β(D) phase transition Raman experiment carried out in the $\nu_2(PD_3)$ region. Films B and C possibly contain both γ and β phases.

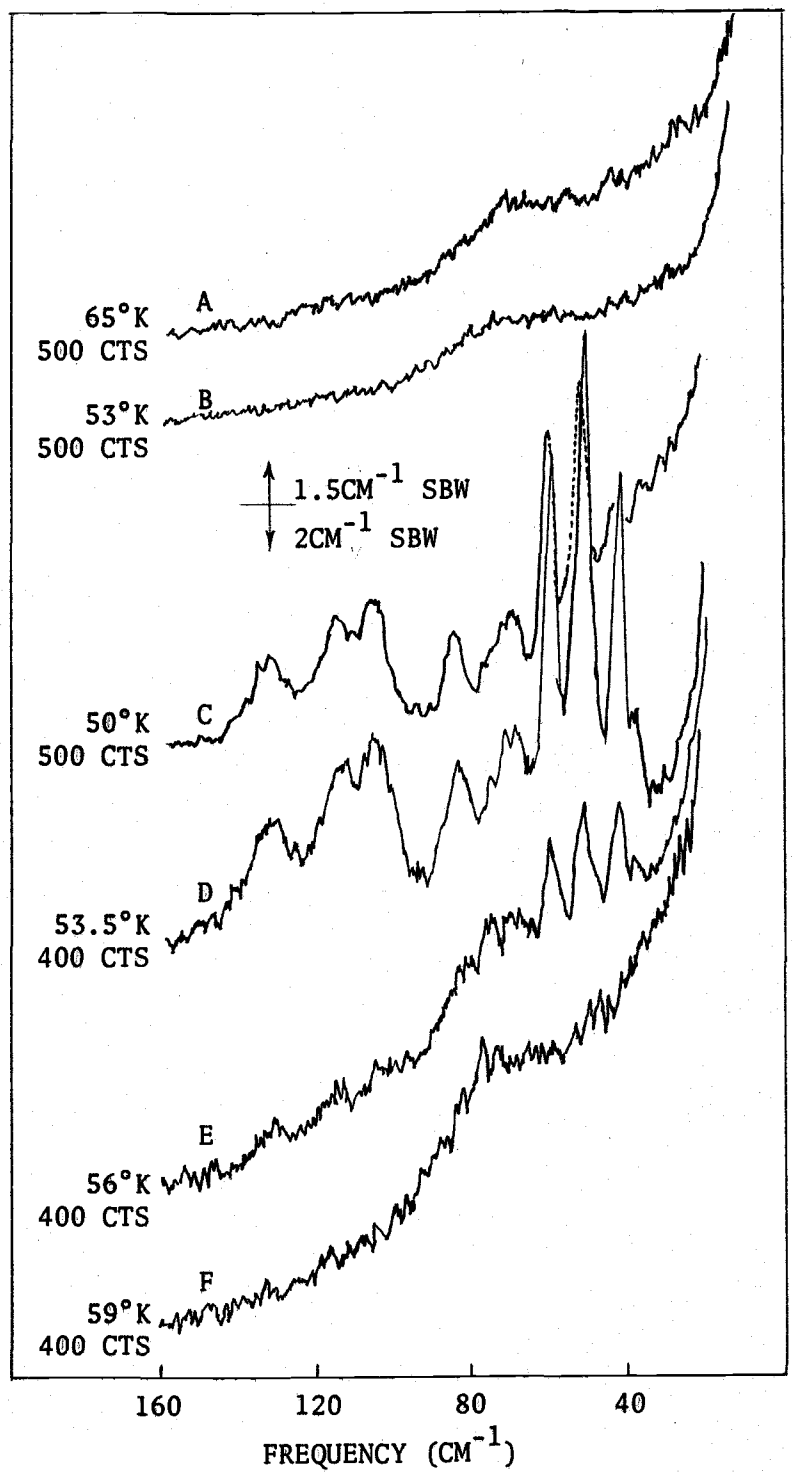

Figure 19. This figure shows the cycle of $\beta \rightarrow \gamma \rightarrow \beta$ phase transition observed, in letter order, in the lattice region of solid PD_3 in the Raman spectrum.

the γ peak at 974.1 cm^{-1} .

	14 hrs (38°K)	22 hrs (39°K)	32 hrs (38°K)	43 hrs (37°K)	63 hrs (38°K)
$A(974.1) - A(\beta)$	.380	.40	.410	.45	.63
$A(\beta)$	.4	.270	.230	.230	.24

It does not seem possible to completely convert the whole slab sample into the γ phase in three days as SG did. This is understandable. SG's 2.446 moles of the solid sample were obtained by cooling the gaseous sample into liquid and then into solid. In this three dimensional solid, domains were larger and better associated, while the IR sample that we used was in the form of a very thin slab which was composed of loosely aggregated polycrystaline material.

Although the transition $\beta \rightarrow \gamma$ is slow, it was found possible to convert the β,γ mixture rapidly to a δ,γ mixture and vice versa, simply by cooling the sample which had been maintained at 39°K below the $\beta \leftrightarrow \delta$ transition temperature near 30°K. Upon warming again to about 39°K, the β,γ mixture was recovered, and the slow conversion $\beta \rightarrow \gamma$ was then allowed to proceed further. This is shown in Fig. 11.

The course of $\delta \rightarrow \gamma$ conversion was described by the intensity decrease of the doublet, 980.3 cm^{-1} and 982.1 cm^{-1} , and the gain in intensity of the bands at 974.1 cm^{-1} and 988.0 cm^{-1} . One notices that the growth of the 974.1 cm^{-1} peak is not in the same rate as that of the 988.0 cm^{-1} one.

Incidentally, the letters used in the figures in this chapter indicate the order that the spectra were recorded.

At the end of the long $\beta \rightarrow \gamma$ conversion (Fig. 10), the film was further subjected to a series of phase transitions among the δ, β, and γ phases. Fig. 12 (trace A corresponds to trace D of Fig. 10) shows these experiments. In these experiments, temperature could be and was held fairly steady with the help of the build-in heater of the Displex Refrigerator. Consequently, the $\delta \leftrightarrow \beta$ transition(recognized by the appearing and disappearing of the doublet at the middle) point can be narrowed down to the range 28.5°-28.7°K. According to SG, the lowest first-order-transition-point of PH_3 is 30.29°K. Comparing our transition point with SG's, two remarks are due. First, the transition that we observed is the first order one at 30.29°K and not the lambda point. Second, our temperature readings in the IR experiments are 1.7°K lower than the precise thermodynamical one. The major contribution to this discrepancy is the fact that the measuring junction of the thermocouple was not in direct contact with the solid film. A minor contribution can be attributed to the accuracy of our thermocouple calibration curve.

The $\gamma \leftrightarrow \beta$ phase transition, as shown by Fig. 10 and traces E and F of Fig. 12, is easily recognizable. The latter two traces indicate that this transition point is between 49.5°K and 53.3°K, which is slightly higher than the literature value, 49.43°K. This temperature deviation will be accounted for at the end of this chapter.

In previous infrared experiments, we found it was very difficult to reach the gamma phase of PH_3. Francia attempted and failed to do so in her infrared work on PH_3. However, our gamma phase PH_3 sample for the Raman experiment was obtained accidentally and rather easily. Described in the following paragraph is how our gamma phase sample was obtained.

The vapor of PH_3 sample trapped in an ethanol-liquid-nitrogen slushy bath near 155°K was allowed to deposit continuously on the shiny aluminum substrate at about 45°K. After the deposition, the film was cooled immediately down to about 20°K in 5 minutes or so. During the cooldown process, the film flaked continuously. Eventually, all of the sample became detached from the substrate. As soon as the peeled sample beads dropped onto the room-temperature-glass-window through which laser entered the cold cell, evaporation started and caused the beads to move irregularly. (When the moving beads got hit by laser, beautiful flashing light was emitted.) Since the parallelepiped substrate was only about one inch away from the bottom window, the evaporated PH_3 molecules(maybe at the melt point, 140°K, or even colder) were recondensed back on the substrate directly. Most of this recondensation occurred at about 20°K. At the end, the recondensed film was annealed up to 83°K once and 79°K twice. In the final annealing cycle, the film was warmed up to 37°K rather slowly and then cooled quickly down to 19°K, while laser was being focused at the same domain.

Thereafter, all of the high resolution Raman gamma scans of

PH_3 presented in following chapters were recorded. They are believed to represent the gamma phase due to the following reasons. First, they resemble their counterparts in PD_3 whose gamma phase was readily reached in the infrared experiments. Second, after the high resolution scans, the apparent gamma phase was warmed up until there appeared to be appreciable changes in both the ν_2 (see Fig. 13) and the lattice (see traces A to D, Fig. 14) regions. The temperature (45↔53° K), at which the spectral changes emerged, agrees better with the gamma-to-beta than the delta-to-beta transition point. Furthermore, when the film was cooled back down to 20°K quickly, the lattice, stretching, and ν_2 spectra (traces E of Figs. 14, 15, and 13) exhibited unmistakeable difference from the apparent gamma phase. For example, the lattice bands above 100 cm^{-1} (except the plasma band at 117 cm^{-1}) had disappeared. And the spectra in the region below 100 cm^{-1} had undergone noticable changes too. In addition, in the ν_2 region, the weak doublet near 980 cm^{-1} was clearly replaced by noise, although the position and band half-width of the strong feature remained essentially unchanged.

Therefore, we conclude that Fig. 13 and traces A to D of Fig. 14 do stand for a transition which ought to be the gamma-to-beta phase change. In connection, we note that the 107.4 cm^{-1} band of the gamma phase is fairly temperature dependent, and that the band near 80 cm^{-1} is almost completely temperature independent (slight down-stream shift from trace A to trace B and no detectable

shift from B to C, as the rest of the bands show).

One observation is very noteworthy before we proceed to prove that the transformation from films D to films E in Figs. 13, 14, 15, and 16 represents a transition which should be the beta-to-delta one. In the Raman PH_3 experiment prior to this one, the successfully deposited film exhibited no appreciable spectral change accompanying the delta-beta and gamma-beta transitions which we consistently obtained in the absorption experiments. On the other hand, the gamma phase was obtained very easily this time. This prompted us to speculate that a deposited film may consist of many domains. Some domains, somehow, can be subjected to these two gamma phase transitions more readily than the other. So, we moved the laser target quite a distance away from the one which had just given rise to all of the high resolution spectra of the gamma phase. What we recorded in the stretching region was nothing but the one like trace J of Fig. 15(actually the completely supercooled beta phase at 20°K). Our speculation was, thus, verified. Recall that in almost three day of maintaining the beta phase near 39°K in the absorption experiment, some of the sample(or rather domains) in the slab still stayed in the beta phase. This observation is consistent with what was just described above. As to the beta-to-delta transition in IR, the supercooling of the beta phase might have actually occurred. All of the traces in Fig. 29 and trace A in Fig. 11 were obtained by quickly cooling the film which contained mostly the beta phase below 30°K. The supercooled beta phase might have raised

their background and affected the resolution. It is noted that HH and Francia's ν_2 spectra are slightly better resolved.

Now back to the apparent beta-to-delta transition which was performed following the gamma-to-beta transition. Just looking at traces D and E of Fig. 14, it may seem possible that E is merely a temperature intensification of D. (Note that films labeled with the same letter were taken at the same step in the sequence of annealings and, thus, represent the same domain and the same phase.) However, comparing trace E of Fig. 16 with trace D of Fig. 13, one sees intuitively the spectral change due to cooling through 30°K. Although it is possible that this change is a consequence of the temperature effect too, trace K of Fig. 16 shows the initial state (the supercooled beta phase here) and the final state(i.e. the weak feature at high frequency-side of the strong one) can coexist at one temperature. Therefore, the event of changing from traces D to traces E can not be simply due to temperature dropping and must also be involved in a transition between the beta and some other phase which is most probably the delta phase. Incidentally, a solid system, such as PH_3, with a lambda point tends to be supercooled when temperature drops through the lambda point rapidly. This is why we observed unequivocal coexistence of the supercooled beta and the delta phase in trace K of Fig. 16.

The delta-beta transition point, as shown by traces H and J, is 25↔29.5°K. We believe traces H are the better representation of the delta phase than traces E, since the high frequency-side of

the main feature of the E trace in Fig. 16 indicates that the sample still contains some of the supercooled beta phase. Moreover, Fig. 30 shows that trace H of Fig. 16 corresponds to the delta phase in the infrared experiment. Trace J is recognized as the beta phase, instead of the supercooled beta phase, because of its smoothness when compared with trace I.

Traces H, I, J, and K in Figs. 15 and 16 were obtained by simply warming film E up and then cooling it down several times. During these annealing cycles, the laser target was shifted too. Besides showing the delta-beta transition, Fig. 15 also exhibits, as Fig. 16 does, the coexistence of the supercooled beta and the delta phase in different proportions. In Fig. 15, film I has higher supercooled-beta content than film E and in Fig. 16, film K higher than E. It is noted that these spectra with the supercooled beta phase are strikingly different from their counterparts in IR in appearance.

PD_3

The phase transitions of PD_3 in the infrared were performed several times. The sequence shown in Fig. 17 is just one of them. Traces E and F are recognized as the delta phase ν_2, since their high resolution version(dot-dashed trace, Fig. 31) resembles the structure-rich-ν_2 of the delta phase. The beta-to-gamma phase transition of solid PD_3 is fairly rapid. When the film was cooled down from about 60°K, it usually took only about 6 minutes to complete the conversion. The exact temperature at which this tran-

sition occurs most readily was not pinpointed. Many experiments were performed to measure the gamma-to-beta transition point which averaged out to be 56 ± 1°K, i.e. about 7° higher than in PH_3. The delta-beta transition point was averaged from several runs to be 33 ± 1°K which is about 3° higher than in PH_3. It is difficult to determine whether this temperature is the lambda point or the first order transition point.

Trace I of Fig. 17 shows that the relative intensities of the gamma phase doublet was reversed. This occurred because temperature passed through the gamma-to-beta transition point during the scan.

The gamma-to-beta transition shown in Fig. 18 is characterized by the change in band half-width and by the slight increase of peak position. The spectral change accompanying this transition is more obvious in the lattice region(Fig. 19). The transition temperature agrees well with the infrared observation. The slight deviation in the transition temperature will be discussed at the end of this chapter.

We have not directly observed the delta-beta transition in Raman. It was deduced in the following that the delta phase of PD_3 was actually observed in the Raman. The two Raman traces in Fig. 31 were recorded immediately after the survey scan which promptly followed the deposition at 14°K in quick spurts. They are distinctly different from the gamma phase ν_2 of solid PD_3(trace A, Fig. 18), the main difference being the absence of the weak doublet whose center is at about 720 cm^{-1}, but look rather like the delta phase

ν_2 of PH_3(trace A, Fig. 30). Since the delta phase of PD_3 is rather unstable with respect to the gamma phase, it is possible that the two delta traces contain some gamma phase.

The apparent transition temperatures are summarized in the following.

	PH_3(Raman)	PH_3(IR)	PD_3(Raman)	PD_3(IR)
$\gamma \rightarrow \beta$	47.5-53.5°K	49.5-53.5°K	56°K	56°K
$\beta \leftrightarrow \delta$	25-29.5°K	28.5-28.7°K	?	33°K

In the following, we will explain the transition temperature deviations that we observed. The γ-to-β transition shown in Fig. 13 is unique because of the coexistence of the final and initial phases (trace B and C) at more than one temperature. Since the coexistence of states is the characteristics of all first order transitions, trace B can be interpreted as the representation of the transition point. Thus, laser has caused a local heating of 4.4°K. SG found that the gamma phase can be superheated 0.25°K above the transition point before conversion starts. It is possible that some of the unit cells still existing in the gamma phase underwent phase change, while the rest of them were superheated, as temperature was rising from 45°K to 51°K. It, then, took another 2-degree-rise in temperature to convert the residual gamma phase into the beta phase. (The temperature of complete conversion is the same for both the infrared and the Raman experiments.) That it took a temperature rise of 8 degrees, instead of 0.25 degrees, to remove the superheating indicates that much longer time should

have been allowed for thermal equilibrium.

In Fig. 12, the delta-beta transition temperature was measured to be 1.7 degrees lower than the literature value, 30.29°K. On the other hand, trace E of the same figure seems to suggest that the gamma-beta transition point is higher than the literature value, 49.43°K. It is likely that trace E represents the coexistence of the gamma and the beta phases. The difficulty of attaining thermal equilibrium and the possibility of superheating the gamma phase might have caused the transition point to be too high.

The low nominal transition temperature measured in the first half of the beta – gamma – beta transition cycle of solid PD_3 (Fig. 19) may be due to local heating by laser. (This transition temperature as observed in the IR experiments is 56±1°K.) Although trace E of the last half cycle can be considered as an indication of state coexistence, the transition temperature observed in the last half cycle is still higher than that which observed in the first half cycle. This may be due to the fact that the gamma phase is thermodynamically more stable and, thus, is farther away from the potential top than the beta phase is.

The gamma-to-beta transition series in the PD_3-ν_2 region (Fig. 18) looks different from its counterpart in the PH_3-ν_2 region. Note that the strong gamma peak (970 cm^{-1} for PH_3, 713.1 cm^{-1} for PD_3) and the beta peak (972.6 cm^{-1} for PH_3, 714.5 cm^{-1} for PD_3) are farther apart for PH_3. Traces B and C of Fig. 18 might actually contain both the beta and the gamma components which were not properly resolved.

There is one point in Figs. 15 and 16, which is difficult to explain. The two E traces did not contain the same amount of the supercooled beta phase, despite the fact that they were subjected to the same thermocycling and were taken at the same time. The corresponding ν_4 scan contains even more of the supercooled beta phase than what trace I of Figure 15 shows.

VI. THE INFRARED AND RAMAN SPECTRA OF SOLID PHOSPHINE

It is well established that gaseous phosphine molecules belong to the C_{3v} point group. The fundamental vibrational species of phosphine are $2A_1 + 2E$. In dealing with solid phosphine, the usual convention of indexing the intramolecular vibrations has been adopted. Thus the totally symmetric stretching mode is called ν_1, the totally symmetric bending mode ν_2, the degenerate stretching mode ν_3, and the degenerate bending mode ν_4. A similar convention has been used for the intermediate species PH_2D and PHD_2, using correlation, i.e. the degenerate modes are split into ν_k' and ν_k'', respectively symmetric and antisymmetric to the plane of symmetry.

Natta and Casazza (20) have determined the structures of PH_3 and AsH_3 at 103°K, using X-ray diffraction. They found PH_3 and AsH_3 were isomorphous; the unit cell contains 4 molecules, and the heavier atoms correspond to the fcc structure. The unit cell dimensions for PH_3 are 6.31 ± 0.01Å, for AsH_3 6.40 ± 0.02Å. The structures of the beta, the delta, and the gamma phases of PH_3 have not been determined.

The vibrational frequencies of solid PH_3 and PD_3 in various phases are presented in Tables I, II, and III.

The Survey Scans

PH_3

Figure 20 shows the spectra of the liquid and the alpha phases

Table I. Vibrational frequencies* of PH_3 and PD_3 in the gamma phase

	PH_3			PD_3	
	Raman(19°K)	Infrared(13°K)	ω^H/ω^D	Raman(18°K)	Infrared(13°K)
	41 m		1.017	40.3 m	
	45.6 s		1.020	44.7 s	
	57.5 vs		1.065	54.0 vs	
				57.8 w	
				60 w	
	64.3 vs		1.022	62.9 s	
	~70 w		1.062	65.9 w	
ν_L					
	78.8 s		1.108	71.1 m	
	86.6 m		1.150	75.3 w	
	~92.5 w		1.194	77.5 w	
	107.4 m		1.225	87.7 m	
	134.8 s		1.257	107.2 m	
	146.7 m		1.240	118.3 m	
	177.7 m		1.302	136.5 m	
	970 vs			713.1 vs	
		974.1 s			715.7[a] s
ν_2	979 vw			719.4 vw	
	981 vw			721.2 vw	
		988 vs			725.1[a] vs
	992 vvw	991.7 vw			728.7[a] vw
	1088 s			783 m	
	1094.5 w	1093.8 s		~788 w sh	787.4[b] s
	1099 s	1098.8 w		790.2 s	
ν_4		1100.8 s			792.5[b] s
	1101.8 s				
		~1103 w sh			795.1[b] m
	1106 m			795.6 s	
	2301.5 vs			1668 vs	
ν_1	2303.8 m	2304.2 s		1670.6 w	1670.6 s
		2307 vw			
	2308.6 m			1673 w	1673 m
		2309 w sh			1678.3 m
	2311.2 vw			1677.8 vw	
	2312.7 w	2313 vs bd		1679.6 w	
ν_3					1682.6 vs bd
	2316 m	2316.5 vw		1684 m	
					1686.5 w
	2319.2 w	2319.5 s		1688.3 w	1688.4 m
	2322.6 s			1690.5 s	

Table I. (continued)

$2\nu_2$	1433	1429
$\nu_3 + \nu_4$		~1499 w ~1505 w 1509 s 1514 s
$2\nu_4$	1580	~1573 w 1579.2 s
$\nu_L + \nu_1, \nu_3$	(1761 + 56) = ~1727 (1683 + 62) = ~1745 (1671 + 87) = 1758 (1671 + 105) = 1776 (1683 + 116) = 1799 (1683 + 136) = 1819	
$\nu_2 + \nu_3$		2399 w
$\nu_4 + \nu_1$		2453 s
$\nu_4 + \nu_3$		2462 s 2466 s 2473 s
$(\nu_2 + \nu_3)^{**}$		(3299)m
$2\nu_1$		3309 m 3313 m 3318 m
$\nu_1 + \nu_3$		3331 w
$2\nu_3$		3348 3352 w

* frequencies are in cm^{-1} .
s = strong, m = medium, w = weak, bd = broad, v = very, sh = shoulder
a : during this scan temperature rised from 18°K to 38°K.
b : during this scan temperature rised from 34°K to 43°K.
ν_L : lattice frequency
** : belongs to guest species PH_3.

Table II. Vibrational frequencies of PH_3 and PD_3 in the delta phase

	PH_3				PD_3	
	Raman(20°K)		Infrared(20°K)		Raman(14°K)	Infrared**
	22.5	w				
	31.7	w				
	37.8	s				
	45	w				
	48.6	s				
ν_L	55.8	m				
	60.5	w				
	66.4	s				
	~75	s				
			150	bd		
			969.6	m		712.3 w
	970.2	vvs	~971.6	vw	712.7 vs	
	972.7	vvw				
	974.7	vvw	974.2	s		715.4 m
	976.1	vvw	975.6	s		716.7 m
	977.6	vvw	977	m		~717.6 vw
ν_2	979.1	vvw	978.8	m		~719.1 vw
	981	vvw	980.3	s		720.1 s
	983	vvw	982.1	s		721.5 m
	984.1	vvw	983.3	vw		
	985.4	vvw	984.9	s		723.6 m
			987.3	w		
			989.6†	w		
			~1093	sh		
ν_4			1095.5	s		790 bd
	1102.5	bd	1102	m		
	2300*	vs				1669 s
ν_1	2301.2*	m				1673.2 s
	2302.2*	m	2302	s		1674.5 vw
	2310.2*	vw				1677.7 vw
	2312.8*	vw	2312	vs bd		1681.2 vs
						1682.7
	~2323*	vvw				1684.7 w
3			2322	vw		1686.5 w
			2328.5	m		1690 m
						1695 s

Table II. (continued)

$\nu_3+\nu_1$		1247*	m bd
$2\nu_2$	~1950 vw	1947*	w
$\nu_2+\nu_4$		2081	m
$2\nu_4$		2196	s
$\nu_4+\nu_1$		2447	s
$\nu_3+2\nu_4$	~3185 vw		
$\nu_3+\nu_3$	~3283 vw	3283	m
$\nu_4+\nu_1$	~3390 vw	3389	s

* : taken at 25°K.
** : ν_2 was recorded at 18°K, ν_1, ν_3, and ν_4 at 13°K.
† : not observed persistently.

Table III. Vibrational frequencies of PH_3 in liquid, alpha, and beta phases and PD_3 in beta phase

	PD_3 Δ		PH_3			
	beta phase		beta phase		α phase	liquid
	Raman	IR	Raman†	IR††	IR*	IR**
ν_L	~75 w bd		70			
ν_2	714.5	719	972.6	980.6	982.6	986.6
ν_4	791	793	1102.5	1100	1104	1106
ν_1 & ν_3	1665 s 1684 w bd		2300.6 s 2313.5w bd	~2305 2313	~2310	~2310
$2\nu_2$			~1940 vw			
$\nu_2+\nu_4$		1510		2088	2085	2090
$2\nu_4$		1580		2198	2210	
$\nu_2+\nu_3$			~3280 vw	3284	~3294	~3299
$\nu_4+\nu_1$		2455	~3390 vw	3396	3398	3400
$\nu_4+\nu_3$		2468				
$2\nu_2+\nu_1$		3260				
$2\nu_1$		3312				
$2\nu_3$		3353				

** : temperature fluctuated from 142°K to 152°K.

* : in the region, 2085 cm^{-1} to 2310 cm^{-1}, temperature fluctuated from 120°K to 131°K. For the other bands, temperature varied from 91°K to 96°K.

† : taken at 64°K.

†† : temperature changed from 74°K to 85°K, except the 2313 cm^{-1} band which was recorded at 59°K.

Δ : except the combination-overtone region which was recorded at 63°K, the running temperature was about 60°K.

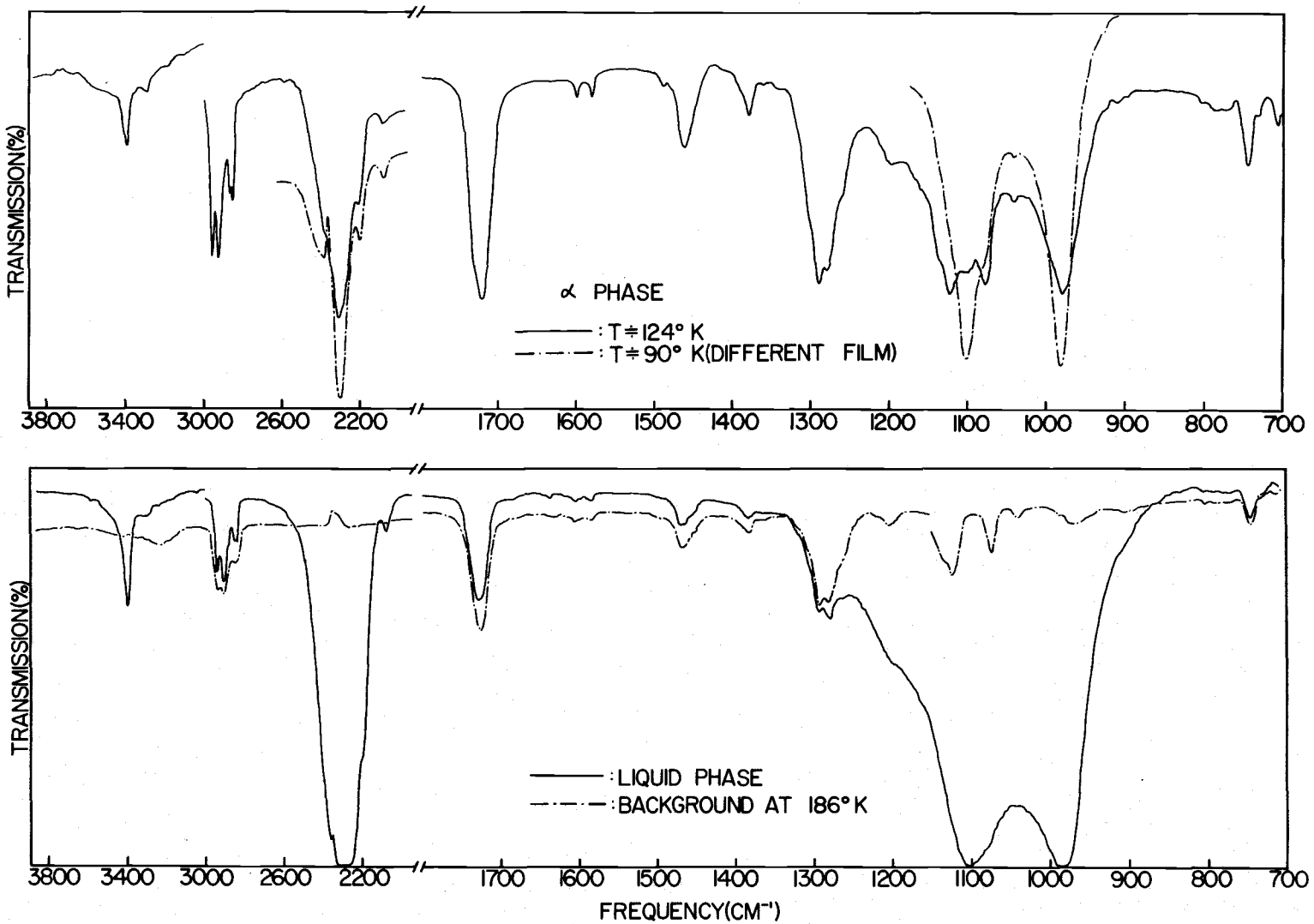

Figure 20. The infrared spectra of PH_3. The liquid cell was used in obtaining these two liquid spectra. The upper and the lower spectra were recorded in different runs.

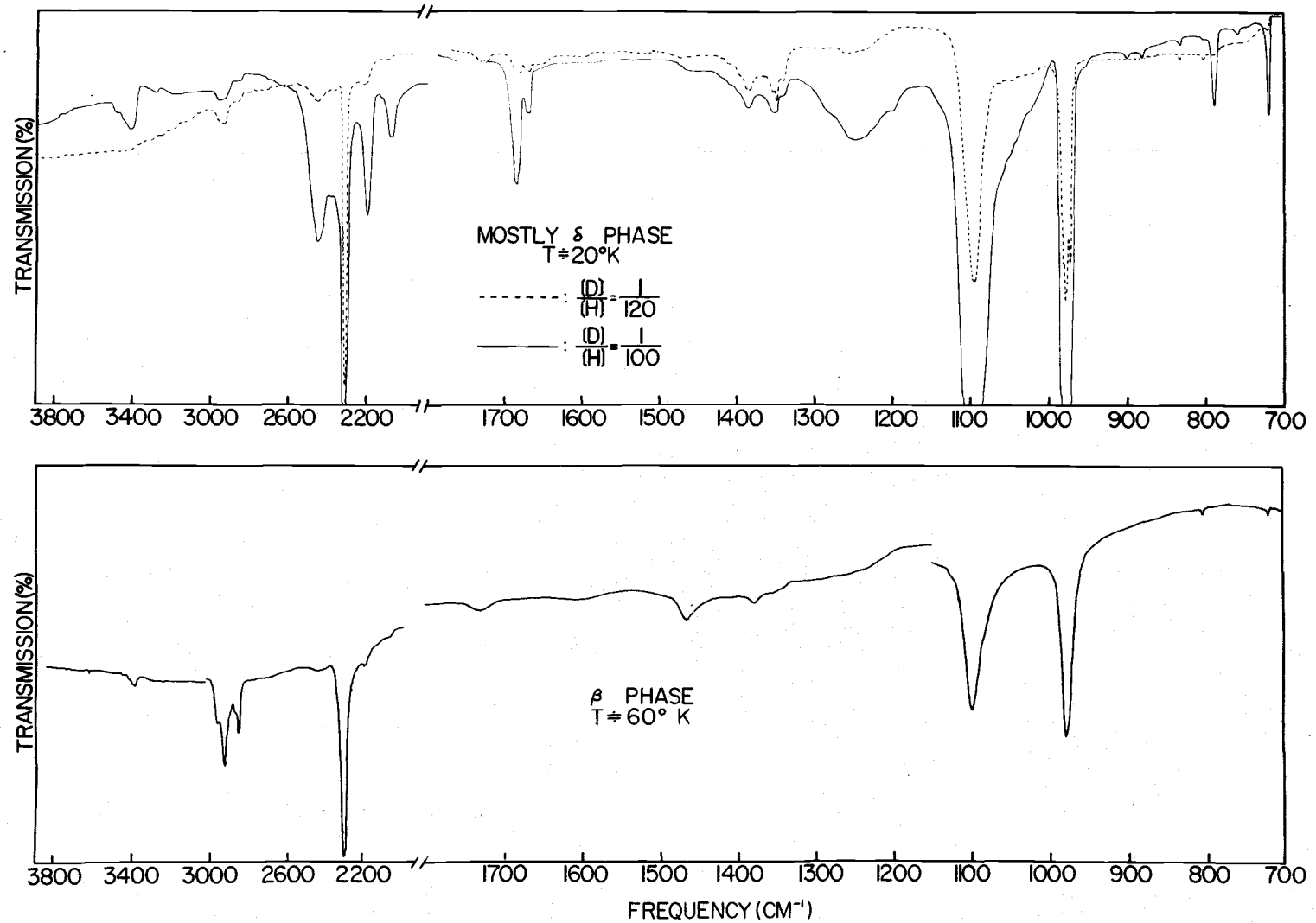

Figure 21. The infrared spectra of solid PH_3. Each sample was deposited on the CsI window.

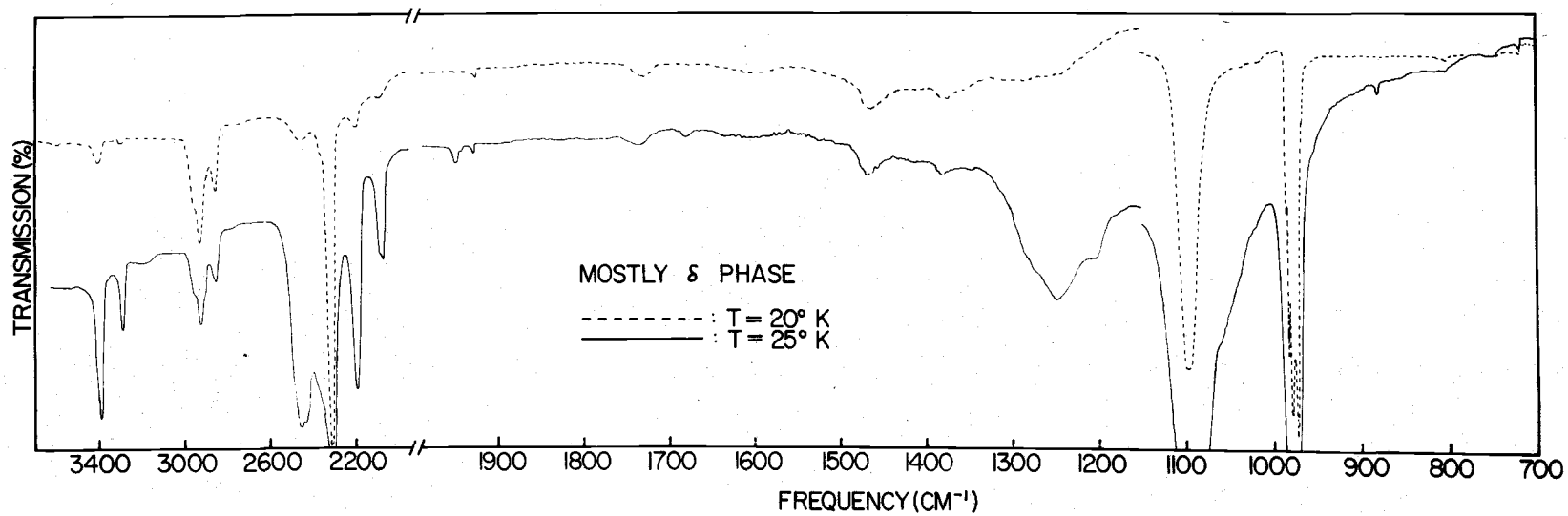

Figure 22. The infrared spectra of solid PH_3. The films were obtained by deposition in different runs.

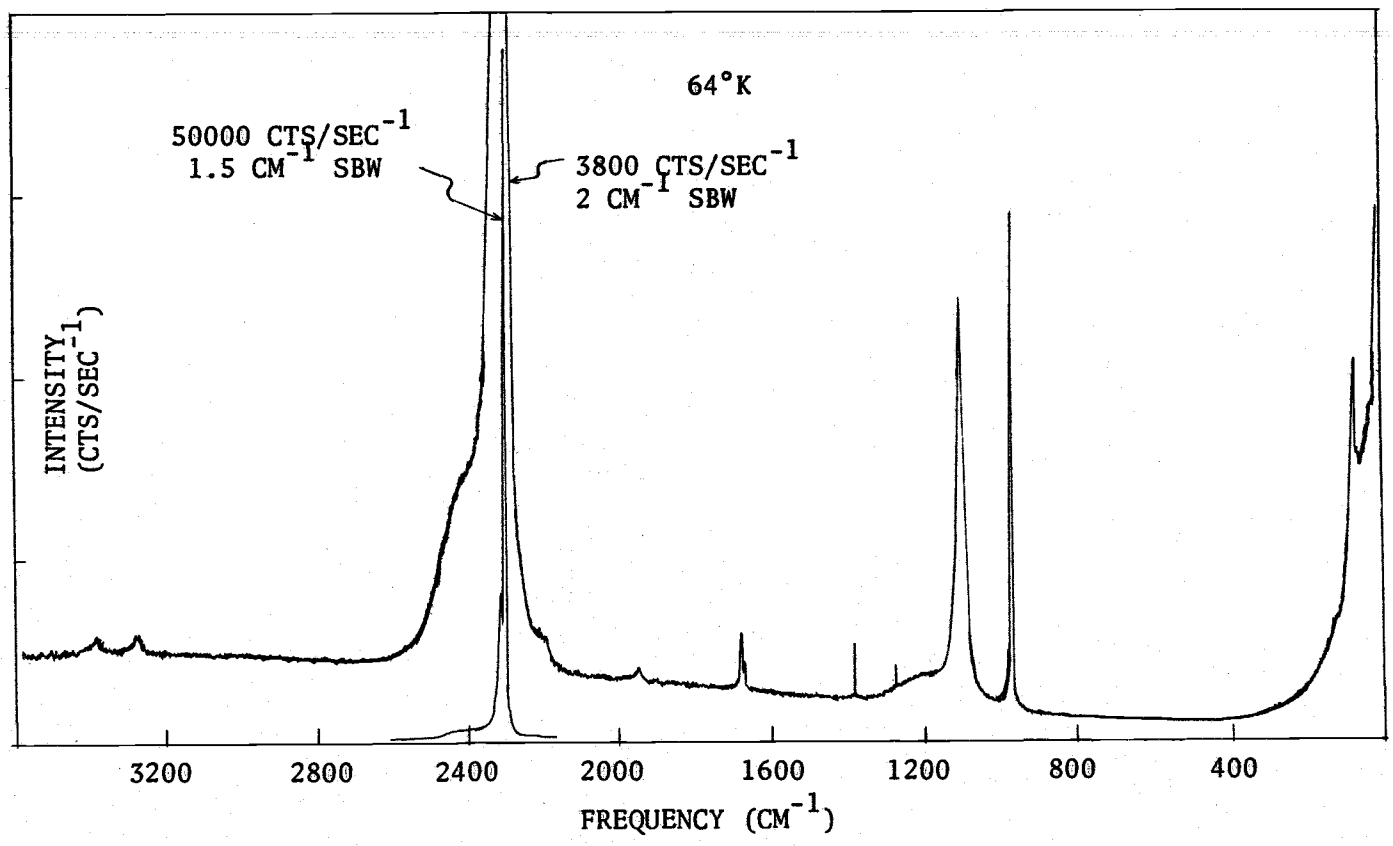

Figure 23. The Raman spectrum of the beta phase of PH_3 containing 0.5% deuterium.

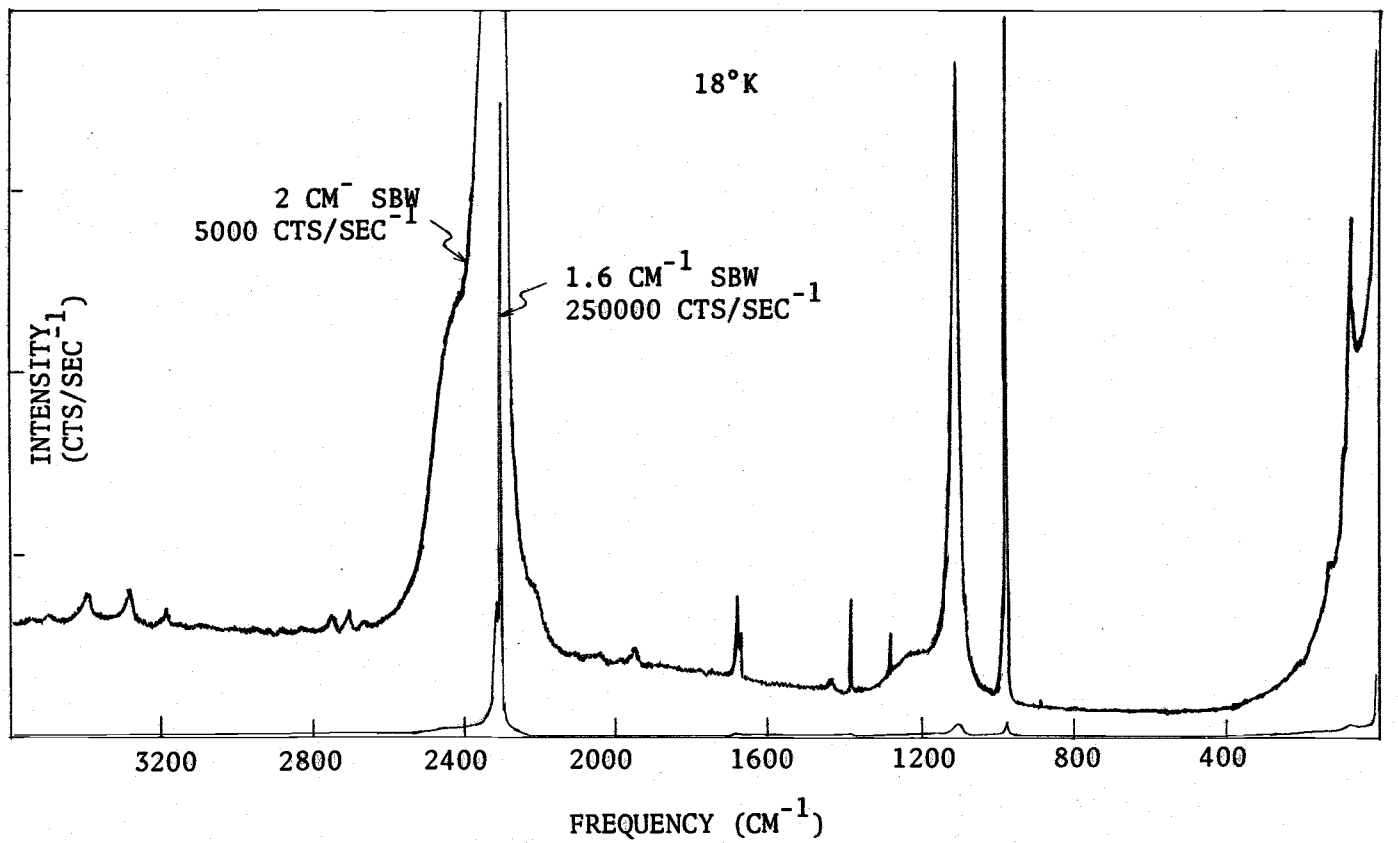

Figure 24. The Raman spectrum of the supercooled β phase of PH_3 containing .5% deuterium.

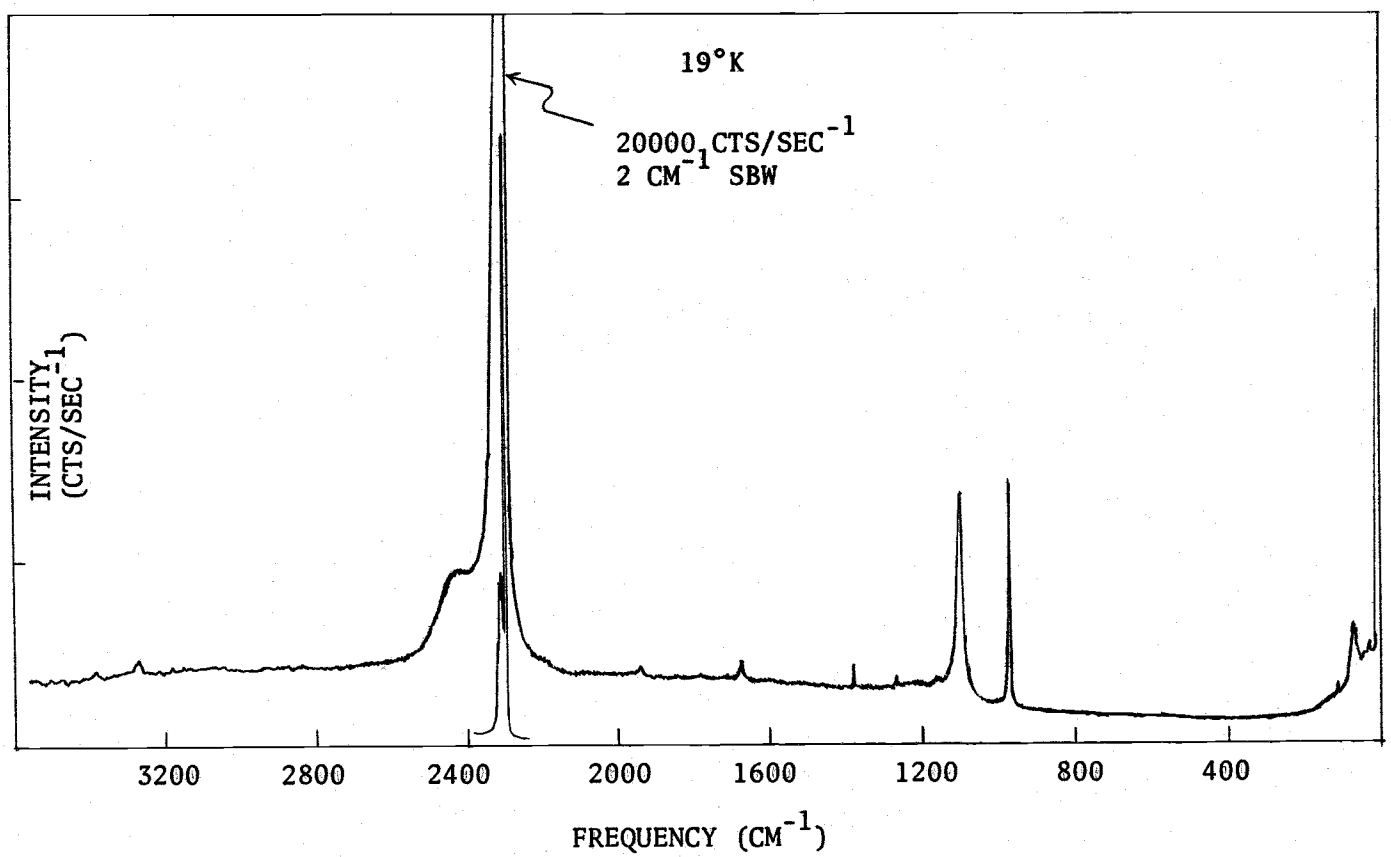

Figure 25. The Raman spectrum of solid PH_3 (with a small amount of deuterium) containing mostly the gamma phase. This film is different from the other Raman survey scans of solid PH_3.

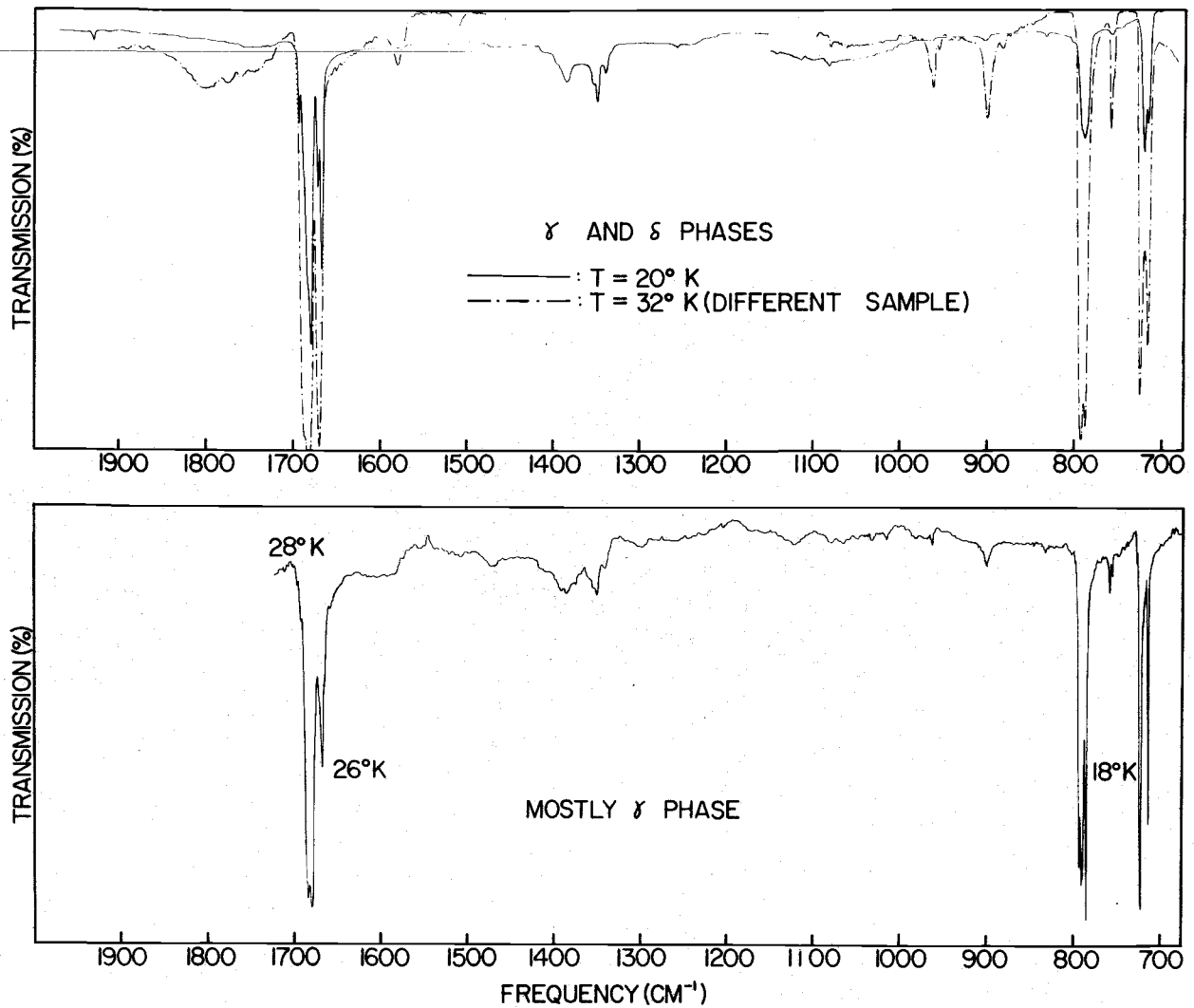

Figure 26. The infrared spectra of solid PD_3. The solid traces were recorded in the same run.

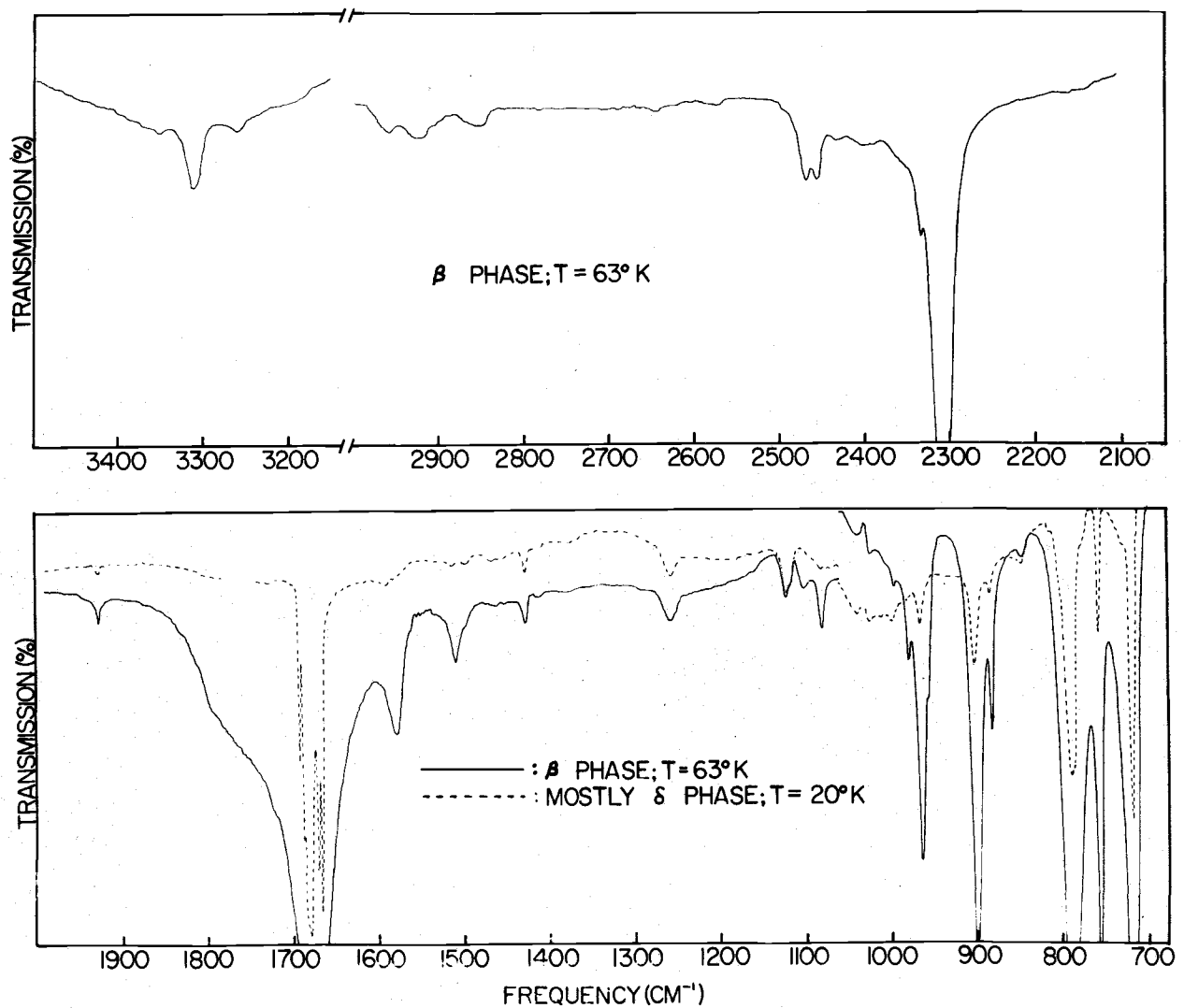

Figure 27. The infrared spectra of solid PD_3. The sample for the upper and the lower solid traces was purposely doped with 0.5% PH_3. The dotted trace was obtained from a used PD_3 sample.

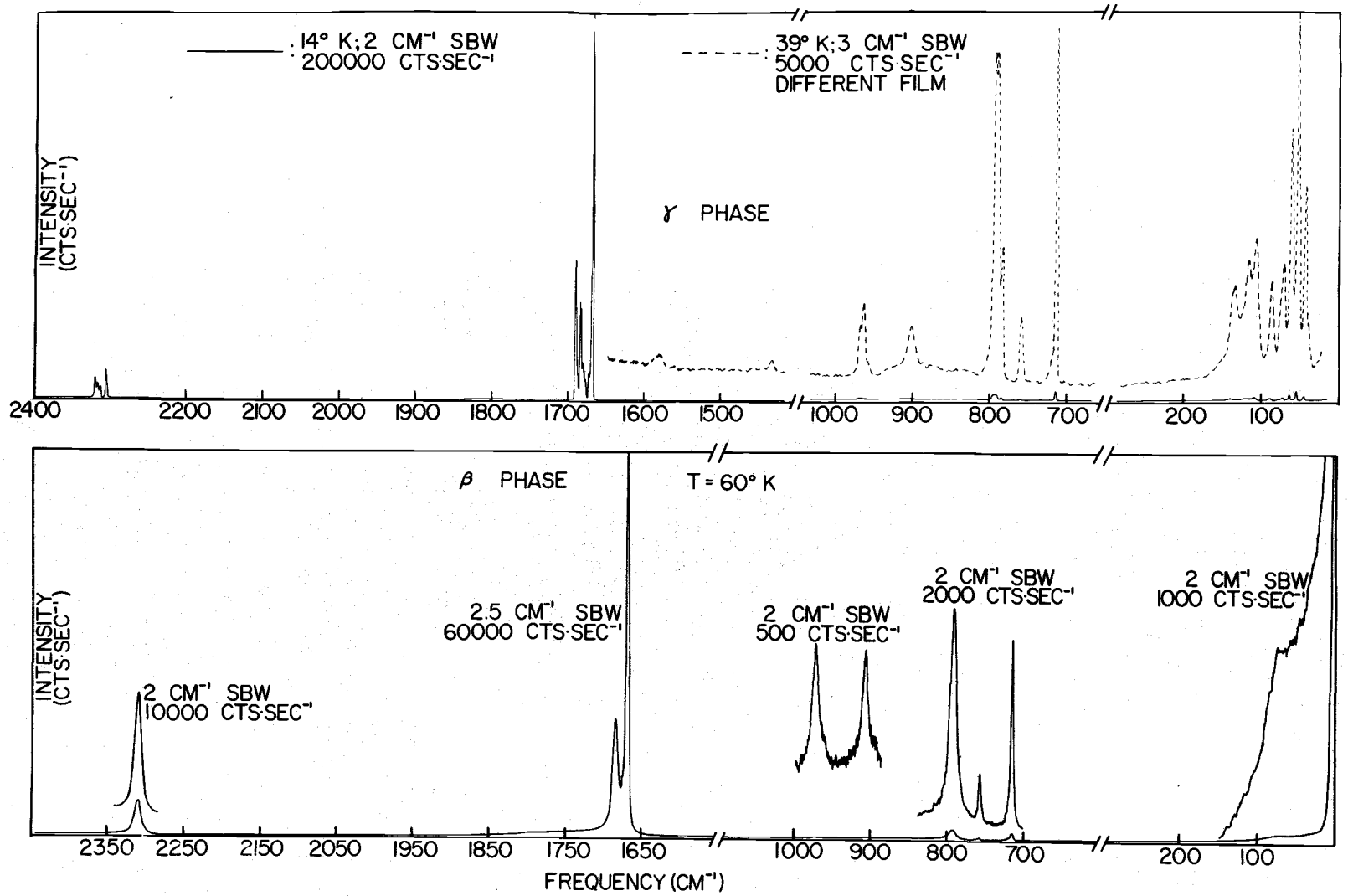

Figure 28. The Raman spectra of solid PD_3. The solid traces were taken from the same film.

of PH_3. The liquid cell had to be used to obtain the spectra, because PH_3 has too high a vapor pressure at the running temperature to allow for the use of the deposition technique. The low temperature cell used was the Cryo-Tip working in the hydrogen expansion mode. It was very difficult to hold temperature in the liquid-phase range steady. During the liquid scan, the temperature dropped from 152°K in the bending region down to 148°K in the stretching region, and 142°K in the combination region.

The temperature profile for the dot-dashed trace of the upper spectrum is 96°K at the symmetric bending region, 91°K at the degenerate bending region, and 90°K at the stretching region. For the solid trace of the upper spectrum, the temperature changed from 120°K in the bending region to 126°K in the stretching region. In the combination region, the temperature was 98°K.

Many impurity absorptions are also shown in Figure 20. Every effort was made to remove the impurities without success. The same impurity absorptions persisted in all the runs. The two strongest background bands at about 1730 cm^{-1} and 2900 cm^{-1} may be due to the C=O and CH stretching vibrations, respectively, of some organic compound such as the stopcock grease, etc. Solid P_2H_4 has the strongest absorption at 1050 cm^{-1} (21). The background did not seem to indicate the presence of solid P_2H_4.

In the lower spectra, the weak band at 2090 cm^{-1} can be assigned as $\nu_4 + \nu_2$, the stronger one at 3400 cm^{-1} as $\nu_4 + \nu_1$, and the weak and broad one at about 3300 cm^{-1} as $\nu_2 + \nu_3$. If the assignment

of the last two combinations are correct, ν_1 should occur at about 2296 cm^{-1} and ν_3 at about 2314 cm^{-1}, taking 985 cm^{-1} for ν_2 and 1104 cm^{-1} for ν_4. The same idea may be used to estimate the positions of ν_1 and ν_3 in other phases whenever they are difficult to resolve. This method is rather crude, since the nonfundamentals are complicated by anharmonicity and dispersion. In the upper spectrum, the two-quanta absorption of ν_4 at about 2210 cm^{-1} is better resolved. The structure at the high frequency side of the stretching mode is believed to be the combination of a lattice mode and the stretching mode.

Shown in Figure 21 are the survey scans of the beta phase and the delta phase containing about 1% deuterium. During the beta survey scan, the temperature dropped from 75°K at ν_2 and 74°K at ν_4 down to 59°K at the stretching region and 41°K at the combination region. Comparing the background of Figure 20 with the lower spectrum of Figure 21, there is no direct relation between the impurity absorption at 2900 cm^{-1} and the rest of the impurity absorptions. It can be seen that the background is by no means unique to the experiments using the liquid cell.

As the temperature drops from room temperature down to 20°K, a slight decrease in energies of the four fundamentals is observed. When a pure system undergoes gas-to-liquid and liquid-to-solid transitions, the interaction among molecules increases, which is evidently responsible for the slight frequency decrease. There are also some changes in the appearance of the bands. As usual, the

liquid band structures are broad, due to the random orientation of the molecules, and a drop in temperature makes the band half-width smaller, but absorbance at the peak greater.

Although the interaction between ν_1 and ν_3 is forbidden by symmetry, the closeness in energies makes it rather difficult to resolve them. This is especially true when both bands are broad at high temperatures. They, however, have been resolved at 20°K where the bands are much sharper.

By comparison, the background can be subtracted easily from the survey scans in Figure 21. The assignment of the bands in the lower spectra of Figure 21 is the same as that for the liquid and alpha phases. The features at 720 cm^{-1}, 790 cm^{-1}, 1670 cm^{-1}, and 1680 cm^{-1} of the upper spectra are believed to be the ν_2, ν_4, ν_1, and ν_3 of PD_3 isolated in solid PH_3, which was mostly in the delta phase. The two weak bands between 800 cm^{-1} and 860 cm^{-1} are very likely impurity absorptions. The weak features at 760 cm^{-1}, 900 cm^{-1}, and 960 cm^{-1} can be assigned as $\nu_2(A')$, $\nu_4(A')$, and $\nu_4(A'')$ of PHD_2 isolated in PH_3. It is unlikely that the weak band at 880 cm^{-1} belongs to the $\nu_2(A')$ of PH_2D, in spite of the fact that its frequency fits the calculated value (the calculation to be shown in chapter IX). The reason is that Figure 22 shows the same band with the same intensity. The PH_3 sample used in obtaining Figure 22 possessed only the natural abundance (0.016%) of deuterium. The broad band at 1250 cm^{-1} can be attributed to the combination of the lattice mode and the degenerate bending mode. The reason for

excluding the symmetric bending mode in this assignment is that the highest lattice mode ever observed is only about 150 cm^{-1}. The assignment of combinations and overtones are essentially the same as was previously done except for the structure at 2447 cm^{-1}, which may be assigned as the combination of the lattice mode (150 cm^{-1}) and the symmetric stretching mode. The degenerate stretching mode may also contribute to this combination band, since it is fairly broad.

The main purpose of adding Figure 22 is to depict some of the previously-shown combination-overtone bands more clearly. The weak feature at 1947 cm^{-1} corresponds to $2\nu_2$ which has not been shown so far. One also unmistakably recognizes the multiplet structure of the delta phase of ν_2 in Figure 22.

Figures 23, 24, and 25 are the Raman survey scans of the beta, the supercooled beta, and the gamma phases of phosphine containing a very small amount of deuterium. Note that the gamma phase survey scan was observed to have a weaker background scattering in the lattice region than the supercooled beta phase one does, although this is not faithfully shown in Figures 24 and 25 due to the difference in cts/sec. Another vaguely recognizable difference between Figures 24 and 25 is in the ν_3 region. The multiplet structure in the ν_3 region (the high frequency-side of the strong ν_1 feature) of the gamma phase appears as spikes in the lower trace of Figure 25, whereas the beta and the supercooled beta phases show only one spike in the same region in Figures 23 and 24. In Figure 25 there

is not any indication of fine structure in the ν_2 and ν_4 regions. This may be due to the resolution and the scan speed.

The sharp features at 1280 cm^{-1} and 1385 cm^{-1} are the result of the Fermi interaction between ν_1 (Σ_g) and $2\nu_2$ ($\Sigma_g + \Delta_g$) of CO_2 as a stubborn impurity. Note that the intensity ratio of these two bands is about 1-to-2. The band at 1680 cm^{-1} and the very weak one at 884 cm^{-1} of Figure 24 are due to the $\nu_1(A')$ and $\nu_2(A')$, respectively, of PH_2D. The other totally symmetric modes, $\nu_3(A')$ at 2320 cm^{-1} and $\nu_4(A')$ at 1080 cm^{-1} (these two frequencies are calculated in chapter IX) might have been embedded in the respective bands of of the host sample.

The weak and broad features at 1950 cm^{-1}, 3280 cm^{-1}, and 3390 cm^{-1} appear, persistently, in these three Raman survey scans. They have been observed in the absorption experiment and can be assigned as $2\nu_2$, $\nu_2 + \nu_3$, and $\nu_1 + \nu_4$ respectively. It is noted that these overtone and combinations are broader than the isolated Fermi doublet of CO_2 mentioned in last paragraph. The width of the band at 1680 cm^{-1} does not seem to be that of a matrix-isolated species. It is likely that the broadness of this band is due to contributions from not only PH_2D but also PD_3 and PHD_2 (for absorptions of PHD_2 see the calculation in chapter IX). Note that it is not impossible to have small amout of PD_3 and PHD_2 in the sample of PH_3 containing small amount of deuterium, if the equilibrium constant for an isotopic substitution reaction of the phosphine system were entered in the calculation performed in the section on "preparation of matrix isolated species" in chapter II.

$\nu_2 + \nu_4$ and $\nu_1 + \nu_L$ appear as shoulders at the low and high frequency sides of the stretching band. This ν_L corresponds to the infrared active one at about 150 cm^{-1}. High resolution scans over the intermolecular regions of the beta and the supercooled beta phases did not reveal any further information than that shown by these two survey scans, i.e., the stronger structure at 74 cm^{-1} and a very weak one at 132 cm^{-1}. The plasma emmission accompanying the 5145Å excitation line has the strongest component at 521 cm^{-1} and a much weaker one at 77 cm-1. Thus the spectrum does not immediately rule out the possibility of the sample contribution to the band at 74 cm-1.

The upper spectrum in Figure 24 shows four weak features(1440 cm^{-1}, 2700 cm^{-1}, 2748 cm^{-1}, and 3185 cm^{-1}) which have not been recorded in the infrared work. The band at 3185 cm^{-1} can be assigned as $2\nu_4 + \nu_2$.

In the molecular frame of reference, the totally symmetric vibration usually causes more distortion of the electron cloud (i.e. larger $\partial\alpha/\partial q$) than the nontotally symmetric ones do. So, the former generally give rise to more intense Raman scattering. This account was found to be approximately correct for solid phosphine. ν_1 was observed to be more intense than the other fundamentals, particularly ν_2 and ν_4. (The intensity scales are linearly expressed in terms of how many counts of scattered photons received per second by the photomultiplier. The peak height is thus directly proportional to the intensity of radiation scattered by the various modes of vibrations.) However, as shown in Figure 25, the ν_2 of PH_3 is of

about the same intensity as ν_4. In the β phase of PD_3 (Fig. 28), ν_4 is even stronger than ν_2.

Actually the total intensity(I_t) of a Raman band for a solid system does not simply depend on $\partial\alpha/\partial q_k$(the molecular polarizability change with respect to the molecular vibrational coordinate), but rather on $\partial\alpha/\partial Q_k$(unit cell polarizability change with respect to the vibration coordinate of the unit cell) and some other factors. I_t for a molecular system has been derived in chapter 3, reference 22 to be proportional to

$$\nu^4 \frac{N_{n''}}{g_{n''}} \left| \langle \alpha \rangle_{n''n'} \right|^2$$

where ν^4 ≡ frequency of the emitted radiation ≡ $\tilde{\nu}_o \pm \nu_{n''n'}$,

$g_{n''}$ ≡ degeneracy of the initial state

$N_{n''}$ ≡ population of the initial state

$\langle \alpha \rangle_{n''n'} = \int \Psi^*_{n'} \alpha \Psi_{n''} d\tau$ ≡ transition moment or polarizability matrix element

$\tilde{\nu}_o$ ≡ 19429.9cm^{-1}(laser line used in this work)

$\nu_{n''n'}$ ≡ frequency of the transition.

Within mechanical harmonic-approximation, the unit cell polarizability α is expanded in Taylor series around the equilibrium position of the unit cell coordinates as

$$\alpha = \alpha_{eq} + \sum_i \left(\frac{\partial \alpha}{\partial Q_i} \right)_{eq} Q_i$$

Since α_{eq} is for Rayleigh scattering, we have for Raman scattering

$$\alpha = \sum_i \left(\frac{\partial \alpha}{\partial Q_i} \right)_{eq} Q_i .$$

If the crystal structure is known, the Q_i's can be expressed as linear combinations of the q_i's by correlating the molecular point group to the unit cell symmetry via the site symmetry. Then, the vibrational wave function of the crystal can be formulated by the exciton method(23). To determine the Raman tensor$(\partial\alpha/\partial Q_i)$ for the i^{th} mode of the crystal, one has to refer to the behavior of the unit cell polarizability under the symmetry species of the factor group. Thus, the Raman band intensity for PH_3 and PD_3, whose structures are still unknown, are affected by so many factors that $\partial\alpha/\partial q_i$ is just not sufficient to account for the observed relative intensities.

Similarly, the IR intensity of solid can not be simply predicted from the molecular basis too. This will be clear looking at the following equation(valid for solid with sites of higher than Td symmetry) given by Vedder and Hornig(24).

$$\int_{band} \gamma d\nu = \frac{1}{n_\infty}\left(\frac{n_\infty^2 + 2}{3}\right)^2 \frac{N\pi}{c}\left(\frac{\partial\mu}{\partial Q}\right)^2$$

where $n \equiv$ refractive index at high frequency

$N \equiv$ # of molecules per unit volume

$\gamma \equiv$ absorption coefficient

$\mu \equiv$ dipole moment of the unit cell.

The maximum information which can be obtained from Raman polarization experiments with crystals requires the use of single crystal samples with well defined directions of the incident and scattered radiation relative to the crystal axes(25). Since these conditions obviously cannot be satisfied in the present work, it is interesting to inquire whether the opposite limit of randomly oriented molecules,

appropriate to the gas or liquid phase, is of any use in the interpretation. For a polycrystalline sample, it might be appropriate to consider randomly oriented unit cells. The theoretically expected depolarization factors for plane polarized incident radiation might then be

$$\rho_l = \frac{3\beta^2}{45\alpha^2 + 4\beta^2}$$

in which α would vanish for modes which are less than totally symmetric in the unit cell, hence $\rho_l = 0.75$, and $\rho_l \leq 0.75$ for the totally symmetric modes.

Depolarization experiments were performed on all the fundamentals of solid PH_3 and PD_3. The analyzer was always held perpendicular to the scattering plane, while the incident electric vector was rotated 90° by turning the half-wave plate 45° . No significant changes in either the vibrational frequencies or the intensities were observed for all the intra- and inter-molecular modes of the delta and the gamma phases of phosphine when the incident elctric vector was rotated. The depolarization factor of gaseous AsH_3 was found to be 0 for ν_2 (905 cm^{-1}), 0 for ν_1 (2113 cm^{-1}), 0.6 for ν_3 (2126 cm^{-1}). Thus, the agreement with the expected values of 0.75 for the E modes, and much less than 0.75 for the A_1 modes is good. When the depolarization experiment was done on liquid CCl_4, slight deviations from the predicted values were observed. The depolarization ratios of ν_1 (459 cm^{-1}), ν_2 (218 cm^{-1}), ν_3 (760 cm^{-1} and 790 cm^{-1}), and ν_4 (315 cm^{-1}) are 0.06, 0.39, 0.34, and 0.41, respectively. The degree of agreement is not so good as that

observed for gases. In turn, the agreement for solids is too poor to be compared with that for liquids.

For a pure solid (or liquid) in which hydrogen bonding is important, there is usually a drastic energy change for the vibrational modes, which is affected by this hydrogen bonding, when the compounds are condensed. Solid ammonia, water, and hydrogen chloride all show hydrogen bonding. We present the vibrational frequency shifts (gas minus solid) for the above-mentioned compounds, and phosphine and phosphine-d_3 in the following table to substantiate this point.

	NH_3	ND_3	HCl	DCl	H_2O	D_2O	PH_3	PD_3
ν_1	+134	+101	+166.5	+167	+257	+150	+22	+26
ν_2	-110#	-66#			- 25	- 32	+13	+11
ν_3	+36(?)	+55			+536	+350	+14	+16
ν_4	-19	- 5					+20	+13

take the average of the inversion doublet.

For the phosphine system, the beta phase data from this work and the gas phase data from reference 26 are used. The frequencies of HCl and DCl used here are the averages of the values given by reference 27. The frequencies of ammonia and water are taken from references 28 and 29 respectively. Examining these shifts, one sees immediately that the hydrogen bonding does not seem to be important in solid phosphine.

PD_3

The infrared and Raman survey scans of PD_3 in the beta, delta, and gamma phases are shown in Figures 26, 27, and 28. In Fig. 26, the upper broken trace represents gamma + some delta phase , but the upper solid trace delta phase as evidenced by the high resolution spectra of the same sample shown in Fig. 34. Curiously, when the film in the delta phase was thickened by depositing more sample, the resultant sample, whose spectrum is shown in the lower trace of Fig. 26, was apparently converted to the gamma phase. The main purpose of showing this lower trace (in spite of the noise level) is to eliminate the background absorption at about 1350 cm^{-1} from the upper solid trace and to help recognize the sequence of the delta-gamma transition (best demonstrated in the bending regions). It also represents the best PD_3 sample (containing the least H) ever made in our laboratory.

The bands belonging to solid PD_3 are self-evident. As in the case of solid PH_3, we assign the band lower in energy in the stretching region to ν_1. The bands at about 750 cm^{-1}, 900 cm^{-1}, and 960 cm^{-1} are, respectively, the $\nu_2(A')$, $\nu_4(A')$, and $\nu_4(A'')$ vibrations of PHD_2. The very weak bands at the low frequency sides of the 900 cm^{-1} and 960 cm^{-1} bands can be assigned to the $\nu_2(A')$ and $\nu_4(A'')$ of the isolated PH_2D species, respectively. The first band to the right of the stretching modes is the first overtone of ν_4, and thd second band to the right is the combination of ν_2 and ν_4. The broad band to the immediate left of the stretching modes is

clearly the combination of the latter with the intermolecular vibrations. The peak maximum is separated by about 120 cm^{-1} from the stretching frequencies, and the width approximately covers the range of the lattice modes observed in the Raman scattering experiments. The very weak peak at 1927 cm^{-1} is assigned as $2\nu_4(A")$ of PHD_2 for two reasons (besides the frequency fit). Its sharpness implies that it is due to an isolated species. In the next figure, its intensity increases with the film thickness. This band differs from the other overtone-combinations in that it is free from the influence of the intermolecular anharmonicity and crystal dispersion.

In Fig. 27, the broken trace, which represents the film for all the infrared traces in Fig. 43 and traces C in Figs. 36 and 38, dot-dashed trace in Fig. 31, and trace D in Fig. 38, serves not only to represent the delta phase but also to enable subtraction of the impurity bands from solid trace which represents the film for all the broken traces in Fig. 40 and trace C of Fig. 33. The thicker film also contained PH_3 in an amount less than that of PH_2D. PHD_2 is more concentrated than PH_2D in this PD_3 film. The spectra of the absorption bands of these guest species under high resolution repeated themselves when their concentrations were reduced in another run. Thus, no intermolecular coupling of the vibrations of the guest species was involved.

In addition to the bands discussed in the second paragraph, we attribute the bands at 980 cm^{-1} (to the immediate left of the ν_4

(A") of PHD_2), 1100 cm^{-1} (broad and very weak), and 1080 cm^{-1} to the ν_2 and ν_4 of PH_3 and the $\nu_4(A')$ of PH_2D, respectively. The contributions from the ν_1 and ν_3 of PH_3, the $\nu_3(A')$ of PHD_2 (particularly), and the $\nu_3(A')$ and $\nu_3(A")$ of PH_2D drove the band at 2310 cm^{-1} off scale. This band was resolved in a thinner film containing fewer isotopic impurities. The overtone and combination transitions not accounted for as yet are the poorly resolved doublet at 2455 cm^{-1} ($\nu_4 + \nu_1$) and 2468 cm^{-1} ($\nu_4 + \nu_3$), the strong peak at 3312 cm^{-1} ($2\nu_1$) and its satellites at 3260 cm^{-1} ($2\nu_4 + \nu_1$) and 3353 cm^{-1} ($2\nu_3$).

Fig. 28 shows the Raman spectra of the gamma and beta phases. The overtones shown only in the upper trace are $2\nu_1$ at 1433 cm^{-1} and $2\nu_4$ at 1580 cm^{-1}. Three obvious changes occurred as the solid changed from the gamma to the beta phase. The crystal became disordered as indicated by the broadening of the bands. The merging into one broad feature of the lattice spectrum is compatible with the PH_3 scattering experiments. The scattering cross section of ν_4 increases relative to that of ν_2. The opposite is found in the PH_3 experiments.

The spectra in Fig. 28 show the bending fundamentals of PHD_2 but do not show the Raman shift due to the $\nu_4(A")$ of PH_2D, which should have occurred at 955 cm^{-1}. The 60°K- and 14°K-scans in this figure were obtained from the same film. Since a scan with 2 cm^{-1} slit width and 500 counts per second sensitivity at 60°K did not reveal any scattering of PH_2D, it is very unlikely that the 2310

cm^{-1} structure taken at 14°K with the same slit width but with 400 times less sensitivity have any contribution from the $\nu_3(A')$ and $\nu_3(A'')$ of PH_2D, even though the stretching vibrations usually have larger scattering cross sections and lowering the temperature can usually intensify a band.

The High Resolution Scans

PH_3

Figure 29 shows the IR spectral variation of the delta ν_2 as a function of deposition condition. All the traces in this figure and the infrared trace in the following figure were recorded in different runs. There are noticeable differences in spectra due to changes in the deposition techniques. It appears that the slowly-and-continuously-deposited (at sufficiently high temperature), solid sample (trace A) is not so well crystallized as that deposited in short spurts (trace C). Film A and C, particularly the former, contained the gamma phase, and the existence of a small amount of the gamma phase in the delta phase might have affected the spectroquality. Note that film B contains the least amount of the gamma phase. It seems fair to conclude that slow deposition at an elevated temperature tends to give rise to a higher concentration of the gamma phase in the delta phase.

The existence of the gamma in the delta host was recognized by the gain in intensity of the 974.1 cm^{-1} band (the second peak from the right) and the addition of the 988.0 cm^{-1} band (the second

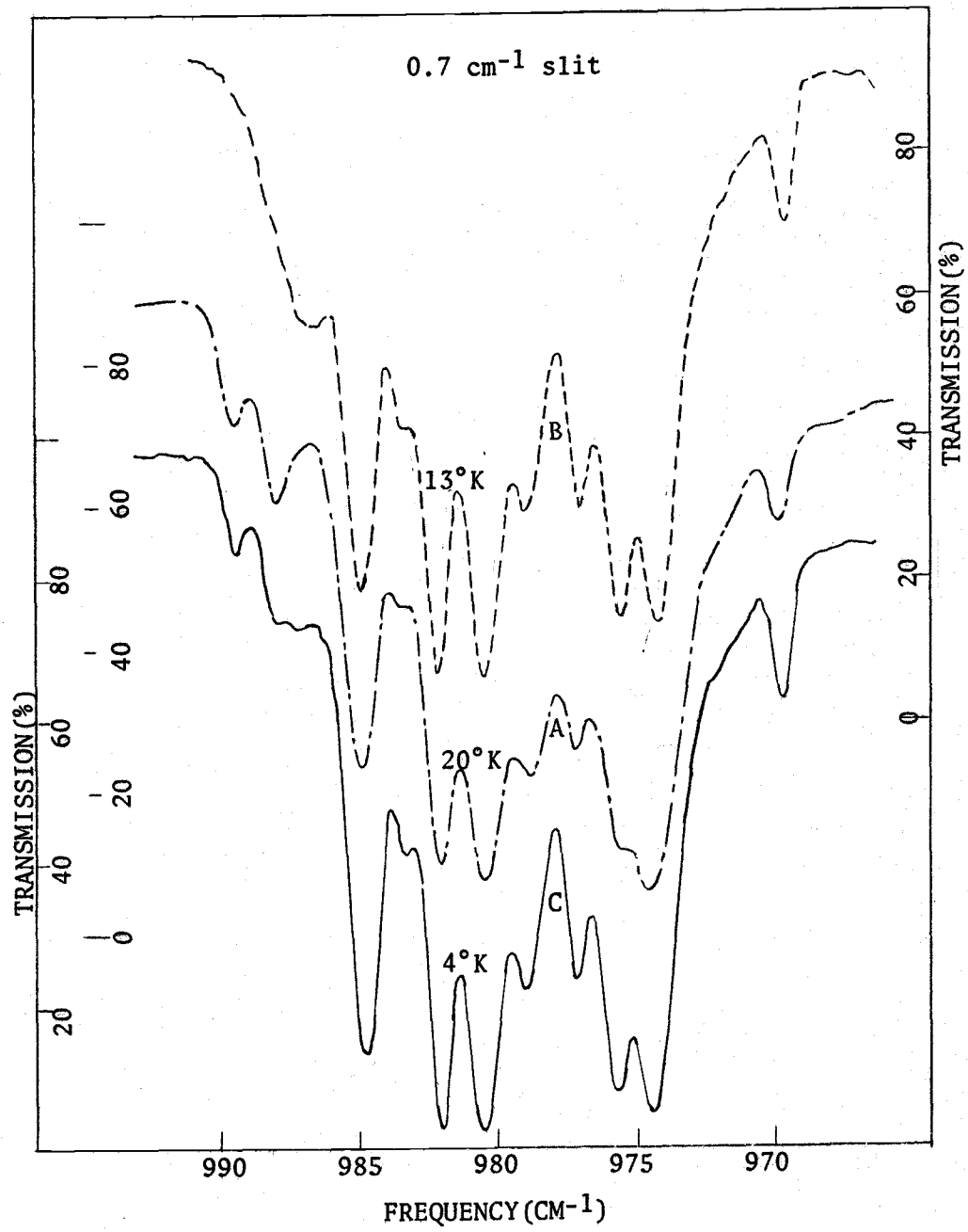

Figure 29. This figure shows the IR spectrum variation of the ν_2 mode of solid PH_3 with respect to deposition temperature and technique. For trace A the film was deposited at 74°K slowly and continuously, trace C in the range of 55°K to 46°K during cooldown in quick spurts. Trace B was taken by warming the film shown as trace C in Fig. 11 up to 53°K and then cooling immediately down to 13°K.

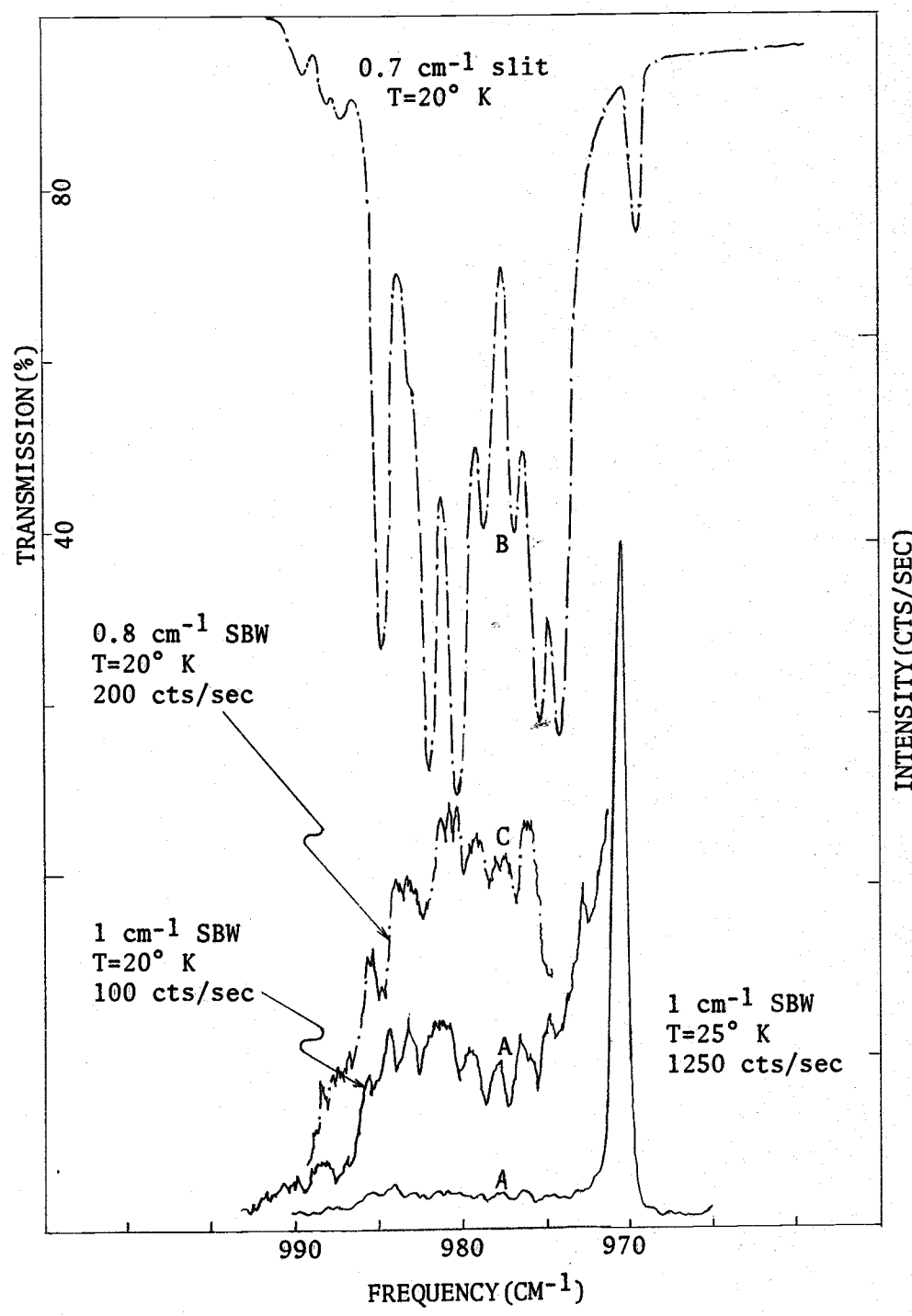

Figure 30. A comparison between the infrared(upper) and the Raman(lower) spectra of the ν_2 mode of the δ phase of PH_3 . The IR sample contained 1% deuterium. The two A traces were taken from tne same film and represent the same phase. Trace C is the blown-up version of trace E, Fig. 16.

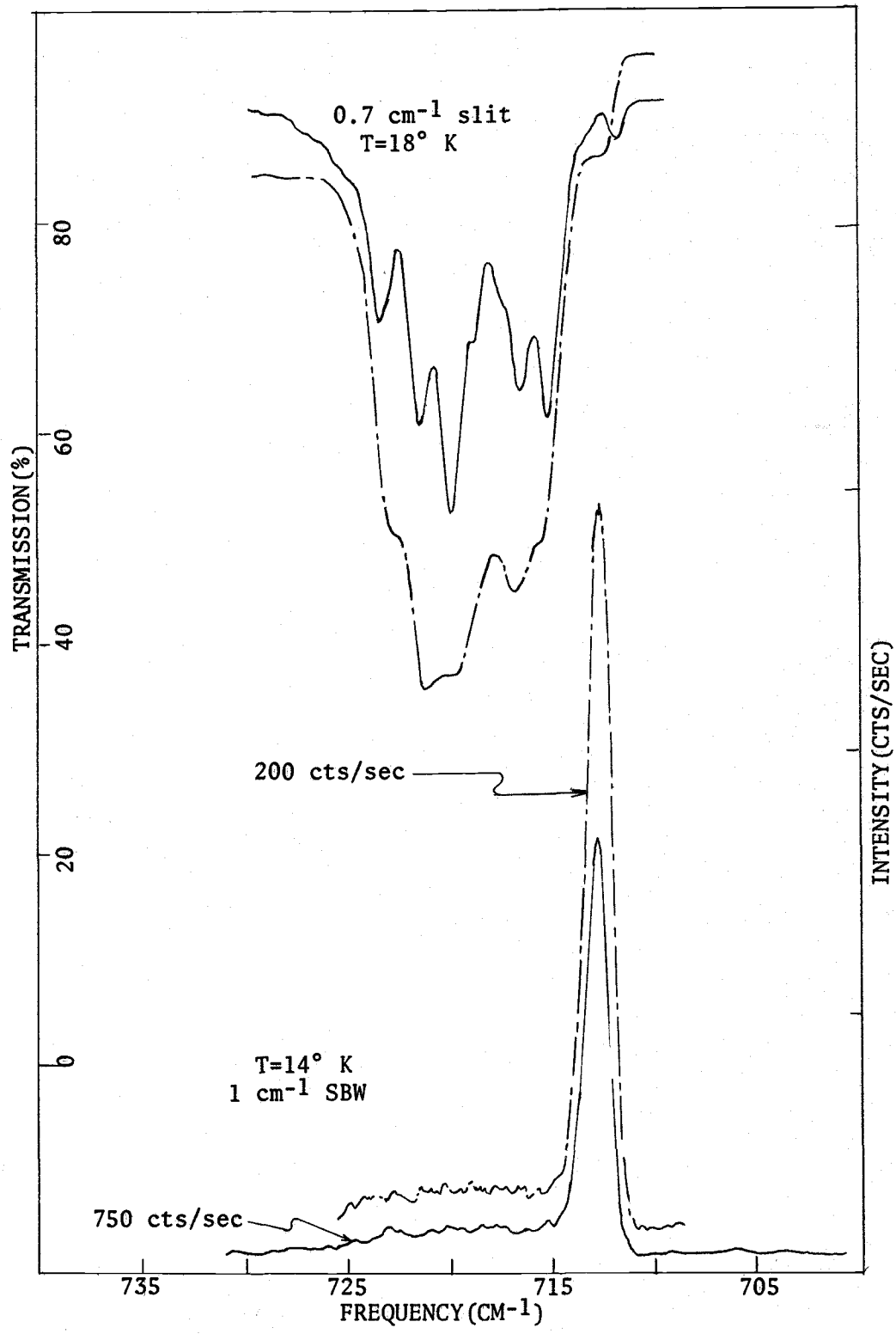

Figure 31. A comparison between the IR and the Raman spectra of the ν_2 mode of the δ phase of PD_3. The two Raman spectra were taken from the same film and the two IR traces from different film.

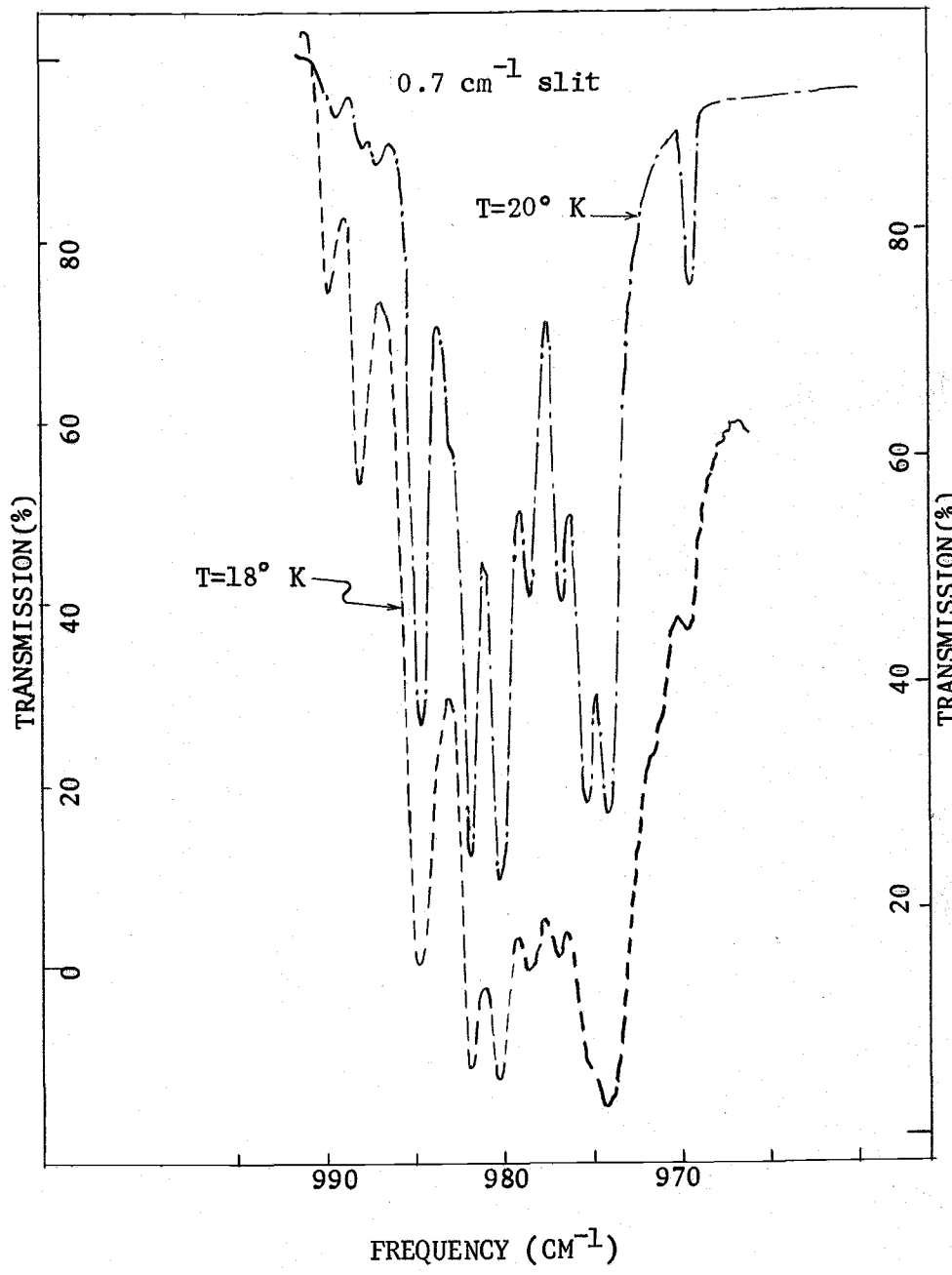

Figure 32. The ν_2 spectra of the delta phase of PH_3 shown here suggest that the film (broken trace which was obtained by specular reflection) deposited on the shiny aluminum substrate contains more gamma than the one deposited on the CsI window (dot-dashed trace) does.

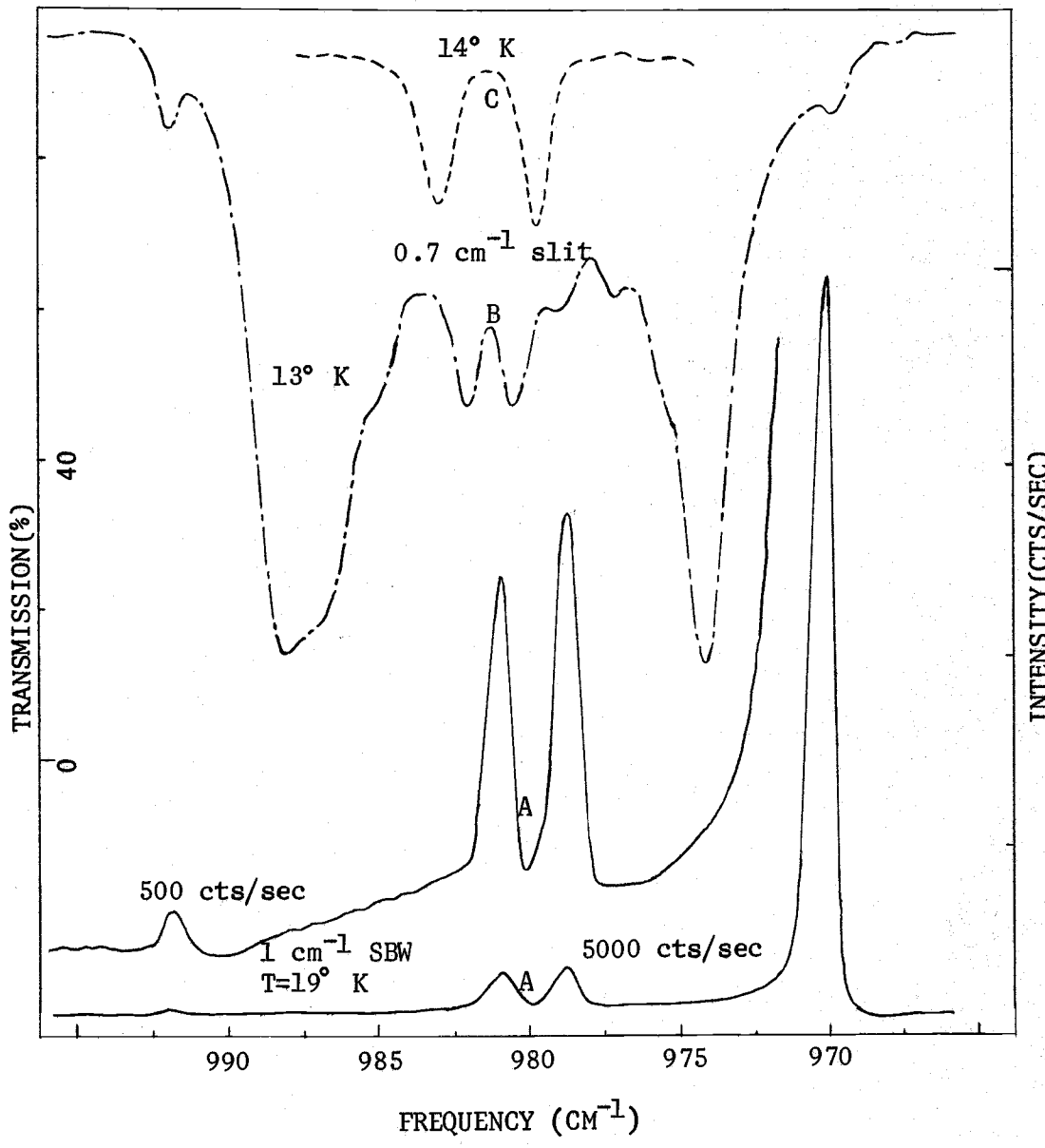

Figure 33. The infrared and the Raman spectra of the symmetric bending mode of solid PH_3 in the gamma phase(A) and mostly gamma phase(B). For trace C, the PH_3 molecules were isolated in the gamma phase of PD_3 purposely doped with 0.5% PH_3.

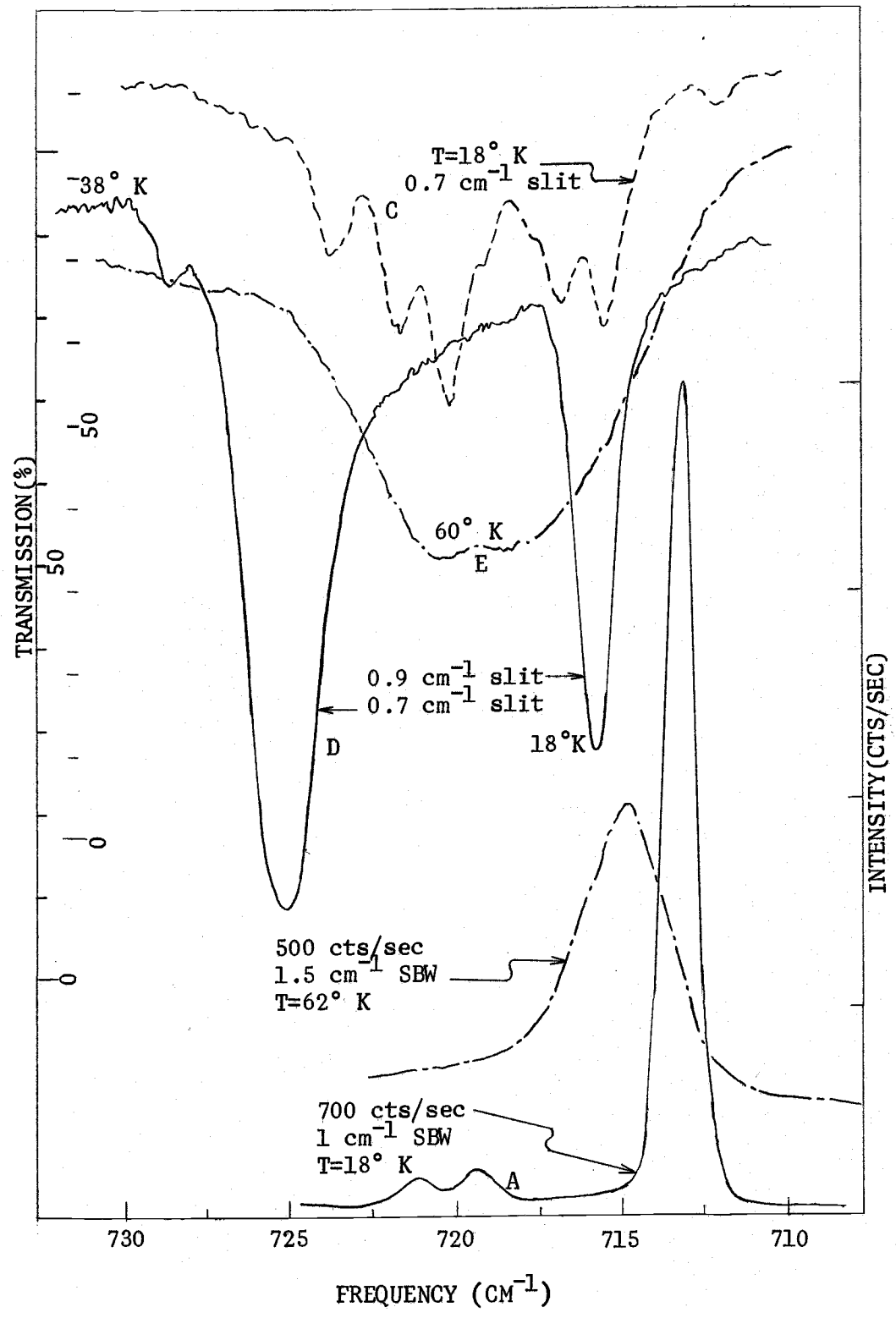

Figure 34. The infrared and the Raman spectra of the symmetric bending mode of the PD_3 solid in the γ (A and D), the β (B and E), and the δ (C) phases.

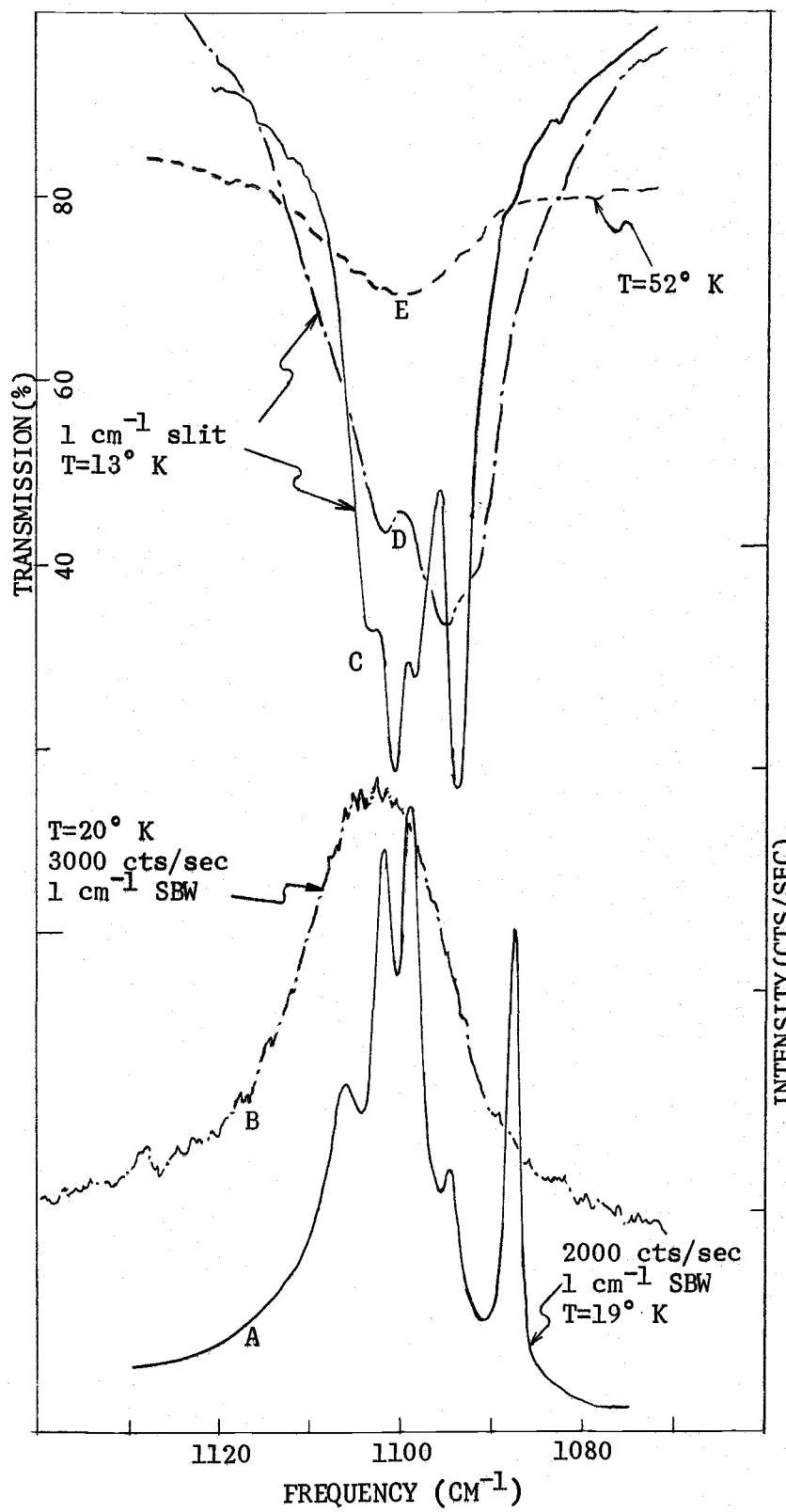

Figure 35. The IR and the Raman spectra of the ν_4 of solid PH_3 in the γ(A and C), the δ(D), the β(E), and the supercooled β(B) phases.

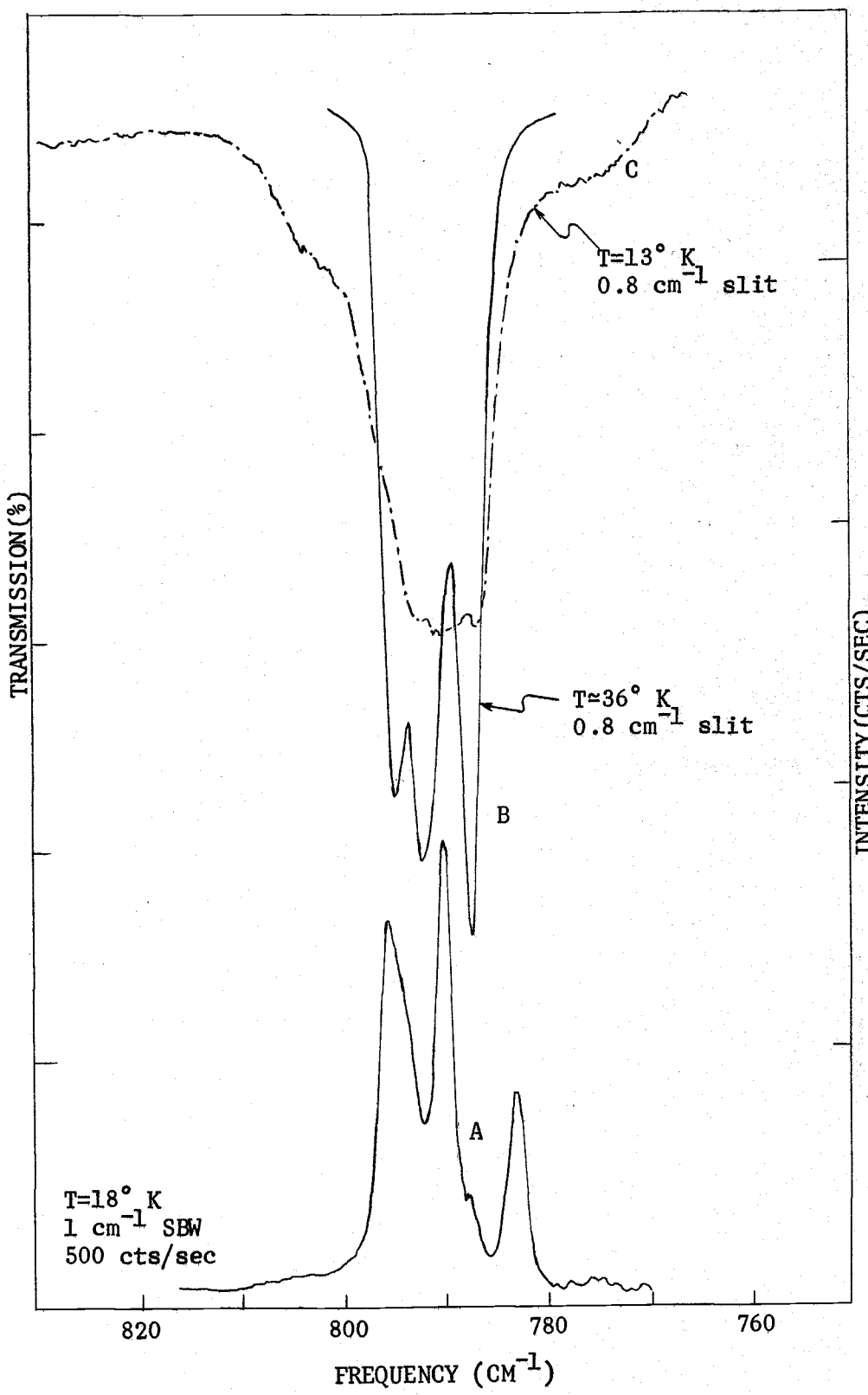

Figure 36. The IR and the Raman spectra of the ν_4 of solid PD_3 in the γ(A and B) and the δ(C) phases.

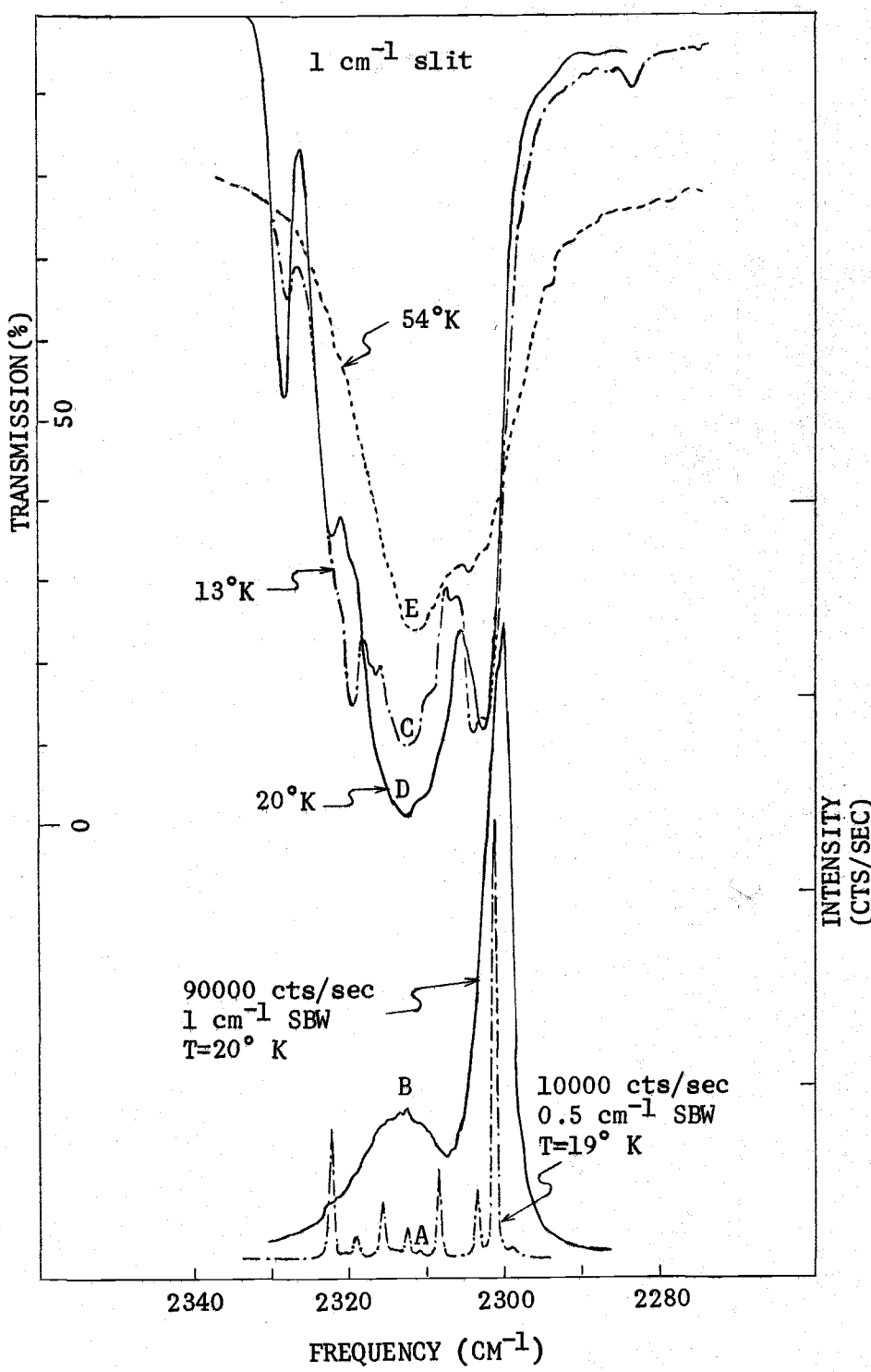

Figure 37. The infrared and the Raman spectra of the two stretching modes of solid PH_3 in different phases. For traces A and C the films were mostly in the gamma phase, trace B mostly in the frozen beta phase, trace D mostly in the delta phase. Trace E was taken in a different run in which the film was completely in the beta phase.

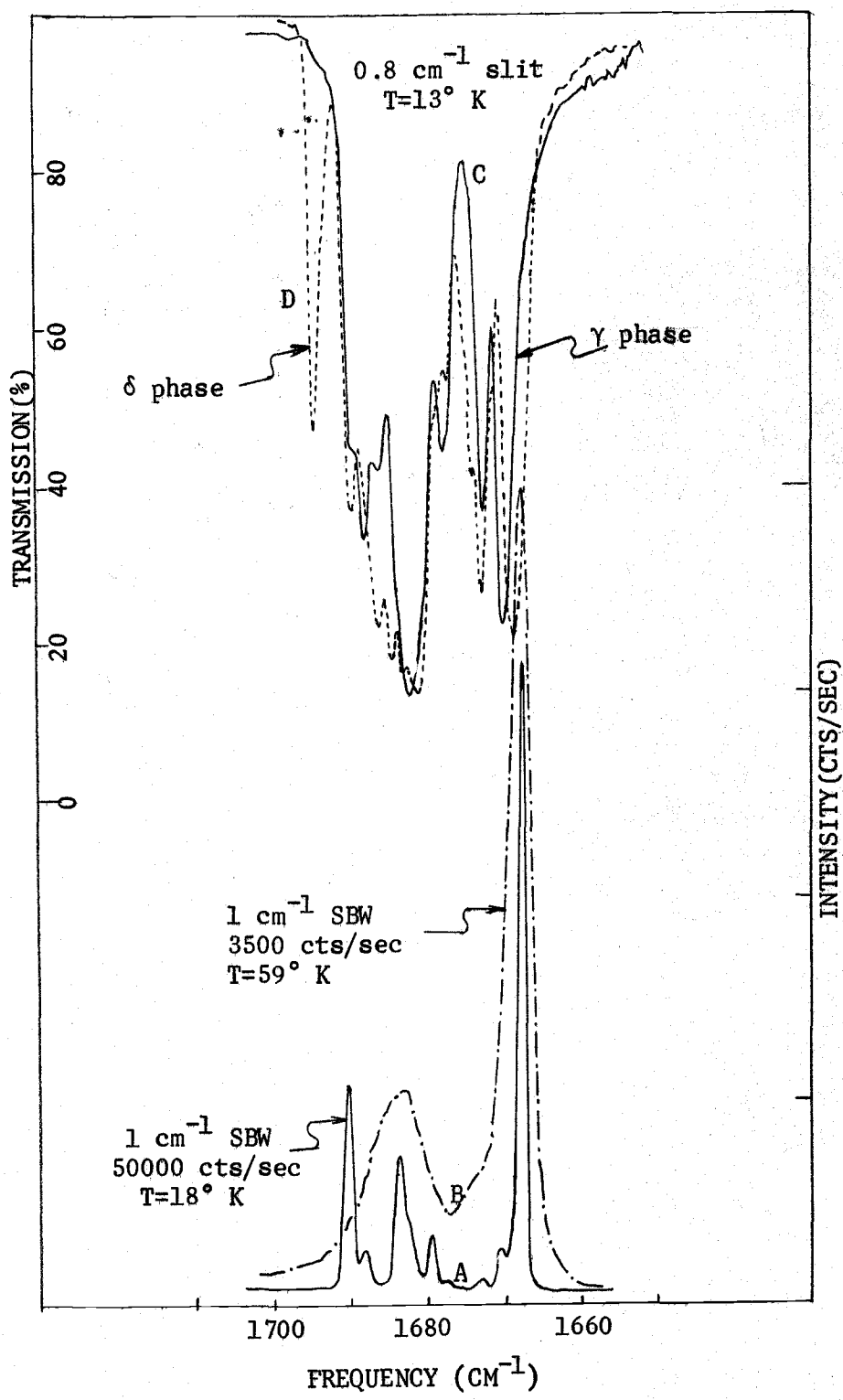

Figure 38. The infrared and the Raman spectra of the two stretching modes of solid PD_3 in different phases, traces A and C the gamma phase, trace B the beta phase, trace D the delta phase.

peak from the left of trace A). The gamma phase ν_2 is shown in Figures 10, 11, and 33. Since the 988.0 cm^{-1} band of the gamma phase ν_2 is at least as strong as the 974.1 cm^{-1} one, the second peak from the right of trace A in Fig. 29 cannot be solely attributed to the gamma phase. In other words, the delta phase ν_2 also absorbs energy at 974.1 cm^{-1}. Thus, it seems that trace B of Fig. 29 best represents the delta phase ν_2 (because the band at 988.0 cm^{-1} almost completely disappeared), while trace A and C of the same figure represents the delta phase plus a small amount of the gamma phase.

HH disagreed with SG concerning structure of phosphine below 10°K. From their infrared work, HH believed that phosphine exists in still another phase below 10°K. But SG's observation showed that both the delta phase and the gamma phase extended from 30.29°K and 49.43°K, respectively, down to 0°K. Our 4°K-experiment was carried out mainly to clarify this point. The 4°K scan in Fig. 29 supports SG's observations. Another purpose of running the 4°K experiment was to see if the relative intensity of the features in the symmetric bending region changes as the temperature is lowered, assuming that the crystal structure remains the same. This relative intensity change, if any, could cast some light on the interpretation of this structure-rich-ν_2. Although trace A and C of Fig. 29 were not taken from the same film they both contain a small amount of the gamma phase. It would be more sensible to compare A with C for this purpose. The relative intensity change was slight but detectable.

As temperature dropped from 20°K to 4°K, the 982.1 cm^{-1} and 977 cm^{-1} bands became more intense with respect to the 980.3 cm^{-1} and 978.8 cm^{-1} ones, respectively.

The structure of the symmetric bending mode presented here resembles the ones given by HH and Francia (whose excellent resolution resolved the peak at 974.2 cm^{-1} into two). Our frequencies in this region agree with theirs within 1 cm^{-1}. This slight discrepancy can be accounted for by the instrument calibration. HH did not report the very weak feature at 983.3 cm^{-1}. From the absence of the weak feature at 988.0 cm^{-1} and the relative intensity of the doublet at 974.2 cm^{-1} and 975.6 cm^{-1}, it is concluded that both HH and Francia's films contained no significant amount of the gamma phase.

A comparison between the infrared and the Raman spectra of the symmetric bending mode of the delta phase is given in Fig. 30. In this figure, trace C is the blown-up version of trace E, Fig. 16. Unequivocally, the weak Raman features are not noise. There seems to be agreement between the infrared and the very weak Raman bands.

In Fig. 32, the broken trace was obtained using the specular reflection optics described in page 23. This experiment was performed with the goal of doing the IR absorption and the Raman scattering simultaneously, i.e. as soon as a given phase of the solid PH_3 slab was established in the IR, an investigation of the same phase was to be carried out in the Raman immediately. Unfortunately, the cell leaked and all of the sample evaporated during the cell-transferring process. (Without this one-to-one correspondence of

phases between the IR and the Raman, the phases in the Raman experiment could still be established (please see chapter V).) In connection, we mention the technique of obtaining a thin film for the IR, but a thick slab for the Raman on the same substrate. The trick is to deposit the sample on the surface opposite to the one on which the IR beam will fall (please refer to Fig. 2). During the process of deposition, it was observed that some sample did go around the parallelepiped substrate and deposited on the IR-surface. Comparing the two traces in Fig. 32, one conclusion may be drawn. The choice of substrate (shiny aluminum or CsI) does affect the crystal structure to some extent. This specular reflection spectrum was obtained from a film deposited at high temperature in quick spurts. The only difference between this film and other ones deposited on the CsI window with the same technique would be the gamma phase content, which is higher for the former.

Shown in Fig. 33 is a comparison between the Raman and the IR spectra of ν_2 in the gamma phase. Among the bands of trace B, only the two strong ones and the weak one at 991.7 cm^{-1} belong to the gamma phase. The weak doublet at the middle of the spectrum can not be due to the gamma phase, because it broadens out in 28.5°—28.7°K (the nominal delta-beta transition point), and, also, because the ν_2 of the gamma phase of PD_3 in Fig. 34 does not have this doublet.

Trace C of Fig. 33 represents the ν_2 of PH_3 isolated in the gamma phase of PD_3. (A complete conversion of the PD_3 host into

the gamma phase was indicated by the appearance of the two strong bands in the ν_2 region.) The oscillating dipole of the ν_2 of the guest PH_3 molecules was believed to be decoupled from those of the host, since they are too far apart in energy (260 cm^{-1} from the ν_2 and 700 cm^{-1} from the ν_1 of the host). In other words, these PH_3 molecules see only the electrostatic environment but do not interact dynamically with their isotopical neighbors in the primitive cell of the host solid. Therefore, the factor group splitting cannot occur for any of the vibrations of these guest molecules, and the existence of the doublet for this ν_2 vibration would have to be attributed to the site effect.

The concentration of the guest molecules has been reduced in order to make sure that each guest molecule is well isolated by the host ones. Nevertheless, the doublet persisted. Therefore, the splitting must not be due to the residual interaction among the guest molecules.

The splitting of a non-degenerate vibrational band of PH_3 isolated in its isotopical host solid PD_3 may be attributed to nonequivalent sites. If, in a perfect molecular crystal, the molecules reside at two distinct kinds of sites of either the same symmetry or different symmetries in a unit cell, then the nondegenerate vibration of an ideally isolated isotopic molecule in the same lattice can exhibit two bands.

It appears, from trace B of Fig. 33, that the isolated molecule "found" that the other nonequivalent site in the same unit

cell was occupied by another molecule of its kind, and they have something in common (their first excited states of the ν_2 mode are close). Therefore an interaction occurs between these two states. Since a unit cell can be treated as if it were a molecule in dealing with a pure solid system, this interaction resembles the famous Fermi resonance, existing within a molecular system in which the anharmonic (or the interaction) term in the potential energy expansion causes two excited vibrational states of the same symmetry to perturb each other.

Upon examination of the B and C traces of Fig. 33, it was found that the center of gravity was at 980.9 cm^{-1} before triggering the interaction and at 981 cm^{-1} after (assuming equal intensity for the two strong gamma peaks). This suggests that the intersite Fermi resonance might have occurred in the gamma phase. Provided that this was true, we solved the following secular equation:

$$\begin{vmatrix} \omega_1^2-\omega^2 & f \\ f & \omega_2^2-\omega^2 \end{vmatrix} = 0$$

where ω_1 and ω_2 are, respectively, the unperturbed angular frequencies, $2\pi c(979.6\ cm^{-1})$ and $2\pi c(982.8\ cm^{-1})$; f the interaction constant; ω the perturbed angular frequencies, $2\pi c(974.i\ cm^{-1})$ and $2\pi c(988\ cm^{-1})$. When the latter is put back into the secular equation separately, two different interaction constants are obtained: $4.79 \times 10^{-14}\ sec^{-2}$ and $4.68 \times 10^{-14}\ sec^{-2}$. There is a 2% difference in these interaction constants. This difference can be accounted

for by the interaction among the translationally equivalent molecules throughout the whole crystal. Designating this intermolecular interaction constant as f_{11} and including it in the secular equation, we have

$$\begin{vmatrix} \omega_1^2 + f_{11} - \omega^2 & f_{12} \\ f_{12} & \omega_2^2 + f_{22} - \omega^2 \end{vmatrix} = 0$$

Assuming the f_{11}'s are negligible, we have solved the simpler secular equation and obtained two eigenvectors :

$$\left[0.78,\ -0.62\right] \quad \text{and} \quad \left[0.62,\ 0.78\right] .$$

These two vectors form the row space of the following C matrix

$$Q = Cq \text{ or } \begin{matrix} Q_1 = 0.78q_1 - 0.62q_2 \\ Q_2 = 0.62q_1 + 0.78q_2 \end{matrix}$$

where q_1 and q_2 are the unperturbed coordinates, and Q_1 and Q_2 the mixed ones. $C^{-1} = C^{\dagger}$, since the coordinate transformation is orthogonal. Therefore,

$$q = C^{-1}Q \text{ or } \begin{matrix} q_1 = 0.78Q_1 + 0.62Q_2 \\ q_2 = -0.62Q_1 + 0.78Q_2 \end{matrix}$$

From this equation, the intensity ratio of the two perturbed bands can be calculated. The intensity of an absorption band of a solid system is given by the equation in page 86. Thus,

$$\frac{I(Q_2)}{I(Q_1)} = \frac{\left(\frac{\partial \mu}{\partial Q_2}\right)^2}{\left(\frac{\partial \mu}{\partial Q_1}\right)^2} = \frac{\left(\frac{\partial \mu}{\partial q_1}\frac{\partial q_1}{\partial Q_2} + \frac{\partial \mu}{\partial q_2}\frac{\partial q_2}{\partial Q_2}\right)^2}{\left(\frac{\partial \mu}{\partial q_1}\frac{\partial q_1}{\partial Q_1} + \frac{\partial \mu}{\partial q_2}\frac{\partial q_2}{\partial Q_1}\right)^2}$$

$$= \frac{\left(\frac{\partial \mathcal{G}_1}{\partial Q_2} + \alpha \frac{\partial \mathcal{G}_2}{\partial Q_2}\right)^2}{\left(\frac{\partial \mathcal{G}_1}{\partial Q_1} + \alpha \frac{\partial \mathcal{G}_2}{\partial Q_1}\right)^2}, \quad \text{where } \alpha = \frac{\frac{\partial \mu}{\partial \mathcal{G}_2}}{\frac{\partial \mu}{\partial \mathcal{G}_1}} \approx \left[\frac{I(\mathcal{G}_2)}{I(\mathcal{G}_1)}\right]^{\frac{1}{2}}$$

$$= \frac{(0.62 + 0.78\alpha)^2}{(0.78 - 0.62\alpha)^2}$$

$$\approx 73 \quad \because \alpha \text{ was observed to be } (1.03)^{\frac{1}{2}}$$

The observed intensity ratio is about 3. This very large disagreement of the predicted and observed intensity ratio for the coupled modes in the unit cell assumes that the transition dipole moments at the two sites are parallel, and is of course sensitive to the frequency spacings. Nevertheless, it forces one to search for a more probable explanation of the doublet due to PH_3 isolated in γ-PD_3, particularly because there are plausible models for the γ-phase structure which require only one site, which explain the overall spectrum reasonably well, and in particular, account well for the spectra of PH_2D and PHD_2 isolated in PD_3.

The spectra of the degenerate bending and stretching vibrations are presented in Figs. 35 and 37. Traces C in these two figures were taken right after trace C in Fig. 11, and trace D in Fig. 35 immediately after trace A in Fig. 11. Traces A and B in Fig. 35 were taken successively from different domains of the same film, and trace E from a different film than traces C and D. The 1094.5 cm^{-1} and the 1102 cm^{-1} bands of the Raman specta are very likely real, although the plasma lines at 1101 cm^{-1} and 1094 cm^{-1} have peak heights of 6 and 3 respectively (please refer to page 31

for the plasma lines and their peak heights). First of all, the observed ratio of the intensity of the 1102 cm^{-1} peak to the intensity of the 1094 cm^{-1} peak is much greater than 2. Therefore, the 1102 cm^{-1} band cannot be completely due to the contribution from the plasma line, if at all. Secondly, when the solid was transformed to the beta phase and the spectrophotometer was set at a slightly higher sensitivity, these two peaks did not show on the top of the broad structure of ν_4. On the other hand, the 77 cm^{-1} (peak height 21) and the 117 cm^{-1} (peak height 26) plasma lines accompanied the lattice spectrum persistently while the 161 cm^{-1} (peak height 3) plasma line did not appear at all.

All of the Raman high resolution scans of the gamma phase of PH_3 were obtained from the film represented by the survey scan in Fig. 25. Since the latter shows the existence of the intermediate species, it is desirable to see if the latter complicates the high resolution spectra of PH_3 or not. The fundamental regions, which may be complicated, are the stretching ones. In another high resolution scan (not shown and taken from the same film as trace A of Fig. 37) over the stretching regions with 1 cm^{-1} spectral band width and as low a sensitivity as 150,000 counts per second, exactly the same spectrum as trace A of Fig. 37 was obtained. Comparing this scan with the survey scan in Fig. 25, it is clear that the weak 1670 cm^{-1} band of the intermediate species in the survey scan will not be detected as the sensitivity decreases more than seven times. Therefore, it is concluded that all the bands of trace A in Fig. 37 are due to PH_3.

In this paragraph, we elucidate that the γ-Raman spectra are essentially free from the delta phase interference, but the γ-IR ones are not. (All of the IR high resolution scans of the γ phase were consecutively recorded from the same film, and all of the Raman ones from the same domain in the same film.) The amount of the residual δ phase in the particular domain focused on by the laser can be estimated from the very weak band at the low energy side of the strongest one in spectrum A of Fig. 37. It is almost negligible. The Raman ν_3 region of the γ phase is free from the δ phase interference, since ν_3 in Raman is much weaker than ν_1. From trace C of Fig. 11, it can be easily seen that the IR-γ-film still contained some amount of the δ phase. However, in the IR ν_4 and the stretching regions (especially in the former) it is hard to discriminate between the contribution from the residual δ phase and that from the predominant γ phase. The weak shoulder at about 2302.8 cm^{-1} may be due to the δ phase. The 2329 cm^{-1} band of the IR ν_3 is likely due to the δ phase too, since its intensity depends on the δ phase concentration. The slight change in energy can be caused by the temperature difference and/or by the adding of a small Gaussian curve to a strong one.

It is difficult to draw a demarcation between ν_1 and ν_3 in the Raman stretching region of the γ phase (trace A , Fig. 37). The Raman spectrum of ν_2 shows at least one strong and two weak peaks. One expects the same thing to happen in the ν_1 region. This is why we assign the 2308.6 cm^{-1} peak to ν_1 instead of ν_3. This assignment

allocates five Raman bands to ν_3, in parallel with the assignment in the ν_4 region done in the last paragraph in page 111. In the IR stretching region of the γ phase (trace C, Fig. 37), we tentatively assign the strong band at 2304.2 cm^{-1} and the very weak one at 2307 cm^{-1} to ν_1, and the rest (except the δ phase contribution at 2329 cm^{-1}) to ν_3 (please see Table I).

Trace D, Fig. 37 and trace H, Fig, 15 show, respectively, the IR and the Raman spectra in the stretching regions of the δ phase. In the IR trace, the band lowest in energy is assigned to ν_1 and the other bands to ν_3. In the Raman spectra, the three sharp bands most likely belong to ν_1 and the weak and broad ones to ν_3. It is possible that some of the ν_1 modes are embedded in the broad ν_3 one, and vice versa. It is noted that this IR-δ film is too thick to resolve the fine structure in the stretching regions. With a higher resolution and thinner film, Francia resolved more components in this region than we did.

In the delta phase, there exists a similarity among the fundamental molecular regions. That is the nondegenerate bands are sharp but degenerate ones are quite diffusive. Another similarity is the Raman-IR coincidence. Although it is difficult to find so many coincidences in the ν_1 region as in the ν_2 region, it is true that in both ν_1 and ν_2 regions the strong IR band agrees with the weak Raman feature. There seems to be some agreements in the ν_3 and ν_4 regions also.

The spectra of all the fundamentals of the beta phase agree in the broadness of the bands. The broadness indicates that the beta phase is disordered. For a disordered solid, one naturally expects the Raman frequencies to agree with their counterparts in the infrared. (In Figs. 35 and 37, the Raman spectra of the ν_4, ν_1, and ν_3 of the beta phase were not shown, because they are not appreciably different from those of the supercooled beta phase.) Comparing the B traces with the E traces of Figs. 35 and 37, one sees that this is not true for ν_1 and ν_4, but is approximately true for ν_3. The disagreement is even worse for ν_2 (please refer to Figs. 11 and 13). The table in page 28 shows that Savoie and Anderson's Toronto-arc-Raman frequencies in the intramolecular region of crystalline HCl at 10°K are slightly lower than our laser-Raman values obtained at 16°K. Thus, a slight up-stream shift of the Raman ν_4 frequency from the IR one in the beta phase (and, perhaps, in other phases too) might well be due to our Raman sampling optics (please refer to Fig. 3). However, for the ν_1 and ν_2 vibrations of the beta phase, the Raman frequencies are lower than the corresponding IR ones. Later we will point out that the Raman frequencies of the ν_1, ν_2, and ν_4 of the beta phase of PD_3 are also lower than the corresponding IR ones. So, it appears rather difficult to exclude any relationship between these lower Raman frequencies relative to the corresponding IR ones and the low temperature Raman sampling optics that we used.

From the comparison between the infrared and the Raman spec-

tra of the four internal fundamentals of the gamma phase in Figs. 33, 35, and 37, it seems possible that the gamma phase is not centrosymmetric. For a crystal with inversion symmetry, the mutual exclusion principle must be obeyed. And there cannot be any coincidence between the Raman and the infrared peaks. Our gamma spectra seem to indicate some Raman-IR coincidences in every fundamental region. Apparently, there is one coincidence in the ν_2 region (Fig. 33), i.e. the weakest band at the highest energy (992 cm^{-1}). The apparent coincidence in the ν_1 region is between the strong (rather than weak) IR peak and the weak Raman feature at 2304.2 cm^{-1}. Modes of the same symmetry in the molecular point group have to generate the same number of vibrations with the same symmetry in the unit cell. (This will be illustrated with correlations in a later chapter.) So far as the number of Raman-IR coincidence is concerned, the A_1-type molecular fundamental regions are compatible with this rule. For the E-type molecular fundamental regions, this rule appears to hold too. The coincidences at 2312.7 cm^{-1}, 2316 cm^{-1}, and 2319.2 cm^{-1} (all are Raman frequencies) appear to be true. In the ν_4 region there seems to be only two, instead of three, coincidences. They are at Raman frequencies 1094.5 cm^{-1} and 1099 cm^{-1}.

It is possible that part or the entirety of the above-mentioned Raman-IR coincidences are caused by our particular Raman sampling technique. Therefore, we do not intend to rule out the proba-

bility that the gamma-PH_3 is centrosymmetric. Another possibility is that either the A_1-type molecular fundamental modes or the E-type ones have Raman-IR coincidences. Because it is possible that the symmetries of the site and the unit cell are such that the E species of C_{3v} is correlated via site symmetry to the unit cell species active in both infrared and Raman, but the A_1 species to either Raman or infrared active species, or vice versa.

We have noted that the beta phase is disordered before. From the sharpness of the fundamental bands, the gamma phase is easily recognized to be ordered. Whether the delta phase is ordered or not is difficult to tell solely from the appearance of the spectra of the fundamentals. The high resolution scans of ν_2, both in the infrared and in the Raman experiments, show unequivocally that the delta phase is ordered. The Raman stretching spectra seems to favor this concept, which is further supported by SG's work. They extrapolated the entropies of the delta and the gamma phases to zero as the temperature approached zero degrees Kelvin. This means that, for both the delta and the gamma phases, the thermodynamical probability, P, in the following equation (30) is one.

$$S_m^\circ = R \ln P = Nk \ln P = k \ln P^N$$

where S_m° is the entropy smoothly extrapolated to T = 0 and is not necessarily the entropy at T = 0. Therefore, the phosphine molecules in the delta and gamma phases assume only one orientation as the temperature approaches zero degree Kelvin. These two phases

are thus perfect crystals. We do believe the delta phase is ordered, although the infrared high resolution scans of the ν_4 and the stretching vibrations seem to indicate the opposite. The Raman scan of the ν_4 of the delta phase, which appeared to be almost the same as that of the supercooled beta structure and was, thus, not reproduced here, also suggested disorder.

PD_3

The ν_2 spectrum of the delta phase of PD_3 is shown in Fig. 31. We were able to produce the solid infrared trace only in one experiment using the hydrogen expansion Cryo-Tip. After the more convenient Displex Cryogenic Refrigerator was available, this multiplet structure was never repeated with the same deposition technique even at lower temperatures. The dot-dashed infrared trace is one of the unresolved delta ν_2. The two Raman traces were recognized as the delta phase ν_2 towards the end of chapter V. Besides the slightly larger band half-width of the main Raman feature and the unresolved trace, the ν_2 spectra of the delta-phase-PD_3 closely resemble those of PH_3 shown in Fig. 30. This similarity confirms our previous conception of ν_2 of the delta phase.

Fig. 34 shows mainly the beta and gamma phases of PD_3 in the ν_2 region. The Raman traces in this figure were taken from the same film. After trace C of the same figure had been recorded, the film was reinforced and subjected to a few thermocyclings. Then trace D, which represents the same film as the solid lower spectrum

of Fig. 26, was recorded. During the D trace scan, the Cryo-Tip was deplugged temporarily, and the temperature dropped down to 18° K at the second-strong peak. In the strongest band region, the temperature increased from 30° K to 35° K. Trace E was taken in another run.

In several other infrared high resolution scans of the γ phase at 13° K, two weak shoulders, one at the low energy side of the strongest band and the other at the blue side of the second-strong band, appeared persistently. But the weakest band at 728.7 cm^{-1} did not appear at all. These two strong bands were observed at 716 cm^{-1} and 724.5 cm^{-1}, which agreed with the values listed in Table I within experimental uncertainty. These scans resembled trace B of Fig. 33 except the two weak bands on the sides and the four bands at the middle, and seemed to indicate that the solid was not so well crystallized as that represented by trace D in Fig. 34.

An overall agreement between the ν_2 spectra of γ-PH_3 and that of γ-PD_3 is manifest, although small and apparent differences exist. The marked differences are the band half-width of the strong Raman bands and the absence of a doublet from the infrared spectrum of γ-PD_3. The latter point further confirms that the infrared film of γ-PH_3 still contained some delta structure. The intensity ratio of the strongest infrared band of the gamma phase of PD_3 to the second-strong band was calculated to be about 3. This ratio should remain the same for PH_3. As shown in Fig. 33, the ratio for PH_3 containing some delta phase is less than 3. It is observed from

Fig. 10 that the intensity of the strongest band increases at a greater pace than that of the second-strong band. Therefore, it is likely that the ratio of 3 will be kept as all of the PH_3 sample is converted into the gamma phase. In spite of the slight discrepancies, the following agreement makes us more confident in our assessment of γ-ν_2. Its Raman spectrum consists of at least one strong and two very weak bands. (The Raman scan of γ-PD_3 was not extended to the region corresponding to the weakest band of γ-PH_3 at 922 cm^{-1}. Therefore, the existence of the latter band in ν_2 of γ-PD_3 is still uncertain.

In the Raman spectra of PH_3 and PD_3, the strongest ν_2 bands of the gamma phase agree with those of the delta phase within experimental error. In the ν_2 region, these two phases differ only in the structure at the high frequency side of the strongest bands. In the infrared spectra of PH_3 and PD_3, the second-strong band of the gamma phase coincides with one of the many sharp features of the delta phase, while the strongest and the weakest ones find no counterparts in the delta phase.

When solid PD_3 was transformed from beta to delta, the center of gravity of ν_2 (at 719 cm^{-1}) was preserved. This is also true in solid PH_3 (see Fig. 11). However, the center of gravity of ν_2 was shifted up higher to 722 cm^{-1}, as solid PD_3 underwent the beta-to-gamma transition. Again, this is in parallel with the PH_3-observation (see Fig. 10). However, in the Raman experiment, the band centers of the beta phase of both PH_3 and PD_3 were shifted towards

blue with respect to the strongest bands of the delta and the gamma phases (see Figs. 13, 16, 18, and 34). Perhaps, this abnormal band-center-shift in the scattering experiment is related to our particular sampling optics.

Fig. 36 shows the ν_4 spectrum in the Raman and the infrared. No Raman high resolution scan over the ν_4 region of the supercooled beta, the beta, or the delta phase has been recorded. The Raman frequency of ν_4 of the beta phase reported in Table 3 was taken from a survey scan and, so, may be in error slightly because of the scan speed and the scale contraction. Although the dot-dashed trace in Fig. 36 was taken with the Displex refrigerator which is more capable of freezing-in the solid sample, the dot-dashed infrared trace, Fig. 31 recorded along with this ν_4 trace indicates that the latter trace does represent the delta phase. Note that the Raman scan over the ν_4 region of PH_3 showed before that no appreciable difference exists among the beta, the supercooled beta, and the delta phases. A ν_4 scan taken immediately after trace C in Fig. 34 showed no appreciable difference either.

Thus we will concentrate only on the gamma phase. Trace B of Fig. 36 was recorded immediately before trace D of Fig. 34 when the Cryo-Tip was plugged. At the peak lowest in energy, the temperature was 34° K, at the middle peak, 29° K, and at the weakest peak, 43° K. Several gamma-ν_4-scans taken from the same film as trace C confirmed that trace B represents the best crystallized film. The gamma spectra of ν_2 (traces A and D of Fig. 34) imply that the films

from which traces A and B of Fig. 36 were taken did not contain any delta phase which is rather unstable with respect to the gamma phase. The Raman intensity pattern in the ν_4 region of solid PH_3, which contained the gamma phase, almost completely, does not appear to be exactly the same as that of PD_3, but the number of peaks is actually the same. The asymmetric band, 795.6 cm^{-1}, of PD_3 can be resolved into at least two Gaussian curves. Thus, including the weak shoulder at 788 cm^{-1}, there will be five bands in the Raman ν_4 region. The infrared spectrum of PD_3 can similarly be supposed to consist of four components (like PH_3), if one believes that the slightly asymmetric middle feature conceals an unresolved shoulder. Within experimental error, there possibly are two coincidences between the Raman and the infrared bands in the ν_4 region of gamma-PH_3. Referring to the coincidence pattern in PH_3, it is very likely that the strongest infrared band in ν_4 of gamma-PD_3 coincides with the weak Raman shoulder at about 788 cm^{-1}. Invoking the asymmetry of the second-strong infrared band, the second coincidence might well be between this asymmetry and the middle Raman band. This is again very likely , because ν_4 of gamma-PH_3 exhibits a similar coincidence (see Fig. 35). We have mentioned that there seems to be three coincidences in ν_3 of gamma-PH_3. There may also be three coincidences in ν_4 of gamma-PD_3, if the asymmetry of the Raman band highest in energy is actually a hidden shoulder.

In the stretching region, one expects that $\nu_1(A_1)$ will have the same number of components as $\nu_2(A_1)$ and that $\nu_3(E)$ will have the

same number of components as $\nu_4(E)$. Of course, one may not resolve as many components in one region as the other and since ν_1 is close to ν_3, it may be more difficult to recognize the components associated with ν_1 and ν_3 respectively. From our experience with ν_2, we might expect three or four Raman components of ν_1 and four or five of ν_3. According to the intensity pattern of the Raman spectrum in the ν_3 region of gamma-PH_3, it is most likely that the first five features from the left of trace A, Fig. 38 belong to ν_3, but the shoulder at the low frequency side of the second-strong band in the group is probably not due to PD_3. In order to be compatible with the one-strong and two-very-weak pattern in the Raman ν_2 region, the first three bands from the right are assigned to ν_1.

Next, we want to elucidate that the scattering of the intermediate species does not significantly complicate the stretching region of gamma-PD_3, although their existence in the PD_3 is not negligible. Our calculation (to be presented later) shows that the ν_1 (A'), ν_3(A"), and ν_3(A') of PHD_2 absorb energy at 1668 cm^{-1}, 1675 cm^{-1}, and 2320 cm^{-1}, respectively. We have concluded previously that the survey scan of the gamma phase of PD_3 (upper solid trace of Fig. 28) was free from the PH_2D interference. The Raman stretching scan in Fig. 43 was recorded immediately after trace A of Fig. 38. The 2305 cm^{-1} band in Fig. 43 would have been 25 times weaker than it was (i.e. almost twice as intense as the weak band at 1670.6 cm^{-1} of trace A in Fig. 38), if it were scanned at a sensitivity of 50,000 counts per second. Assume that the 2305 cm^{-1} band

in Fig. 43 is the $\nu_3(A')$ of PHD_2. Then, since in the Raman effect, vibrations of A' type may have a larger scattering power than those of the A" type, it is reasonable to say either the weak band at 1673 cm^{-1} or the very weak one at 1677.8 cm^{-1} is due to $\nu_3(A")$ which can also be masked by the host band at 1679.6 cm^{-1}. The ν_1 (A') band is very likely embedded in the strongest band of ν_1 of the host solid. We know definitely that none of the bands in the Raman stretching region of PH_3 belongs to PH_2D (not to mention PHD_2). We are therefore inclined to believe that the $\nu_3(A")$ of PHD_2 is embedded in the host band in order that the PH_3-spectrum-pattern in the stretching region be preserved in the PD_3 spectra.

We believe that none of the components in traces C and D, Fig. 38 depends on the intermediate species to any significant extent either. The reason follows. The sample represented by the lower solid film of Fig. 26 contained much less of the isotopic impurities than that represented by the broken film of Fig. 27 did. The intensity pattern of the stretching spectrum obtained from the former sample was observed to be exactly (with two trivial exceptions, see below) the same as that obtained from the latter sample in the same phase (i.e. trace D, Fig. 38). If any component in spectrum D, Fig. 38 depended significantly on the isotopic impurities, the relative intensity should have changed. It is possible that the absorptions of the intermediate species are embedded in the host ones.

The above-mentioned stretching spectrum, obtained from the upper solid film in Fig. 26 (same batch of sample as the lower solid

trace in the same figure), was recorded immediately after trace C of Fig. 34. Therefore, trace D of Fig. 38 represents the delta phase, although trace C of Fig. 36 indicates disorder. The two exceptions accompanying this stretching spectrum were the absorptions of water which combined the third and the fourth bands from the left of the broken trace in Fig. 38, and which made the asymmetry at the high energy side of the second strong band from the right of the same trace stand out markedly. Thus, trace D of Fig. 38 appears free from water interference. So is trace C of the same figure, since they were taken from the same film and in the same run.

In the infrared stretching spectrum of gamma-PD_3 (trace C of Fig. 38), the first two bands from the right are assigned to ν_1, in parallel with the observation in ν_2, and the rest to ν_3. As to the assignment over the same region of delta-PD_3, the demarcation between ν_1 and ν_3 was tentatively drawn and shown in Table II.

The Raman-IR coincidence in ν_3 of gamma-PD_3 resembles that of gamma-PH_3 in the following sense. In both cases, it is the second Raman peak from the left, which coincides with the first strong IR peak from the left. Moreover, the strong and broad IR band is in close coincidence with either the third (PD_3) or the fourth (PH_3) Raman peak from the left. The third coincidence for the gamma phase of PD_3 seems to occur at the third IR peak from the right and the fourth Raman peak from the left. Thus, gamma-PD_3 might have three Raman-IR coincidences as the gamma-PH_3 does. In contrast to the ν_2 region of the same molecular symmetry, there may be two coinci-

dences between the two weak Raman and the two strong IR bands in ν_1 of gamma-PD_3. In gamma-PH_3, we observed coincidence between strong IR and weak Raman bands also, but the number of coincidences was only one.

VII. COMBINATIONS AND OVERTONES

When photons excite vibrational modes of a crystal system, the former are actually interacting with the optical phonons of the crystal. This interaction can be expressed by dispersion curves:

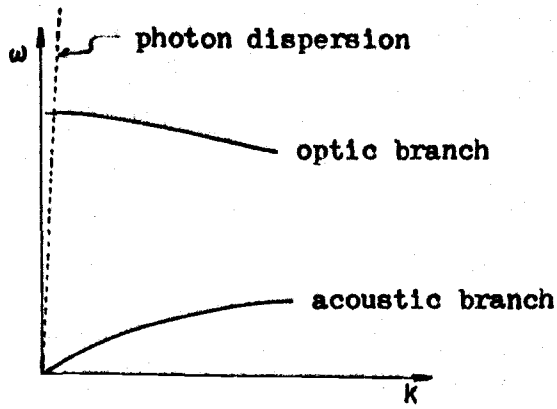

The optic branch intersects the photon dispersion at $k \simeq 0$; since, for photons, $\omega = ck$ (c = the speed of light), and the slope of ω-vs-k, is very large. Therefore, in the experiments where light interacts with the vibrational normal modes, we require $\sum_i K_i \simeq 0$ where i indexes the normal modes, i.e., we require that vibrations be in phase throughout the whole crystal.

Now, for the excitation of two optic phonons, one quantum each, by the incident photon, it might happen that these two phonons, ν_2 and ν_4 of the alpha phase of PH_3, for example, have the following highly schematic dispersion.

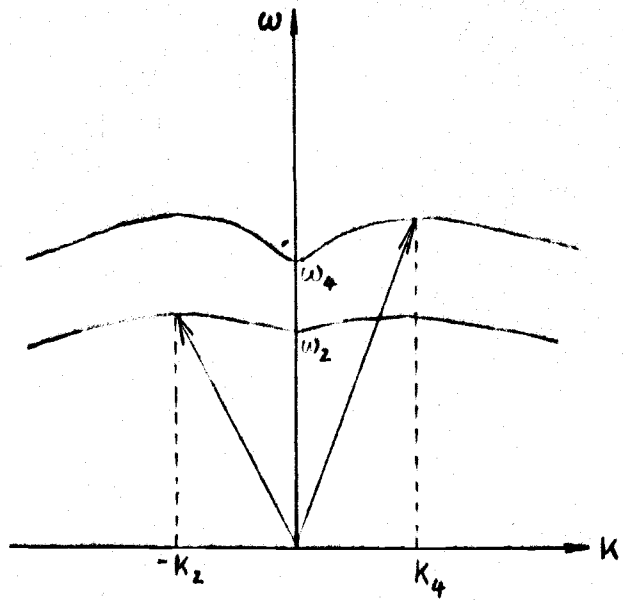

For the combination vibration of ν_2 and ν_4 to be in phase throughout the whole crystal, one would have to pick a positive value of k for ν_4 to be combined with the negative k of ν_2, or vice versa. Moreover, Kittel (31) showed that $\mathcal{D}(\omega) \propto \frac{1}{V_g^3}$, where $\mathcal{D}(\omega)$ is the density of states (or modes of vibration) and V_g is the group velocity, which is the velocity of energy transmission in the medium. V_g is also equal to $\frac{\partial \omega}{\partial K}$. Thus the arrows in the dispersion are drawn to the flat portion of the curves at which the two $\mathcal{D}(\omega)$'s have their singularities and, in turn, the combination transition will be the most intense. One, also notices that the arrows may sweep to cover the neighborhood of singularities where the $\mathcal{D}(\omega)$'s are still great, while keeping the total $\underset{\sim}{k}$ zero or almost zero. The upshot of the argument is that the observed combination in the crystal can be close to or even greater than the sum of the fundamentals involved, in spite of the fact that the inter- and intramolecular anharmonicities are usually negative (the major exception

being the alkali halides). The observed value of $\nu_2 + \nu_4$ of the alpha phase, as an example, is quite close to the sum of ν_2 and ν_4 The sum is even closer in the beta phase. Moreover, the bands will become broad, because the $\underline{k}$ vectors can vary continuously across the maxima. Of course if the fundamental modes are not widely dispersed, the breadth of the two phonon spectrum will be small.

In the overtone region a similar situation exists. In the following figure,

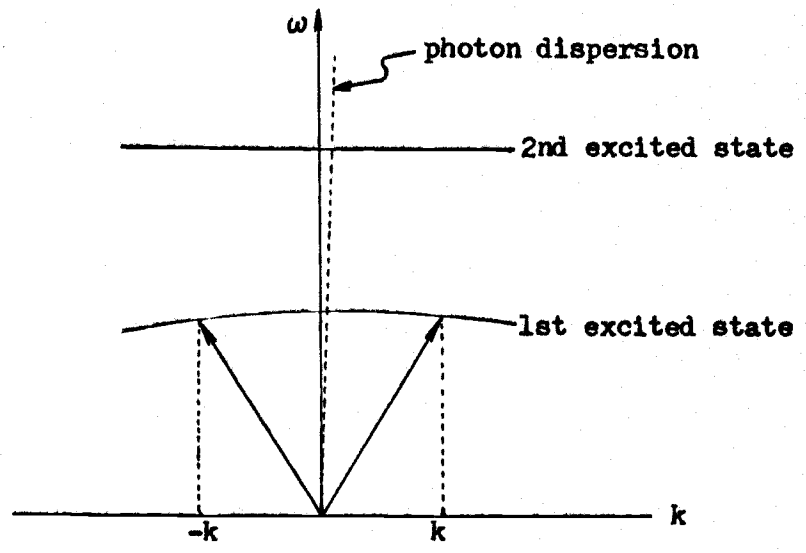

we have the anharmonic first overtone, whose energy is slightly lower than two times the fundamental value because of the inter- and intramolecular anharmonicities, and the process in which one photon creates two phonons and in which there are essentially no anharmonicities. However, the energy decreases (according to this dispersion curve) as the two $\underline{k}$ vectors sweep out simultaneously. Again broadening will be observed. The $2\nu_2$ (1430 cm^{-1}) and $2\nu_4$

(1579 cm^{-1}) observed in the gamma phase of PD_3 resemble the two-phonon process.

A combination-overtone band of a solid is further complicated by the fact that the symmetry species have to be determined from the factor group active species using the method described in reference 22. The alternative is to delocalize the site wave functions correctly. Both methods should give rise to the same vibrational species in the factor group. If there are more than two molecules per unit cell and the factor group has much higher symmetry than the site group; there will be very many vibrationally active species in a combination-overtone region in the factor group. When the resolution is not high enough, these numerous species will simply give rise to a broad band. When the resolution is high, it is particularly difficult to assign the components of an anharmonic band without an accurate knowledge of the crystal structure. Also, the two-phonon effects have been described as if $\underline{k}$ were one-dimensional, but in fact $\underline{k}$ can range in three dimensions over the entire Brillouin zone.

Previously, we have assigned the anharmonic modes simply as sums and multiples of the intramolecular modes. This is only roughly correct when we inspect the high resolution scans of the gamma phase of PD_3 in Figures 39 and 40. The bands, $2\nu_2$, $2\nu_4$, $\nu_2 + \nu_3$, $\nu_1 + \nu_3$ and $2\nu_3$ are broad, indicating the continuous variation of $\underline{k}$. The crude method of assignment is sufficient. For $\nu_2 + \nu_4$, $\nu_L + \nu_1$ and ν_3, $\nu_4 + \nu_1$, $\nu_4 + \nu_3$, and $2\nu_1$ one has to invoke the factor group activity for correct assignment.

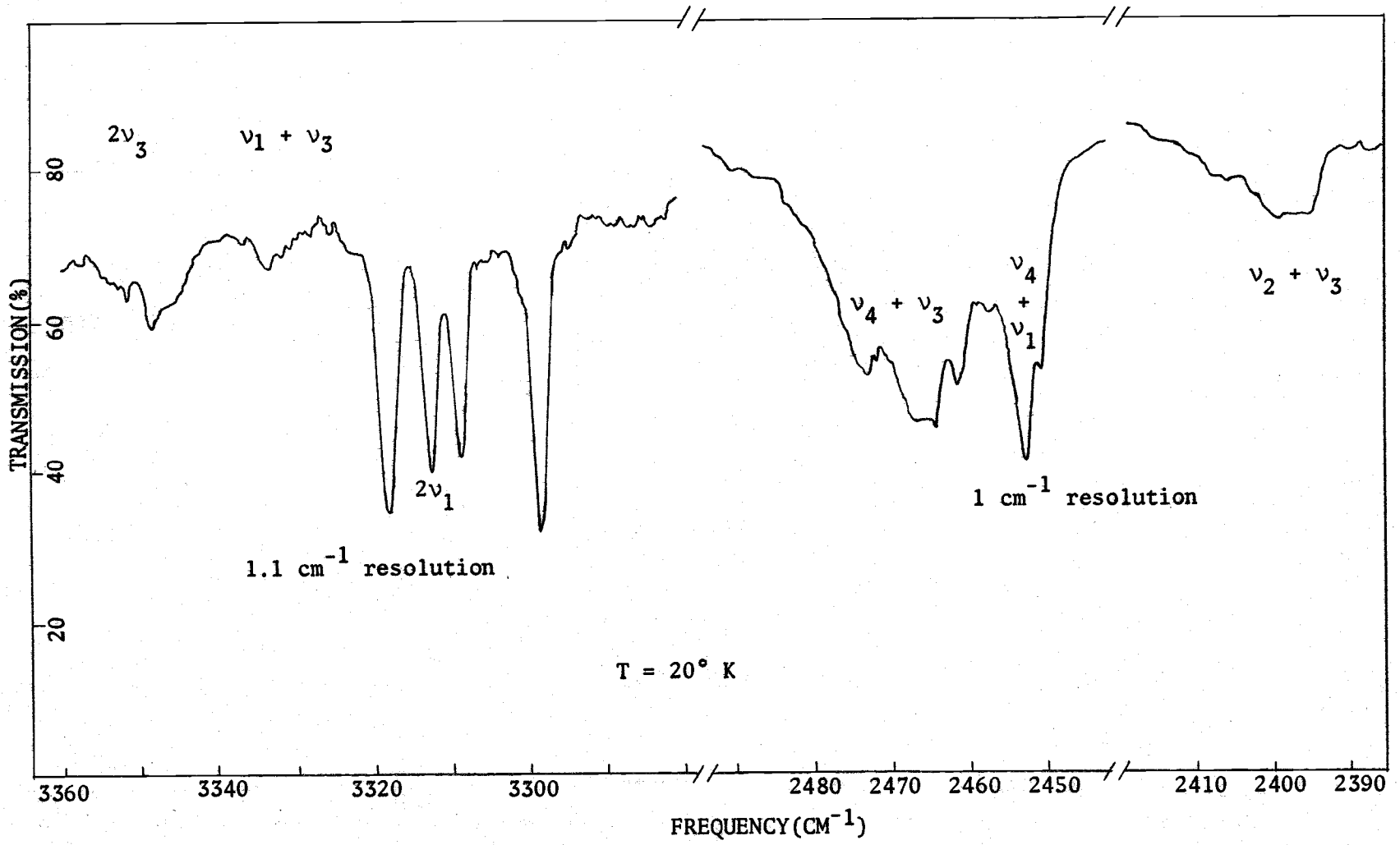

Figure 39. The infrared spectra of the combination-overtone of solid PD_3 which was mostly in the gamma phase.

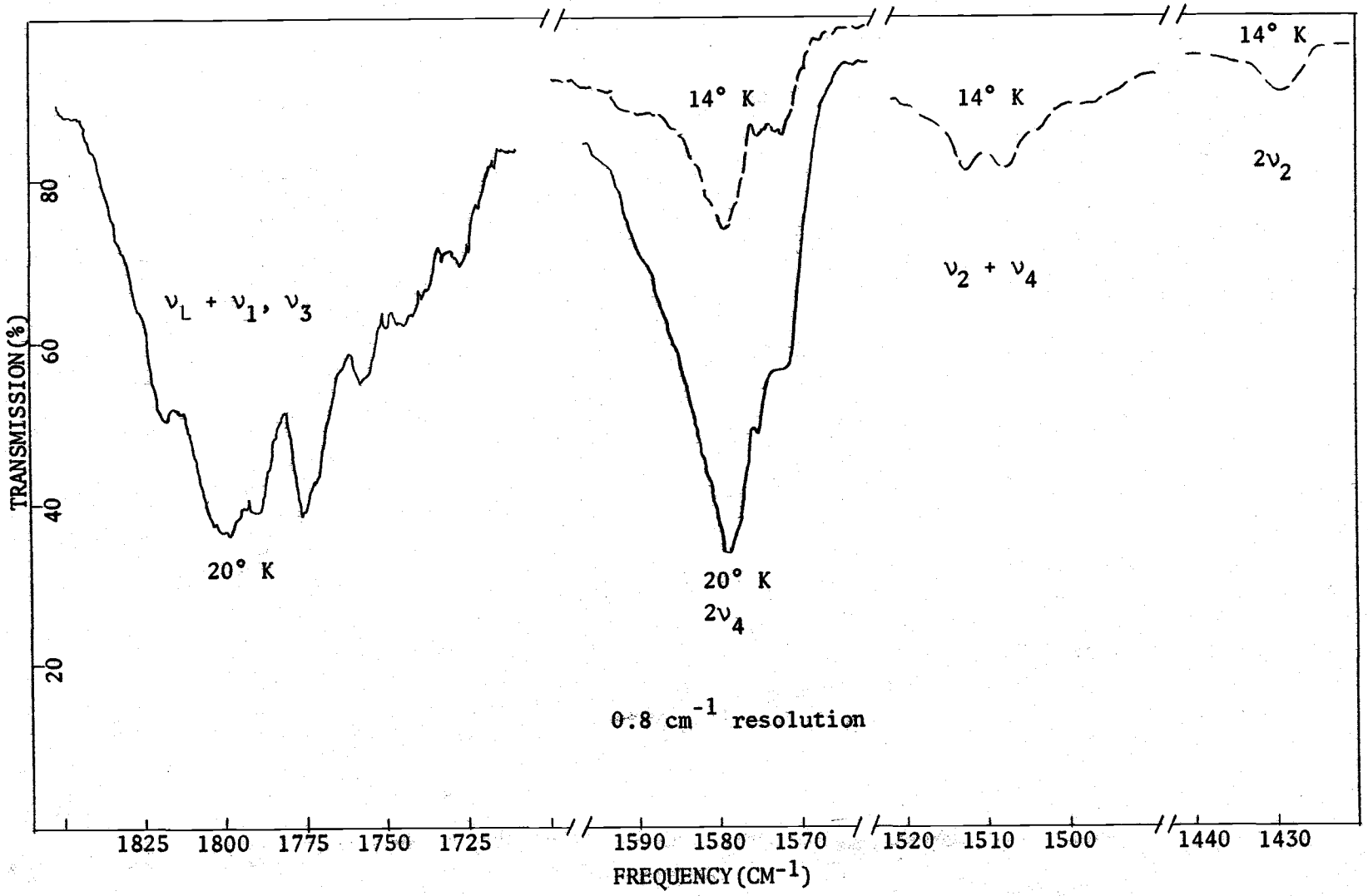

Figure 40. The infrared spectra of the combination-overtone of solid PD_3 mostly in the gamma phase. The film for the broken traces contained less of the delta phase than the solid traces.

The combinations of the lattice modes and the internal modes are usually broader than those of the internal modes, in agreement with the expectation that the lattice modes are more dispersed. The broad band at 1800 cm^{-1} is certainly of this type. In Table I each component was decomposed into the sum of an internal energy and a lattice energy. Some of the decompositions are not unique and may turn out to be incorrect when the inter- and intramolecular anharmonicities are known.

Among the overtone regions, the one at 3310 cm^{-1} is distinct. The components are well resolved and sharp, the pattern being accidentally similar to the spectrum of a matrix isolated species such as the solid trace in the stretching region in Figure 43. The solid trace s in Figures 39 and 40 and 43 were obtained from such a thick PD_3 (doped with 0.8% PH_3) film that the strongest band of PHD_2 at 900 cm^{-1} absorbed 50% and the ν_4 of PH_3, 25% in the survey scan. The observed frequency (about 3310 cm^{-1}) could conceivably be attributed to the mixed isotopic species, but is much more likely due to the overtone $2\nu_1$, which could easily have as many as four components (recall that ν_1 has five components distributed between the infrared and Raman.) Twice the smallest and largest components of ν_1 gives 3336 cm^{-1} and 3346 cm^{-1} respectively; the anharmonicity (about 15 cm^{-1}) does not seem unreasonable.

Most of the combination-overtones were assigned except for the 1440 cm^{-1}, 2700 cm^{-1}, and 2748 cm^{-1} ones observed in the Raman PH_3 experiments.

VIII. THE INTERMOLECULAR VIBRATIONS

The Beta, Supercooled Beta, and Delta Phases

The far infrared experiment was done with solid PH_3 only during the early stages of this project. We were still not able to obtain the gamma phase at that time. What we recorded was only a broad band around 150 cm^{-1} (half-width is about 100 cm^{-1}) of the delta phase. Due to the high noise-to-signal ratio, the spectrum is not reproduced in this thesis.

In the Raman experiments, it was found that the beta phase of PD_3 has a single, broad and weak lattice band at about 75 cm^{-1}, and the beta phase of PH_3, a moderately strong band at about 70 cm^{-1}. We have not recorded the lattice spectrum of the delta phase of PD_3, since it is relatively unstable with respect to the gamma phase.

The dot-dashed trace in Figure 41 is the same as trace E in Fig. 14. We concluded before that this particular domain contained some of the supercooled beta phase which also has only a fairly broad band in the lattice region. The background of this dot-dashed trace is very likely due to the supercooled beta phase.

Before we proceed to discuss the gamma-lattice-vibration, we will try to identify the spurious plasma emission in the lattice spectrum. The 66 cm^{-1} plasma line has a peak height of 7, the 77 cm^{-1} line of 21, the 117 cm^{-1} line of 26, and the 161 cm^{-1} line of 3. In the two traces in Figure 41, the strongest plasma emission stands alone. Its intensity can be compared with those of the bands at which the other plasma lines are located, taking into account the

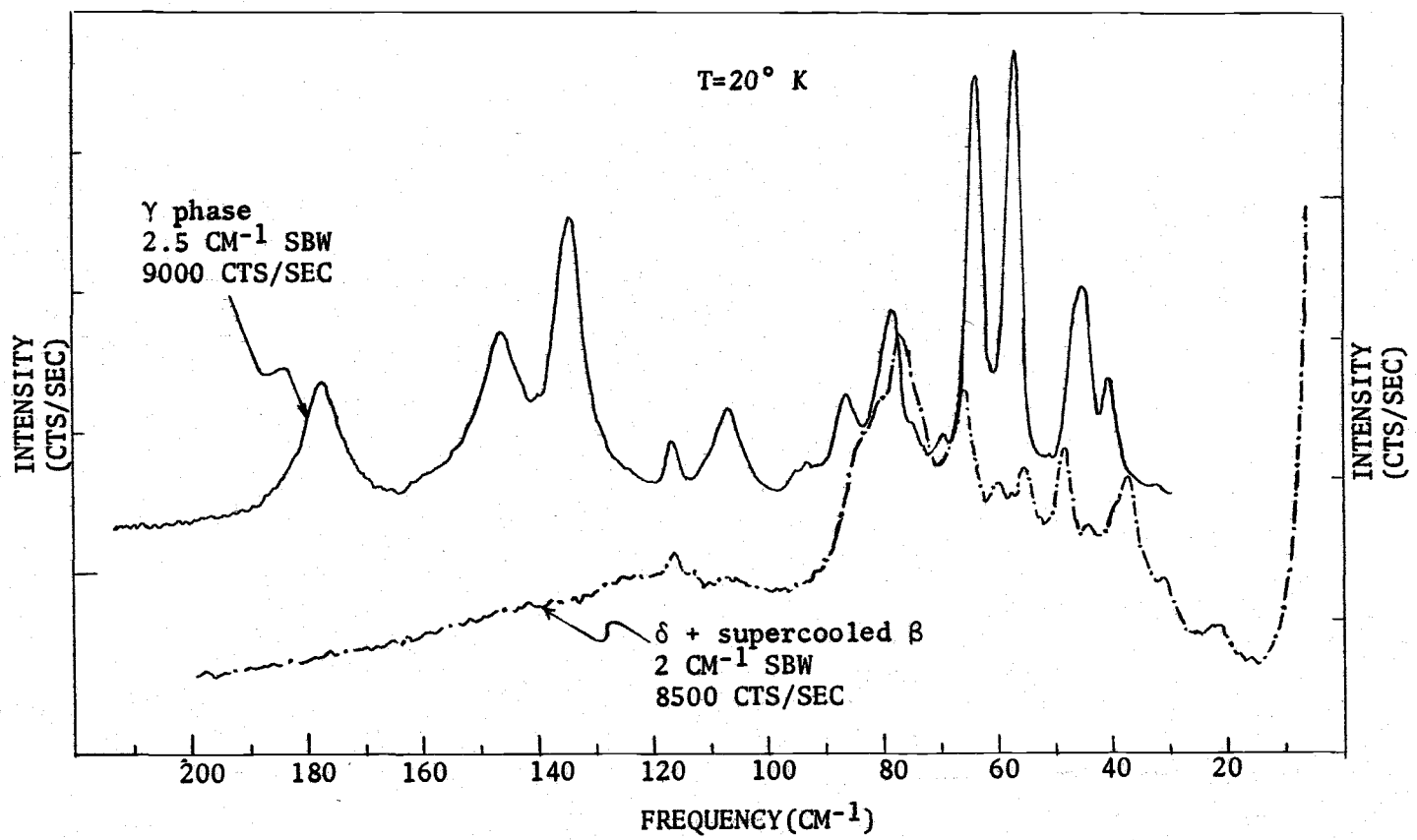

Figure 41. The intermolecular Raman spectra of solid PH_3.

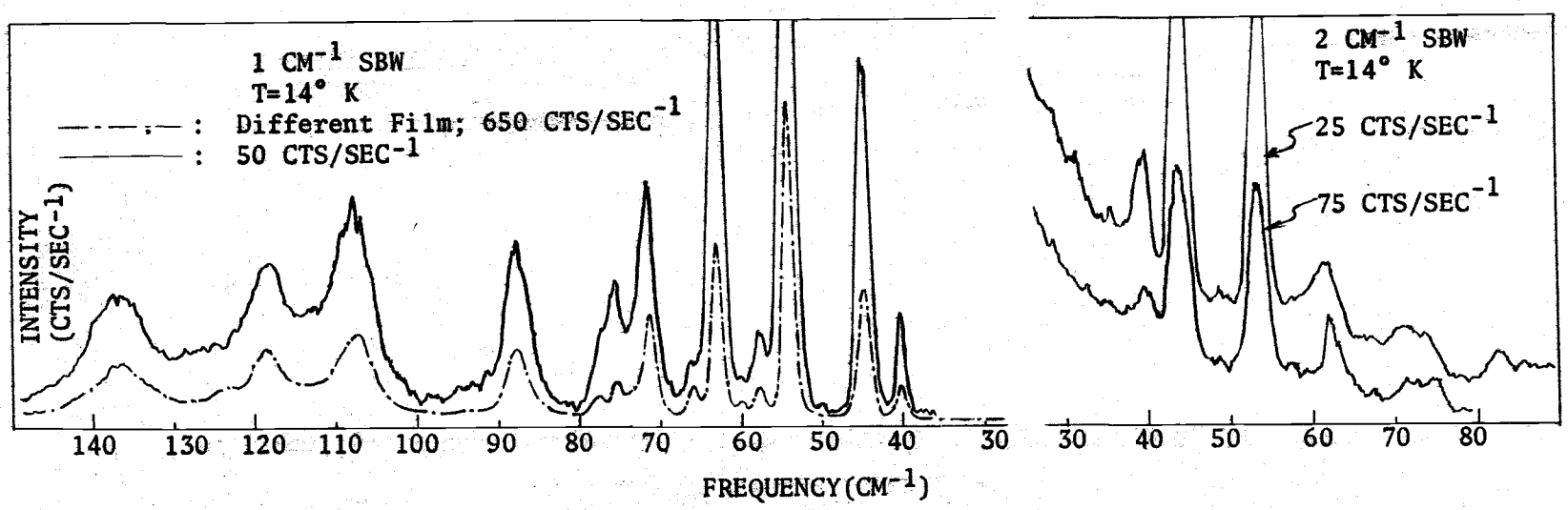

Figure 42. The intermolecular Raman spectra of solid PD_3 in the gamma phase. The Stokes shifts are at the left and the anti-Stokes ones at the right.

relative peak heights of the latter. It was found that the 75 cm^{-1} and the 78.8 cm^{-1} bands of the dot-dashed trace and the solid trace, respectively, are real, while the weak shoulder at about 75.5 cm^{-1} of the solid trace may not be due to the sample.

It is not so easy to eliminate the plasma contribution from the lattice spectra of PD_3. There is no plasma emission standing alone for comparison. However, the alternative is to compare the spectrum of PD_3 with that of PH_3, remembering the appearance of the plasma band, and to compare the Stokes lines with the anti-Stokes lines (if available). First, we examine the 66 cm^{-1} band which corresponds to the very weak band at 70 cm^{-1} in the PH_3 scan. The latter is plasma free, so the 66 cm^{-1} band comes from the sample. The 70 cm^{-1} -80 cm^{-1} region of PD_3 can be correlated to the 75 cm^{-1} -100 cm^{-1} region of PH_3. This correlation makes it clear that the 77.5 cm^{-1} band of PD_3 is real. Similarly, we say the PD_3 band at 118.3 cm^{-1} is real.

It was found that the anti-Stokes lines cannot assist in determining if the suspicious bands are real or not, because the anti-Stokes lines are equivalent to the hot bands in the infrared, and the population diminishes exponentially as the energy of the initial state increases.

The Gamma Phase

Since the lattice spectrum of the delta phase of PD_3 is not available, it is impossible to deduce the origins of the bands in the lattice spectrum of the delta phase of PH_3. However, it is

possible to do so for the gamma bands. We now attempt to find out which of these lattice bands are translational and which are librational using the isotopic product rule developed in reference 22.

In Cartesian coordinates, the G matrix for the solid is diagonal, The blocks correspond to the internal modes, the translational modes, and the librational modes. For the F matrix, the interaction elements between the internal and external modes are not zero but are negligible. Therefore, in the secular equation, $|FG - \lambda| = 0$, for solids, the lattice modes can usually be separated from the internal modes. Now suppose the interaction force constant between the translational vibrations and the librational ones can further be neglected. Then, from reference 22, we have

$$\frac{\omega_T^H}{\omega_T^D} = \left(\frac{M^D}{M^H}\right)^{\frac{1}{2}} = 1.043$$

$$\frac{\omega_{R_{xx}}^H}{\omega_{R_{xx}}^D} = \frac{\omega_{R_{yy}}^H}{\omega_{R_{yy}}^D} = \left(\frac{I_{xx}^D}{I_{xx}^H}\right)^{\frac{1}{2}} = \left(\frac{B_{xx}^H}{B_{xx}^D}\right)^{\frac{1}{2}} = \left(\frac{133478.3\ \text{Mc}}{69470.41\ \text{Mc}}\right)^{\frac{1}{2}} = 1.386$$

$$\frac{\omega_{R_{zz}}^H}{\omega_{R_{zz}}^D} = \left(\frac{m^D}{m^H}\right)^{\frac{1}{2}} = 1.414$$

where $\omega = 2\pi\nu$, M is the molecular weight, m the atomic weight, I the moment of inertia, B the rotational constant, and MC = megacycle (32). The subscript T means translation, and R_{zz}, libration around the molecular Z-axis.

A ratio of close to unity for the translational modes shows that the frequency is only slightly shifted on deuteration. This has to be true, because translational motions depend on the total mass of the molecule concerned. Any deviation from this value suggests that the motion responsible is not purely translational. The rotational constant around the molecular axis of PD_3 is not readily available; but, since the moment of inertia equals $\sum_i m_i r_i^2$ and the molecular geometry remains the same on deuteration, our third equation above is valid. It is noticed that the librational frequency ratio around the molecular Z-axis happens to be quite close to that around the other two axes perpendicular to the former, i.e. phosphine is fairly close to a spherical rotor. Again, if the observed librational frequency ratios are different from the calculated ones, the modes concerned are very likely not purely librational.

The experimental ratios of ω^H/ω^D are listed in Table 1 along with the corresponding frequencies of PH_3 and PD_3. It seems reasonable to say that the librational vibrations are actually coupled with the translational ones. Although there is a general agreement between the calculated ratios and the observed ones, each of the latter deviates from the appropriate value calculated. This deviation is the worst for the modes whose energies lie close to those of the other kinds of modes. It is also noticed that there is no clear demarcation between the translational and librational bands, so far as the ratios are concerned. Nevertheless, it is almost certain that the five low energy bands of PH_3 are transla-

tional. (The two unmatched bands of PD_3 at 57.8 cm^{-1} and 60 cm^{-1} may also be translational.) The four high energy bands can be assigned with confidence as librational ones. Although the product rule does not show unequivocally the nature of the vibrations responsible for the PH_3 bands at 78.8 cm^{-1}, 86.6 cm^{-1}, and 92.5 cm^{-1}, we can point to the spectral similarity existing between these spectra and the corresponding spectra of hydrogen and dueterium halides (12, 13) for which a general agreement on the band assignment has been arrived at by many workers in the past. In the Raman spectra of the hydrogen and deuterium halides, the translational bands are much stronger and are concentrated in a rather narrow low-frequency region, while the librational modes are distributed over a wide range at higher frequency. Moreover, the librational modes are not only weaker but also broader than the translational ones. Thus, these three bands were assigned as librational bands.

The anti-Stokes Raman shifts are shown on the left hand side of the spectra in Figure 42, while the Stokes Raman shifts are shown on the right. Both the infrared absorption and the Raman scattering experiments involve the interaction between the incident photons and the system concerned. In the former, certain photons with $hc\tilde{\nu} = \Delta E$, the transition gap, are absorbed by the system and are shown by a decrease in transmitted energy in the spectra. In the latter, the scattering system is first excited by the incident light from the laser ($h\nu_i$) to some virtual states and then emits photons $h\nu_s$ (Stokes) and $h\nu_{as}$ (anti-Stokes) which are monitored by the monochromator. The shifts of the emitted photon energies from the

excitation energy, or the differences, $h(\nu_i - \nu_s)$ and $h(\nu_i - \nu_{as})$ are recorded in the form of a spectrum.

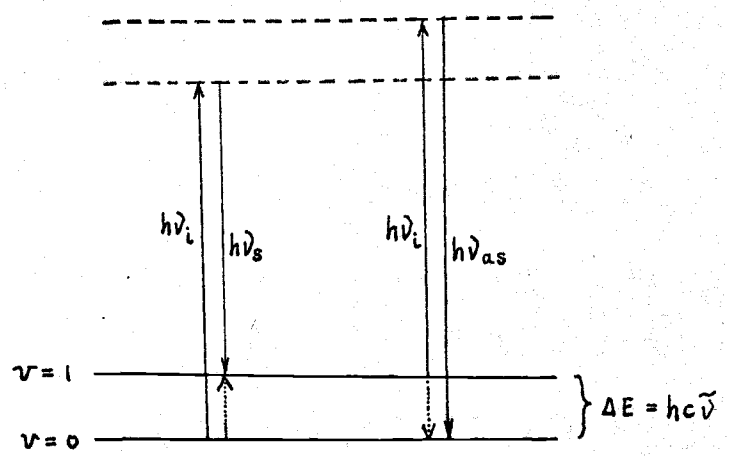

The two arrows on the left in the figure above show the Stokes Raman process, and the two arrows on the right the anti-Stokes process. The broken arrows represent the Raman shifts that are recorded. Experimentally, one has to switch to the high energy side of the exciting line to scan the anti-stokes bands. The sensitivity of the instrument must also be increased; because the anti-Stokes transitions start from the excited state, and the ratio of the population on this level to that on the ground level is $e^{-1.44\tilde{\nu}/T}$ $e^{-0.102\tilde{\nu}}$ for $T = 14^{\circ}K$. Thus, in addition to the volumetric change of the polarizability ellipsoid of the unit cell with respect to the vibrational coordinates, the Boltzman factor also governs the anti-Stokes intensity. This is why the 44.7 cm^{-1} band is as strong as the 57.8 cm^{-1} band in the anti-Stokes spectrum, while their intensity ratio in the Stokes spectrum is 1/2.39. It appears that the Boltzman factor is not obeyed quantitatively. In the Stokes and

anti-Stokes spectra, the intensity ratios obtained by subtracting a background correction (more serious in the anti-Stokes region — see Fig. 42) are as follows:

40.3 cm^{-1}	44.7 cm^{-1}	54.0 cm^{-1}	62.9 cm^{-1}	
1.00	4.00	9.55	5.30	
	1.00	2.39	1.33	Stokes
		1.00	0.56	
1.00	4.00	4.10	1.70	
	1.00	1.03	0.43	anti-Stokes
		1.00	0.42	
1.00			0.67	
1.00	0.64	0.24	0.10	Boltzman ratio at 14°K
1.00	2.54	2.33	0.52	expected anti-Stokes

The last anti-Stokes ratio is obtained from the upper trace in Fig. 42 and the rest of the anti-Stokes ratios from the lower one of the same figure. Comparing the expected and the observed anti-Stokes ratios, one sees that the intensity ratios of the 40.3 cm^{-1}-to-44.7 cm^{-1}, the 54.0 cm^{-1}-to-62.9 cm^{-1}, and the 40.3 cm^{-1}-to-62.9 cm^{-1} have larger discrepancies than that of the 44.7 cm^{-1}-to-54.0 cm^{-1} when the lower anti-Stokes trace in Fig. 42 is used. However, if we use the upper anti-Stokes trace of Fig. 42, the agreement of the 40.3 cm^{-1}-to-62.9 cm^{-1} ratio is much better. All these are most likely due to (1) the anti-Stokes band at 40.3 cm^{-1} of the lower trace in Fig. 42 is so weak that its peak height is very sensitive to error in background correction, (2) the peak height of the 62.9 cm^{-1} band of the lower trace in Fig. 42 is spurious when compared with the intensity of the same band in the upper trace.

The following calculation not only substantiates the point we have just brought out, but also checks the accuracy of our temper-

ature measurement. From the Raman intensity expression given in page 87, it can be easily calculated that

$$\frac{I_s(2)/I_s(1)}{I_A(2)/I_A(1)} = \frac{N_{n'}(1)/N_{n''}(1)}{N_{n'}(2)/N_{n''}(2)}$$

$$= \frac{e^{-1.44\,\tilde{\nu}_1/T}}{e^{-1.44\,\tilde{\nu}_2/T}}$$

$$= e^{-1.44\,\Delta\tilde{\nu}/T}$$

where $\Delta\tilde{\nu} = \tilde{\nu}_2 - \tilde{\nu}_1$, $\tilde{\nu}_i$ = wavenumber of mode i

$I_s(i)$ = Stokes intensity (peak height, actually used) of mode i

$I_A(i)$ = anti-Stoke intensity of mode i

$N_{n'}(i)$ = upper state population of mode i

$N_{n''}(i)$ = lower state population of mode i

The last equation can be simplified to be

$$T = 0.625\,\frac{\Delta\tilde{\nu}}{\log I'} \qquad \text{where } I' = \frac{I_s(2)/I_s(1)}{I_A(2)/I_A(1)}$$

Although it is not feasible to determine the intensity ratio of the corresponding Stokes and anti-Stokes lines due to instrumental reason (such as slit width variation), the expression above allows us to calculate the running temperature from the intensity ratio of a pair of bands in Stokes and the corresponding ratio of the same pair in anti-Stokes. Given below are the pairs and the temperature calculated.

	lower anti-Stokes trace	upper anti-Stokes trace
40.3 cm^{-1} — 44.7 cm^{-1}	*	
40.3 cm^{-1} — 62.9 cm^{-1}		16°K
44.7 cm^{-1} — 54.0 cm^{-1}	16°K	
44.7 cm^{-1} — 62.9 cm^{-1}	23°K	
54.0 cm^{-1} — 62.9 cm^{-1}	44°K	

* = undefined, but the background correction can change the situation

For the reason given above, one would naturally choose 16°K as proper expectation of the running temperature. This is consistent with our observation in chapter V, i.e. laser has caused a local heating of a few degrees.

That the anti-Stokes spectrum exists for solid PD_3 means that a level of as high as 63 cm^{-1} above the ground state still has finite population at 14°K. It is likely that the equivalent levels of solid PH_3 are also finitely populated.

IX. THE INFRARED AND RAMAN SPECTRA OF THE ISOLATED SPECIES

Frequency Calculation of PH_2D and PHD_2 Isolated in Solid PH_3 and PD_3

To a very high order of approximation, it is correct to assume that the isotopic molecules have the same vibrational force field (or potential function), because they have the same electronic structure, which affects the motion of the nuclei (or skeletal vibration). Therefore, it is necessary to calculate the force constants of our system (PX_3 where X may be H and/or D) from the observed frequencies of PH_3 and PD_3 and then apply the calculated force field to PH_2D and PHD_2 in order to calculate the latter's frequencies.

Under the simple force field (valence and central) assumption, it is usually not necessary to make use of the vibrational frequencies of a second isotopic species to obtain an additional equation in the same unknowns (or force constants), when one wants to determine the force constants. The reason is that both the valence- and the central-force-field assumptions neglect the cross terms in the harmonic potential energy equation. However, these simple force fields do not give rise to satisfactory results in many cases. Therefore, the most general force field (i.e., retaining all the interaction force constants) must be used. The harmonic approximation in the expansion of the potential energy is also made in order to simplify the calculation. There usually are more unknowns (force constants) than the number of equations (3N-6 or 5), when the most general quadratic force field is used. Therefore, the

frequencies of one or more additional isotopic molecules must be used in order to have enough equations in the same unknowns. This is one of the reasons for our interest in solid PD_3.

For polyatomic molecules, it is often quite tedious to calculate the most general force field by hand, even with the harmonic approximation. A computational approach (Schachtschneider's program) has been used for this purpose. Alternatively, a more sophisticated calculation (high-low frequency separation) can be done by hand with fairly good results.

The vibrational frequencies of PH_2D and PHD_2 isolated in solid PH_3 and PD_3 were first calculated by hand using the FG matrix method (22) and the high-low frequency separation approximation (22). The result was then compared with that obtained from the computer refinement of the force field using Schachtschneider's program (33, 34). These two results were further checked against actual observation. The agreement is good, as can be seen easily from Table IV. In this table the assignment of the observed stretching frequencies is still uncertain.

Schachtschneider's program not only calculated the G matrices (both symmetrized and unsymmetrized) but also refines the force field of a polyatomic molecule, using the least squares method. In this refinement, we started out with the six force constants of a free phosphine molecule given by Duncan and Mills (35):

$$f_r = \underset{3.048291}{3.10} \text{ mdyn Å}^{-1}, \quad f_r' = \underset{-0.025107}{-0.07} \text{ mdyn Å}^{-1}, \quad f_\alpha = \underset{0.679957}{0.73} \text{ mdyn Å},$$

$$f_\alpha' = \underset{-0.023022}{0.01} \text{ mdyn Å}, \quad f_{r\alpha} = \underset{-0.152548}{-0.16} \text{ mdyn}, \quad f_{r\alpha}' = \underset{-0.006128}{-0.22} \text{ mdyn}.$$

The force constants of the internal coordinates are defined in the following potential energy equation within harmonic approximation.

$$2V = f_r \sum_{i}^{3} (\delta r_i)^2 + 2f'_r \sum_{i,j}^{3} (\delta r_i)(\delta r_j) + r_e^2 f_\alpha \sum_{i}^{3} (\delta \alpha_i)^2 + 2r_e^2 f'_\alpha \sum_{i,j}^{3} (\delta \alpha_i)(\delta \alpha_j)$$
$$+ 2r_e f_{r\alpha} \sum_{i,j}^{6} (\delta r_i)(\delta \alpha_j) + 2r_e f'_{r\alpha} \sum_{i,j}^{3} (\delta r_i)(\delta \alpha_j)$$

where the unit of each term has been made the same by multiplying r_e and r_e^2. When this question is expressed in matrix language ($2V = R^+ F R$), F takes the same form as the G matrix in the Appendix I.

These six beginning constants were first adjusted to fit the eight fundamental frequencies of PH_3 and PD_3 in solid PD_3 and PH_3 (at 20°K) respectively. After seven perturbations, the calculated frequencies of PH_2D and PHD_2 deviated greatly from both the observed frequencies and those calculated by hand. Finally, we added four observed frequencies of PH_2D and PHD_2, 758 cm^{-1}, 901 cm^{-1}, 964 cm^{-1}, and 2318 cm^{-1}. So the six beginning constants were adjusted to fit 12 frequencies. The resulting force constants after six perturbations were listed below the beginning ones shown above. The final frequencies of PH_2D and PHD_2 were recorded in column "CR" in Table IV. In the Appendix I, we included the symmetrized and unsymmetrized G matrices at points where a comparison with the counterparts calculated by hand is most convenient. Also contained in the same Appendix are the Cartesian coordinates that were put into the computer calculation of the G matrix.

In these calculations it was important to predict the frequencies of the intermediate species PH_2D and PHD_2 from the observed

values of PH_3 and PD_3. However, experience has shown (Pimentel and Nibler, 36) that the interaction force constants in the potential function are not well determined by the frequencies of PH_3 and PD_3 alone. The reason is that the G matrices of PH_3 and PD_3 differ mostly by a simple scale factor since μ_H, $\mu_D > \mu_p$ so that the additional equations from PD_3 do not supply information which is significantly different from those for PH_3. Pimentel and Nibler showed that the force constants were better determined by using the mixed isotopic species, but to do so here would in a sense circumvent the need for an independent prediction. Therefore an independent calculation, making the high-low frequency separation was carried out. The stretching frequencies were calculated approximately by setting the bending force constants equal to zero, i.e., merely leaving out the rows and columns of $\underline{F}$ (symmetrized force constant matrix) and $\underline{G}$ in the secular equation, $|\underline{FG} - \lambda| = 0$, which correspond to the coordinates whose diagonal force constants vanish. In calculating the bending frequencies, the $\underline{F}$ and $\underline{G}$ matrices were inverted, and thus the reciprocal secular equation,

$$|CK - \phi E| = 0 \quad (37)$$

where $C = \underline{F}^{-1}$, $K = \underline{G}^{-1}$, and $\phi = 1/\lambda$, was obtained. The high-low frequency separation was then applied, now assuming the stretching compliance elements are zero.

Before the secular equation was used to calculate the λ's of PH_2D and PHD_2, the force constants were calculated from the observed frequencies of PH_3 in solid PD_3 and PD_3 in solid PH_3, and the respective G matrices (which were obtained using the gas phase

geometry and the G matrix element diagrams from reference 22). In this precalculation, we also relied on the high-low frequency separation approximation.

The frequencies of PH_3 and PD_3 mentioned above were taken from the 20°K-experiments performed with PH_3 isolated in PD_3 and vice versa, instead of from experiments performed with the pure solids, the reason being that it was easier to carry out experiments using PH_2D or PHD_2 in solid PD_3 or PH_3 than those using pure solid PH_2D or PHD_2. Further, it makes more sense to use the force constants of PH_3 isolated in solid PD_3 to calculate the frequencies of PH_2D or PHD_2 isolated in solid PH_3 or PD_3 than to use the force constants of the pure solid; since the latter are certainly involved in the intermolecular interaction, while the former are not.

The details of the hand calculation are supplied in the Appendix I. The frequencies calculated by hand are listed in column "HLS" in Table IV. The gas phase frequencies of all four species, PH_3, PD_3, PH_2D, and PHD_2, are also supplied in Table IV. It is noticed that the gas phase frequencies are generally higher than the frequencies of isolated species.

The sum rule check (38) for the calculated frequencies of PH_2D and PHD_2 is performed in the following. This rule states that "whenever there exists a chemical exchange reaction involving only isotopic variations of a single type of molecule, such that the reaction is balanced at each atomic position of the molecule," then

$$\sum_i n_i \sum_j \tilde{\nu}_{ij}^2 = 0$$

where i identifies an isotopic form of the type of molecule concerned

n is the stoichiometric coefficient, positive for the reactants and negative for the products

j indexes all the equivalent species of the fundamental vibrations in the reactants and the products.

The isotopic exchange reaction of the PH_3 type of molecules can be expressed as

$$PH_3 + PD_3 \rightleftharpoons PH_2D + PHD_2.$$

And the correlation between the point groups (C_{3v} and Cs) of the isotopic forms is

	C_{3v}	Cs	
ν_1, ν_2	A_1	A'	$\nu_1(A'), \nu_2(A'), \nu_3(A'), \nu_4(A')$
	A_2		
ν_3, ν_4	E	A''	$\nu_3(A''), \nu_4(A'')$

Thus, there are two separate sums to be checked. First, sum over the A' vibrations of the Cs forms and the A_1 and E vibrations of the C_{3v} forms.

$$\sum_{j=\nu_1,\nu_2}^{\nu_3,\nu_4} \left[\tilde{\nu}_j^2\ (PH_2D) + \tilde{\nu}_j^2\ (PHD_2)\right] = 11590\ cm^{-2}\ (10633.9\ cm^{-2})$$

$$\sum_{j=\nu_1,\nu_2}^{\nu_3,\nu_4} \left[\tilde{\nu}_j^2\ (PH_3) + \tilde{\nu}_j^2\ (PD_3)\right] = 11550\ cm^{-2}\ (11542.9\ cm^{-2})$$

The difference between these two sums implies the magnitude of anharmonicity. Next, the sum is over the A" vibrations of the Cs forms and the E vibrations (and the A_2 vibrations too, if there were

any A_2 active vibration) of the C_{3v} forms.

$$\sum_{j=\nu_3}^{\nu_4''} \left[\tilde{\nu}_j^2 \ (PH_2D) + \tilde{\nu}_j^2 \ (PHD_2) \right] = 5914 \text{ cm}^{-2} \ (5910.2 \text{ cm}^{-2})$$

$$\sum_{j=\nu_3}^{\nu_4} \left[\tilde{\nu}_j^2 \ (PH_3) + \tilde{\nu}_j^2 \ (PD_3) \right] = 5882 \text{ cm}^{-2} \ (5878 \text{ cm}^{-2})$$

The anharmonicity involving these vibrations is greater than the one associated with the vibrations in the first case. Nevertheless, the calculated frequencies of PH_2D and PHD_2 must agree with observed ones fairly well, since the differences in the sums are small. The numbers in parentheses above are the result obtained from the computer calculated frequencies.

The main conclusions from both calculations are as follows. First, some of the H or D stretching vibrations of the mixed isotopic species are not sufficiently shifted compared with PH_3 or PD_3 to permit unequivocal assignment. For example, ν_3 of PH_3 is very close to $\nu_3(A'')$ of PH_2D. Second, the bending modes of the mixed species are well resolved, and an unequivocal assignment is possible, which assists in the estimation of the relative amounts of the various isotopic species present in any sample.

Spectra of PH_2D and PHD_2 Isolated in Solid PH_3 and PD_3

The spectra of PH_2D and PHD_2 isolated in the gamma phase and the delta phase of solid PD_3 are illustrated in Figure 43. Although the delta phase of solid PD_3 is relatively unstable with respect to

TABLE IV. Infrared frequencies of isolated PH_2D, PHD_2, PH_3, and PD_3

		gas[a]	HLS	CR	in PD_3 ($\gamma \gg \delta$)[b]	in PD_3 ($\delta \gg \gamma$)[b]	in PH_3 ($\delta \gg \gamma$)[c]
	ν_2	992.1	980	986.6	979.6(1) 982.8(1)	~979.4 sh 980.6 s ~982.3 sh	
PH_3	ν_4	1118.3	1097	1104.3	1094(1) 1096.8 vw 1098.5(1)	1095 vw sh 1099.2 s	
	ν_1	2322.9	2301	2306	2304.8(?)		
	ν_3	2327.7	2313	2322	2321.1(?)		
	ν_2	730	719	714.4			717.2 vw 719.5 s [720][d] 721.7 vw
PD_3	ν_4	806	790	786.5			787 vw [792][d] 790.8 s
	ν_1	1694	1668	1662.8			1669 s [1669.5][d]
	ν_3	1700	1682	1672.7			1681.8 s [1683][d]
	$\nu_1(A')$	1692	1668	1674.1			
	$\nu_2(A')$	902	886	880.1	~881 vw sh 882.8(2) 885.2(1)	~879 w sh 883.3	~882 [883.5]
PH_2D	$\nu_3(A')$	2328	2318	2310.2			
	$\nu_4(A')$	1084	1079	1080.3	1082		
	$\nu_3(A'')$	2328	2326	2320.8			
	$\nu_4(A'')$	972	952	954.5	955.4(1) 957.4(2)	~957	

TABLE IV (Continued)

	$\nu_1(A')$	1691	1668	1668.1		
	$\nu_2(A')$	766	754	752.2	756.2(1) [~757] 759.7(2) [759.7]	758.8	758.7
	$\nu_3(A')$	2323	2320	2314.3	2305.4(?) [2305.1(?)]		
PHD_2						~899 sh	
	$\nu_4(A')$	917	897	898.9	901.3 [901.8]	902.8 s	~902
	$\nu_3(A'')$	1697	1673	1675.4			
	$\nu_4(A'')$	982	963	961.3	963.3(2) [964.4(2)] 968.5(1) [969.5(1)]	~957 w sh 966.0 s ~969 w sh	
	$2\nu_4(A'')$				1927		

the numbers in brackets are the Raman wavenumbers
HLS: obtained from High Low frequency Separation
CR: obtained from Computer Refinement of force field
a: frequencies for PH_2D and PHD_2 are taken from ref. 41, those for PH_3 and PD_3 from ref. 26
b: the 1082 cm^{-1} of PH_2D was taken from the lower solid trace in Fig. 27 and 1.5 cm^{-1} slit, the rest from the same film at 14°K. The number in parenthesis indicates the intensity rating among the components of a fundamental region.
c: IR frequencies were taken at 20°K
d: taken at 16°K when the PH_3 host was in the supercooled beta phase

TABLE V. IR frequencies of PH_3 in inert gases

	Ar	Kr	Xe
ν_2	988.5 s	988.5 m	983.5 w
ν_4	1106 1111.5 w db	1115 w	1110 w
ν_1 & ν_3	~2312 m sh 2325.4 vs ~2347.2 m sh ~2360 w sh	2335.2 sh 2340.3 s db 2342 2346 sh	2324.4 s 2337 w sh

1. observed at 20°K

2. The concentration of PH_3 in Ar, Kr, and Xe are 1/1083, 1/650, 1/300 respectively.

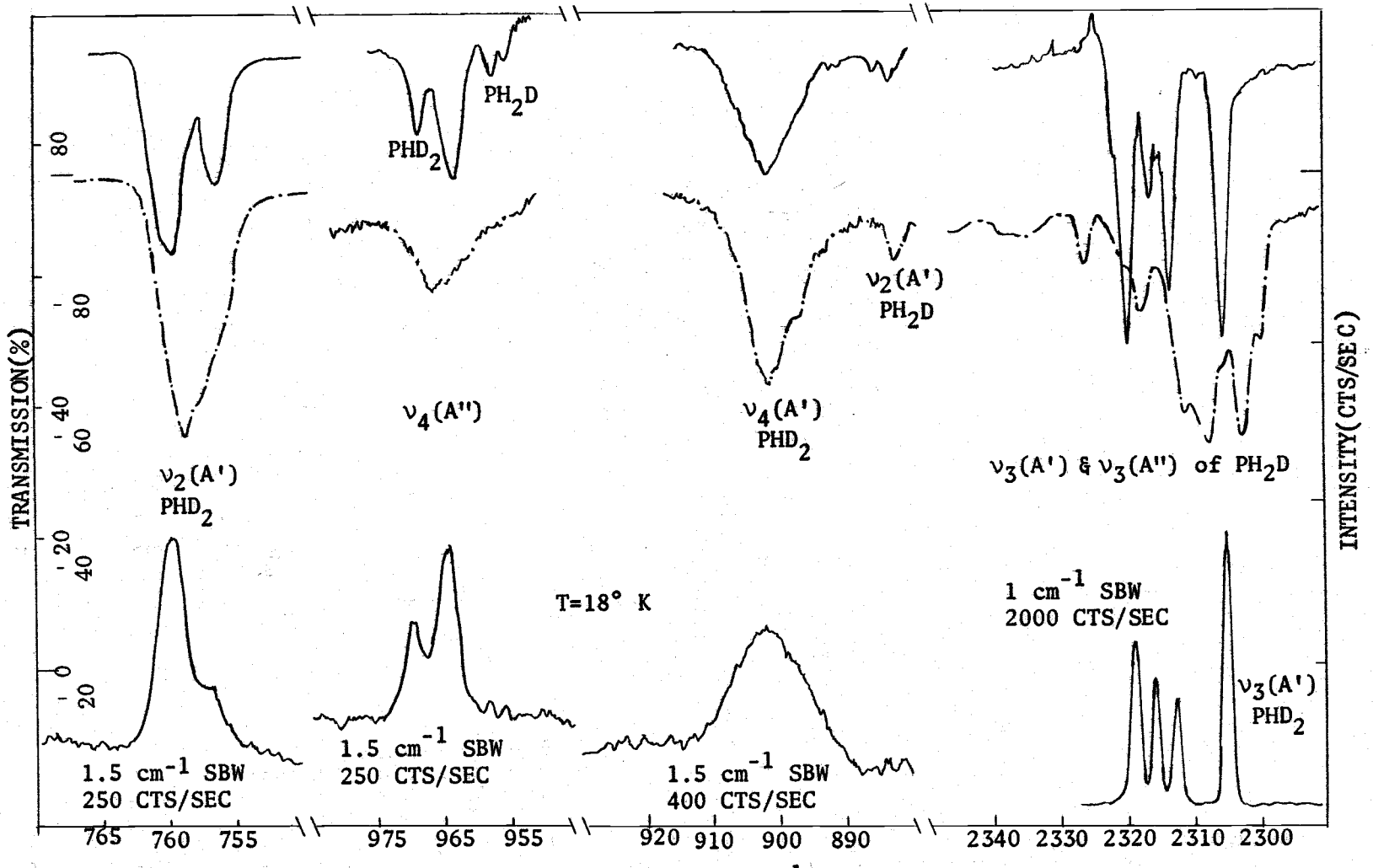

Figure 43. The IR and Raman spectra of PHD_2 and PH_2D isolated in the γ(solid traces) and the δ(dot-dashed ones) phases of PD_3. All the IR traces were taken from the same film at 12° K with a resolution of 1 cm-1 or better.

the gamma phase and the beta phase tends to be frozen-in during a sudden chilling, the dot-dashed traces were shown, in the section on the high resolution stretching spectra of solid PD_3, to correspond to the delta phase rather than to the supercooled beta phase of the host system. The phase of the host system to which the solid traces correspond was recognized as the gamma, judging from the characteristics of the symmetric bending spectra.

Presentation of the spectra in Figure 43 not only confirms the result of the coordinate analysis in the last section but also suggests that the site of the PH_2D and PHD_2 molecules in the gamma phase of PD_3 must be Cs. All of the symmetry species to which the vibrational modes of PH_2D and PHD_2 belong are nondegenerate. That is, their vibrational spectra would not be split by lowering the site symmetry. However, if the site is Cs, then the orientational effect (39 and 40) will split the individual band into two bands. The PH_2D molecule isolated in the gamma phase of solid PD_3 may assume one of the three orientations shown below with respect to the symmetry plane. The molecules in the middle and left

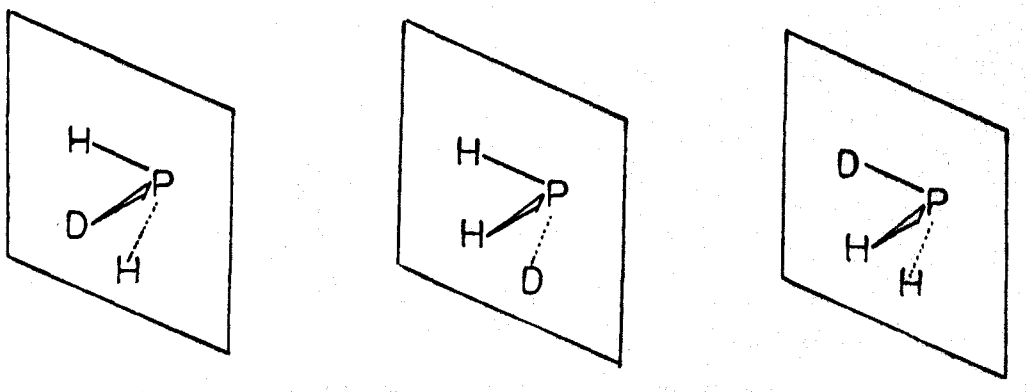

orientations will "see" the same potential, which is different from that seen by the molecule in the orientation on the right. Thus we expect a 2-to-1 intensity ratio for the split doublets whose corresponding vibrations are most sensitive to this potential plane of symmetry. The nonsplitting of the $\nu_4(A')$ of PHD_2 may be interpreted in this way. This particular vibration is not affected to any significant extent by the plane of the potential symmetry. In other words, under this vibration, the molecules in the three above-mentioned positions experience almost the same or only slightly different potentials.

The agreement between the infrared and the Raman spectra confirm our reasoning about the site symmetry of the gamma phase. Although the $\nu_2(A')$ of PHD_2 was not well resolved in the Raman experiment, there was an indication of the existence of the weaker feature. In the $\nu_2(A')$-of-PHD_2 region, the higher Raman shift (759.7 cm^{-1}) coincides exactly with the corresponding infrared frequency, while the lower Raman shift (~757 cm^{-1}) is about 0.8 cm^{-1} higher. For the $\nu_4(A')$ of PHD_2, the Raman frequency (901.8 cm^{-1}) is 0.5 cm^{-1} higher, and for the $\nu_4(A'')$, the Raman frequencies (969.5 cm^{-1} and 964.4 cm^{-1}) are, respectively, 1.0 cm^{-1} and 1.1 cm^{-1} higher. The frequency differences seem to be quite random. It is understood that all of the infrared active vibrations of PHD_2 and PH_2D must also be Raman-active, and so the infrared frequencies of PH_2D and PHD_2 should coincide with the Raman ones. The two larger frequency differences are within what the compound error in Raman and infrared frequency measurements can account for.

The Raman bending spectra of PH_2D are not much stronger than the noise level. They are thus left unassigned.

Before assuming that the region from 2300 cm^{-1} to 2320 cm^{-1} (Fig. 43) arises solely from the H stretching modes of the mixed isotopic species, one might consider overtones and combinations of the host PD_3. Binary combinations of one stretch and one band would fall between 2400 cm^{-1} and 2475 cm^{-1} which is much too high even admitting some anharmonicity.

Concerning the spectra illustrated in Figures 43 and 44 we can estimate the relative abundance of the several isotopic species as follows. The sample illustrated in Fig. 43 shows absorbances for the mode ν_2 of PD_3, PHD_2, PH_2D which are roughly in the ratio of 40:10:1. These numbers imply a statistical distribution corresponding to 92% D, 8% H which amounts to the following mole fractions: 0.78 PD_3, 0.20 PHD_2, 0.02 PH_2D and a negligible amount, namely 0.0005 PH_3. Thus we would assume that in the stretching region only the modes $\nu_1(A')$ of PHD_2 and $\nu_3(A')$ and $\nu_3(A'')$ of PH_2D should contribute, the latter being about ten-fold weaker. It is obviously difficult to interpret the 2300 to 2320 cm^{-1} region on this basis.

The sample illustrated in Fig. 44 unlike the previous one did not have an equilibrium distribution of isotopes because of the deliberate doping with PH_3. Comparison of the bending intensities suggests that the mole fractions of the species PH_3 and PHD_2 are very approximately equal and that less of PH_2D is present than in Fig. 43. The proximity of all the H stretching modes makes it difficult to make assignments, but one can at least understand that the solid

trace in the H stretch region of Fig. 44 should be different from the dot-dash trace because of the presence of significant amounts of PH_3.

Spectra of PH_3 Isolated in Solid PD_3 and Vice Versa

Among the spectra in Figure 44, we first point out the splitting of ν_4, which belongs to the E species in the molecular group, in the gamma phase of PD_3. Since PH_3 molecules were isolated in solid PD_3, no factor group splitting could have occurred to ν_4. Therefore the splitting must be due to the site effect. Thus the isolated PH_3 molecules must have resided at a C_s or C_1 site.

Within the framework that we have constructed about the gamma phase, the ν_2 (nondegenerate) doublet is the most difficult to explain. We believe the phosphine molecules occupy C_s sites in the gamma phase. But the orientational effect cannot split ν_2 in PH_3, due to its threefold symmetry; the doublet cannot be caused by lowering site symmetry either, because ν_2 is already nondegenerate in the molecular group. The dynamic interaction of the PH_3 molecule with its neighbors in the primitive cell did not exist, so the doublet was not caused by factor group splitting.

The concentration of the guest molecules was reduced to make sure that each molecule is well isolated by the host ones. Nevertheless, the doublet persisted.

However, if there are two distinct kinds of C_s sites in a primitive cell, then the nondegenerate vibration can exhibit a two-band spectrum. But, then, each of the distinct kinds of sites

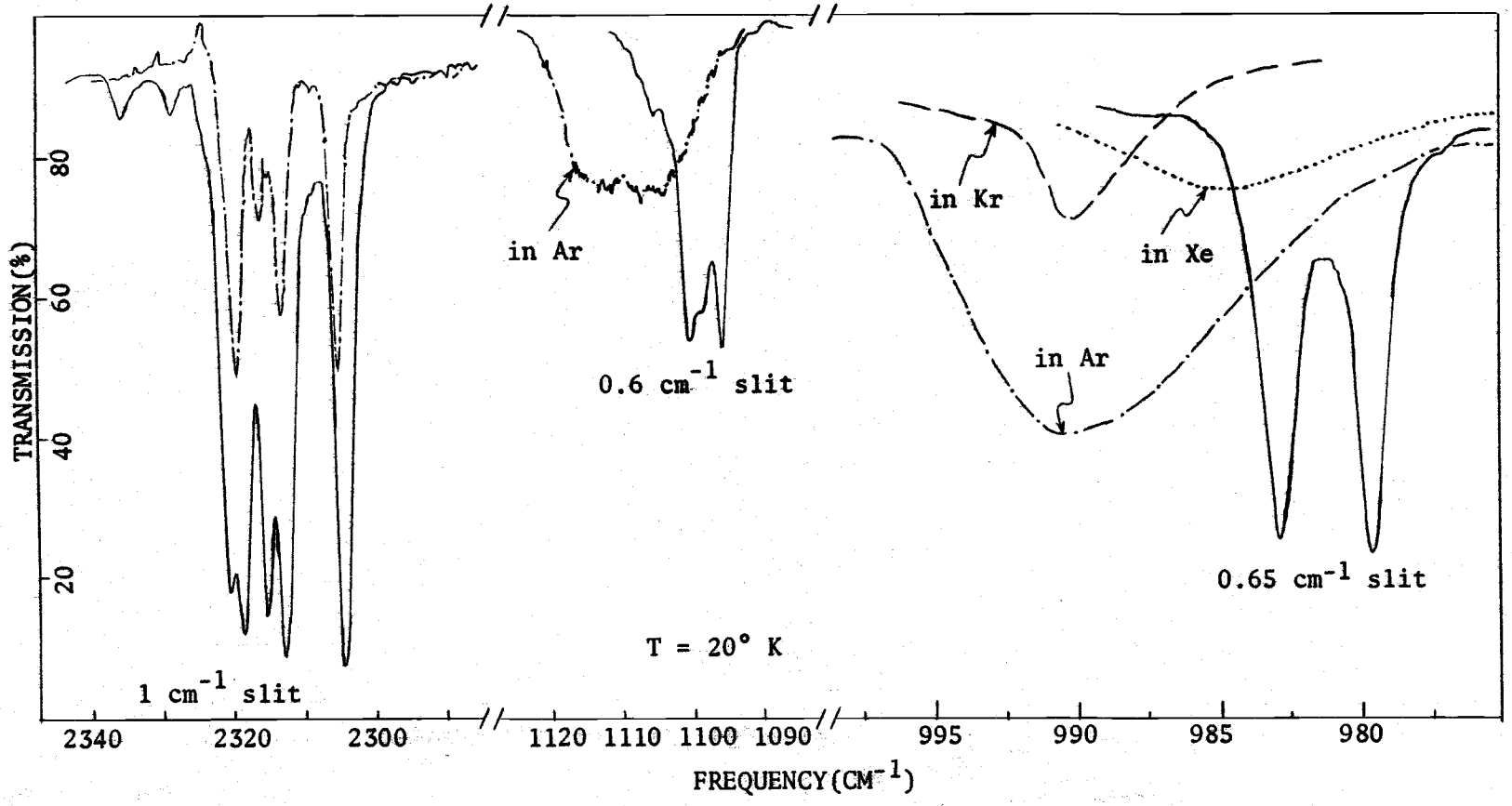

Figure 44. The infrared spectra of the fundamentals of PH_3(solid traces) isolated in solid PD_3 which was purposely doped with 0.8% PH_3 and was mostly in the gamma phase. The dot-dashed trace in the stretching region was obtained from a PD_3 sample undoped with PH_3. The stretching region was complicated by the PH_2D and PHD_2 absorptions.

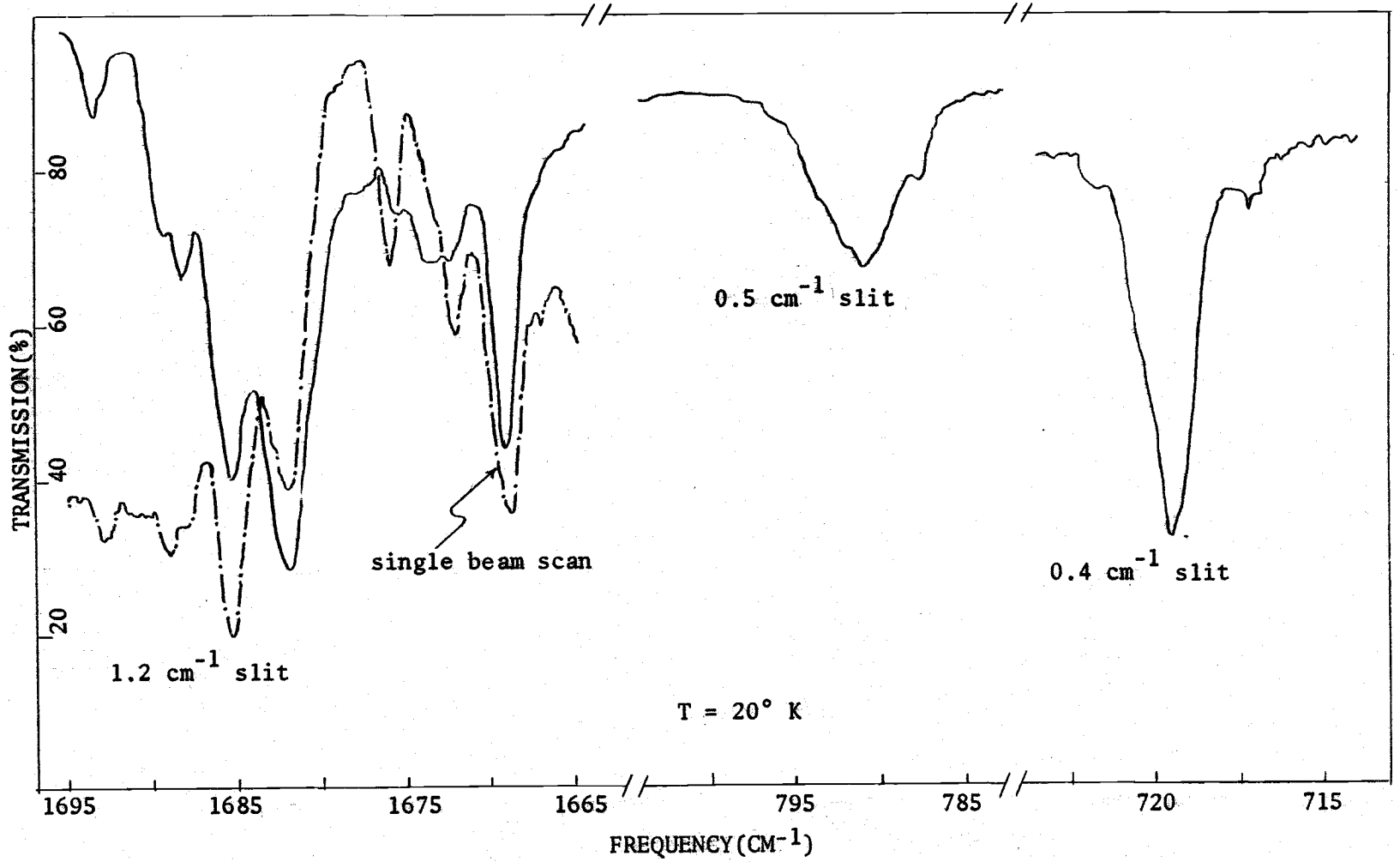

Figure 45. The infrared spectra of the fundamentals of PD_3 isolated in solid PH_3 which was purposely doped with 1% PD_3 and was mostly in the delta phase. The film was the same as the one used to obtain the upper solid trace of Figure 21.

will give rise to a totally symmetric vibration when they are correlated spearately to the factor group species. This means there should be two totally symmetric vibrations in the factor group, and two strong features for the gamma phase in the Raman experiments, instead of one strong and two weak bands. Moreover, one would also expect more structure for the bands of the mixed isotopic species due to the combined effects of distinct sites and orientation.

Although inversion doubling is unlikely for reasons to be stated later, it is a possibility. Also, the relative intensity of the doublet fits inversion doubling the best. Actually a PH_3 molecule does not have to follow the molecular Z-axis in order to reach the inverted position. Some kind of libration or combination of motions may also lead to an inversion of the molecule and thus result in a doubling of the band.

The ν_2 spectrum of PH_3 in inert gases seems to indicate that the symmetric bending motion of PH_3 is least perturbed in the Xe matrix and is perturbed to about the same extent in Kr and Ar matrices. This effect is in the same direction as the size variation of the various kinds of holes in these matrices. Among these matrices, Xe has the largest octahedral, tetrahedral, and substitutional holes, those of Kr are smaller, Ar even smaller. The most important result of the PH_3 in inert gas experiments is that there exists no splitting in the ν_2 region. This information helps exclude the idea of inversion from the interpretation of the structure-rich ν_2 of the delta phase.

In another run represented by the broken trace in Figure 27 the ν_2 doublet of the guest PH_3 merely merged into a singlet at 980.6 cm^{-1} (i.e. the center of gravity slightly shifted towards red), when the host PD_3 solid was converted from the gamma to the delta phase. (This host phase change was recognized by the merging of the two strong bands in the ν_2 region into a strong one.) The ν_4 doublet of the guest PH_3 also became a singlet under this host phase transition, but the center of gravity was roughly unmoved. These ν_2 and ν_4 spectra of PH_3 in the delta PD_3 resemble the equivalent one in Figure 45 and are, thus, not shown.

We concluded in the last section that only PHD_2 and PH_2D contributed to the dot-dashed trace in the stretching region in Figure 44. The solid trace overlapping this dot-dashed one contains almost as much PH_3 as PHD_2 and negligible amount of PH_2D as shown by the intensities of the bending vibrations in the survey scan (not presented in this thesis because of the scattering background) of a PH_3-in-PD_3 experiment. Thus, we are inclined to believe that the bands of this solid trace are due to the $\nu_3(A')$ (2314.3 cm^{-1}) of PHD_2 and ν_1 (2306 cm^{-1}) and ν_3 (2322 cm^{-1}) of PH_3. The band lowest in energy probably contains both the stronger band of the $\nu_3(A')$ doublet of PHD_2, and the ν_1 of PH_3 which must have shifted the compound band from the PHD_2 band slightly toward red. The band at 2321 cm^{-1} is most probably caused by the ν_3 of PH_3. The two bands at 2328.6 cm^{-1} and 2336.3 cm^{-1} may be or may not be due to PH_3. Including the last two weak bands, there will be one too many for the $\nu_3(E)$ of PH_3 sitting at the C_s site of PD_3 solid.

The 2319.1 cm^{-1} band of the solid trace was shifted down from the equivalent one of the dot-dashed trace probably by the ν_3 absorption of PH_3. The doublet at the middle of the solid trace undoubtedly has contribution from PH_3. It is not certain whether the contribution is from ν_1 or ν_3, and whether ν_1 is split or not.

The stretching region in Figure 45 is interfered with by water and PHD_2 but not by PH_2D (refer to the section on the survey scan of solid PH_3). The single beam scan reveals that the 1685 cm^{-1} band may be completely due to water, since water has a very strong absorption at 1685 cm^{-1}. Thus, disregarding the weak bands we assign the strong bands at 1669 cm^{-1} and 1681.8 cm^{-1} to be the ν_1 and ν_3 of PD_3. This assignment not only agrees, in frequency, with the Raman spectra of ν_1 and ν_3 of PD_3 in the supercooled beta phase of PH_3, but also agrees, in number of bands, with ν_2 and ν_4 in Figure 45. The $\nu_1(A')$ (1668.1 cm^{-1}) of PHD_2 is most probably embedded in the ν_1 of PD_3, while the $\nu_3(A'')$ (1675.4 cm^{-1}) may correspond to the weak broad band, to which the 1671.5 cm^{-1} water absorption also contributes, to the left of the ν_1 of PD_3. The weak band higher in energy must belong to water. The two weak bands at the high energy side of this region are most probably due to the sample and are difficult to identify.

That the ν_2 and ν_4 doublets of the guest PH_3 molecules merged into one band as the host structure changed from the gamma phase into the delta phase suggested two possibilities relating to the delta phase structure. The first possibility that the phase is disordered must be neglected, since SG showed the delta phase was

ordered. The second possibility is that the site occupied by the guest PH_3 molecules must be either C_3 or C_{3v}, whose symmetry is high enough such that the molecular E species will not be split and also the orientational effect (in relation with the spectra of PHD_2 and PH_2D in the δ phase of PD_3) cannot occur. A neater high-resolution scan in the stretching region of the guest species needs to be done in order to verify the site symmetry of the delta phase.

X. PHASE TRANSITIONS AND STRUCTURAL INTERPRETATION

Phase Transitions

When the first derivatives of the Gibbs function, $S=-\left(\frac{\partial G}{\partial T}\right)_p$ and $V=\left(\frac{\partial G}{\partial P}\right)_T$ undergo finite changes during a phase transition while G changes continuously through the transition point; then, this transition is called "first order." Since the transition occurs at constant temperature and pressure, $C_p = T\left(\frac{\partial S}{\partial T}\right)_p = \infty$ at the transition point where the two phases coexist. Thus the phase transitions of PH_3 at 185.38°K, 139.35°K, 88.10°K, 49.43°K, and 30.29°K are all first order transitions. Among these first order transitions, clearcut spectroscopic changes generally accompanied the ones at 30.29°K and 49.43°K. At these two transition points, the coexistence of the initial and final phases was clearly observed in the Raman experiments but not in the infrared experiments. No spectroscopic changes were observed at 139.35°K and 81.1°K.

If the second derivatives of the Gibbs function, $C_p = T\frac{\partial}{\partial T}\cdot\left(-\frac{\partial G}{\partial T}\right) = -T\cdot\frac{\partial^2 G}{\partial T^2}$, undergo change at a transition point, but G and $\frac{\partial G}{\partial T}$ changes continuously through the transition point, then the transition is called "second order." Thus, in a second order phase transition, the entropy and the volume are the same at the end of the process as they were in the beginning. Zemansky (42) stated that a lambda transition was slightly different from a second order transition.

Likewise, a third order phase transition is characterized by a

finite change in $\frac{\partial^3 G}{\partial T^3}$ at the transition point through which G, $\frac{\partial G}{\partial T}$, and $\frac{\partial^2 G}{\partial T^2}$ must be continuous. In the following, we quote the molar entropy change(ΔS) for each transition of a phosphine system from SG. Use will be made of the ΔS's later.

The molar entropy changes and temperatures of the phase transition follows:

phase transition		ΔS	T
gas-liquid		18.1 cal/deg.mole or eu	185.38°K
liquid-alpha		1.94 cal/deg. mole	139.35°K
alpha-beta		1.312 cal/deg. mole	88.1°K
beta-delta	lambda point	1.533	35.66°K
	first order	0.647 2.18 cal/deg. mole	30.29°K
beta-gamma		3.757 cal/deg. mole	49.43°K

The Gas-Liquid, Liquid-Alpha, and Alpha-Beta Transitions

The high molar entropy change associated with the gas-liquid phase transition is understandable. Gaseous molecules move very randomly and occupy a much larger volume than the liquid molecules do. Since $\Delta S = R \ln(V_g - V_\ell)$, the molar entropy change accompanying a gas-liquid phase transition must be large. Spectroscopically the rotational fine structure shows this change most vividly.

In liquids, molecules can orient themselves randomly, although they cannot rotate and translate as freely as the gaseous molecules do. The spectral bands become broad, as a result. When a system transforms into the solid state, the molecules arrange themselves in regular arrays. The broad structure will be split again,

not due to free rotation of the molecules but to the site symmetry of the molecules and the interaction among the molecules in a unit cell. As was shown in the previous survey scans, we observed neither the splitting in the alpha and the beta phases nor any spectral change accompanying the alpha-beta phase transition except a slight shift in the center of gravity of the intramolecular fundamentals. The broadening of the fundamentals in the alpha and the beta solids is believed to be due to the crystal disorder (hydrogen atoms distributing themselves among several equilibrium positions around fixed phosphorus atoms).

The molar entropy change for the alpha-beta transition is slightly smaller than that for the liquid-alpha transition, both being quite small compared with that for the liquid-gas transition. Even though the alpha and the beta phases are disordered, the crystal skeletons of these two phases are still ordered, whereas liquid molecules are completely disordered. Therefore, it is reasonable to say that the liquid-alpha transition is associated with more entropy change than the alpha-beta transition is.

It is also reasonable to assume that no skeletal change of the crystal is involved in the alpha-beta transition, since the transition between them has the smallest entropy change among all the phase transitions of a PH_3 system. The difference between these two structures is very likely in the equilibrium positions of the hydrogen atoms. The energy differences among the equilibrium positions of the alpha phase may differ from those of the beta phase. In other words, the hydrogen atoms have a greater tendency

to distribute themselves, or distribute faster in one phase than in the other. The beta phase may also differ from the alpha phase in the number of equilibrium positions of hydrogen atoms.

The Beta-Gamma Phase Transition

We noticed in chapter V that the increase in absorbance of one of the gamma bands was not compatible with the principle of the cooperative action (43) in the solid. Since the cooperative action is mainly responsible for the second-order phase transition, we reason that the beta-to-gamma transition, which we observed, is not of the second order.

The difficulty of this beta-to-gamma transition, compared with the easy beta-to-delta transition (see next section), suggests that crystal repacking might have been involved in this transition. Natta and Casazza (20) determined that the alpha phase of phosphine is a cubic system. It is possible and also likely that the beta phase is also in the cubic closest packing pattern which undergoes, in a very slow manner, some rearrangement and eventually turns into a rather different packing. This repacking needs a thermal energy, kT, which means excitation of some intermolecular motion in the solid might have occurred during this repacking process. The reason follows. Since $h\nu$ corresponds to kT, $\tilde{\nu} = T/1.439\ cm^{-1} \approx 30\ cm^{-1}$, the energy of this intermolecular motion. A motion whose excitation energy centers around 30 cm^{-1} must be a collective mode of the solid. (However, the only lattice mode of the beta phase

observed so far is the 70 cm^{-1} one recorded in the Raman experiment.) This is quite logical in the sense that any crystal rearrangement must be related to the interaction among molecules, particularly the translation and libration of molecules.

Another way of explaining the transition difficulty would be to say that this process has a larger activation energy. Since $k = A \exp(-E_a/RT)$, according to Arrhenius, the high activation energy will result in a small converting rate.

Unlike PH_3, the delta phase of solid PD_3 can be converted directly to the gamma phase. Nevertheless, the delta-to-gamma transition occurred in a much slower manner than the beta-to-gamma transition. Therefore, the former could be spectroscopically monitored more easily.

Generally, the beta and the delta phases of PD_3 were observed to be quite unstable with respect to the gamma phase. In other words, the activation energies for the beta-to-gamma and the delta-to-gamma transitions are much smaller than the corresponding ones of PH_3. However, one expects the opposite to be the case, since PD_3 has the larger mass. So the rate effect observed are apparently not explicable in terms of a potential function.

We mentioned in the section on the high resolution scan of PD_3 that the ν_2-band-center in the infrared was unshifted as the solids PH_3 and PD_3 underwent the beta-to-delta transition, but was shifted as the two solids underwent the beta-to-gamma transition. This implies that going from the ordered delta phase to the beta phase, the spectra merely broaden out, and the crystal becomes disordered

but the phosphorus atom remains unmoved. On the other hand, the gamma-to-beta transition changes the center of gravity in addition to the broadening. This indicates that this transformation not only turns hydrogen atoms loose, but also changes the positions of the phosphorus atoms. This argument is in line with the idea of crystal repacking associated with the beta-gamma but not the beta-delta transitions.

The beta-gamma transition involves an entropy change of 3.757 eu, almost twice as much as that for the beta-delta transition (2.18 eu) and more than twice that of the alpha-beta transition (1.312 eu). We have concluded previously that both the beta-delta and the beta-gamma transitions are disorder-order ones. It is reasonable to expect larger molar entropy change associated with the disorder-order transitions than with the disorder-disorder transitions. However, the difference in the molar entropy changes of these two disorder-order transitions must be explained. In the next section we will show that the entropy change involved in the beta-delta transition is mainly due to the removal of the hydrogen-disorder entropy (1.533 eu) of the beta phase. Here, we invoke not only the removal of the hydrogen-disorder entropy to account for 1.533 eu of the 3.757 eu of the beta-gamma transition, but also the idea of crystal repacking to account for the rest of the molar entropy change (2.224 eu), which is still relatively large compared with other phase changes.

The Delta-Beta Phase Transition

This transition consists of a first order followed by lambda point phase transition. Guggenheim (30) stated that many lambda points are associated with a sudden change to such an extent that the molecules in the crystal can rotate freely. SG also made the statement that the heat capacity curve between 25°K and 35°K is characteristic of molecular rotation in crystal. However, it appears to be difficult to show this molecular rotation spectroscopically (if it does exist), because neither HH and Francia nor ourselves observed any clues to this phenomenon.

We have noticed that SG's heat capacity curve at the lambda point (35.66°K for PH_3, not known for PD_3 yet) is connected by a dotted line. Whether the heat capacity at this point is a peak or a singularity is uncertain. Nevertheless, the specific heat anomaly is clearly there and indicates a cooperative phenomenon of the crystal.

A cooperative action occurring in the solid state is usually accompanied by the removal of configurational entropy from the crystal. Above the lambda point, the solid is rather disordered. This disorder can mean the long- and short-range randomness of the elements in alloys such as AuCu, $AuCu_3$, etc.; the misalignment of the dipoles in ferroelectric crystals such as Rochelle salt, ammonium dihydrogen phosphate, barium titanate, etc.; the hydrogen disorder of molecular crystals such as hydrogen bromide and hydrogen iodide, methane, etc.; and the different relative orientations

of the threefold degeneracy of the orthohydrogen ground rotational level with respect to the cubic field in solids. These kinds of disorder in crystals may or may not give rise to the lambda transition as the temperature is lowered. If they do, the extra entropy due to the high temperature disorder can be measured from the area between the lambda-shaped band and the smooth background (1.533 eu measured by SG for solid PH_3) and verified by a simple calculation as follows: If the molecules have the possibility of choosing among P configurations or orientations, the excess entropy is $\Delta S = R \ln P$. For PH_3, the excess entropy, ΔS, was measured by SG to be 1.533 eu. This is equivalent to $P = 2.13$. It would seem that the phosphine molecules in the beta phase have two possible orientations, in the crudest approximation. (The P for ice has been calculated by Pauling (44) in a more complicated way.) When the crystal is chilled down to the lambda point, a mutual cooperative action takes place within the crystal to eliminate this disorder. At the end of this process, the configurational entropy is said to have been removed. Thus, the crystal ought to be ordered below the lambda point. Since the delta phase was ordered, the first-order transition at 30.29°K must be an order-to-order transition. Thus a small entropy change is found.

The ground rotational state of a phosphine molecule is associated with 4 spin states (method of calculation was illustrated in reference 45). Depending on the site symmetry in the crystal, different orientations of these spin states have slightly different energies of interaction. Therefore, spin-orientational entropy

might also have been involved in this lambda transition.

Suppose the "two" orientations of the phosphine molecules in the beta phase are separated by an energy gap, Δ. In any solid, there is always an intermolecular potential barrier, δ, which restricts the molecular motion. If $\delta \ll \Delta$, the barrier is not high enough to prevent the transformation between these two states when the thermal energy of the molecules, kT, is larger than Δ. When the crystal is cooled down to $T \approx \Delta/k$, δ is still low but the thermal energy just barely suffices for the transformation. The molecules will start to assume the more stable state. The same principle results in the lambda transition of the solid phosphine. But if $\delta \gg \Delta$, the state-interchange is possible only when the thermal energy is higher than δ. When the crystal is chilled down to $T \approx \delta/k$, the population with the unstable orientation starts to be frozen-in, since the Δ is not sufficient to drive the molecules at the higher state across the barrier, while the rest of the population remains in the lower stable state. When this crystal is cooled down to zero degree Kelvin, the entropy will be nonzero, since the crystal still has two possible states. The famous examples are the solids, CO, NNO, H_2O, etc. Solid phosphine happens to be one of the examples of the $\delta \ll \Delta$ case.

It is now proper to introduce Guggenheim's concept (p 278-85, ref. 30) about a "second order" transition which he contrasted with a first order phase change via the following two figures:

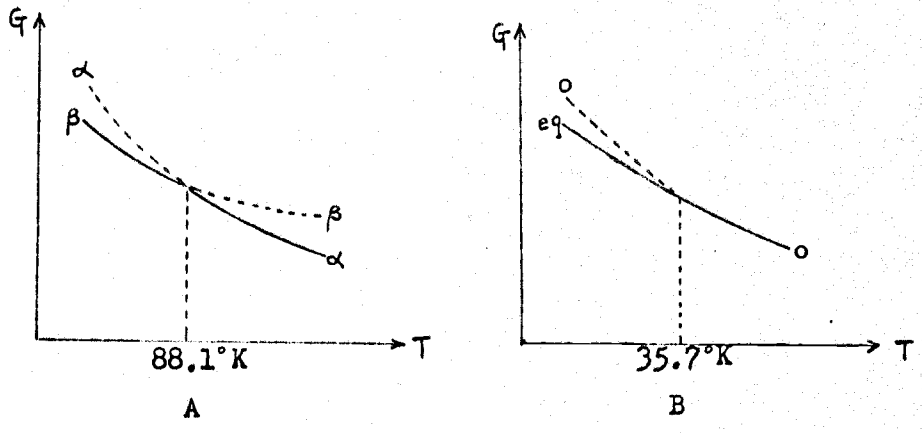

Figure 49. Contrast between the first order phase change (A) and the lambda point (B)

Diagram A shows a phase change between the alpha phase and the beta phase. A second-order transition, as shown in diagram B, is not defined to be a phase change. The broken curve o stands for the Gibbs function of a hypothetical phase with $\sigma = 0$, where σ is called the degree of order (p 163, ref. 43), $\sigma = 0$ is usually associated with complete randomness. The broken curve is metastable with respect to the solid curve labeled eq, since the former is higher in energy.

When a crystal is cooled below the lambda point reasonably slowly, the solid will be in the eq stable phase. The metastable phase can sometimes be realized by sudden chilling from a temperature above the lambda point. This sudden chilling is more likely in the Raman experiments in which a metal substrate and the Displex TM Cryogenic Refrigerator, which has a faster cooling than the Cryo-Tip used in most of the infrared experiments, were used.

Assuming this has actually happened in the experiments, we have correlated the solid o curve with the beta phase, the broken o curve with the supercooled beta phase (because it showed disorder) and the solid eq curve with the delta phase. The coexistence of the delta and the supercooled beta phases (traces E, I, and K of Figures 15 and 16) can be accounted for in the following way:

Right below the lambda point, some of the solid sample was in the stable phase and the rest of the sample in the metastable phase. The proportion of these two phases depends on the rate of chilling. It should also depend on the stability of the metastable phase with respect to the stable phase, because a certain amount of the former might already have transformed into the latter before the succeeding first-order transition took place. When the first-order transition was reached, the metastable phase remained unaffected; but the stable phase transformed into the delta phase with respect to which the metastable phase is relatively stable. Because the disordered structures persisted at 20°K, the supercooled beta phase (or the metastable phase) cannot be the one which underwent the transition at 30.29°K.

The Gamma Phase Structure Deduction

Under the framework that we have built up about the gamma phase so far, it is still impossible to propose a unique model for the structure of this phase. Nevertheless, we will try two hexagonal and one tetragonal examples on the assumption that the site is

of C_s symmetry, bearing in mind that the ν_2 spectrum of PH_3 in γ-PD_3 contradicts a single C_s site and two sites contradict the spectra of PH_2D and PHD_2 isolated in γ-PD_3.

A hexagonal structure must have a factor group possessing one of the following point-group symmetries: C_3, D_3, C_{3i}, C_{3v}, D_{3d}, C_{3h}, D_{3h}, C_6, D_6, C_{6v}, C_{6h}, and D_{6h}. The PH_3 molecules in this phase definitely reside at C_s site whose symmetry group must be the subgroup of not only the free-molecule-point group, but also the unit-cell-factor group. Therefore, C_3, D_3, C_{3i}, C_6, and D_6 which do not contain the C_s subgroup (46, 47) can be excluded from the list above. We further impose the factor group activity requirement on the remaining point groups, C_{3v}, D_{3d}, C_{3h}, D_{3h}, C_{6v}, C_{6h}, and D_{6h}.

It was observed before the ν_2 had one strong and at least two (maybe three) weak Raman bands, and two strong IR bands (maybe one weak IR band, in addition). Thus, we expect the correct factor group symmetry to give rise to one totally symmetric and at least two nontotally symmetric Raman active modes (we will try to eliminate the possibility of two distinct sites shortly), and at least two IR active modes in the ν_2 region. In the ν_4 region, it is desired to have either three or four infrared active and five Raman active vibrations. Likewise, we expect the same activity for the stretching regions.

Among the last possibilities of factor group symmetry, C_{3h} and C_{6h} are rejected because of the fact that they cannot account for the numbers of bands observed in all of the regions. C_{3v} and D_{3d}

have to be neglected, because they will give rise to one strong and one weak Raman band over the ν_2 and ν_1 regions and also because they will result in only three Raman bands (one weak and two strong) in the ν_3 and ν_4 regions. C_{6v} predicts that the infrared and the Raman bands should have two coincidences in the ν_1 and ν_2 regions, and three in the ν_3 and ν_4 regions. It is not too likely that there would be so many coincidences in these regions.

In view of the number of bands, the number of coincidences between the infrared and the Raman bands, and the Raman intensity pattern, D_{3h} and D_{6h} appear to be the most probable symmetries of the gamma phase. D_{3h} can have two kinds of C_s subgroups, one with σ_h element, the other with σ_v. The former will give rise to two coincidences in all the intramolecular fundamental regions. Therefore, D_{3h} with C_s (σ_h) is in the same class as C_{6v}. For the factor group, D_{3h}, with C_s (σ_v)site, the correlation is as follows:

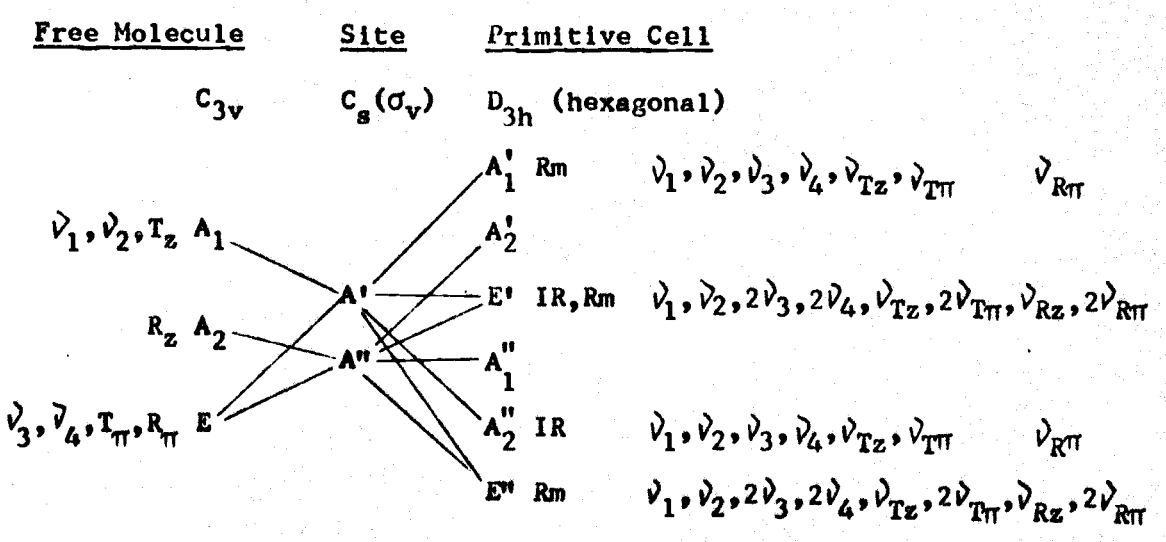

	ν_1	ν_2	ν_3	ν_4	ν_T	ν_L
IR & Rm	1	1	2	2	2	3
Rm	3	3	5	5	7	7
IR	2	2	3	3	3	4

For the factor group, D_{6h}, we can briefly correlate the molecular species to the unit cell active species in the following manner.

	$C_s(\sigma_h)$	$C_s(\sigma_v$ or $\sigma_d)$
$A_1 \longrightarrow$	$A_{1g} + 2E_{2g} + 2E_{1u}$	$A_{1g} + E_{1g} + E_{2g} + E_{1u} + A_{2u}$
$A_2 \longrightarrow$	$2E_{1g} + A_{2u}$	$E_{1g} + E_{2g} + E_{1u}$
$E \longrightarrow$	$A_{1g} + 2E_{2g} + 2E_{1u} + A_{2u} + 2E_{1g}$	$A_{1g} + 2E_{1g} + 2E_{2g} + 2E_{1u} + A_{2u}$

Subtracting three degrees of crystal-translational freedom from the IR active (mutual exclusion rule applies here) unit cell species and remembering the symmetries of fundamental molecular motions, we expect the following number of bands in each fundamental region for each of the three alternative sites

	ν_1	ν_2	ν_3	ν_4	ν_T	ν_L
Raman	3	3	5	5	8	7
IR	2	2	3	3	3	4

In the following, we first list the predictions of these two models, which seem to agree with our observation, and then we point out their disadvantages.

1. Both predict the same number of infrared and Raman active modes in the intramolecular regions, namely, 2 infrared-

and 3 Raman-active modes in the ν_1 and ν_2 region, and 3 infrared- and 5 Raman-active modes in the ν_3 and ν_4 regions. This prediction generally agrees with our observation except that ν_2 and ν_4 of both PH_3 and PD_3 seem to have one weak band or shoulder in excess.

2. In the Raman ν_1 and ν_2 region, there must be one strong and two weak bands. Agreement between theory and experiment is very good.

3. In the infrared ν_2 and ν_1 (particularly PD_3) the intensities of the two strong bands are not equal. This is not incompatible with the predictions of the model (except the D_{6h} with $C_s(\sigma_h)$ site) which say one of the two bands is nondegenerate, while the other is degenerate. Note that as a whole, the nondegenerate ν_1 and ν_2 bands of solid PH_3 and PD_3 in the infrared are observed to be weaker than the degenerate ν_3 and ν_4 bands.

4. In the intermolecular region, two strong translational modes and one strong librational mode were observed. This is particularly clear in the PH_3 spectrum. Thus, the 57.5 cm^{-1} and 64.3 cm^{-1} bands of PH_3, and the 54.0 cm^{-1} and 62.9 cm^{-1} of PD_3 can be assigned as the totally symmetric translational modes, while the 134.8 cm^{-1} band of PH_3 and 107.2 cm^{-1} band of PD_3 can be assigned as the totally symmetric librational mode. In connection with this assignment, we note that the intensity pattern in the lattice region of PD_3 is not in complete agreement with that of PH_3.

This is because the PD_3 sample contained more impurities (PHD_2 and PH_2D) than the PH_3 sample did. The presence of impurities in a perfect crystal could destroy the translational symmetry to some extent, and the translational symmetry is the basis of the crystal selection rule.

5. D_{3h} predicts exactly the same number of translational and librational modes in the lattice region as were observed. D_{6h} predicts only one translational mode in excess.

The basic disagreement between the D_{3h} and D_{6h} models is the number of molecules per primitive cell and the inversion property of the crystal. The number of molecules per primitive cell is obtained by dividing the order of the factor groups by the order of the site symmetry group. Thus D_{6h} predicts 12 molecules per primitive cell, while D_{3h}, 6. The latter is more likely. A crystal with D_{6h} symmetry must obey the mutual exclusion rule. But there seems to have Raman-IR coincidences in each fundamental region. D_{3h} predicts one coincidence between the infrared and Raman bands in the ν_1 and ν_2 region, and two coincidences in the ν_3 and ν_4 region. We observed one coincidence in the ν_2 of γ-PH_3 (the equivalent coincidence in γ-PD_3 is uncertain). At least one IR frequency in ν_1 of γ-PH_3 and γ-PD_3 coincides with the Raman one in a different manner from that in ν_2. It was also observed that there may be two or three coincidences in ν_4 and ν_3. All these are in favor of the D_{3h} model. On the other hand, one may argue that the above-mentioned coincidences may not be real because of our Raman sampling technique.

Thus, the D_{6h} model is no less likely than the D_{3h} model.

Another possible structure for the γ phase is the tetragonal D_{4h} with single $C_s(\sigma_v$ or $\sigma_d)$ site, if one believes that the Raman-IR coincidences are not real. We show the simplified correlation and number of components in each fundamental region for C_s (σ_v) site ($C_s(\sigma_d)$ site will lead to essentially the same correlation) as follows.

$$A_1 \longrightarrow A_{1g} + B_{1g} + E_g + A_{2u} + E_u$$

$$A_2 \longrightarrow B_{2g} + E_g + E_u$$

$$E \longrightarrow A_{1g} + B_{1g} + 2E_g + A_{2u} + 2E_u + B_{2g}$$

	ν_1	ν_2	ν_3	ν_4	ν_T	ν_L
Raman	3	3	4	4	8	7
IR	2	2	3	3	3	4

The critical points which make this model a potential alternative are the predictions of one-strong-and-two-weak Raman bands and two unequal intensity IR bands in ν_1 and ν_2, and two totally symmetric ν_T but one totally symmetric ν_L in the Raman region. Moreover, except the ν_3 and ν_4 regions, it predicts the same number of components as the D_{6h} model does.

From refs. 46 and 47, the space groups which belong to the D_{3h} and D_{6h} factor groups with single C_s site are D_{3h}^2, D_{3h}^4, and D_{6h}^2. For the tetragonal D_{4h}, the possible space groups are numerous. We point out that all of the three models predict only one totally

symmetric mode in the ν_3 and ν_4 regions. It seems difficult to identify this mode in the ν_3 and ν_4 spectra.

We have pointed out that the ν_2 doublet of PH_3 in γ-PD_3 could be due to two distinct sites in the unit cell. If this is true, then each of these two distinct sites should give rise to a doublet of 2:1 intensity for the isolated PH_2D and PHD_2 due to the orientation effect. A total of 4 bands should have been observed for each mode of the latter species isolated in the γ-host. That this is not actually the case implies a contradication. However, the spectra of PH_3, PH_2D, and PHD_2 in the γ-host might indicate rotational tunnelling which would yield a doublet of equal intensity for PH_3 and a doublet of 2:1 intensity for PH_2D and PHD_2 (Professor J. C. Decius, private communication). The implication of rotational tunnelling in the pure crystal have not yet been worked out.

Interpretation of the ν_2 Spectrum of the Delta Phase

Inversion is Unlikely

The interpretation of the nondegenerate ν_2 spectra of the delta phase of both PH_3 and PD_3 is rather difficult, because they contain at least ten fine bands in the infrared, and one very strong and maybe nine very weak bands in the Raman, while the degenerate ν_4 spectrum shows an essential lack of any fine structure except for the high noise level at the band plateau in both the infrared and Raman. HH invoked the idea of inversion doubling to split each of the ν_2 bands in two and thus only need to account for half of the many bands in the ν_2 region. Their reasons follow: They

calculated the decrease in force constants for all the internal modes as gaseous phosphine was cooled down to "4°K," using their solid frequencies. This decrease in force constants suggests that the crystal field perturbation must have relaxed the barrier of inversion; and, since the ν_2 motion was in the direction of lowering the barrier, the doubling is likely to occur.

For the following reasons, we believe that inversion doubling is not likely to occur in solid PH_3 and PD_3.

1. For pyramidal C_{3v} molecules of the form, XY_3, XH_3 has a much larger inversion splitting than XD_3, because the states of the XD_3 are closer to the minima in the same potential function and also because XD_3 has smaller tunneling capability due to the larger reduced mass. For the same reasons, the inversion splitting of XY_3 with heavier X atom is much smaller than that with lighter X atom. We supply the following splittings ($\Delta\tilde{\nu}$) in various states (v) to substantiate this idea.

Molecules	$\Delta\tilde{\nu}(cm^{-1})$			
	$v = 0$	$v = 1$	$v = 2$	barrier
NH_3	0.8*	36.6*	313	2077*
ND_3	0	2.4	70	
PH_3	4.76×10^{-4}*	2.38×10^{-4}*		6085*
AsH_3	3.7×10^{-18}*	6×10^{-16}*		11220*

* Obtained from reference 48.
ND_3 datum is taken from reference 49.

According to Nielson and McConaghie's work (50), gaseous PH_3 did not show inversion doubling. Solid NH_3 did not show inversion doubling either. Thus, PH_3 molecules in the solid state may not invert. If the delta phase is associated with inversion, the spacing between the components of the ν_2 spectrum of PH_3 should be much greater than that for PD_3. The bands in the ν_2 region were observed to be separated by about 1.6 cm^{-1} in the delta phase of PH_3, while in PD_3 they were separated by about 1.0 cm^{-1}. This decrease in the spacing, going from the delta phase of PH_3 to that of PD_3, is not great enough to be caused by inversion.

2. If the barrier were lowered by the crystal field perturbation, for a given ν_2 vibration in the unit cell, its

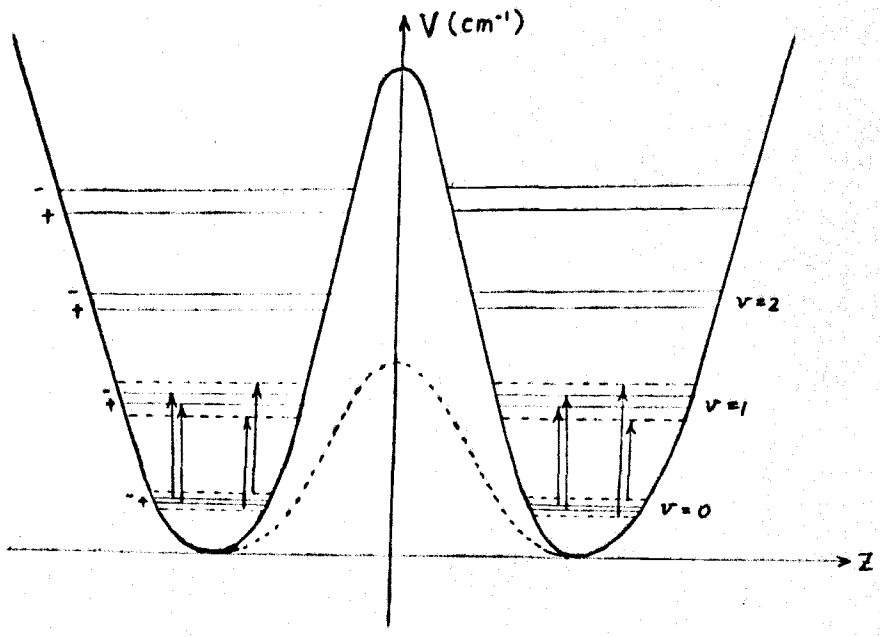

Figure 46. The potential function of an inversion doubling system

states (horizontally dotted lines in Figure 46) with quantum numbers v = 0 and v = 1 would have been split more than the unperturbed states (horizontal solid lines), because the perturbed states are closer to the barrier top. The two arrows on the left in the right-hand potential well in Figure 46 show the infrared transitions (antisymmetric state to symmetric state and vice versa) which occur in a gaseous PH_3 molecule (the splittings of the v = 0 and 1 states are exaggerated), and two arrows on the right show the infrared transitions of the perturbed states in the delta phase. One of the delta phase frequencies would have been higher and the other lower than the gas phase frequency, if the crystal field perturbation were working. The ν_2 of the delta phase of PH_3 occurred at 22 cm^{-1} below its gas phase value, and for PD_3, 11 cm^{-1} below. None of the ν_2 frequencies is larger than the gas phase value.

3. If the ν_2 fine structure was really involved in inversion doubling, the spacing between the Raman bands would have had to be smaller than the infrared spacing, and the Raman inversion doublet would have had to be between the corresponding one in the infrared spectrum. This will be clear when one compares the distances of the transition arrows (from symmetric state to symmetric state and antisymmetric to antisymmetric) in the left-hand well in Figure 46 with the corresponding ones in the right-hand

well. From the Raman frequencies of the ν_2 of the delta phase given in Table 2, it is found that the spacing is not smaller and no two neighboring frequencies are sandwiched between two neighboring infrared frequencies.

Finally, we point out that ν_2 exhibits no sign of inversion in the spectra of PH_3 in Ar, Kr, and Xe.

Hindered Rotation

The appearance of the ν_2 Raman spectra looks rather like a strong Q band with very weak R bands and missing P bands of a gaseous system. Moreover, there appears to be a regular spacing between two neighboring bands; this spacing is about 1.6 cm^{-1} in PH_3 and about 1 cm^{-1} in PD_3. In a gaseous system, the spacing of the rotational fine structure in a vibrational band is approximately 2B, where B is the rotational constant. The ratio of rotational spacing of PH_3 to PD_3 is found to be about 2. This ratio roughly agrees with what was observed. These findings prompted a relative vibration-rotational-line intensity calculation for a hypothetical phosphine gas at 20°K and at 4°K.

The result of the calculation performed by using the computer program written by Prof. J. W. Nibler (based on the line strength expression given in page 110, ref. 48) are shown in the next two pages.

In this calculation, it was assumed that the rotor is rigid, and that there is no interaction between vibration and rotation and no difference between the rotational constants in the upper and

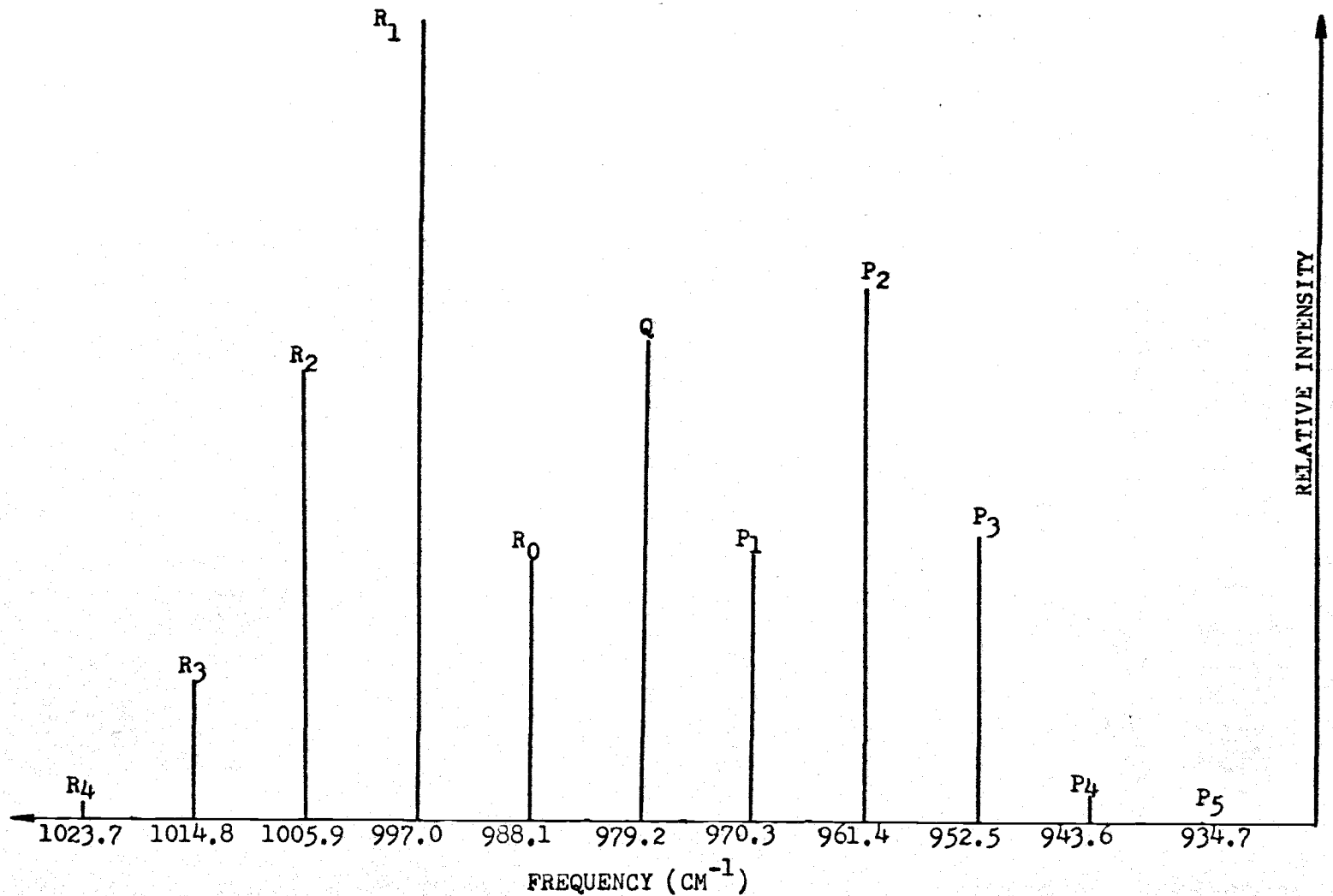

Figure 47. Relative rotational line intensity in the infrared ν_2 region of a hypothetical PH_3 gas at 20°K

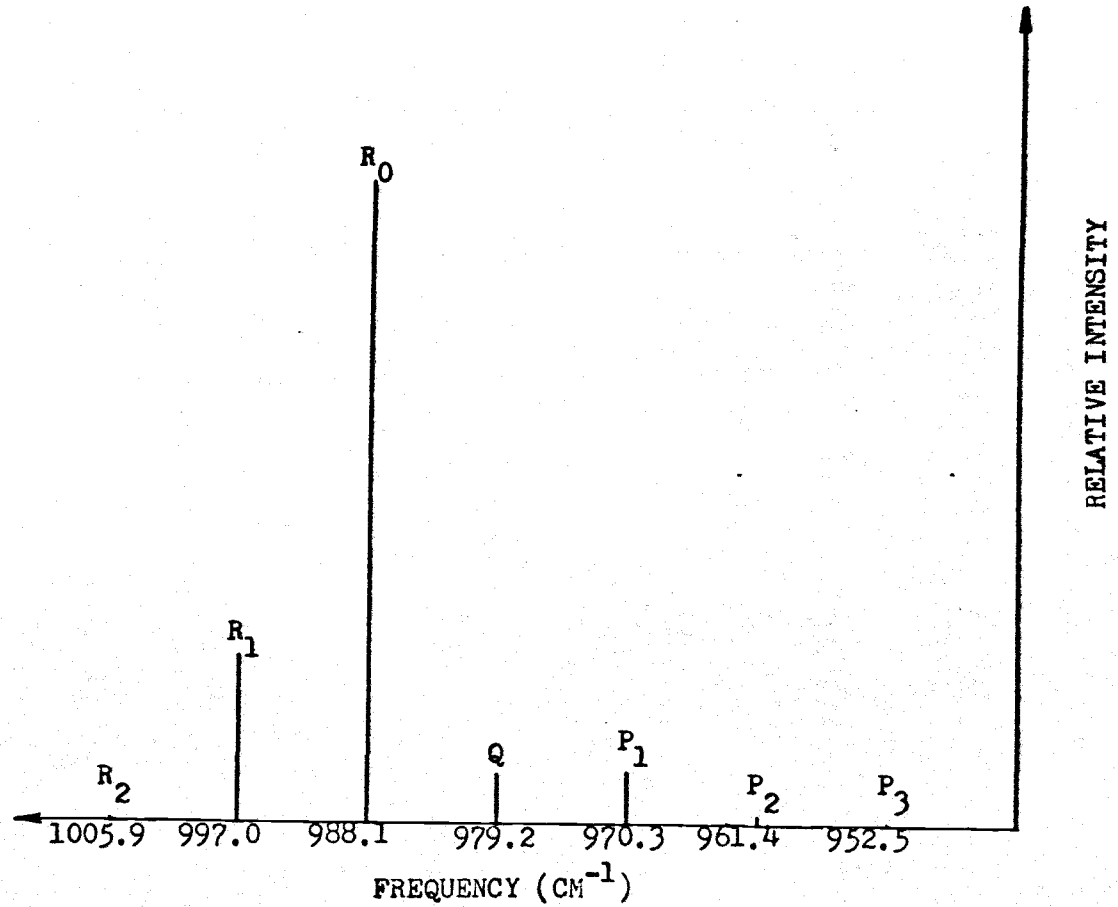

Figure 48. Relative rotational line intensity in the infrared ν_2 region of a hypothetical PH_3 gas at 4°K

lower vibrational states. This is why the rotational lines in the next two figures are equally spaced. It is noticed that the intensity pattern of the 20°K PH_3 gas bears slight resemblance to that shown in Figure 29. A more practical comparison between these two patterns can be realized by adjusting the spacing in the hypothetical model to fit the actual one. Although, we do not believe the idea of free rotation, this slight analogy in intensity pattern at least suggests that the multiplet structure is related to some motion similar to rotation — restricted rotation. If the multiplet structure were due to free rotation at all, our 4°K experiment should have given rise to a drastically different spectrum as indicated by Figure 48, instead of merely the very tiny differences which we pointed out in the section on the high resolution spectra of solid PH_3. The restricted rotation may not be in contradiction with the 4°K experiment. If the initial states of the transitions in this restricted rotational model are quite close, then the temperature effect will not have marked influence on the relative population change. A slight temperature effect on two pairs of the bands in the ν_2 region was observed. In order for this restricted rotation to appear in the ν_2 region, some coupling must exist between the restricted rotation and vibration. It may be that the ν_2 vibration of a molecule interacts with the restricted rotation of its neighbor in the same primitive cell.

Many molecules per primitive cell

After the completion of this work, Francia's infrared studies on solid phosphine at low temperature became available. Her work, under higher resolution, showed a structure-rich stretching spectrum of delta-PD_3 and delta-PH_3 (particularly). Our stretching spectrum of delta-PD_3 (the broken IR trace, Fig. 38) resembles closely her corresponding one, although our delta-PH_3 film was too thick to resolve fine structure. From the stretching and the ν_2 spectra, it is possible and likely that the delta-phase is consisted of many molecules per unit cell.

APPENDIX I

FREQUENCY CALCULATION OF PH_2D and PHD_2 ISOLATED IN SOLID PH_3 AND PD_3

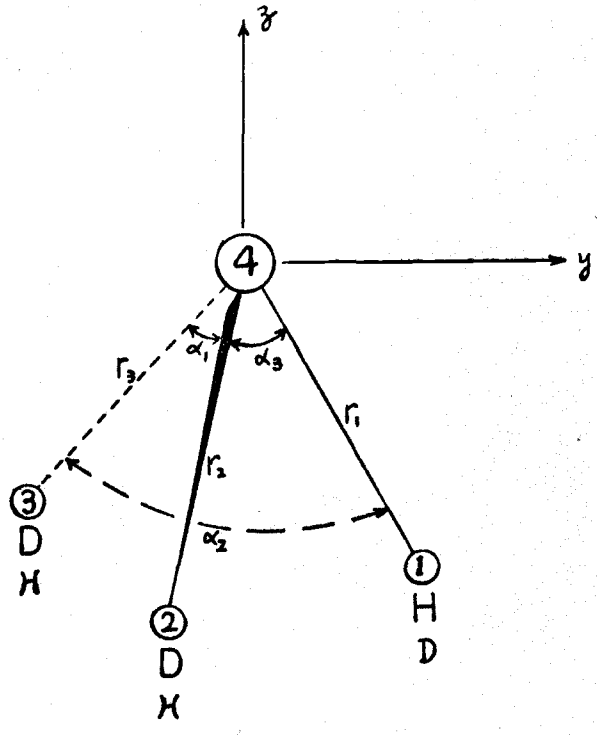

The Cartesian coordinates in the figure above is the moving frame of reference. For PH_3, r_i = 1.42 Å and α_i = 93° 50'. In this appendix, the symbol, δ, is always used to mean the infinitesimal change of the quantity which follows this symbol. Atom 2 is pointing up from the paper (zy) plane, atom 3 down from the zy plane. The Cartesian coordinates of the 4 atoms, which were used in the computer calculation, are

atom #	x	y	z
4	0	0	0
1	0	1.197553	-0.763064
2	1.037111	-0.598776	-0.763064
3	-1.037111	-0.598776	-0.763064

The unsymmetrized G matrix of PH_3 and PD_3 take the following form:

$$
\begin{array}{c|cccccc}
 & \delta r_1 & \delta r_2 & \delta r_3 & \delta\alpha_1 & \delta\alpha_2 & \delta\alpha_3 \\
\hline
\delta r_1 & G_r & G_r' & G_r' & G_{r\alpha}' & G_{r\alpha} & G_{r\alpha} \\
\delta r_2 & & G_r & G_r' & & G_{r\alpha}' & G_{r\alpha} \\
\delta r_3 & & & G_r & & & G_{r\alpha}' \\
\hline
\delta\alpha_1 & & & & G_\alpha & G_\alpha' & G_\alpha' \\
\delta\alpha_2 & & & & & G_\alpha & G_\alpha' \\
\delta\alpha_3 & & & & & & G_\alpha
\end{array}
$$

, where the blocks and the whole matrix are symmetric.

Similarly, the unsymmetrized G matrix of the intermediate species PH_2D and PHD_2 is

$$
\begin{array}{cccccc}
G_{r_1} & G_r' & G_r' & G_{r\alpha}' & G_{r\alpha} & G_{r\alpha} \\
 & G_r & G_r' & & G_{r\alpha}' & G_{r\alpha} \\
 & & G_r & & & G_{r\alpha}' \\
\hline
 & & & G_\alpha & G_\alpha' & G_\alpha' \\
 & & & & G_{\alpha_1} & G_{\alpha_1}' \\
 & & & & & G_{\alpha_1}
\end{array}
$$

, where the blocks and the whole matrix are symmetric.

The unsymmetrized F matrix of all the four molecules is of the same form as the unsymmetrized G matrix of PH_3 and PD_3 within the harmonic

approximation. In terms of molecular parameters and atomic masses, the G matrix of the four molecules can be generally written as the one shown in next page. In order to make the units of the terms in the potential energy expansion the same, some of the force constants have to be multiplied by r, and some by r^2. These r and r^2 will cancel the r^{-1} and r^{-2} factors in the G matrix, when the G and F matrices are multiplied together. It is preferred to leave the r^{-1} and r^{-2} factors out now, so that the force constants do not have to be multiplied by r or r^2 later. This is why the factors, r^{-1} and r^{-2}, are missing from the elements of the unsymmetrized G matrix next page.

The parameters to be substituted into the elements of the matrix in the next page are

$$\sin \alpha = \sin 93°50' = 0.99776$$

$$\cos \alpha = \cos 93°50' = -0.06685$$

$$\mu_H = 0.992236; \quad m_H = 1.007825$$

$$\mu_P = 0.03228534; \quad m_P = 30.973803$$

$$\mu_D = 0.496500; \quad m_D = 2.014097$$

In the same matrix, H_1 represents the deuterium atom, and H_2 and H_3 the hydrogen atoms in the case of PH_2D. Similarly, H_1 represents the hydrogen agom, and H_2 and H_3 the deuterium atoms in the case of PHD_2.

Replacing the numerical values into this general G matrix, the following four G matrices were obtained. After these four matrices, the ones calculated by computer are supplied. Note that Schachtschneider's program did not omit the factors, r^{-1} and r^{-2}.

$\mu_p+\mu_{H_1}$ $\mu_p\cos\alpha$ $\mu_p\cos\alpha$ $-\mu_p\frac{\sin 2\alpha}{1+\cos\alpha}$ $-\mu_p\sin\alpha$ $-\mu_p\sin\alpha$

$\mu_p+\mu_{H_2}$ $\mu_p\cos\alpha$ $-\mu_p\frac{\sin 2\alpha}{1+\cos\alpha}$ $-\mu_p\sin\alpha$

$\mu_p+\mu_{H_3}$ $-\mu_p\frac{\sin 2\alpha}{1+\cos\alpha}$

$\mu_{H_2}+\mu_{H_3}+2(1-\cos\alpha)\mu_p$ $\mu_{H_3}\frac{\cos\alpha}{1+\cos\alpha}+\mu_p\frac{(3\cos\alpha+1)(1-\cos\alpha)}{1+\cos\alpha}$ $\mu_{H_2}\frac{\cos\alpha}{1+\cos\alpha}+\mu_p\frac{(3\cos\alpha+1)(1-\cos\alpha)}{1+\cos\alpha}$

$\mu_{H_1}+\mu_{H_3}+2(1-\cos\alpha)\mu_p$ $\mu_{H_1}\frac{\cos\alpha}{1+\cos\alpha}+\mu_p\frac{(3\cos\alpha+1)(1-\cos\alpha)}{1+\cos\alpha}$

$\mu_{H_1}+\mu_{H_2}+2(1-\cos\alpha)\mu_p$

$G_{PH_3}^{-}$

$$\begin{bmatrix} 1.024521 & -0.002158 & -0.002158 & 0.0046154 & -0.032213 & -0.032213 \\ & 1.024521 & -0.002158 & & 0.0046154 & -0.032213 \\ & & 1.024521 & & & 0.0046154 \\ & & & 2.053359 & -0.0415743 & -0.0415743 \\ & & & & 2.053359 & -0.0415743 \\ & & & & & 2.053359 \end{bmatrix}$$

$G_{PD_3}^{-}$

$$\begin{bmatrix} 0.528785 & -0.002158 & -0.002158 & 0.0046154 & -0.032213 & -0.032213 \\ & 0.528785 & -0.002158 & & 0.0046154 & -0.032213 \\ & & 0.528785 & & & 0.0046154 \\ & & & 1.061887 & -0.0060602 & -0.0060602 \\ & & & & 1.061887 & -0.0060602 \\ & & & & & 1.061887 \end{bmatrix}$$

$G_{PH_2D}^{-}$

$$\begin{bmatrix} 0.528785 & -0.002158 & -0.002158 & 0.0046154 & -0.032213 & -0.032213 \\ & 1.024521 & -0.002158 & & 0.0046154 & -0.032213 \\ & & 1.024521 & & & 0.0046154 \\ & & & 2.053359 & -0.0415743 & -0.0415743 \\ & & & & 1.5576232 & -0.0060602 \\ & & & & & 1.5576232 \end{bmatrix}$$

$G_{PHD_2}^{-}$

$$\begin{bmatrix} 1.024521 & -0.002158 & -0.002158 & 0.0046154 & -0.032213 & -0.032213 \\ & 0.528785 & -0.002158 & & 0.0046154 & -0.032213 \\ & & 0.528785 & & & 0.0046154 \\ & & & 1.061887 & -0.0060602 & -0.0060602 \\ & & & & 1.5576232 & -0.0415743 \\ & & & & & 1.5576232 \end{bmatrix}$$

$G_{PH_3}^{-}$

$$\begin{bmatrix} 1.024521 & -0.002158 & -0.002158 & 0.003250 & -0.022685 & -0.022685 \\ & 1.024521 & -0.002158 & & 0.003250 & -0.022685 \\ & & 1.024521 & & & 0.003250 \\ & & & 1.018330 & -0.020619 & -0.020619 \\ & & & & 1.018330 & -0.020619 \\ & & & & & 1.018330 \end{bmatrix}$$

$G_{PD_3}^{-}$

$$\begin{bmatrix} 0.528786 & -0.002158 & -0.002158 & 0.003250 & -0.022685 & -0.022685 \\ & 0.528786 & -0.002158 & & 0.003250 & -0.022685 \\ & & 0.528786 & & & 0.003250 \\ & & & 0.526626 & -0.003006 & -0.003006 \\ & & & & 0.526626 & -0.003006 \\ & & & & & 0.526626 \end{bmatrix}$$

$G_{PH_2D}^{-}$

$$\begin{bmatrix} 0.528786 & -0.002158 & -0.002158 & 0.003250 & -0.022685 & -0.022685 \\ & 1.024521 & -0.002158 & & 0.003250 & -0.022685 \\ & & 1.024521 & & & 0.003250 \\ & & & 1.018330 & -0.020619 & -0.020619 \\ & & & & 0.772478 & -0.003006 \\ & & & & & 0.772478 \end{bmatrix}$$

$$G_{PHD_2} = \begin{pmatrix} 1.024521 & -0.002158 & -0.002158 & 0.003250 & -0.022685 & -0.022685 \\ & 0.528786 & -0.002158 & & 0.003250 & -0.022685 \\ & & 0.528786 & & & 0.003250 \\ & & & 0.526626 & -0.003006 & -0.003006 \\ & & & & 0.772478 & -0.020619 \\ & & & & & 0.772478 \end{pmatrix}$$

To symmetrize the F and G matrices, use is made of the famous Wigner crank (or the projection operator)

$$S^{(\Upsilon)} = \text{const.} \sum_R \chi_R^{(\Upsilon)*} R \, \Delta i$$

where Υ refers to all of the representations in the molecular point group.

Δi refers to the internal coordinate, i, in a symmetrically equivalent set (p 85, ref. 22) e.g. $\delta\alpha_1$, $\delta\alpha_2$, $\delta\alpha_3$ is a set, and δr_1, δr_2, δr_3 is also a set.

R is the symmetry element in the molecular point group.

$\chi_R^{(\Upsilon)}$ is the character corresponding to a given representation, Υ, and symmetry element, R.

The summation is over all elements in the molecular point group. For example,

C_{3v}	E	$2C_3$	$3\sigma_v$
A_1	1	1	1
A_2	1	1	-1
E	2	-1	0

C_s	E	σ_v
A'	1	1
A"	1	-1

Note that σ_v is the paper plane in the figure, page 192

Under C_{3v} (refer to page 192 for internal coordinates,)

$$S_1^{(E)}(\delta r_1) = \text{const.}\,[2E\delta r_1 + (-1)\,C_3\delta r_1 + (-1)\,C_3^2\delta r_1 + 0\,3\sigma_v\delta r_1]$$

$$\hat{S}_1^{(E)}(\delta r_1) = \frac{1}{\sqrt{6}}\,(2\delta r_1 - \delta r_2 - \delta r_3).$$

Likewise, one has

$$\hat{S}_2^{(E)}(\delta r_2) = \frac{1}{\sqrt{6}}\,(-\delta r_1 + 2\delta r_2 - \delta r_3)$$

$$\hat{S}_3^{(E)}(\delta r_3) = \frac{1}{\sqrt{6}}\,(-\delta r_1 - \delta r_2 + 2\delta r_3)$$

These three S vectors belong to a vector space whose basis vectors are the symmetrized coordinates (transform as the E species) which we are looking for, and which can be obtained by the row-echelon technique as follows:

$$\begin{bmatrix} 2 & -1 & -1 \\ -1 & 2 & -1 \\ -1 & -1 & 2 \end{bmatrix} \sim \begin{bmatrix} 2 & -1 & -1 \\ -1 & 2 & -1 \\ 0 & 3 & -3 \end{bmatrix} \sim \begin{bmatrix} 2 & -1 & -1 \\ 0 & 3 & -3 \\ 0 & 3 & -3 \end{bmatrix} \sim \begin{bmatrix} 2 & -1 & -1 \\ 0 & 1 & -1 \\ 0 & 0 & 0 \end{bmatrix}.$$

Thus, this E-vector space is spanned by the following two linearly independent vectors.

$$\vec{S}_1^{(E)}(\delta r) = 2\delta r_1 - \delta r_2 - \delta r_3$$

$$\vec{S}^{(E)}(\delta r) = \qquad \delta r_2 - \delta r_3$$

$\vec{S}^{(E)}(\delta r)$ can also be obtained by the famous Gram-Schmidt orthogonalization process.

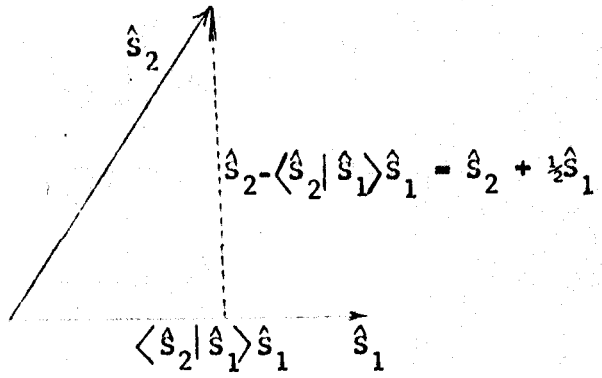

where $|\hat{S}_1| = \langle\hat{S}_1|\hat{S}_1\rangle = 1$

Therefore, the new vector perpendicular to the $\hat{S}_1$ is

$$\vec{S}^{(E)}(\delta r) = \frac{1}{\sqrt{6}}(-\delta r_1+2\delta r_2-\delta r_3) + \frac{1}{\sqrt{6}}\frac{1}{2}(2\delta r_1-\delta r_2-\delta r_3)$$

$$= \frac{3}{2\sqrt{6}}\delta r_2-\frac{3}{2\sqrt{6}}\delta r_3$$

$$\hat{S}^{(E)}(\delta r) = \frac{1}{\sqrt{2}}(\delta r_2-\delta r_3).$$

Totally, the following symmetrized coordinates are obtained.

ν_1 ····· $\hat{S}_r(A_1)=\frac{1}{\sqrt{3}}(\delta r_1+\delta r_2+\delta r_3)$ $\quad$ $\nu_1(A')$ ····· $\hat{S}_r(A')=\delta r_1$

ν_2 ····· $\hat{S}_\alpha(A_1)=\frac{1}{\sqrt{3}}(\delta\alpha_1+\delta\alpha_2+\delta\alpha_3)$ $\quad$ $\nu_2(A')$ ····· $\hat{S}_\alpha(A')=\delta\alpha_1$

ν_3 ····· $\hat{S}_r(E) = \frac{1}{\sqrt{6}}(2\delta r_1-\delta r_2-\delta r_3)$ $\quad$ $\nu_3(A')$ ····· $\hat{S}_{r_k}(A')=\frac{1}{\sqrt{2}}(\delta r_2+\delta r_3)$

$\hat{S}'_r(E) = \frac{1}{\sqrt{2}}(\delta r_2-\delta r_3)$ $\quad$ $\nu_3(A'')$ ····· $\hat{S}_{r_k}(A'')=\frac{1}{\sqrt{2}}(\delta r_2-\delta r_3)$

ν_4 ····· $\hat{S}_\alpha(E) = \frac{1}{\sqrt{6}}(2\delta\alpha_1-\delta\alpha_2-\delta\alpha_3)$ $\quad$ $\nu_4(A')$ ····· $\hat{S}_{\alpha_k}(A')=\frac{1}{\sqrt{2}}(\delta\alpha_2+\delta\alpha_3)$

$\hat{S}'_\alpha(E) = \frac{1}{\sqrt{2}}(\delta\alpha_2-\delta\alpha_3)$ $\quad$ $\nu_4(A'')$ ····· $\hat{S}_{\alpha_k}(A'')=\frac{1}{\sqrt{2}}(\delta\alpha_2-\delta\alpha_3)$

where k may be 2 or 3.

Note that the basis vectors of a vector space, such as the space spanned by the unit vectors, $\hat{S}_r(A')$ and $\hat{S}_{r_k}(A')$, is not unique. Thus, this $S_r(A')$ space can be alternatively spanned by

$$\hat{S}'_r(A') = \frac{1}{\sqrt{3}} (\delta r_1 + \delta r_2 + \delta r_3)$$

and $\hat{S}'_{r_k}(A') = \frac{1}{\sqrt{6}} (2\delta r_1 - \delta r_2 - \delta r_3)$.

Now that the coordinates are symmetrized, the F and G matrices also have to be symmetrized. Let the linear transformation, which take Δ_j into S_i, be U, then

$$\vec{S} = U\vec{\Delta} \quad \text{or} \quad S_i = \sum_j U_{ij}\Delta_j.$$

This equation can be written as

$$\begin{pmatrix} S_r(A_1) \\ S_\alpha(A_1) \\ S_r(E) \\ S'_r(E) \\ S_\alpha(E) \\ S'_\alpha(E) \end{pmatrix} = \begin{pmatrix} \frac{1}{\sqrt{3}} & \frac{1}{\sqrt{3}} & \frac{1}{\sqrt{3}} & 0 & 0 & 0 \\ 0 & 0 & 0 & \frac{1}{\sqrt{3}} & \frac{1}{\sqrt{3}} & \frac{1}{\sqrt{3}} \\ \frac{2}{\sqrt{6}} & -\frac{1}{\sqrt{6}} & -\frac{1}{\sqrt{6}} & 0 & 0 & 0 \\ 0 & 0 & 0 & \frac{2}{\sqrt{6}} & -\frac{1}{\sqrt{6}} & -\frac{1}{\sqrt{6}} \\ 0 & \frac{1}{\sqrt{2}} & -\frac{1}{\sqrt{2}} & 0 & 0 & 0 \\ 0 & 0 & 0 & 0 & \frac{1}{\sqrt{2}} & -\frac{1}{\sqrt{2}} \end{pmatrix} \begin{pmatrix} \delta r_1 \\ \delta r_2 \\ \delta r_3 \\ \delta\alpha_1 \\ \delta\alpha_2 \\ \delta\alpha_3 \end{pmatrix}$$

where the U has been normalized. $U^+U = U^*U = 1$, since U is a coordinate transformation. This U will remain the same for the species PH_2D and PHD_2, if the alternative bases vectors for the $S_r(A')$ and $S_\alpha(A')$ spaces are used.

In the chapter on the spectra of the isolated species, the following equation has been used.

$2V = \vec{\Delta}^+ F \vec{\Delta}$, which can be transformed into

$$2V = (U^{-1}\vec{S})^+ F(U^{-1}\vec{S})$$
$$= S^+ (U^{-1})^+ FU^{-1}S$$

$$= S^{+}\,(UFU^{+})S$$

$$= S^{+}\underline{F}S$$

where $\underline{F}$ is the symmetrized F matrix, which can be written as

$$\underline{F} = UFU^{+}$$

$$U^{-1}\underline{F} = FU^{+}$$

$$\sum_j U^{+}_{ij}\ \underline{F}_{jk} = \sum_m F_{im}\ U^{+}_{mk}$$

$$\sum_j U_{ji}\ \underline{F}_{jk} = \sum_m F_{im}\ U_{km}$$

Since species of different symmetries do not interact, the $\underline{F}_{jk}$ with $j \neq k$ must vanish. So, we have simply

$$U_{ki}\ \underline{F}_{kk} = \sum_m F_{im}\ U_{km}$$

or $$\underline{F}_{kk} = \frac{1}{U_{ki}} \sum_j F_{ij}\ U_{kj}$$

The last equation is called "Lipmann short cut." A similar equation can be obtained for the symmetrized $\underline{G}$ matrix elements. As an example, the $\underline{F}_{11}$ element is calculated in the following.

$$\underline{F}_{11} = \frac{1}{U_{1i}} \sum_j F_{ij}\ U_{1j}$$

$$= \frac{1}{U_{1i}}\left[F_{i1}U_{11}+F_{i2}U_{12}+F_{i3}U_{13}+F_{i4}U_{14}+F_{i5}U_{15}+F_{i6}U_{16}\right]$$

$$= \frac{1}{U_{11}}\left[F_{11}U_{11}+F_{12}U_{12}+F_{13}U_{13}\right]+\frac{1}{U_{12}}\left[F_{21}U_{11}+F_{22}U_{12}+F_{23}U_{13}\right]$$

$$+ \frac{1}{U_{13}}\left[F_{31}U_{11}+F_{32}U_{12}+F_{33}U_{13}\right]$$

$$= \frac{1}{\sqrt{3}}\left(\frac{3}{\sqrt{3}}F_r+\frac{6}{\sqrt{3}}F'_r\right)$$

$$= F_r + 2F'_r$$

The elements of the symmetrized $\underline{G}$ matrix of PH_3 and PD_3 were calculated in exactly the same way. This $\underline{G}$ matrix takes the following form.

	$S_r(A)$	$S_\alpha(A)$	$S_r(E)$	$S_\alpha(E)$	$S_r(E)$	$S_\alpha(E)$
$S_r(A)$	$G_r+2G'_r$	$G'_{r\alpha}+2G_{r\alpha}$	0	0	0	0
$S_\alpha(A)$	$G'_{r\alpha}+2G_{r\alpha}$	$G_\alpha+2G'_\alpha$	0	0	0	0
$S_r(E)$	0	0	$G_r-G'_r$	$G'_{r\alpha}-G_{r\alpha}$	0	0
$S_\alpha(E)$	0	0	$G'_{r\alpha}-G_{r\alpha}$	$G_\alpha-G'_\alpha$	0	0
$S_r(E)$	0	0	0	0	$G_r-G'_r$	$G'_{r\alpha}-G_{r\alpha}$
$S_\alpha(E)$	0	0	0	0	$G'_{r\alpha}-G_{r\alpha}$	$G_\alpha-G'_\alpha$

Replacing the numerical values into the matrix above, we obtain

$$\underline{G}_{PH_3} = \begin{bmatrix} 1.020205 & -0.0598106 & 0 & 0 & 0 & 0 \\ -0.0598106 & 1.9702104 & 0 & 0 & 0 & 0 \\ 0 & 0 & 1.026679 & 0.0368284 & 0 & 0 \\ 0 & 0 & 0.036828 & 2.0949333 & 0 & 0 \\ 0 & 0 & 0 & 0 & 1.026679 & 0.0368284 \\ 0 & 0 & 0 & 0 & 0.0368284 & 2.0949333 \end{bmatrix}$$

$$\underline{G}_{PD_3} = \begin{bmatrix} 0.524469 & -0.0598106 & 0 & 0 & 0 & 0 \\ -0.0598106 & 1.04976654 & 0 & 0 & 0 & 0 \\ 0 & 0 & 0.530943 & 0.0368284 & 0 & 0 \\ 0 & 0 & 0.036828 & 1.067947 & 0 & 0 \\ 0 & 0 & 0 & 0 & 0.530943 & 0.0368284 \\ 0 & 0 & 0 & 0 & 0.0368284 & 1.067947 \end{bmatrix}$$

The computer-calculated $\underline{G}_{PH_3}$ and $\underline{G}_{PD_3}$ follow

$$\underline{G}_{PH_3} = \begin{bmatrix} 1.020204 & -0.042120 & 0 & 0 & 0 & 0 \\ -0.042120 & 0.977092 & 0 & 0 & 0 & 0 \\ 0 & 0 & 1.026679 & 0.025936 & 0 & 0 \\ 0 & 0 & 0.025936 & 1.038949 & 0 & 0 \\ 0 & 0 & 0 & 0 & 1.026679 & 0.025936 \\ 0 & 0 & 0 & 0 & 0.025936 & 1.038949 \end{bmatrix}$$

$$\underline{G}_{PD_3} = \begin{bmatrix} 0.524469 & -0.042120 & 0 & 0 & 0 & 0 \\ -0.042120 & 0.520614 & 0 & 0 & 0 & 0 \\ 0 & 0 & 0.530944 & 0.025936 & 0 & 0 \\ 0 & 0 & 0.025936 & 0.529632 & 0 & 0 \\ 0 & 0 & 0 & 0 & 0.530944 & 0.025936 \\ 0 & 0 & 0 & 0 & 0.025936 & 0.529632 \end{bmatrix}$$

The symmetrized $\underline{G}$ matrix of PH_2D and PHD_2 cannot be obtained by the short method described in ref. 22. Instead, it was obtained by literally multiplying out $U\ G\ U^{+}$. After the tedious manipulation, one gets the matrix in the following page.

Substituting the numerical values into the matrix elements of the matrix in next page, one gets

$$\underline{G}_{PH_2D} = \begin{pmatrix} 0.8549596 & -0.0598106 & -0.2336923 & 0 & 0 & 0 \\ & 1.6800626 & 0 & 0.2169507 & 0 & 0 \\ & & 0 & 0.6961883 & 0.0368284 & 0 & 0 \\ & 0 & & & 1.9415260 & 0 & 0 \\ & 0 & 0 & 0 & 0 & 1.026679 & 0.036828 \\ & 0 & 0 & 0 & 0 & & 1.563683 \end{pmatrix}$$

$$\underline{G}_{PHD_2} = \begin{pmatrix} 0.6897143 & -0.0598106 & 0.2336923 & 0 & 0 & 0 \\ & 1.3565813 & 0 & -0.2169509 & 0 & 0 \\ & & 0 & 0.8614336 & 0.0368284 & 0 & 0 \\ & 0 & & & 1.2213546 & 0 & 0 \\ & 0 & 0 & 0 & 0 & 0.530943 & 0.036828 \\ & 0 & 0 & 0 & 0 & & 1.599197 \end{pmatrix}$$

The computer-calculated $\underline{G}_{PH_2D}$ and $\underline{G}_{PHD_2}$ are

$$G_{PH_2D} = \begin{pmatrix} 0.854959 & -0.042120 & -0.233692 & 0 & 0 & 0 \\ & 0.824933 & 0 & 0.107593 & 0 & 0 \\ & & 0 & 0.696189 & 0.025936 & 0 & 0 \\ & 0 & & & 0.962869 & 0 & 0 \\ & 0 & 0 & 0 & 0 & 1.026679 & 0.025936 \\ & 0 & 0 & 0 & 0 & & 0.775484 \end{pmatrix}$$

$$G_{PHD_2} = \begin{pmatrix} 0.689714 & -0.042120 & 0.233692 & 0 & 0 & 0 \\ & 0.672774 & 0 & -0.107593 & 0 & 0 \\ & & 0 & 0.861434 & 0.025936 & 0 & 0 \\ & 0 & & & 0.605712 & 0 & 0 \\ & 0 & 0 & 0 & 0 & 0.530944 & 0.025936 \\ & 0 & 0 & 0 & 0 & & 0.793097 \end{pmatrix}$$

We are now ready to calculate the frequencies of PH_2D and PHD_2. The stretching frequencies will be first calculated and then the bending ones. For the first purpose, we replace the calculated $\underline{G}$ and the observed $\lambda = (2\pi c\tilde{\nu})^2$ of PH_3 into the following secular equation to

	$S_r(A')$	$S_\alpha(A')$	$S_{rE}(A')$	$S_{\alpha E}(A')$	$S_{rE}(A'')$	$S_{\alpha E}(A'')$
$S_r(A')$	$\frac{1}{3}(G_{r_1}+2G_r+6G'_r)$	$G'_{r\alpha}+2G_{r\alpha}$	$\frac{\sqrt{2}}{3}(G_{r_1}-G_r)$	0	0	0
$S_\alpha(A')$	$G'_{r\alpha}+2G_{r\alpha}$	$\frac{1}{3}(G_\alpha+4G'_\alpha+2G'_{\alpha_1}+2G_{\alpha_1})$	0	$\frac{\sqrt{2}}{3}(G_\alpha+G'_\alpha-G'_{\alpha_1}-G_{\alpha_1})$	0	0
$S_{rE}(A')$	$\frac{\sqrt{2}}{3}(G_{r_1}-G_r)$	0	$\frac{1}{3}(2G_{r_1}+G_r-3G'_r)$	$G'_{r\alpha}-G_{r\alpha}$	0	0
$S_{\alpha E}(A')$	0	$\frac{\sqrt{2}}{3}(G_\alpha+G'_\alpha-G_{\alpha_1}-G'_{\alpha_1})$	$G'_{r\alpha}-G_{r\alpha}$	$\frac{1}{3}(2G_\alpha-4G'_\alpha+G'_{\alpha_1}+G_{\alpha_1})$	0	0
$S_{rE}(A'')$	0	0	0	0	$G_r-G'_r$	$G'_{r\alpha}-G_{r\alpha}$
$S_{\alpha E}(A'')$	0	0	0	0	$G'_{r\alpha}-G_{r\alpha}$	$G_{\alpha_1}-G'_{\alpha_1}$

obtain a force constant for a given vibration, assuming the high and low frequencies are separable.

$$|\underline{F}\,\underline{G} - \lambda| = 0$$

Next, the same calculation is repeated for PD_3 to find another force constant of the same vibration. The averaged value of these two force constants is then replaced, along with the $\underline{G}_{PH_2D}$ and $\underline{G}_{PHD_2}$, into the corresponding secular equation to find the eigenvalues of PH_2D and PHD_2. The following illustrates this calculation in steps. The stretching frequencies of PH_2D:

$$\lambda_m = \omega_m^2 = (2\pi c\tilde{\nu}_m)^2 = \frac{f}{m} = fg_m$$

where the subscript m means that the unit used is in terms of a single atom rather than a mole of atom which was previously used in our $\underline{G}$ matrix calculation. Expressed in the molar unit, the above equation becomes

$$\lambda_M = \frac{(2\pi c\tilde{\nu}_m)^2}{N} = \frac{f}{Nm} = f_M g_M \qquad \text{where } N = \text{Avogadro's number}$$

$$= \left[\frac{\tilde{\nu}_m}{\left(\frac{N}{4\pi^2 c^2}\right)^{\frac{1}{2}}}\right]^2 \qquad c = \text{speed of light}$$

$$= \left[\frac{\tilde{\nu}_m}{1.302876 \times 10^{0.5}}\right]^2 \text{ cm}^2 \cdot \text{sec}^{-2}$$

$$= \left[\frac{2301}{1302.876}\right]^2 \times 10^5 \text{ sec}^{-2}$$

$$= 3.11897 \times 10^5 \text{ sec}^{-2}$$

Since the $\underline{G}_{PH_3}$ and $\underline{F}_{PH_3}$ are in nice diagonal-block form, it is possible to decompose the whole secular equation into sub-

secular-equations each of which corresponds to one of the diagonal blocks. The first block is of A_1 symmetry.

$$\left| \begin{bmatrix} \underline{F}_{11} & \underline{F}_{12} \\ \underline{F}_{21} & \underline{F}_{22} \end{bmatrix} \begin{bmatrix} 1.020205 & -0.0598106 \\ -0.0598106 & 1.9702104 \end{bmatrix} - \begin{bmatrix} \lambda & 0 \\ 0 & \lambda \end{bmatrix} \right| = 0$$

Now, the high-low frequency separation approximation says that it is roughly correct to leave out the column and row corresponding to the coordinate whose diagonal force constant (i.e. the ν_2 constant here) vanishes.

$$\underline{F}_{11}\underline{G}_{11} = \lambda_1 \quad \text{or} \quad \underline{F}_{11} = \frac{3.11897 \times 10^5 \text{ sec}^{-2}}{1.020205 \text{ g}^{-1}} = 3.0572 \text{ mdyne}\cdot\text{Å}^{-1}$$

Likewise,

$$\lambda_3 = \left(\frac{2313.2}{1302.876}\right)^2 \times 10^5 \text{ sec}^{-2} \Rightarrow \underline{F}_{33} = \frac{3.15213 \times 10^5 \text{sec}^{-2}}{1.026679 \text{ g}^{-1}} =$$

$$3.07022 \text{ mdyne}\cdot\text{Å}^{-1}$$

In the same manner, the following quantities are obtained for PD_3 (prime refers to deuterium).

$$\lambda_1' = \left(\frac{1667.7}{1302.876}\right)^2 \times 10^5 \text{sec}^{-2} \Rightarrow \underline{F}_{11}' = \frac{1.638912 \times 10^5 \text{ sec}^{-2}}{0.524469 \text{ g}^{-1}} =$$

$$3.1249 \text{ mdyne}\cdot\text{Å}^{-1}$$

$$\lambda_3' = \left(\frac{1682}{1302.876}\right)^2 \times 10^5 \text{sec}^{-2} \Rightarrow \underline{F}_{33}' = \frac{1.66659 \times 10^5 \text{ sec}^{-2}}{0.530943 \text{ g}^{-1}} =$$

$$3.13893 \text{ mdyne}\cdot\text{Å}^{-1}$$

The average force constants are

$\underline{F}_{11} = 3.0911$ mdyne A^{-1}

$\underline{F}_{33} = 3.1046$ mdyne A^{-1}.

The next step is to apply the high-low frequency separation approximation to the 4x4 block and the 2x2 blocks of the secular equation, $|\underline{FG}-E\lambda| = 0$, of PH_2D and PHD_2. The result is a simpler equation as the one shown below. Note that the $\underline{F}_{13}$ and $\underline{F}_{31}$ elements are both zero, since $F_{r_1} = F_r$. For simplicity, the 10^5 factor of the λ's, and the units of the λ's and the $\underline{F}_{ii}$'s are left out in the following calculation.

$$\left|\begin{bmatrix} \underline{F}_{11} & 0 & 0 \\ 0 & \underline{F}_{33} & 0 \\ 0 & 0 & \underline{F}_{33} \end{bmatrix}\begin{bmatrix} \underline{G}_{11} & \underline{G}_{13} & 0 \\ \underline{G}_{31} & \underline{G}_{55} & 0 \\ 0 & 0 & G_{55} \end{bmatrix} - \begin{bmatrix} \lambda & 0 & 0 \\ 0 & \lambda & 0 \\ 0 & 0 & \lambda \end{bmatrix}\right| = 0$$

$$\left|\begin{bmatrix} 3.0911 & 0 & 0 \\ 0 & 3.1046 & 0 \\ 0 & 0 & 3.1046 \end{bmatrix}\begin{bmatrix} 0.85496 & -0.23369 & 0 \\ -0.23369 & 0.69619 & 0 \\ 0 & 0 & 1.02668 \end{bmatrix} - \begin{bmatrix} \lambda & 0 & 0 \\ 0 & \lambda & 0 \\ 0 & 0 & \lambda \end{bmatrix}\right| = 0$$

(i) $\lambda_3(A'') = 3.1046 \times 1.02668 = 3.1874$

$\tilde{\nu}_3(A'') = \sqrt{3.1874(1302.9)^2} = 2326.1$ cm^{-1}

(ii)

$$\left|\begin{bmatrix} 2.64277 & -0.72236 \\ -0.72551 & 2.16139 \end{bmatrix} - \begin{bmatrix} \lambda & 0 \\ 0 & \lambda \end{bmatrix}\right| = 0$$

$$\lambda^2 - 4.80416\,\lambda + 5.18798 = 0$$

$$\lambda = \frac{4.80416 \pm 1.52579}{2}$$

$$\lambda_1(A') = 1.63919 \Rightarrow \tilde{\nu}_1(A') = \sqrt{1.63919(1302.9)^2} = 1668.1 \text{ cm}^{-1}$$

$$\lambda_3(A') = 3.16498 \Rightarrow \tilde{\nu}_3(A') = \sqrt{3.16498(1302.9)^2} = 2317.9 \text{ cm}^{-1}$$

The stretching frequencies of PHD_2 :

$$\left|\begin{bmatrix} 3.0911 & 0 & 0 \\ 0 & 3.1046 & 0 \\ 0 & 0 & 3.1046 \end{bmatrix}\begin{bmatrix} 0.6897143 & 0.2336923 & 0 \\ 0.2336923 & 0.8614336 & 0 \\ 0 & 0 & 0.530943 \end{bmatrix} - \begin{bmatrix} \lambda' & 0 & 0 \\ 0 & \lambda' & 0 \\ 0 & 0 & \lambda' \end{bmatrix}\right| = 0$$

(i) $\lambda_3(A'') = 3.1046 \times 0.530943 \Rightarrow$

$$\tilde{\nu}_3(A'') = \sqrt{1.64837(1302.9)^2} = 1672.8 \text{ cm}^{-1}$$

(ii) $\lambda^2 - 4.8064\,\lambda + 5.18763 = 0$

$$\lambda = \frac{4.8064 \pm 1.5333}{2}$$

$$\lambda_1(A') = 1.6366 \Rightarrow \tilde{\nu}_1(A') = 1668 \text{ cm}^{-1}$$

$$\lambda_3(A') = 3.16985 \Rightarrow \tilde{\nu}_3(A') = 2319.7 \text{ cm}^{-1}$$

At this stage, it is desired to see if the high-low frequency separation has caused any significant error in calculated frequencies or not. According to the product rule, one has (if the separation is valid)

$$\frac{F'_{11}G'_{11}}{F_{11}G_{11}} = \frac{\lambda'_1}{\lambda_1} = \frac{\nu'^2_1}{\nu_1^2}$$

or $\dfrac{G'_{11}}{G_{11}} = \dfrac{\nu'^2_1}{\nu_1^2}$, since the force field of PD_3 is the same as that of PH_3.

$$\frac{G'_{11}}{G_{11}} = \frac{0.5524469}{1.020205} = 0.5141$$

$$\frac{\nu_1'^2}{\nu_1^2} = \left(\frac{1667.7}{2301}\right)^2 = 0.5253$$

Thus, the theoretical value is $\frac{0.5253-0.5141}{0.5253} \times 100 = 2.1\%$ off with respect to the observed one. This 2.1% is in the order of magnitude of anharmonicity. Therefore, the high and low frequencies are separable.

The bending frequencies of PH_2D and PHD_2:

To find the bending frequencies of PH_2D and PHD_2, one has to invert both the $\underline{F}$ and $\underline{G}$ matrices. The following inverse $\underline{G}$ matrices, $\underline{K}$'s, were obtained. The 4x4 blocks of $\underline{G}_{PH_2D}$ and $\underline{G}_{PHD_2}$ were inverted by computer.

$$\underline{K}_{H_3} = \begin{bmatrix} 0.9819427 & 0.0298093 & 0 & 0 & 0 & 0 \\ 0.0298093 & 0.5084649 & 0 & 0 & 0 & 0 \\ 0 & 0 & 0.9746288 & -0.01713373 & 0 & 0 \\ 0 & 0 & -0.01713373 & 0.4776433 & & \\ 0 & 0 & 0 & 0 & 0.9746288 & -0.0171337 \\ 0 & 0 & 0 & 0 & -0.01713373 & 0.4776433 \end{bmatrix}$$

$$\underline{K}_{D_3} = \begin{bmatrix} 1.919159 & 0.1093444 & 0 & 0 & 0 & 0 \\ 0.1093444 & 0.958822 & 0 & 0 & 0 & 0 \\ 0 & 0 & 1.887957 & -0.06510664 & 0 & 0 \\ 0 & 0 & -0.06510664 & 0.9386212 & 0 & 0 \\ 0 & 0 & 0 & 0 & 1.887957 & -0.0651066 \\ 0 & 0 & 0 & 0 & -0.06510664 & 0.9386212 \end{bmatrix}$$

$$\underline{K}_{H_2} = \begin{bmatrix} 1.2916979 & 0.0477374 & 0.4343074 & -0.0135726 & 0 & 0 \\ 0.0477374 & 0.6057035 & 0.0196243 & -0.0680550 & 0 & 0 \\ 0.4343074 & 0.0196243 & 1.5838840 & -0.0322472 & 0 & 0 \\ -0.0135726 & -0.0680550 & -0.0322372 & 0.5232749 & 0 & 0 \\ 0 & 0 & 0 & 0 & 0.9748379 & -0.0229597 \\ 0 & 0 & 0 & 0 & -0.0229597 & 0.6400564 \end{bmatrix}$$

$$\underline{K}_{D_2} = \begin{bmatrix} 1.6042150 & 0.0749622 & -0.4363280 & 0.0264726 & 0 & 0 \\ 0.0749622 & 0.7622315 & -0.0261582 & 0.1361850 & 0 & 0 \\ -0.4363280 & -0.0261582 & 1.2810741 & -0.0432757 & 0 & 0 \\ 0.0264726 & 0.1361850 & -0.0432757 & 0.8442587 & 0 & 0 \\ 0 & 0 & 0 & 0 & 1.8864548 & -0.0434437 \\ 0 & 0 & 0 & 0 & -0.0434437 & 0.6263141 \end{bmatrix}$$

The compliance matrix, $\underline{C}$, takes the same form as its inverse, $\underline{F}$.

$$\underline{C} = \begin{pmatrix} \underline{C}_{11} & \underline{C}_{12} & 0 & 0 & 0 & 0 \\ \underline{C}_{21} & \underline{C}_{22} & 0 & 0 & 0 & 0 \\ 0 & 0 & \underline{C}_{33} & \underline{C}_{34} & 0 & 0 \\ 0 & 0 & \underline{C}_{43} & \underline{C}_{44} & 0 & 0 \\ 0 & 0 & 0 & 0 & \underline{C}_{33} & \underline{C}_{34} \\ 0 & 0 & 0 & 0 & \underline{C}_{43} & \underline{C}_{44} \end{pmatrix}$$

To calculate the averaged compliance elements of the bending vibrations, the rows and columns of this compliance matrix, whose diagonal elements correspond to the stretching vibrations are set equal to zero. Thus, the secular equation, $|\underline{K}\,\underline{C} - \phi E| = 0$, of PH_3 reduces to two simple equations.

(i) $\underline{C}_{22}\underline{K}_{22} = \frac{1}{\lambda_2}$

$$\underline{C}_{22} = \frac{1}{\underline{K}_{22}\lambda_2} \quad \frac{1}{0.5084649\ g} \left(\frac{1302.9}{980}\right)^2 10^{-5}\,sec^2 =$$

$$3.476233 \cdot 10^{-5}\ dyne^{-1}\ cm$$

$$= 3.476233\ (mdyne)^{-1}\ \text{Å}$$

(ii) $\underline{C}_{44}\underline{K}_{44} = \frac{1}{\lambda_4}$

$$\underline{C}_{44} = \frac{1}{\underline{K}_{44}\lambda_4} = \frac{1}{0.4776433g}\left(\frac{1302.9}{1097}\right)^2 \quad 10^{-5}\ sec^2$$

$$= 2.953283\ (mdyne)^{-1}\ \text{Å}$$

In the case of PD_3, one has

$$(i)\quad \underline{C}'_{22}\underline{K}'_{22} = \frac{1}{\lambda'_2} \Rightarrow \underline{C}'_{22} = \frac{1}{0.95882}\left(\frac{1302.9}{719}\right)^2 10^{-5}\ g\cdot sec^2 =$$

$$3.424730\ (mdyne)^{-1}\ \text{Å}$$

$$(ii)\quad \underline{C}'_{44}\underline{K}'_{44} = \frac{1}{\lambda'_4} \Rightarrow \underline{C}'_{44} = \frac{1}{0.9386212}\left(\frac{1302.9}{790}\right)^2 10^{-5}\ g\ sec^2 =$$

$$2.89786\ (mdyne)^{-1}\ \text{Å}$$

The average compliance constants for ν_2 and ν_4 are

$$\underline{C}_{22} = 3.450482\ (mdyne)^{-1}\ \text{Å}$$

$$\underline{C}_{44} = 2.925572\ (mdyne)^{-1}\ \text{Å}$$

These average compliance constants and the $\underline{K}_{PHD_2}$ and the K_{PH_2D} are replaced in the secular equation, $|\underline{K}\,\underline{C} - E| = 0$, of PH_2D and PHD_2. The rows and columns whose diagonal elements correspond to the stretching vibrations are again set equal to zero. (In the following calculation, the units of the λ's and the $\underline{C}_{ii}$'s and the factor 10^{-5} are dropped out.)

For PH_2D,

$$\left|\begin{pmatrix} 0.6057035 & -0.068055 & 0 \\ -0.068055 & 0.5232749 & 0 \\ 0 & 0 & 0.6400564 \end{pmatrix}\begin{pmatrix} 3.450482 & 0 & 0 \\ 0 & 2.925572 & 0 \\ 0 & 0 & 2.925572 \end{pmatrix} - \begin{pmatrix} \frac{1}{\lambda} & 0 & 0 \\ 0 & \frac{1}{\lambda} & 0 \\ 0 & 0 & \frac{1}{\lambda} \end{pmatrix}\right| = 0$$

$$\begin{vmatrix} 2.0899690-\frac{1}{\lambda} & -0.1990998 & 0 \\ -0.2348226 & 1.5308784-\frac{1}{\lambda} & 0 \\ 0 & 0 & 1.8725311-\frac{1}{\lambda} \end{vmatrix} = 0$$

(i) $\frac{1}{\lambda_{4}(A'')} = \underline{G}_{44}\underline{K}_{4} = 1.8725311 = \left(\frac{1302.9}{\tilde{\nu}_4(A'')}\right)^2$

$$\tilde{\nu}_4(A'') = \sqrt{\frac{(1302.9)^2}{1.8725311}} = (0.9065528)^{\frac{1}{2}} \times 10^3 = 952.1 \text{ cm}^{-1}$$

(ii) $(2.0899690 - \lambda^{-1})(1.5308784-\lambda^{-1}) - 0.0467531 = 0$

$$\lambda^{-1} = \frac{3.6208474 \pm 0.7068201}{2}$$

$$\frac{1}{\lambda_2(A')} = 1.457014 \Rightarrow \tilde{\nu}_2(A') = \sqrt{\frac{(1302.9)^2}{1.4570136}} = 1079.4 \text{ cm}^{-1}$$

$$\frac{1}{\lambda_4(A')} = 2.1638337 \Rightarrow \tilde{\nu}_4(A') = \sqrt{\frac{(1302.9)^2}{2.1638337}} = 885.7 \text{ cm}^{-1}.$$

For HD_2,

$$\left|\begin{bmatrix} 0.7622315 & 0.1361850 & 0 \\ 0.1361850 & 0.8442587 & 0 \\ 0 & 0 & 0.6263141 \end{bmatrix}\begin{bmatrix} 3.450482 & 0 & 0 \\ 0 & 2.925572 & 0 \\ 0 & 0 & 2.92557 \end{bmatrix}\begin{bmatrix} \lambda^{-1} & 0 & 0 \\ 0 & \lambda^{-1} & 0 \\ 0 & 0 & \lambda^{-1} \end{bmatrix}\right| = 0$$

$$\begin{vmatrix} 2.6300661-\lambda^{-1} & 0.3984190 & 0 \\ 0.4699039 & 2.4699396-\lambda^{-1} & 0 \\ 0 & 0 & 1.8323270-\lambda^{-1} \end{vmatrix} = 0$$

(i) $\frac{1}{\lambda_4(A'')} = 1.8323270 \Rightarrow \tilde{\nu}_4(A'') = \sqrt{\frac{(1302.9)^2}{1.8323270}} = 962.5 \text{ cm}^{-1}$

(ii) $(2.6300661-\lambda^{-1})(2.4699396-\lambda^{-1})-0.1872186 = 0$

$$\lambda^{-1} = \frac{5.1000057 \pm 0.8800653}{2}$$

$$\frac{1}{\lambda_2(A')} = 2.1099702 \Rightarrow \tilde{\nu}_2(A') = \sqrt{\frac{(1302.9)^2}{2.1099702}} = 897 \text{ cm}^{-1}$$

$$\frac{1}{\lambda_4(A')} = 2.9900355 \Rightarrow \tilde{\nu}_4(A') = \sqrt{\frac{(1302.9)^2}{2.9900355}} = 753.5 \text{ cm}^{-1}$$

BIBLIOGRAPHY

1. A. H. Hardin and K. B. Harvey. Infrared Absorption of Solid Phosphine. Canadian Journal of Chemistry 42:84. 1964.

2. Von A. Heinemann. Infrarotspektroskopische Untersuchungen an kristallinem Phosphorwasserstoff, Phosphoniumbromid and Phosphoniumchlorid. Bericht der Bunsengesellschaft fur Physikelische Chemie 68:280. 1964.

3. Marie D. Francia. Infrared Studies of Crystalline and Matrix Isolated Phosphine. Ann Arbor, Michigan. 1970. 193 p.

4. C. C. Stephenson and W. F. Giauque. A Test of the Third Law of Thermodynamics by Means of Two Crystalline Forms of Phosphine. The Heat Capacity, Heat of Vapor Pressure of Phosphine. Entropy of the Gas. The Journal of Chemical Physics 5:149. 1936.

5. R. E. Weston, Jr. and Jacob Bigeleisen. Kinetics of the Exchange of Hydrogen between Phosphine and Water: A Kinetic Estimate of the Acid and Base Strengths of Phosphine. Journal of American Chemical Society 76:3074. 1954. and Equilibrium in the Exchange of Hydrogen between Phosphine and Water. The Journal of Chemical Physics 20:1400. 1952.

6. Solomon Zwerdling and Ralph S. Halford. Direct Production of Spectroscopic Specimens from Single Crystals by Controlled Growth from a Vapor. The Journal of Chemical Physics 23:2215. 1955.

7. R. L. Powell, M.D. Bunch, and R. J. Corruccini. Low Temperature Thermocouples--I. Gold-Cobalt or Constantan versus Copper or Normal Silver. Cryogenics 1:139. 1961.

8. Ralph L. Rosenbaum. Some Low Temperature Thermometry Observations. The Review of Scientific Instruments 40:577. 1969.

9. Ralph L. Rosenbaum. Some Properties of Gold-Iron Thermocouple Wire. The Review of Scientific Instruments 39:890. 1968.

10. R. E. Rondeau. Slush Baths. Journal of Chemical and Engineering Data 11:124. 1966.

11. Raymond Guenther et al. Carbon Resistors for Secondary Cryogenic Thermometry. Cryogenic Technology, March/April 1970, p 13-15.

A. C. Anderson et al. Transfer Heat Below 0.15°K. The Reviews of Scientific Instruments 32:1110. 1961.

J. R. Clement et al. The Low Temperature Characteristics of Carbon-Composition Thermometers. The Review of Scientific Instruments 23:213. 1952.

12. C. H. Wang and P. A. Fleury. Raman Studies of Molecular Motion in Liquid and Solid HCl. The Journal of Chemical Physics 53:2243. 1970.

13. Mitsuo Ito et al. Raman Spectra of Hydrogen and Deuterium Halide Crystals. The Journal of Chemical Physics 50:2949. 1969.

14. R. Savoie and A. Anderson. Infrared and Raman Studies of Crystalline HCℓ, DCℓ, HBr, and DBr. The Journal of Chemical Physics 44:548. 1965.

15. Beckman Instruments Inc. IR-7 Infrared Spectrophotometor Instruction Manual. Fullerton, California. Beckman Instruments Inc. 1960.

16. Cary Instruments (a Varian Subsidiary) Cary Model 82 Laser Raman Spectrophotometer Instruction Manual. 2724 S. Peck Road/

Monrovia, California 91016. Cary Instruments. 1971.

17. Air Products and Chemicals, Inc. Cryo-Tip Instruction and Operating Manual. Advanced Products Department, Allentown, Pennsylvania. Air Products and Chemicals, Inc. 1967.

18. Air Products and Chemicals, Inc. Technical Manual for Displex TM 77°K Helium Refrigerator. Advanced Products Department, 1919 Vultee Street, Allentown, Pennsylvania. Air Products and Chemicals, Inc. 1971.

19. Cryogenic Technology, Inc. Bulletin TDS 5096. Kelvin Park, 266 Second Avenue, Waltham, Massachusetts 02154. Cryogenic Technology, Inc.

20. G. Natta and E. Casazza. La struttura dell'idrogeno fosforato (PH_3) e deil'idrogeno arsenicale (AsH_3). Gazzetta Chimica Italiana 60:851-9. 1930.

21. Eugene R. Nixon. The Infrared Spectrum of Biphosphine. The Journal of Chemical Physics 60:1054. 1956.

22. E. Bright Wilson, Jr., J. C. Decius, and Paul C. Cross. Molecular Vibrations. New York, McGraw-Hill, 1955. p 47.

23. D. P. Craig and S. H. Walmsley. Excitons in Molecular Crystals. New York, W. A. Benjamin, Inc., 1968. 172 p.

24. W. Vedder and D. F. Hornig. Advances in Spectroscopy. Vol. II. New York, Interscience Publishers Inc., 1961. p 189.

25. S. P. S. Porto. Light Scattering with Laser Sources. 13 XII: No 2. 1968. The Spex Speaker.

26. Takehiko Shimanouchi. Tables of Molecular Vibrational Frequencies Part 1. The Superintendent of Documents, U. S. Government

Printing Office, Washington, D. C. 1967. 56 p.

27. E. Lee et al. Investigations on the Vibration Spectra of Certain Condensed Gases at the Temperature of Liquid Nitrogen II. The Infrared and Raman Spectra of Hydro-and Deuterochloric Acid at Liquid Nitrogen Temperatures. Proceedings of Royal Society (London) A176:493. 1940.

28. F. P. Reding and D. F. Hornig. The Vibrational Spectra of Molecules and Complex Ions in Crystals V. Ammonia and Deutero-Ammonia. The Journal of Chemical Physics 19:594. 1951.

29. Kazuo Nakamoto. Infrared Spectra of Inorganic and Coordination Compounds. New York. John Wiley and Sons. 1963. p 83.

30. E. A. Guggenheim. Thermodynamics. 2d ed. New York, Interscience Publishers. 1950. p 150.

31. C. Kittel. Introduction to Solid State Physics. 3d ed. New York, John Wiley and Sons, 1966. p 175.

32. C. H. Townes and A. L. Schawlow. Microwave Spectroscopy. New York. McGraw-Hill, 1955.

33. J. H. Schachtschneider. Vibrational Analysis of Polyatomic Molecules. VI. Fortran IV Programs for Solving the Vibrational Secular Equation and for the Least-Squares Refinement of Force Constants. Emeryville, California, Shell Development Company, 1964.

34. J. H. Schachtschneider. Vibrational Analysis of Polyatomic Molecules. V. Fortran IV Programs for Setting-up the Vibrational Secular Equation. Emeryville, California, Shell Development Company, 1964.

35. J. L. Duncan and I. M. Mills. The Calculation of Force Constants and Normal Coordinates--IV XH_4 and XH_3 Molecules. Spectrochimica Acta 20:523-46. 1964.

36. J. W. Nibler and G. C. Pimentil. Force Constant Displays of Unsymmetric Molecular Isotopes of H_2O, H_2S, H_2Se, and HCCH. Journal of Molecular Spectroscopy 26:294. 1968.

37. J. C. Decius. Compliance Matrix and Molecular Vibrations. The Journal of Chemical Physics 38:241. 1963.

38. J. C. Decius and E. Bright Wilson, Jr. Sum Rules for the Vibration Frequencies of Isotopic Molecules. The Journal of Chemical Physics 19:1409. 1951.

39. Elliot R. Bernstein. Site Effects in Isotopic Mixed Crystals--Site Shift, Site Splitting, Orientational Effect, and Intermolecular Fermi Resonance in the Vibrational Spectrum of Benzene. The Journal of Chemical Physics 50:4842. 1969.

40. Laurance L. Oden and J. C. Decius. The Infrared Spectrum of Ammonium Thiocyanate from 90° to 300°K. Spectrochimica Acta 20:667-74. 1964.

41. L. V. Belyavskaya, V. N. Shabur, and V. P. Morozov. On the Calculation of Fundamental Frequencies and Vibrational Forms of Mono-and Deutero-Substituted Pyramidal Hydrides. Optics and Spectroscopy 25(1):62-66. 1968.

42. Mark W. Zemansky. Heat and Thermodynamics. 5th ed. New York, McGraw-Hill, 1968. p 377-78.

43. E. S. R. Gopal. Specific Heats at Low Temperatures. New York, Plenum Press, 1966. p 161.

44. Linus Pauling. The Nature of Chemical Bonding.

45. E. Bright Wilson, Jr. The Statistical Weights of the Rotational Levels of Polyatomic Molecules, Including Methane, Ammonia, Benzene, Cyclopropane, and Ethylene. The Journal of Chemical Physics 3:276. 1935.

46. W. G. Fateley et al. Infrared and Raman Selection Rules for Lattice Vibrations: The Correlation Method. Applied Spectroscopy 25:155. 1971.

47. Ralph S. Halford. Motions of Molecules in Condensed Systems: I. Selection Rules, Relative Intensities, and Orientation Effects for Raman and Infrared Spectra. The Journal of Chemical Physics 14:8. 1946.

48. Harry C. Allen, Jr. and Paul C. Cross. Molecular Vib-rotors. New York, John Wiley and Sons, Inc., 1963. p 76.

49. Gerhard Herzberg. Molecular Spectra and Molecular Structure. Vol. 2. Princeton, New Jersey, D. Van Nostrand Company, Inc., 1945. p 224.

50. V. M. McConaghie and H. H. Nielson. The Fundamental Absorption Bands in the Infrared Spectrum of Phosphine. The Journal of Chemical Physics 21:1836. 1953.